UNICA

UNIVERSITÀ
DEGLI STUDI
DI CAGLIARI

Ph.D. DEGREE IN
Physics

Cycle XXXVII

TITLE OF THE Ph.D. THESIS

Phenomenology of Neutrino Interactions for Coherent Neutrino-Nucleus Scattering and Dark Matter Experiments

Scientific Disciplinary Sector(s)

FIS/02 & FIS/01

Ph.D. Student:	Mattia Atzori Corona
Supervisor	Dott. Matteo Cadeddu

Final exam. Academic Year 2023/2024
Thesis defence session: January 2025

UNIVERSITÀ DEGLI STUDI DI CAGLIARI

PhD School of Physics
Faculty of Science

THESIS FOR THE DEGREE OF DOCTOR OF PHILOSOPHY

Phenomenology of Neutrino Interactions for Coherent Neutrino-Nucleus Scattering and Dark Matter Experiments

---

Academic Advisor:
Dott. Matteo Cadeddu

PhD Candidate:
Mattia Atzori Corona
200/1053/65064
Cycle: XXXVII
Submitted 2023/2024

Short Abstract

Despite the success of the Standard Model in describing electromagnetic, weak, and strong forces, several unanswered questions indicate that it is incomplete. Therefore, searching for any deviations from this framework is highly intriguing.
This thesis focuses on an in-depth examination of the Standard Model by leveraging the signals from the faintest particle, i.e. the neutrino. To do so, we will exploit neutrino elastic scattering at low energies to search for new physics signatures in coherent elastic neutrino-nucleus scattering (CEνNS) and dark matter experiments. Furthermore, by leveraging the formalism described in the thesis, we will precisely compute the signals from both CEνNS and neutrino elastic scattering off atomic electrons (νES) in the upcoming DarkSide-20k dark matter experiment. Throughout this thesis, we will give a detailed overview of the emerging field of CEνNS searches, describing the main features of the measurements available at the time of writing this thesis, provided by the COHERENT and NCC-1701 detectors. In addition, we will discuss the details of the upcoming NUCLEUS experiment. Using currently available data, we will not only provide insights into electroweak and nuclear physics but also establish some of the strongest existing bounds in the literature on new physics scenarios predicting exotic neutrino properties. We will also deeply investigate the neutrino charge radius, the only non-zero neutrino electromagnetic property predicted by the Standard Model, whose imprint in experimental data is so small that it has never been experimentally observed. By refining the theoretical description of the neutrino charge radius contribution to the CEνNS process, we will obtain competitive bounds on this quantity. In addition, in this thesis, we will explore the existence of new light gauge bosons that can mediate the CEνNS interaction. This work demonstrates the potential of low-threshold CEνNS experiments to impose leading constraints on a variety of light mediator models. Throughout the thesis, we will also study the sensitivity of future COHERENT and NUCLEUS CEνNS experiments in detecting such new physical signatures, as well as their ability to extract electroweak or nuclear physics parameters.

Contents

List of Publications

List of the publications in which I was involved that are discussed in this thesis work

[1] **M. Atzori Corona**, M. Cadeddu, N. Cargioli, M. Finelli, P. Vorabbi, "*Incorporating the weak mixing angle dependence to reconcile the neutron skin measurement on ^{208}Pb by PREX-II*", Phys.Rev.C 105 (2022) 5, 055503

[2] **M. Atzori Corona**, M. Cadeddu, N. Cargioli, F. Dordei, C. Giunti, Y.F. Li, E. Picciau, C.A. Ternes, Y.Y. Zhang, "*Probing light mediators and (g-2)$_\mu$ through detection of coherent elastic neutrino nucleus scattering at COHERENT*", Published in Journal of High Energy Physics 05 (2022) 109

[3] **M. Atzori Corona**, M. Cadeddu, N. Cargioli, F. Dordei, C. Giunti, Y.F. Li, C.A. Ternes, Y.Y. Zhang, "*Impact of the Dresden-II and COHERENT neutrino scattering data on neutrino electromagnetic properties and electroweak physics*", Published in Journal of High Energy Physics 09 (2022) 164

[4] **M. Atzori Corona**, W.M. Bonivento, M. Cadeddu, N. Cargioli, F. Dordei, "*New constraint on neutrino magnetic moment and neutrino millicharge from LUX-ZEPLIN dark matter search results*", Published in Physical Review D 107 (2023) 5, 053001

[5] **M. Atzori Corona**, M. Cadeddu, N. Cargioli, F. Dordei, C. Giunti, G. Masia, "*Nuclear neutron radius and weak mixing angle measurements from latest COHERENT CsI and atomic parity violation Cs data*", Published in European Physical Journal C 83 (2023) 7, 683

[6] **M. Atzori Corona**, M. Cadeddu, N. Cargioli, F. Dordei, C. Giunti, "*On the impact of the Migdal effect in reactor CEνNS experiments*", Phys.Lett.B 852 (2024) 138627

[7] **M. Atzori Corona**, M. Cadeddu, N. Cargioli, F. Dordei, C. Giunti, "*Momentum dependent flavor radiative corrections to the coherent elastic neutrino-nucleus scattering for the neutrino charge-radius determination*", JHEP 05 (2024) 271

[8] **M. Atzori Corona**, M. Cadeddu, N. Cargioli, F. Dordei, C. Giunti, "*Refined determination of the weak mixing angle at low energy*", Phys.Rev.D 110 (2024) 3, 033005

[9] **DarkSide-20k Collaboration** "*DarkSide-20k sensitivity to light dark matter particles*", arXiv: 2407.05813

Additional publications in which I was involved that are not discussed in this thesis

[10] **M. Atzori Corona**, R. Murgia, M. Cadeddu, M. Archidiacono, S. Gariazzo, C. Giunti, S. Hannestad "*Pseudoscalar sterile neutrino self-interactions in light of Planck, SPT and ACT data*", JCAP 06 (2022) 06, 010

Additional publications in which I was involved in the context of the DarkSide-20k and Global Argon Dark Matter Collaborations, can be found in Refs. [11–16].

Introduction

During the last century, the Standard Model of particle physics has proven to be an astonishingly successful theory based on a few symmetry principles. Its extraordinary predictive capabilities have led scientists to embrace it as the leading theory for explaining the fundamental components of nature. Despite its success, compelling experimental evidence suggests that the Standard Model is incomplete, with several unresolved issues pointing towards extensions of the standard paradigm. Many of these unresolved issues are related to neutrinos, such as the origin of their small mass and the possibility that they could be Majorana particles, which would imply lepton number violation. Therefore, neutrino interactions provide a crucial tool for testing the Standard Model theory and offer a novel way to probe effects beyond it.

To do so, this thesis will explore the phenomenology of neutrino scattering at low energies, namely coherent elastic neutrino nucleus scattering (CEνNS) and the elastic neutrinos scattering off atomic electrons (νES). Although νES is comprehensively understood both theoretically and experimentally, and its potential for fundamental physics tests is widely acknowledged, the CEνNS era has only just begun. In the CEνNS process, the neutrino interacts with the nucleus as a whole, i.e. coherently, making the cross section roughly proportional to the square of the number of neutrons in the target nucleus. For this reason, the CEνNS cross section can become several orders of magnitude larger than that of other low-energy neutrino interactions, even though the single outcome of this process is a very small nuclear recoil that is extremely difficult to detect. The first CEνNS observation was reported in 2017 by the COHERENT Collaboration, 43 years after its theoretical prediction, and since then it has proven to be a powerful tool for probing a plethora of diverse physics scenarios, particularly in the realm of electroweak interactions. This has inspired a global effort to detect the small nuclear recoil produced by these interactions, through the development of new technolo-

gies and the exploration of various low-energy neutrino sources. Currently, there are three CEνNS measurements reported by the COHERENT Collaboration: one using a cesium-iodide (CsI) scintillator crystal, another with a liquid argon detector (LAr), and a very recent measurement employing germanium crystals. These results were obtained by exploiting neutrinos produced from pion decay at rest at the Spallation Neutron Source, located at Oak Ridge National Laboratory in Tennessee. Additionally, the first observation of CEνNS from reactor antineutrinos was reported by the NCC-1701 detector, installed at the Dresden-II nuclear power plant in Illinois, although this result is still debated within the community. To complete the picture, recent hints of a CEνNS signal from solar neutrinos have been reported by the XENONnT and PandaX dark matter experiments, highlighting the strong complementarity between CEνNS and dark matter searches.

In this thesis, we will benefit from available data from CEνNS and dark matter experiments to probe a variety of physics parameters. These include the weak mixing angle, which determines the strength of the couplings in electroweak theory, the neutrino charge radius, which is the only neutrino electromagnetic property predicted to be non-zero in the Standard Model, and the nuclear neutron radius. Furthermore, these data allow us to explore scenarios beyond the Standard Model, such as those in which the neutrino acquires a magnetic moment or a small electric charge, and we will search for new particles which can mediate neutrino interactions, so-called Z' models.

Building upon the lessons learned by existing data, this thesis will also discuss the prospects for the NUCLEUS experiment, whose aim is to precisely characterize the CEνNS cross section by leveraging neutrinos produced at the Chooz nuclear power plant. The experiment employs advanced technology based on cryogenic calorimeters, featuring gram-scale $CaWO_4$ detectors. Indeed, we will project the physics reach of a NUCLEUS-like experiment under various experimental configurations. We will also emphasize the relevance of CEνNS and νES in direct dark matter searches by computing the expected neutrino signal for the DarkSide-20k experiment.

This thesis is organized as follows.

Chap. 1 will introduce low-energy electroweak physics and will outline the theoretical framework to evaluate the cross sections of CEνNS and νES scattering.

Chap. 2 will accurately compute the neutrino background expected in the DarkSide-20k dark matter experiment due to both the CEνNS and νES channels.

Chap. 3 will discuss the details of the COHERENT detectors whose data have been analysed in this work, together with a detailed description of the statistical methods employed.

Chap. 4 will discuss the current status of CEνNS searches from reactor antineutrino sources. We will also present a critical overview of the NCC-1701 CEνNS observation, discussing, in particular, some well-motivated physical effects which might modify the detector response at low energies.

Chap. 5 will be devoted to the search for CEνNS with the NUCLEUS experiment. It will address the main challenges faced by the experiment and discuss the statistical methods relevant to the NUCLEUS science case.

Chap. 6 will present the constraints on nuclear and electroweak physics obtained from COHERENT CsI, LAr and Dresden-II data.

Chap. 7 will focus on the constraints obtained on neutrino electromagnetic properties from CEνNS and the LUX-ZEPLIN dark matter experiment, considering also the νES channel. Specifically, it will address the neutrino charge radius, the neutrino magnetic moment and the neutrino electric charge.

Finally, Chap. 8 will search for beyond the Standard Model scenarios via the introduction of an additional boson mediator (either vector or scalar), which can arise from the existence of an additional fundamental gauge symmetry.

Through these chapters, we will present the sensitivity of future NUCLEUS and COHERENT experiments for different physics scenarios, starting from the current situation and with an eye towards future developments.

1 Low-Energy Neutrino Elastic Scattering

Opening

This chapter will explore the details of neutrino elastic scattering at low energies, specifically for E_ν below 100 MeV, addressing two processes relevant to this thesis: the elastic scattering off nuclei and off atomic electrons. The theoretical framework to evaluate the cross section from first principles will be presented, describing the phenomenology of the interaction considered. The formalism of radiative correction to such neutrino scattering processes will also be shown, based on the results from Refs. [4, 7], and will be adopted for the rest of this thesis.

1.1 Introduction to Electroweak Physics

The Standard Model (SM) of particle physics is a theoretical framework that describes the fundamental constituents of our universe and the forces governing their interactions. It has been extensively tested and validated through countless experiments over the past several decades, manifesting itself as one of the most significant achievements in the history of science. The SM encompasses three of the four known fundamental forces: electromagnetic, weak, and strong interactions, with the exception of gravity. Within the SM picture, these forces are mediated by gauge bosons, which govern the interactions between the elementary particles, i.e. quarks and leptons, which constitute the ordinary matter we observe. Fig. 1.1 summarizes existing elementary particles and bosons, together with their properties, specifically mass, charge and intrinsic spin. Moreover, the Standard Model predicts that each particle is accompanied by its own antiparticle. Within this particle zoo, this thesis will mainly focus on neutrinos. Their existence was predicted by Pauli around the 1930s while studying the now-familiar β-decay

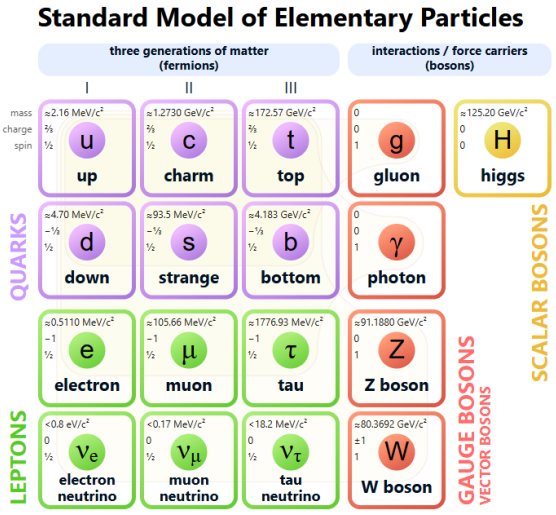

Figure 1.1: Picture [20] collecting the elementary particles which constitutes the Standard Model of particle physics. Quarks, leptons and bosons are identified by different colors, together with their properties, i.e. mass charge and spin.

process, i.e. the radioactive decay of a heavy nucleus into a lighter one [17]. Even though many years have passed since the neutrino discovery in 1953 [18], many open questions are related to them and their study is still offering the possibility to enhance our understanding of the fundamental physics of nature. Neutrinos, indeed, offer a unique tool to study weak interactions and the *electroweak* theory, as we will clarify in a while. They are, in fact, the only known fundamental particles that are electrically neutral, allowing them to interact exclusively through the exchange of the electroweak neutral gauge boson Z^0 and the charged bosons $W^{\pm}$. The W and Z^0 have a mass which is quite well measured [19] and correspond to[1]

$$m_W = 80.379 \pm 0.12 \ \ \text{GeV}/c^2, \qquad m_{Z^0} = 91.1876 \pm 0.0021 \ \ \text{GeV}/c^2. \tag{1.1}$$

If the energy of the interaction considered is much smaller than the mass of the mediator, the electroweak propagator will be roughly suppressed by a factor $1/m^2_{W,Z^0}$ compared to the electromagnetic propagator, which makes such interactions much "weaker" compared to the electromagnetic one.

It is worth commenting on the theory of electroweak interactions. The gauge structure of the weak interaction is $\mathrm{SU}(2)_L$, where the subscript L indicates that weak interactions violate the parity. If the neutral current boson would correspond to the third gauge boson $W^{(3)}$ of the $\mathrm{SU}(2)_L$ gauge symmetry, this would imply that

[1]Note that $c = 299\ 792\ 458$ m/s [19] represents the speed of the light and will be set to unity for the rest of this thesis unless otherwise specified.

the weak neutral current coupled only to left-handed particles and right-handed antiparticles [21]. However, experiments showed that the physical gauge boson responsible for the neutral weak currents couples to both left- and right-handed states, even if not equally. The SM is therefore built based on the Glashow, Salam and Weinberg (GSW) model, which proposes to replace the $U(1)$ gauge symmetry of electromagnetism with a new $U(1)_Y$ local gauge symmetry giving rise to a new gauge field B_μ that couples to a new charge, named weak hypercharge Y. Within the GSW model, the physical photon (γ) and weak neutral current (Z^0) bosons are described by the A_μ and Z_μ fields respectively, obtained as a combination of the B_μ and $W_\mu^{(3)}$ fields mixed by the angle ϑ_W, according to

$$\begin{pmatrix} A_\mu \\ Z_\mu \end{pmatrix} = \begin{pmatrix} \cos\vartheta_W & \sin\vartheta_W \\ -\sin\vartheta_W & \cos\vartheta_W \end{pmatrix} \begin{pmatrix} B_\mu \\ W_\mu^{(3)} \end{pmatrix}. \tag{1.2}$$

In the GSW model of electroweak theory, electromagnetic and weak interactions are hence unified into a unique gauge group $\mathrm{SU}(2)_L \otimes U(1)_Y$, implying that the two interactions are intimately related. The $\vartheta_W \simeq$ is known as the weak mixing angle[2], or Weinberg angle, and it is of pivotal importance in the SM framework. Moreover, this mixing arises naturally in the Higghs mechanism [21]. From the equivalence between the hypercharge of a left-handed electron and a left-handed neutrino, it is easy to extract the relation between the electromagnetic and weak coupling, i.e. [21]

$$e_0 = g \sin\vartheta_W, \tag{1.3}$$

where e_0 is the electric charge and g the coupling of the weak interaction. Similarly, it is possible to relate the coupling associated to the $U(1)_Y$ gauge group, g', to the electric charge, namely

$$e_0 = g' \cos\vartheta_W. \tag{1.4}$$

As could be expected, Eqs. 1.3 and 1.4 depend on the weak mixing angle and combining the latter two equations we find

$$\sin^2\vartheta_W = \frac{g^2}{g^2 + g'^2}. \tag{1.5}$$

The couplings in Eq. 1.5 are proportional to the masses of the gauge bosons medi-

[2]In this thesis we will refer to the square of the sine of this angle, $\sin^2\vartheta_W$, with the same name.

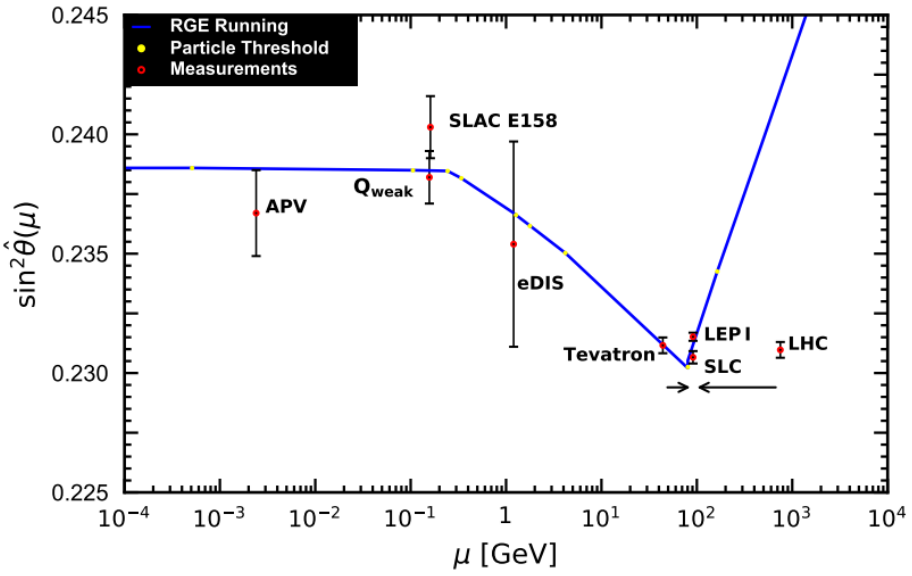

Figure 1.2: Variation of $\sin^2\vartheta_{\mathrm{W}}$ with scale μ as reported by the particle data group (PDG) [19]. The SM prediction is shown as the solid curve, together with experimental determinations in black at the Z^0-pole [19] (Tevatron, LEP1, SLC, LHC), from APV on cesium [22, 23] (APV(Cs)), Møller scattering [24] (SLAC E158), deep inelastic scattering of polarized electrons on deuterons [25] (eDIS) and the result from the proton's weak charge [26] (Q_{weak}). For illustration purposes, the Tevatron and LHC points have been shifted horizontally to the left and right, respectively.

ating the interaction according to the electroweak symmetry breaking, such that the weak mixing angle can be defined in terms of the masses of the W and Z^0 through the simple relation [19, 21]

$$\sin^2\vartheta_W = 1 - \frac{m_W^2}{m_{Z^0}^2}. \tag{1.6}$$

The latter is valid only at tree level, i.e. the lowest order of perturbation theory. In reality, radiative corrections arising from higher-order diagrams in the perturbation theory are responsible for the dependence of the weak mixing angle on the energy scale considered. One popular renormalization scheme, often adopted to evaluate the running of $\sin^2\vartheta_{\mathrm{W}}$, is the so-called minimal subtraction ($\overline{\mathrm{MS}}$) scheme [19], where the quantity

$$\sin^2\hat{\vartheta}_W(\mu) \equiv \frac{\hat{g}'^2(\mu)}{\hat{g}^2(\mu) + \hat{g}'^2(\mu)}\,, \tag{1.7}$$

is defined to be valid at every order of perturbation theory. The couplings $\hat{g}$ and $\hat{g}'$ are defined by the modified minimal subtraction and μ represents an energy scale, often set to be the mass of the Z^0 boson. A summary of the most precise weak mix-

ing angle measurements as a function of the energy scale, μ, is shown in Fig. 1.2, along with the SM predicted running of $\sin^2\vartheta_{\mathrm{W}}$, calculated in the $\overline{\mathrm{MS}}$ renormalization scheme [19, 27, 28] across the whole energy range of experimental measurements. More in detail, at the LEP Collider [29], it was possible to achieve the most precise measurements of $\sin^2\vartheta_{\mathrm{W}}$ in the high-energy electroweak sector, in perfect agreement with other collider determinations [19] (Tevatron, LHC and SLC). In the mid-energy range, the most precise result has been derived from the measurement of the weak charge of the proton, Q_W^p, performed by the Q_{weak} Collaboration and found to be $Q_W^p = 0.0719 \pm 0.0045$ [26], showing an excellent agreement with the predicted SM running. Moving to the low-energy sector [30], the most precise weak mixing angle measurement so far belongs to the so-called atomic parity violation (APV) experiments, also known as parity nonconservation (PNC), using caesium atoms [22, 23], namely $\sin^2\vartheta_W = 0.2367 \pm 0.0018$. This value is slightly smaller than the SM prediction at near zero momentum transfer, $\mathrm{Q} = 0$, calculated in the ($\overline{\mathrm{MS}}$) renormalization scheme, $\sin^2\vartheta_W^{\mathrm{SM}}(\mathrm{Q} \to 0) = 0.23863(5)$ [19, 27, 28][3]. Atomic parity violation is caused by the weak interaction, and it is manifested in P-violating atomic observables [32].

One of the goals of this thesis work is to exploit electroweak probes, and in particular, the neutrino interaction described in the next sections, to perform a test of the SM by constraining the low-energy value of the weak mixing angle, which provides a direct probe of physics phenomena beyond the SM (BSM).

1.2 Coherent Elastic Neutrino Nucleus Scattering

Neutrinos are characterized by an extremely small interaction cross-section with matter, making them very difficult to detect. Among the various neutrino processes that can occur at low neutrino energies ($E_\nu \lesssim 100$ MeV), the coherent elastic scattering of neutrinos with nuclei, also known as CEνNS, has recently gained a lot of attention due to its physical potential of probing a huge number of physics scenarios. In 1974, Freedman predicted that a Z^0 might mediate the interaction of a neutrino with a whole nucleus [33], namely

$$\nu_\ell + {}^{N}_{Z}\mathcal{N} \to \nu_\ell + {}^{N}_{Z}\mathcal{N}, \tag{1.8}$$

[3]During the course of this work, a refined theoretical determination of the weak mixing angle was reported, yielding $\sin^2\vartheta_W(q^2 \to 0) \simeq 0.23873$ [31]. We anticipate that our analysis will remain largely unaffected, as the change is minor when compared to the existing level of precision.

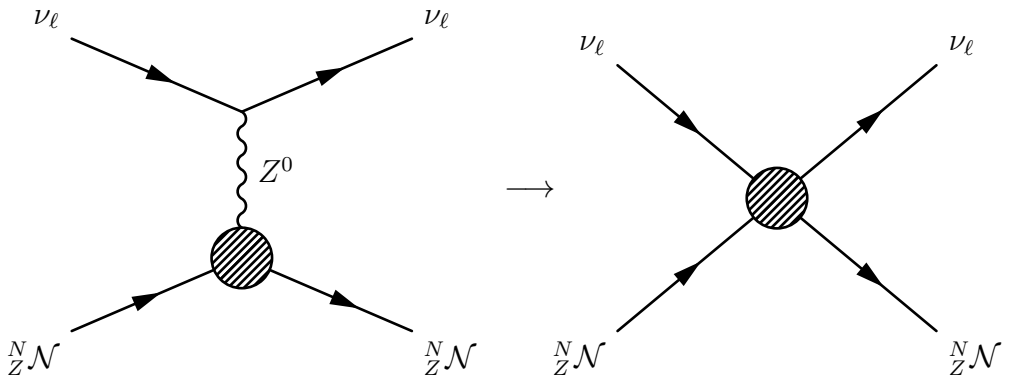

Figure 1.3: Left: Feynman diagram of CEνNS in the Standard Model. ν_ℓ represents a neutrino with flavor $\ell = e,\ \mu,\ \tau$, ${}^N_Z\mathcal{N}$ denotes a nucleus, indicated as a blob, and Z^0 is the Standard Model neutral vector boson which mediates neutral-current weak interactions. Right: effective four-Fermi interaction in the limit $q^2 \ll m_{Z^0}$. In both diagrams, time flows from the left to the right.

where ν_ℓ represents a neutrino with flavor $\ell = e, \mu, \tau$, while $\mathcal{N}$ is a nucleus with Z protons and N neutrons. Note that the total number of nucleons in the nucleus is defined as $A = Z + N$.

The Feynman diagram of the tree-level interaction is illustrated in the left panel of Fig. 1.3. To understand the phenomenology of this process, it is convenient to interpret the de Broglie wavelength of the exchanged Z^0 boson, λ_{Z^0}, as a measure of the spatial dimension probed by the mediator. Moreover, λ_{Z^0} is related to the module of the momentum transfer in the interaction $|\vec{q}|$ through $\lambda_{Z^0} = h/|\vec{q}|$, where h is Planck's constant[4]. Specifically, considering a nuclear radius of about $R \sim 5$ fm, the typical momentum transfer is of the order of

$$|\vec{q}| \sim \frac{197 \text{ MeV fm}}{5 \text{ fm}} \sim 40 \text{ MeV}, \tag{1.9}$$

which represents the energy scale for the neutrino to undergo a coherent interaction. Since the mass of the Z^0 boson is much larger compared to q^2, the interaction can be effectively described by a four-Fermi diagram (right panel in Fig. 1.3). In Fig. 1.4, the coherent enhancement of the CEνNS cross section is shown for Ar, Ge, Cs, and Pb nuclei, and is compared to the cross section for neutrino scattering off atomic electrons in a Cs atom and to that of inverse beta decay (IBD), the

[4]This thesis is adopting naturals units such that $\hbar = h/(2\pi)$ is set to unity.

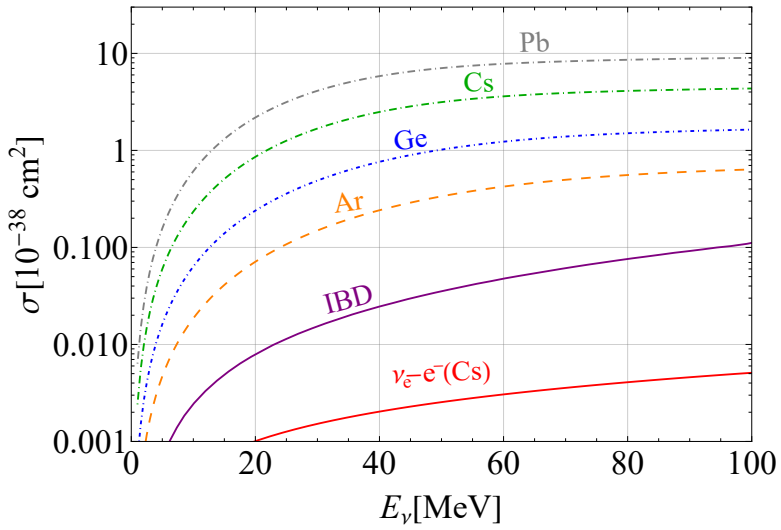

Figure 1.4: Comparison of cross sections for various neutrino interaction processes for $E_\nu \lesssim 100$ MeV. The CEνNS cross sections on argon (Ar), germanium (Ge), cesium (Cs), and lead (Pb) are shown, demonstrating their dominance due to coherent enhancement. For comparison, the cross sections for elastic neutrino-electron scattering on Cs and inverse beta decay are shown.

mechanism employed for neutrino discovery [18]. To better understand the phenomenology of the process, a schematic view of the energy regimes is reported in Fig. 1.5. In the interaction depicted in the left panel, the wavelength of the Z^0 boson that mediates the interaction is larger than the size of the nucleus, $\lambda_{Z^0} \gtrsim 2R$ and all the nucleons respond coherently to the interaction. In this case, the single outcome of the CEνNS interaction is a very small nuclear recoil energy T_{nr}. In the intermediate energy regime (central panel), when $\lambda_{Z^0} \lesssim 2R$, the interaction is no longer fully coherent but there is a high probability that the neutrino interacts with a group of nucleons in the nucleus. The nuclear structure suppresses the coherency, giving room for studying nuclear physics. In this energy range, other compelling effects might occur, such as the excitation of the nucleus to the state $\mathcal{N}^*$ which became more dominant as the neutrino energy increases. At even higher energies, the de Broglie wavelength of the Z^0 boson becomes much smaller than the size of the nucleus, $\lambda_{Z^0} \ll 2R$, the coherency is totally lost, and the Z^0 has a high probability of interacting with a single nucleon in the nucleus giving rise to an inelastic process (right panel) where, for example, a neutron is emitted.

Thanks to its significantly larger interaction cross section with matter compared to other low-energy neutrino processes, CEνNS is particularly relevant for studying a broad range of physics scenarios which will be explored in this thesis, from nuclear physics to extensions of the SM. One of the biggest challenges

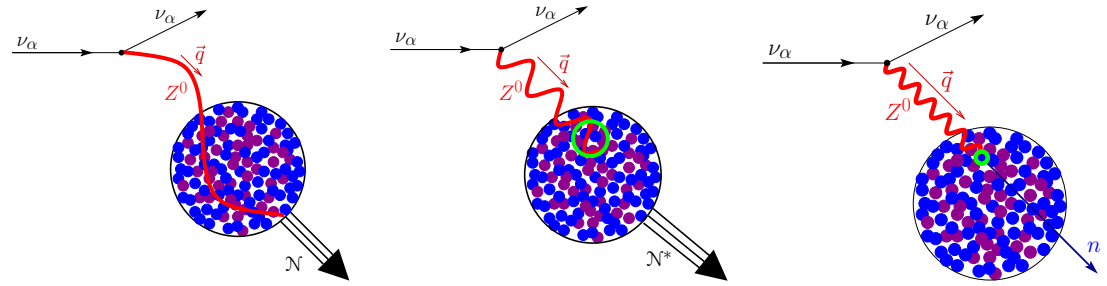

Elastic coherent (CEνNS) $\lambda_{Z^0} \gtrsim 2R$

Elastic incoherent $\lambda_{Z^0} \lesssim 2R$

Inelastic incoherent $\lambda_{Z^0} \ll 2R$

Figure 1.5: Illustration of energy regimes of a neutrino ν_α scattering off a nucleus $\mathcal{N}$. For low energetic neutrinos, i.e. low momentum transfer $\lambda_{Z^0} \gtrsim 2R$, and all nucleons respond coherently to the interaction (CEνNS regime). As the energy increases, the de Broglie wavelength of the Z^0 decreases, $\lambda_{Z^0} \lesssim 2R$, and the full coherence is lost. Inelastic incoherent scattering occurs when $\lambda_{Z^0} \ll 2R$. Image from Ref. [34].

that need to be addressed when designing a CEνNS experiment lies in the necessity of finding a high-intensity neutrino source in the MeV range. This thesis will explore the CEνNS signal from different neutrino sources: pion-decay-at-rest (π-DAR) sources, solar neutrinos, and reactor neutrinos. In addition, CEνNS plays a crucial role in the formation of some of the most devastating events in our universe: the core collapse supernovae explosion [17]. Remarkably, about the 99% of the energy is carried by neutrinos [17] with an energy of tens of MeVs, making CEνNS an excellent channel that can be used to observe supernova neutrinos. In this context, the RES-NOVA experiment [35] aims to use ultra-radiopure lead [36, 37] to detect CEνNS from supernova neutrinos [38] in an underground laboratory. Since CEνNS is an almost flavor-independent process, it allows for a highly precise measurement of the supernova neutrino flux, playing a key role in multi-messenger astrophysics.

1.2.1 Fundamental Theory of the CEνNS Cross Section

The fundamental aspect of the CEνNS process lies in the coherent response of all nucleons to the interaction. From a quantum-mechanical point of view, coherency implies that the amplitude of the process is the sum of the contribution from each quark q within the nucleus, which determines the form of the Lagrangian that describes the interaction. Considering the low-energy limit where $q^2 \ll m_{Z^0}$, the effective Lagrangian $\mathcal{L}_{\text{eff}}$ associated to the process depicted in the right panel of

Fig. 1.3 is

$$\mathcal{L}_{\text{eff}}(\overset{(-)}{\nu}_\ell + \mathcal{N} \to \overset{(-)}{\nu}_\ell + \mathcal{N}) = \frac{G_F}{\sqrt{2}} \sum_q [\bar{\nu}(\gamma^\mu g_V^{\nu_\ell} - g_A^{\nu_\ell}\gamma^5)\nu][\bar{q}(\gamma_\mu g_V^q - g_A^q \gamma^5)q]. \quad (1.10)$$

Here, ν and q represent the neutrino and quark fields, respectively, while γ_μ and γ_5 are the gamma matrices. $G_F = 1.1663787(6) \cdot 10^{-5}$ GeV^{-2} [19] is the Fermi constant, which is a crucial parameter of the electroweak theory and in some sense quantifies the strength of the weak interaction. G_F encodes the dependence of the weak neutral current (NC) propagator in the limit of low momentum transfer and is defined as $G_F = \sqrt{2}g^2/(8m_W^2)$, where g represents the weak coupling. Returning to the form of the Lagrangian in Eq. 1.10, we can clearly identify a lepton current, $L_\mu = \bar{\nu}(\gamma^\mu g_V^{\nu_\ell} - g_A^{\nu_\ell}\gamma^5)\nu$, and a hadronic current, $W^\mu = \sum_q \bar{q}(\gamma_\mu g_V^q - g_A^q\gamma^5)q$, the latter accounting for the interaction of the neutrino with the individual constituents of the nucleus. Note that in Eq. 1.10 the sum over q runs over all quarks within the nucleus. The electroweak theory precisely predicts the fermion vector (axial) couplings g_V (g_A) with the Z^0. In particular, at tree-level, we have $g_{V,A}^{\nu_\ell} = 1/2$ for neutrinos, while the coupling to quarks depends on the weak isospin T_3 and charge Q_q, according to $g_V^q = T_3^q - Q_q \sin^2\vartheta_W$. Explicitly, for the $u,\ c,\ t,\ d,\ s,\ b$ quarks, the couplings are

$$g_V^q = \frac{1}{2} - \frac{4}{3}\sin^2\vartheta_W\,, \qquad q = u, c, t\,, \quad (1.11)$$

$$g_V^q = -\frac{1}{2} + \frac{2}{3}\sin^2\vartheta_W\,, \qquad q = d, s, b\,. \quad (1.12)$$

As the interaction takes place with the protons and neutrons that globally constitute the nucleus, only u and d quarks are relevant. The Lagrangian defined in Eq. 1.10 must be reformulated to explicitly show the interaction with the nucleus rather than its constituents. There are different methods to accomplish this, and in the following, the formalism described in Ref. [39] will be adopted. Within this framework, we introduce the *quark number operators*, $N_q^p(n)$, which projects the quark vector current into nucleon states and returns the number of quarks inside the proton or neutron. It is defined in such a way that if we project the quark

current to the initial and final nucleon states, we obtain

$$\langle n|\bar{q}\gamma^\mu q|n\rangle = N_q^n \bar{n}\gamma^\mu n, \tag{1.13}$$

$$\langle p|\bar{q}\gamma^\mu q|p\rangle = N_q^p \bar{p}\gamma^\mu p, \tag{1.14}$$

$$\langle p|\bar{q}\gamma^\mu q|n\rangle = 0. \tag{1.15}$$

Recalling that the proton is made of $[uud]$, while the neutron is $[udd]$, by projecting the vector quark current $J^\mu = \sum_{q=u,d} \bar{q}\gamma^\mu g_V^q q$ over the nucleon states and using the relations above we obtain

$$\begin{aligned}(\langle n| + \langle p|)\, J^\mu\, ((|n\rangle + |p\rangle)) &= g_V^u N_u^n \bar{n}\gamma^\mu n + g_V^d N_d^n \bar{n}\gamma^\mu n + g_V^u N_u^p \bar{p}\gamma^\mu p + g_V^d N_d^p \bar{p}\gamma^\mu p \\ &= (2g_V^u + g_V^d)\bar{p}\gamma^\mu p + (g_V^u + g_V^d)\bar{n}\gamma^\mu n \\ &= g_V^p \bar{p}\gamma^\mu p + g_V^n \bar{n}\gamma^\mu n. \end{aligned} \tag{1.16}$$

In Eq. 1.16 we have defined the vector neutrino-proton and neutrino-neutron g_V^p and g_V^n respectively, namely

$$g_V^p = 2g_V^u + g_V^d = \frac{1}{2} - 2\sin^2\vartheta_W \simeq 0.0227 \tag{1.17}$$

$$g_V^n = g_V^u + 2g_V^d = -\frac{1}{2}. \tag{1.18}$$

We note here a very important point, which is that the $g_V^n \gg g_V^p$, being the latter suppressed by the weak mixing angle in the limit of low momentum transfer. In other words, neutrinos primarily couple to the neutrons inside the nucleus, making their contribution dominant in the cross section.

Note also that Eqs. 1.17 and 1.18 show no dependence on the flavor ℓ of the incoming neutrino. To meet the outcome of current and upcoming experiments, there is the need to account for radiative corrections that modify the tree-level couplings in Eq. 1.17 and 1.18. In our works [4, 7] we have refined the theoretical description of radiative correction for the CEνNS process, which should be taken into account when comparing the results with experimental data (see Sec. 1.2.3 for a detailed discussion).

The next step in the calculation is to compute the interaction with the entire nucleus. To do so, we introduce the *nucleon number operators*, Z and N, which give the number of protons and neutrons inside the nucleus when projecting over the final and initial nuclear states $|\mathcal{N}\rangle$. Explicitly, using the result in Eq. 1.16 and

projecting the hadronic current over the nucleus state we obtain

$$\langle \mathcal{N}|W^{\mu}|\mathcal{N}\rangle = (g_V^p Z + g_V^n N)\,\bar{\mathcal{N}}\gamma^{\mu}\mathcal{N}. \tag{1.19}$$

The quantity $\mathcal{Q}_W = g_V^p Z + g_V^n N$ is usually referred to as the *weak charge of the nucleus*, and describes the strength of the weak coupling of the neutrino with the nucleus. We are now able to rewrite the effective CEνNS Lagrangian in Eq. 1.10 in a more convenient way

$$\mathcal{L}_{\text{eff}}(\overset{(-)}{\nu}_{\ell} + \mathcal{N} \to \overset{(-)}{\nu}_{\ell} + \mathcal{N}) = \frac{G_F}{\sqrt{2}} \sum_q [\bar{\nu}\gamma_{\mu}\mathbb{P}_L\nu][\mathcal{Q}_W\bar{\mathcal{N}}\gamma^{\mu}\mathcal{N}]. \tag{1.20}$$

where we introduced the left projection operator $\mathbb{P}_L = (1-\gamma_5)/2$. The cross section will be proportional to the matrix element $M^{ss'rr'}$ of the scattering process

$$M^{ss'rr'} = \frac{G_F}{\sqrt{2}}\mathcal{Q}_W[\overline{u}^{s'}(p')\gamma^{\mu}P_L u(p)^s][\overline{u}^{r'}(k')\gamma_{\mu}u^r(k)]\,. \tag{1.21}$$

Here u refers to the Dirac spinor for the neutrino and the nucleus, with s, p (s', p') representing the initial (final) spin and momentum of the neutrino. Likewise, r, k (r', k') indicates the initial (final) spin and momentum of the nucleus. The cross section is related to the average matrix element squared, which is

$$\langle |M|^2\rangle = \sum_{s,s'}\frac{1}{2}\sum_{r,r'}|M^{ss'rr'}|^2\,. \tag{1.22}$$

When evaluating this quantity, we consider that the spin of the left-handed neutrino is fixed, while for the nucleus it is not necessarily true in the most general case. Hence, the average matrix element squared is,

$$\langle |M|^2\rangle = \frac{G_F^2}{2}\mathcal{Q}_W^2 L^{\mu\nu}W_{\mu\nu}\,, \tag{1.23}$$

where we introduced the leptonic $(L^{\mu\nu})$ and adronic $(W^{\mu\nu})$ tensors defined as

$$L^{\mu\nu} = \sum_{s,s'}[\overline{u}^{s'}(p')\gamma^{\mu}P_L u^s(p)][\overline{u}^s(p)\gamma^{\nu}P_L u^{s'}(p')]\,, \tag{1.24}$$

$$W_{\mu\nu} = \sum_{r,r'}[\overline{u}^{r'}(k')\gamma_{\mu}u^r(k)][\overline{u}^{r'}(k)\gamma_{\nu}u^{r'}(k)]\,. \tag{1.25}$$

Recalling that $\sum_s u^s(p)\overline{u}^s(p) = \not{p} + m$, where $\not{p} = \gamma^\mu p_\mu$ and m the mass of the particle, those tensors can be rewritten as

$$L^{\mu\nu} = \text{Tr}[\not{p}'\gamma^\mu P_L \not{p}\gamma^\nu P_L]\,, \tag{1.26}$$

$$W_{\mu\nu} = \frac{1}{4} Tr[(\not{k}' + m_N)\gamma_\mu(\not{k} + m_N)\gamma_\nu]\,, \tag{1.27}$$

where Tr is the trace and m_N is the mass of the nucleus. Defining the Mandeslatam variable t as $t = (k-k')^2$ and $s = (p+k)^2$, we can write the differential cross section as a function of t, which is the only scattering channel involved in the interaction as [21]

$$\frac{d\sigma_{\nu_\ell - \mathcal{N}}}{dt} = \frac{1}{16\pi}\frac{1}{(s - m_N^2)^2}\langle|M|^2\rangle\,. \tag{1.28}$$

Explicitly, the four-momentum of the nucleus before and after the interaction is respectively $k = (m_N, \vec{0})$ and $k' = (E_N, \vec{k}')$, while for the neutrino $p = (E_\nu, E_\nu\hat{k})$ and $p' = (E'_\nu, E'_\nu\hat{u})$, where $\hat{k}$ and $\hat{u}$ represent the direction of the neutrino before and after the interaction, respectively. The energy conservation implies $m_N + E_\nu = E'_\nu + E_N$, where E_N is the energy of the nucleus after being hit by the neutrino. Here we define the physical observable quantity of the experiment, which is the nuclear recoil energy T_{nr} defined as $T_{\text{nr}} = E_\nu - E'_\nu$. The Mandelstam variables t and s can be written as

$$t = -2m_N T_{\text{nr}}\,, \tag{1.29}$$

$$s = m_N^2 + 2E_\nu m_N. \tag{1.30}$$

Now we can rewrite the differential cross section as a function of the nuclear recoil energy, which can be experimentally measured, obtaining

$$\frac{d\sigma_{\nu-\mathcal{N}}}{dT_{\text{nr}}} = \frac{G_F^2}{128\pi}\frac{\mathcal{Q}_W^2}{E_\nu^2 m_N} L^{\mu\nu}W_{\mu\nu}\,. \tag{1.31}$$

From the traces calculations, we get

$$L^{\mu\nu}W_{\mu\nu} \simeq 128E_\nu^2 m_N^2\left(1 - \frac{T_{\text{nr}}}{E_\nu} - \frac{m_N T_{\text{nr}}}{2E_\nu^2}\right), \tag{1.32}$$

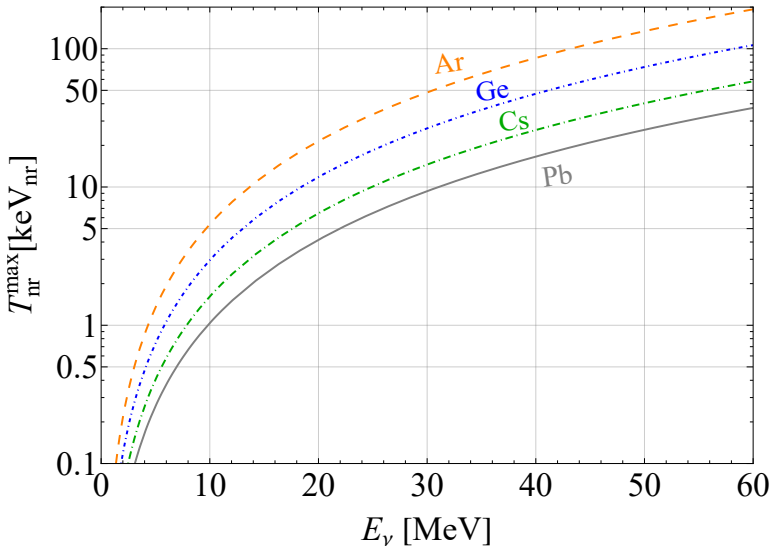

Figure 1.6: Maximum nuclear recoil energy $T_{\rm nr}^{\rm max}$ as a function of the incoming neutrino energy E_ν for different target materials, whose details are reported in Tab. 1.1.

so that the differential cross section becomes[5]

$$\left(\frac{d\sigma_{\nu-\mathcal{N}}}{dT_{\rm nr}}\right)_{q^2\to 0} \simeq \frac{G_F^2}{\pi} m_N \left(1 - \frac{T_{\rm nr}}{E_\nu} - \frac{m_N T_{\rm nr}}{2E_\nu^2}\right)\left[Z g_V^p + N g_V^n\right]^2 . \tag{1.33}$$

The maximum $T_{\rm nr}$ achievable in the interaction is determined by the kinematics and is

$$T_{\rm nr}^{\rm max} = \frac{2E_\nu^2}{m_N + 2E_\nu} \simeq \frac{2E_\nu^2}{m_N}. \tag{1.34}$$

The maximum nuclear recoil energy $T_{\rm nr}^{\rm max}$ as a function of the incoming neutrino energy E_ν is shown in Fig. 1.6 for different target materials whose mass is reported in Tab. 1.1. As the nucleus gets bigger, the CEνNS cross section becomes larger for fixed neutrino energy, but the maximum nuclear recoil achievable decreases. Detecting such small nuclear recoils is extremely challenging from an experimental perspective. Using lighter elements as target materials, however, results in a lower event rate, but is distributed over a broader nuclear recoil spectrum. To conclude, it is also useful to note that we neglected the axial term in the previous discussion. It is usually assumed that the scattering happens with spin-zero nuclei, such that the fundamental state of the nucleus, $J^\pi = 0^+$, is left unchanged in the interaction. This implies that the spin-dependent term $\sum_q \bar{q} g_A^q \gamma^5 q$ inside Eq. 1.10 vanishes. On the other hand, in general, the axial contribution describes the coupling of a neu-

[5]Note that in Eq. 1.33 the term $T_{\rm nr}/E_\nu \ll 1$ and will be neglected in the following.

trino with the unpaired nucleons in the nucleus, such that its contribution will be proportional to $(Z_+ - Z_-)$ or $(N_+ - N_-)$ [40], where $Z_\pm(N_\pm)$ stands for the number of protons (neutrons) with spin up and spin down, respectively. For heavy nuclei, this number is much smaller than the total number of protons and neutrons, such that the amplitude of the spin-dependent contribution will be roughly suppressed by a factor of $1/N$ compared to the vector one, and the cross section will be suppressed by a factor of $\sim 1/N^2$ [40]. On the other hand, when considering scattering off high-spin nuclei or light elements, this term might play a significant role and may no longer be negligible. A recent and detailed discussion of the axial contribution to the CEνNS process can be found in Ref. [41].

1.2.2 The CEνNS Microscope For Probing Nuclear Physics

When the condition $\lambda_{Z^0} \geq 2R$ is not entirely satisfied, the nuclear structure starts to play a role, and needs to be taken into account. To parameterize this effect, a so-called *weak form factor* F_W is introduced, and the CEνNS cross section in Eq. 1.33 takes the form

$$\frac{d\sigma_{\nu-\mathcal{N}}}{dT_{\rm nr}} \simeq \frac{G_F^2}{\pi} m_N \left(1 - \frac{m_N T_{\rm nr}}{2E_\nu^2}\right) \mathcal{Q}_W^2 F_W^2 \,. \tag{1.35}$$

The weak form factor is therefore normalized in such a way that $F_W(q^2 \to 0) = 1$, and it can be shown [42] that by expanding the nucleon form factors in the limit of small momentum transfer, and neglecting the contribution from strange quarks, F_W can be parameterized as

$$F_W \simeq \frac{1}{\mathcal{Q}_W} \left(Z g_V^p F_p(q^2) + N g_V^n F_n(q^2)\right) . \tag{1.36}$$

$F_{p(n)}(q^2)$ are referred to as the proton (neutron) forms factors respectively, and represent the Fourier transform of the distribution of protons (neutrons) inside the nucleus, satisfying as well the condition $F_{p(n)}(q^2 \to 0) = 1$. The differential CEνNS cross section in Eq. 1.35 becomes

$$\frac{d\sigma_{\nu-\mathcal{N}}}{dT_{\rm nr}} \simeq \frac{G_F^2}{\pi} m_N \left(1 - \frac{m_N T_{\rm nr}}{2E_\nu^2}\right) \left[Z g_V^p F_p(q^2) + N g_V^n F_n(q^2)\right]^2 . \tag{1.37}$$

In our notation, the nuclear weak charge is identified with

$$\mathcal{Q}_W = Z g_V^p F_p(q^2) + N g_V^n F_n(q^2) \,, \tag{1.38}$$

which effectively defines the strength of the coupling to the nucleus. The weak charge therefore encodes the nuclear dependence through the proton and neutron form factors.

While the distribution of protons is well known, as it can be tested using electromagnetic probes, the neutron distribution is much more unconstrained. This is because one must rely on hadronic probes, where systematic effects might not be well controlled, or on electroweak probes, which currently lack the statistical precision needed to provide measurements as accurate as those obtained for the charge distribution. For this reason, one of the goals of this thesis is to study the impact of CEνNS data on the extraction of nuclear structure parameters, specifically the neutron radius R_n. This topic will be discussed in Chap. 6.

The distribution of protons inside the nucleus can be parameterized by a symmetrized Fermi (SF) [43–45] function, which in the most general case takes the form [46]

$$F^{\mathrm{SF}}(q^2) = \frac{4\pi^2\rho_0 a^3}{(qa)^2\sinh^2(\pi qa)}\left[\pi qa\,\cosh(\pi qa) - qc\,\cos(qc)\,\sinh(\pi qa)\right] + 8\pi\rho_0 a^3 \sum_{n=1}^{\infty}(-1)^{n-1}\frac{n e^{-nc/a}}{\left[n^2+(qa)^2\right]^2}, \tag{1.39}$$

where ρ_0 represents the nuclear density. The parameter c is known as the *half-density radius*, defined as the radius where the nuclear density becomes 50% of its nominal value, while a is the so-called *diffuseness*, which is instead related to the *surface thickness* (t) through $t = 4\ a\ \ln(3)$. The latter represents the distance over which the nuclear density drops from the 90% of the maximum density to 10%, and is commonly fixed to the value $t = 2.30$ fm. In addition, many theoretical nuclear models predict roughly the same density drop between the proton and neutron distributions. Eq. 1.39 depends on an infinite series, whose contribution is subdominant compared to the current experimental precision, as the radius extracted from the nuclear distribution is modified by less than 0.1% when this term is neglected [46]. Upon imposing the normalization of the form factor, the density ρ_0 is found to be

$$\rho_0 = \left(\frac{4\pi c}{3}\left[(\pi a)^2 + c^2\right]\right)^{-1}, \tag{1.40}$$

and the SF takes the analytic expression

$$F_Z^{\mathrm{SF}}(q^2) = \frac{3}{qc\left[(qc)^2 + (\pi qa)^2\right]} \left[\frac{\pi qa}{\sinh(\pi qa)}\right] \left[\frac{\pi qa \sin(qc)}{\tanh(\pi qa)} - qc\cos(qc)\right]. \tag{1.41}$$

The *root-mean-square* (rms) radius of the distribution is related to a and c through

$$R^2 = 3/5\, c^2 + 7/5\, (\pi a)^2. \tag{1.42}$$

The symmetrized 2pF, which is equivalent to the parameterization in Eq. 1.41, has historically been used to match the results of measurements from muonic atom spectroscopy data [47, 48], which report the measurement of the parameter c. This parameter allows the extraction of the rms radius of the nuclear charge distribution, R_c, once t has been fixed.

Here there is an important point regarding the parameterization of the nuclear structure in the CEνNS interaction. In fact, the cross section defined in Eq. 1.37 depends on the proton and neutron distribution, but the extraction of R_c from an electromagnetic probe will receive a small contribution also from the charge distribution of the neutrons inside the nucleus. For this reason, we convert the measurement of R_c into a measurement of R_p, i.e., the radius of the proton distribution we are interested in, through [49–51]

$$R_p^2 \simeq R_c^2 - \frac{N}{Z}\langle r_n^2\rangle_c, \tag{1.43}$$

where $\langle r_n^2\rangle_c = -0.1161(22), \mathrm{fm}^2$ [52] is the electromagnetic mean-square radius of the neutron. Here we neglected the Darwin-Foldy and the spin-orbit charge density contributions [49, 50] expected to be generally negligible for the nuclei of interest in this thesis. For precision nuclear physics, the contribution from such corrections needs to be carefully estimated.

Given the absence of accurate experimental measurements for the neutron distribution in the elements of interest, we considered a different parameterization for the neutron form factor, known as the Helm form factor [53]

$$F^{\mathrm{Helm}}\left(|\vec{q}|^2\right) = 3\frac{j_1(qR_0)}{qR_0} e^{-|\vec{q}|^2 s^2/2}, \tag{1.44}$$

where $j_1(x) = \sin(x)/x^2 - \cos(x)$ is the order-one spherical Bessel function, and R_0 is the so called *box (or diffraction) radius* which is determined from the first zero

	c [fm]	$R_{\rm ch}$ [fm]	R_p [fm]	R_n [fm]	m_N [GeV]
$^{40}_{18}$Ar	3.6416	3.426	3.447	3.55	37.216
$^{72}_{32}$Ge	4.5926	4.0547	4.073	4.22	66.995
$^{127}_{53}$I	5.5931	4.7492	4.766	5.03	118.221
$^{131}_{54}$Xe	5.6384	4.761	4.778	5.07	122.296
$^{133}_{55}$Cs	5.6710	4.804	4.821	5.09	123.801
$^{208}_{82}$Pb	6.648	5.505	5.521	5.68	192.8

Table 1.1: Values for c of the nuclear charge distribution [47] for different elements, $^{A}_{Z}\mathcal{N}$ with $A = Z + N$, of interest in this thesis. The rms radius of the corresponding nuclear charge distribution ($R_{\rm ch}$) from Eq. 1.42, rms radius of the proton distribution (R_p) from Eq. 1.43 and the values for the neutron radius (R_n) from NSM calculation [41] are also reported for Ar, Ge, I, Xe, Cs and Pb nuclei. The neutron radius of ^{208}Pb comes from *ab-initio* calculation [57]. The nuclear masse for each element is also reported [58].

of the form factor [54]. In this case, the rms radius of the corresponding nucleon distribution is given by $R^2 = 3/5R_0^2 + 3s^2$, where the parameter s quantifies the so-called surface thickness. We consider a value of $s = 0.9$ fm, which is a typical value determined for the proton form factor for this type of nuclei [55]. In the analysis that we will perform in this thesis, the Helm and SF form factors yield practically identical results. Similarly, the Klein-Nystrand form factor [56], which is also widely adopted in the community, provides a description of the nuclear structure very similar to that obtained with the Helm and SF form factors.

In this thesis, we take as a reference the values of the neutron rms radii predicted from theoretical nuclear shell model (NSM) calculations [41]. In Tab. 1.1 the values for the nuclear charge, proton and neutron rms radii for different elements of interest highly employed in this thesis are reported.

In the upper panel of Fig. 1.7, we can observe the behavior of the nuclear proton (dashed lines) and neutron (solid lines) distributions, parameterized with the SF and Helm form factors respectively, as a function of the nuclear recoil energy for different target materials. As expected, the form factors drop to zero for smaller $T_{\rm nr}$ for heavier nuclei, since the coherency condition is lost at lower energies for larger nuclei. The lower panel shows the differential CEνNS cross section for increasing $E_\nu = 30$ MeV, where we can see the impact of two compelling effects taking place at the same time: on the one hand the kinematics (Eq. 1.34) is responsible for the sudden drop in the cross section as it determines the maximum nuclear recoil for a given neutrino energy, on the other hand the cross section is further reduced by the form factors (solid lines).

Although the modification of the cross section may seem modest, it is worth remarking that current CEνNS data are sensitive to nuclear structure parameters, enabling the extraction of the neutron radius R_n. In this sense, CEνNS can be regarded as a *neutrino microscope* for probing nuclear physics.

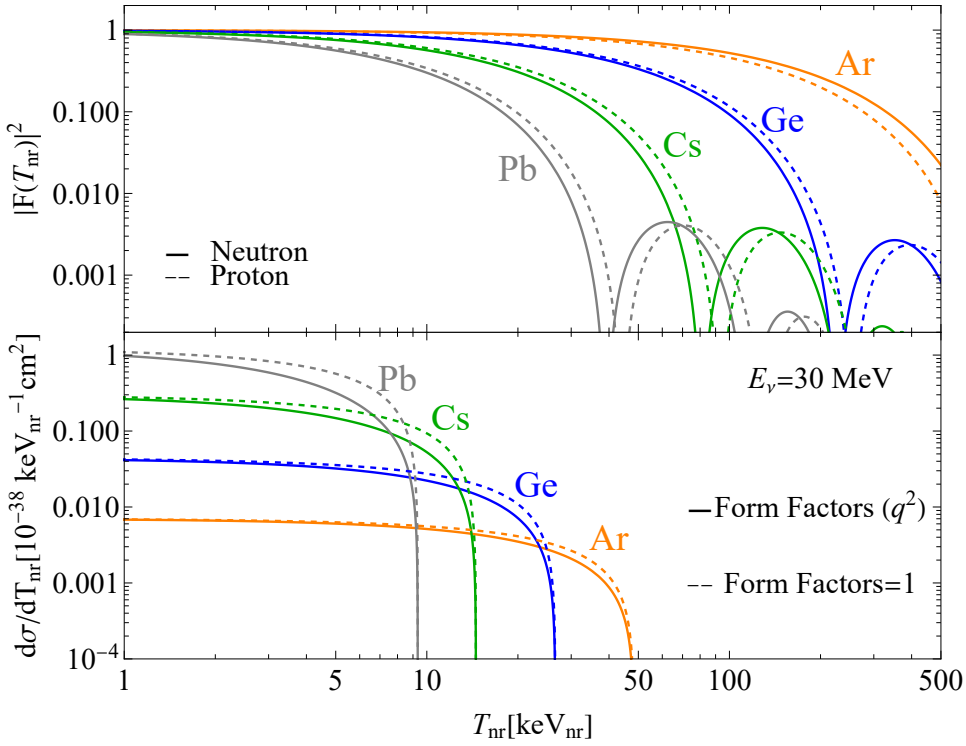

Figure 1.7: Upper panel: Nuclear proton (dashed lines) and neutron (solid lines) form factors as a function of the nuclear recoil energy $T_{\rm nr}$for different target materials. Lower panel: CEνNS differential cross section for different target materials and neutrino energy of $E_\nu = 30$ MeV. The comparison of the cross sections with form factors set to unity (dashed lines) and including their dependence on the momentum transfer (solid lines) is also shown.

1.2.3 Precise Determination of Neutrino Couplings

Another crucial element to be considered to accurately describe the neutrino interaction at low energies, is the inclusion of radiative corrections, which modify the neutrino-fermion coupling. The term "radiative correction" encompasses higher-order diagrams that go beyond the tree-level interaction shown in Fig. 1.3. More precise values are determined by taking into account the radiative corrections in

the $\overline{\text{MS}}$ scheme, following Refs. [5, 19, 59, 60], with a well-defined subtraction of singular terms arising in dimensional regularization, giving rise to expressions with a logarithmic energy scale dependence that is governed by a renormalization group equation (RGE). Choosing this energy scale equal to the momentum transfer of the process under consideration will, in general, avoid spurious logarithms [61]. Specifically, we will consider only 1-loop vertex corrections, as they provide the largest contribution. Within this framework, the ℓ flavor neutrino chiral right and left couplings to fermions $f = e, u, d$ are given by[6]

$$g_L^{\nu_\ell f} = \rho\left[\frac{1}{2} - Q_f\hat{s}_0^2 + \boxtimes_{ZZ}^{fL}\right] - Q_f\varkappa_{\nu_\ell W} + \boxtimes_{WW} \qquad (f = u), \tag{1.45}$$

$$g_L^{\nu_\ell f} = \rho\left[-\frac{1}{2} - Q_f\hat{s}_0^2 + \boxtimes_{ZZ}^{fL}\right] - Q_f\varkappa_{\nu_\ell W} + \square_{WW} \qquad (f = d, e), \tag{1.46}$$

$$g_R^{\nu_\ell f} = -\rho\left[Q_f\hat{s}_0^2 + \boxtimes_{ZZ}^{fR}\right] - Q_f\varkappa_{\nu_\ell W} \qquad (f = u, d, e), \tag{1.47}$$

where $\rho = 1.00063$ represents a low-energy correction for neutral-current processes, while $\hat{s}_0^2$ stands for $\sin^2\vartheta_W(q^2 \to 0)$. The quantities $\boxtimes_{WW}, \square_{WW}$ and $\boxtimes_{ZZ}^{fX}$, where $X \in \{L, R\}$ represents the parity, are the radiative corrections associated with the WW crossed-box, WW box diagram and the ZZ box respectively. On the other hand, $\varkappa_{\nu_\ell W}$ describes the neutrino charge radius (NCR) contribution and introduces a dependence on the neutrino flavor ℓ. Despite being treated as a radiative correction, the NCR is a more fundamental quantity. It is, in fact, the only neutrino electromagnetic property predicted to be non-zero in the SM. Sec. 1.2.4 will further explore the NCR contribution in neutrino scattering experiments, while Chap. 7 will present the constraints on this fundamental quantity using CEνNS data. The contribution of the different loop diagrams can be evaluated and is given by [60]

$$\varkappa_{\nu_\ell W} = -\frac{\alpha}{6\pi}\left(\ln\frac{m_W^2}{m_\ell^2} + \frac{3}{2}\right), \tag{1.48}$$

$$\square_{WW} = -\frac{\hat{\alpha}_Z}{2\pi\hat{s}_Z^2}\left[1 - \frac{\hat{\alpha}_s(m_W)}{2\pi}\right], \qquad \boxtimes_{WW} = \frac{\hat{\alpha}_Z}{8\pi\hat{s}_Z^2}\left[1 + \frac{\hat{\alpha}_s(m_W)}{\pi}\right], \tag{1.49}$$

$$\boxtimes_{ZZ}^{fX} = -\frac{3\hat{\alpha}_Z}{8\pi\hat{s}_Z^2(1-\hat{s}_Z)^2}(g_X^{\nu_\ell f})^2\left[1 - \frac{\hat{\alpha}_s(m_{Z^0})}{\pi}\right], \tag{1.50}$$

[6]Note that, in this notation, we are neglecting the chirality of the neutrino which is always left-handed, while it is made explicit in Ref. [60].

where $\hat{\alpha}_Z = 127.951^{-1}$ is the electromagnetic coupling constant evaluated at the Z^0 boson mass, $\hat{\alpha}_s(m_{Z^0}) = 0.1185(16)$ is the strong coupling evaluated at the Z^0 or W mass, $\hat{s}^2_Z = 0.23122(4)$ is the value of the Weinberg angle at the Z^0 mass, while m_ℓ with $\ell = e, \mu, \tau$ represent the mass of the lepton associated with the neutrino flavor involved in the interaction [19]. Note that in Eq. 1.50 all the $(g_X)^{\nu_\ell f}$ couplings are evaluated at lowest order but replacing the weak mixing angle at zero momentum transfer $\hat{s}^2_0$ by $\hat{s}^2_Z$ and are given by

$$g_L^{\nu_\ell e} = -\frac{1}{2} + \hat{s}^2_Z, \qquad g_R^{\nu_\ell e} = \hat{s}^2_Z, \tag{1.51}$$

$$g_L^{\nu_\ell u} = \frac{1}{2} - \frac{2}{3}\hat{s}^2_Z, \qquad g_R^{\nu_\ell u} = -\frac{2}{3}\hat{s}^2_Z, \tag{1.52}$$

$$g_L^{\nu_\ell d} = -\frac{1}{2} + \frac{1}{3}\hat{s}^2_Z, \qquad g_R^{\nu_\ell d} = \frac{1}{3}\hat{s}^2_Z. \tag{1.53}$$

The left and right coupling for the proton are obtained as

$$g_L^{\nu_\ell p} = 2g_L^{\nu_\ell u} + g_L^{\nu_\ell d} = \frac{\rho}{2} - \rho\hat{s}^2_0 - \varnothing_{\nu_\ell W} + 2\boxtimes_{WW} + \square_{WW} + 2\rho\,\boxtimes^{uL}_{ZZ} + \rho\boxtimes^{dL}_{ZZ}, \tag{1.54}$$

$$g_R^{\nu_\ell p} = 2g_R^{\nu_\ell u} + g_R^{\nu_\ell d} = -\rho\hat{s}^2_0 - \varnothing_{\nu_\ell W} - 2\rho\,\boxtimes^{uR}_{ZZ} - \rho\,\boxtimes^{dR}_{ZZ}\,. \tag{1.55}$$

This enables one to compute the coupling of the neutrino with the proton, i.e. $g_V^{\nu_\ell p} = g_L^{\nu_\ell p} + g_R^{\nu_\ell p}$, which is therefore

$$g_V^{\nu_\ell p} = \rho\left(\frac{1}{2} - 2\hat{s}^2_0\right) + 2\boxtimes_{WW} + \square_{WW} - 2\varnothing_{\nu_\ell W} + \rho(2\boxtimes^{uL}_{ZZ} + \boxtimes^{dL}_{ZZ} - 2\boxtimes^{uR}_{ZZ} - \boxtimes^{dR}_{ZZ}). \tag{1.56}$$

By performing the same calculation to evaluate the coupling of the neutrino with the neutron, the left and right couplings are

$$g_L^{\nu_\ell n} = g_L^{\nu_\ell u} + 2g_L^{\nu_\ell d} = -\frac{\rho}{2} + \rho(\boxtimes^{uL}_{ZZ} + 2\boxtimes^{dL}_{ZZ}) + \boxtimes_{WW} + 2\square_{WW}, \tag{1.57}$$

$$g_R^{\nu_\ell n} = g_R^{\nu_\ell u} + 2g_R^{\nu_\ell d} = -\rho(\boxtimes^{uR}_{ZZ} + 2\boxtimes^{dR}_{ZZ}). \tag{1.58}$$

We finally have the vector coupling the neutrino with the neutron

$$g_V^{\nu n} = -\frac{\rho}{2} + 2\square_{WW} + \boxtimes_{WW} + \rho(2\,\boxtimes^{dL}_{ZZ} + \boxtimes^{uL}_{ZZ} - 2\,\boxtimes^{dR}_{ZZ} - \boxtimes^{uR}_{ZZ}), \tag{1.59}$$

which is independent on the weak mixing angle and on the neutrino charge radius. Numerically, the values of the couplings correspond to

$$g_V^p(\nu_e) \simeq 0.0381, \quad g_V^p(\nu_\mu) \simeq 0.0299, \quad g_V^p(\nu_\tau) \simeq 0.0255, \quad g_V^n \simeq -0.5117\,. \tag{1.60}$$

This formalism can also be applied to determine the radiative correction associated with the axial coupling g_A for the CEνNS process and will be discussed in the following for completeness. Recalling that $g_A = g_L - g_R$, their expressions are

$$g_A^p = \frac{\rho}{2} + 2\boxtimes_{WW} + \square_{WW} + \rho(2\,\boxtimes_{ZZ}^{uL} + \boxtimes_{ZZ}^{dL} + 2\,\boxtimes_{ZZ}^{uR} + \boxtimes_{ZZ}^{dR}), \tag{1.61}$$

$$g_A^n = -\frac{\rho}{2} + 2\square_{WW} + \boxtimes_{WW} + \rho(2\,\boxtimes_{ZZ}^{dL} + \boxtimes_{ZZ}^{uL} + 2\,\boxtimes_{ZZ}^{dR} + \boxtimes_{ZZ}^{uR}), \tag{1.62}$$

which do not depend on the weak mixing angle or the neutrino charge radius and numerically corresponds to

$$g_A^p \simeq 0.4954, \qquad g_A^n \simeq -0.5121\,. \tag{1.63}$$

The same formalism will be adopted in the case of neutrino electron scattering, which will be described in Sec. 1.3. To conclude, we are now able to write the CEνNS cross section making the dependence on the neutrino flavor explicit, namely

$$\frac{d\sigma_{\nu_\ell-\mathcal{N}}}{dT_{\rm nr}} = \frac{G_F^2}{\pi} m_N \left(1 - \frac{m_N T_{\rm nr}}{2E_\nu^2}\right)\left[Z g_V^p(\nu_\ell) F_p(q^2) + N g_V^n F_n(q^2)\right]^2 . \tag{1.64}$$

formalism which will be developed in this thesis will not be implemented in the context of supernova neutrinos, but will be addressed in future studies.

1.2.4 Neutrino Charge Radius and Flavor-Dependent Radiative Corrections

During the realization of this thesis work, in Ref. [7], we refined the formalism of radiative corrections in neutrino scattering experiments to incorporate the momentum transfer dependence on the term ϕ_{ν_ℓ} associated with the neutrino charge radius, which has been so far neglected in the literature of CEνNS works. The neutrino charge radius $\langle r_{\nu_\ell}^2 \rangle$ is related to the radiative correction ϕ_{ν_ℓ} through

$$\langle r_{\nu_\ell}^2 \rangle = \frac{6G_F}{\sqrt{2}\pi\alpha}\phi_{\nu_\ell W} = -\frac{G_F}{2\sqrt{2}\pi^2}\left[3 - 2\ln\left(\frac{m_\ell^2}{m_W^2}\right)\right]. \tag{1.65}$$

This is a constant term, evaluated by definition at $q^2 \to 0$. In the SM, the numerical values of the neutrino charge radius for the different neutrino flavors are

$$\langle r^2_{\nu_e} \rangle \simeq -8.3 \times 10^{-33}\,\mathrm{cm}^2\,, \tag{1.66}$$

$$\langle r^2_{\nu_\mu} \rangle \simeq -4.8 \times 10^{-33}\,\mathrm{cm}^2\,, \tag{1.67}$$

$$\langle r^2_{\nu_\tau} \rangle \simeq -3.0 \times 10^{-33}\,\mathrm{cm}^2\,. \tag{1.68}$$

Historically, the neutrino charge radius was first introduced as one of the radiative contributions to the running of the weak mixing angle. Being an intrinsic neutrino property, it affects the running of the weak mixing angle only in the case of neutrino scattering processes [62, 63]. In such formalism, the neutrino charge radius contribution acquires a momentum dependence due to the non-zero momentum transfer in the real experiment. It can be shown [7] that the momentum dependent radiative correction $\phi_{\nu_\ell W}$ can be effectively parameterized as

$$\begin{aligned}\phi^{\mathrm{eff}}_{\nu_\ell W}(q^2) &= -\frac{\alpha}{\pi}\left(-R_\ell(q^2) + \frac{1}{4}\right) \\ &= -\frac{\alpha}{\pi}\left(-\int_0^1 dx\, x(1-x)\ln\left[\frac{m_\ell^2 - q^2 x(1-x)}{m_W^2}\right] + \frac{1}{4}\right)\,,\end{aligned} \tag{1.69}$$

where the integral $R_\ell(q^2)$ is defined as

$$R_\ell(q^2) = \int_0^1 dx\, x(1-x)\ln\left[\frac{m_\ell^2 - q^2 x(1-x)}{m_W^2}\right]. \tag{1.70}$$

The expression in Eq. 1.69 should then be used in the experimental extraction of the neutrino charge radius whenever $q^2 \neq 0$. Practically speaking, one should carefully correct for the momentum dependence, and this can be done introducing a "neutrino charge radius form factor". We define this form factor by isolating the momentum-dependent NCR with respect to the SM picture, so basically as

$$\mathcal{F}_{\nu_\ell}(T_{\mathrm{nr}}) = \frac{\langle r^2_{\nu_\ell}\rangle^{\mathrm{eff}}(T_{\mathrm{nr}})}{\langle r^2_{\nu_\ell}\rangle^{\mathrm{eff}}(0)} \equiv \frac{\langle r^2_{\nu_\ell}\rangle^{\mathrm{eff}}(T_{\mathrm{nr}})}{\langle r^2_{\nu_\ell}\rangle^{\mathrm{SM}}}\,, \tag{1.71}$$

where we introduced an effective NCR, namely

$$\langle r^2_{\nu_\ell}\rangle^{\mathrm{eff}} = \frac{6G_F}{\sqrt{2}\pi\alpha}\phi^{\mathrm{eff}}_{\nu_\ell W}(q^2) = -\frac{G_F}{2\sqrt{2}\pi^2}\Big[3 - 12R_\ell(q^2)\Big]\,, \tag{1.72}$$

so that, we can obtain the neutrino couplings by using this effective NCR radiative correction[7] instead of the classical one inside Eq. 1.65. The same effect appears in the case of elastic neutrino electron scattering. In this manner, the NCR form factor is naturally normalized to unity for a zero-momentum transfer and decreases as the momentum grows, with a different steepness depending on the considered neutrino flavor. The momentum dependence of $\phi^{\rm eff}_{\nu_\ell W}(q^2)$ comes from $R_\ell(q^2)$ as defined in Eq. 1.70, and its impact becomes relevant for momenta larger than the mass of the corresponding charged lepton ℓ, i.e. $q^2 \gtrsim m_\ell^2$. Thus, for ν_e processes the correction to the couplings becomes visible for $q \gtrsim 0.5\,\mathrm{MeV}$, while for ν_μ only above $\sim 100\,\mathrm{MeV}$. In the case of ν_τ an even higher momentum transfer is needed to appreciate any difference, which is not relevant for the typical momenta of CEνNS experiments that we are considering in this thesis. We remind here that the momentum transfer is derived as a function of the nuclear or electron recoil energy as

$$Q^2 = -q^2 \simeq 2 m_{\rm tar} T\,, \tag{1.73}$$

where $m_{\rm tar}$ is the target mass, so either the nuclear or the electron mass, and T is the nuclear, $T_{\rm nr}$, or electron, T_e, recoil energy, depending on the case. We can now consider the effect of the NCR correction on the neutrino-proton coupling. In Fig. 1.8 we show the variation of the latter as a function of the nuclear recoil energy by comparing the two NCR radiative correction definitions. If we consider the typical momentum transfer (and thus recoil energy) of CEνNS experiments, $Q \sim 10 - 100\,\mathrm{MeV}$, as shown by the shaded light blue area, we can notice that the variation of the coupling is clearly non-negligible for the ν_e case. The effect on the ν_μ proton coupling is, as expected, significant for higher energies, so that, for ν_μ CEνNS at the current precision one can still employ a constant NCR radiative correction. Quantitatively, considering the recoil energy region of interest for CEνNS, the variation of the ν_e proton coupling due to the NCR correction momentum dependence is between $\sim 10 - 20\%$, while we see that there is almost no effect for the other two neutrino flavors.

The overall effect on the CEνNS cross section is small, and the variation affects mainly the coupling to protons, which is naturally suppressed by the weak mixing angle. So in practice, we are dealing with a minor effect. However, if one

[7] Since the NCR is by definition evaluated at zero-momentum transfer and is well-defined physical quantity, it is worth stressing that this effective definition has not to be considered as the actual definition of the neutrino charge radius. This effective definition can be thus viewed as a form factor which incorporates the momentum dependence, in analogy to the nuclear form factor discussed in Sec. 1.2.2.

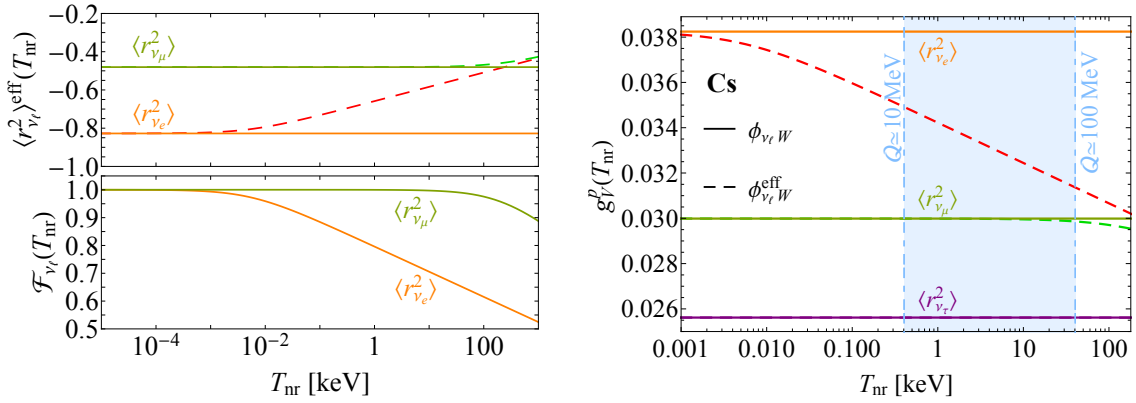

Figure 1.8: Left panel (upper): Comparison between the value of the NCR at zero-momentum transfer (solid lines) and the effective definition (dashed lines) in the case of the muonic flavor (green/lime) and the electron one (orange/red) as a function of the nuclear recoil energy for a cesium target. (Lower) Effective form factor as a function of the nuclear recoil energy for the muon flavor (green) and the electron one (orange). Right panel: Neutrino-proton coupling for the CEνNS process on cesium nuclei as a function of the nuclear recoil energy. The solid lines refer to the couplings considering a constant NCR radiative correction, while the dashed ones refer to the momentum-dependent neutrino charge radius radiative correction case. The vertical light blue lines and the shaded area indicate the typical momentum transfers of CEνNS experiments.

wants also to perform the first neutrino charge radius measurement with future experiments this effect will heavily mislead its extracted value as we will discuss in Sec. 7.1.3. In fact, the quantity that one measures, in particular in the case of the electron neutrinos, is the effective NCR which has to be corrected for the momentum dependence in order to extract the physical NCR.

Moreover, we note here that the use of radiative corrections in the CEνNS process is also relevant in the context of supernova neutrinos. Indeed, if one aims to obtain a precise measurement of the supernova neutrino flux [35] from the CEνNS channel, the effect of radiative corrections, as well as the energy-dependent NCR discussed above, might play a non-negligible role. This study is beyond the goal of this thesis work and might be addressed in future work.

1.3 ν Elastic Scattering Off Free Electrons

Another low-energy process of interest for this thesis work is the elastic scattering of neutrinos with electrons (νES). Historically, this process was used to discover the weak neutral current in 1973 through the Gargamelle experiment [64], which intriguingly resulted in the first attempt to extract the weak mixing angle from this scattering channel, yielding $0.1 < \sin^2\vartheta_W < 0.6$. Recently, it has been widely

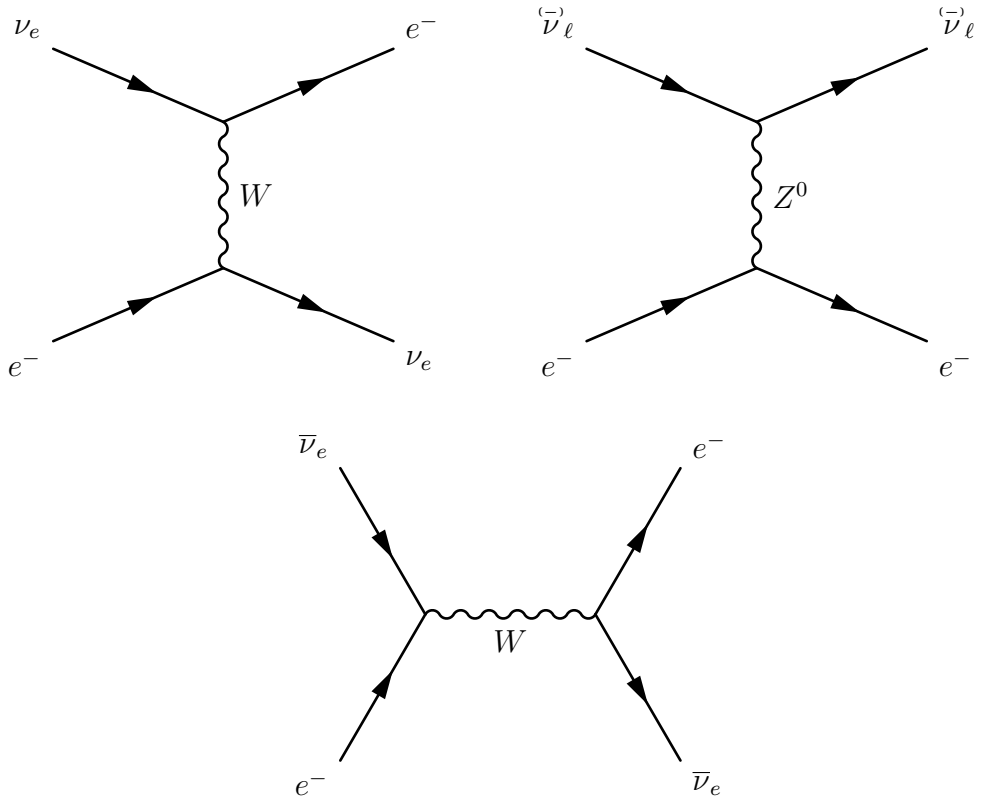

Figure 1.9: Tree-level Feynman diagrams for the charge current interaction for ν_e (upper left) and for the neutral current contribution for all the neutrino flavors $\ell = e, \mu, \tau$ (upper right). The channel described in the lower panel is present only for $\bar{\nu}_e$.

used to constrain electroweak parameters [65–68] and has played a crucial role in enhancing our understanding of solar neutrinos, particularly through the Borexino experiment [69–72]. Moreover, νES represents a significant source of background for direct dark matter searches [73, 74], but provides also additional channels to constrain new physics scenarios (see Chap. 7). The νES process can be of the form

$$\overset{(-)}{\nu}_e \, e^- \rightarrow \overset{(-)}{\nu}_e \, e^-, \tag{1.74}$$

$$\overset{(-)}{\nu}_{\mu,\tau} \, e^- \rightarrow \overset{(-)}{\nu}_{\mu.\tau} \, e^-. \tag{1.75}$$

While Eq. 1.74 can happen via both NC and charged current (CC) interactions, the reaction in Eq. 1.75 is only allowed via the NC process. The tree-level Feynman diagrams for this process are reported in Fig. 1.9. Similarly to the CEνNS process, the mass of the boson carrying the interaction in νES is much larger than the momentum transfer in the energy regimes of interest for this thesis. As a result, the effective four-Fermi weak neutral current and charged current Lagrangians for

νES are given by [75]

$$\mathcal{L}_{\rm NC} = -\frac{G_F}{\sqrt{2}}\left[\overline{\nu}\gamma^\mu(1-\gamma^5)\nu\right]\left[\overline{e}\gamma_\mu(g_V - g_A\gamma^5)e\right], \tag{1.76}$$

$$\mathcal{L}_{\rm CC} = -\frac{G_F}{\sqrt{2}}\left[\overline{\nu}\gamma^\mu(1-\gamma^5)\nu\right]\left[\overline{e}\gamma_\mu(1-\gamma^5)e\right], \tag{1.77}$$

where in the Eq. 1.77 a Fierz transformation has been used [75]. The electroweak theory predicts the coefficients relative to the electron-Z^0 interaction vertex to be $g_V = -1/2 + 2\sin^2\theta_W$ and $g_A = -1/2$ [60].
Considering the scattering of $\overline{\nu}_e$, we can combine the Lagrangians for the NC and CC contributions, obtaining [17]

$$\mathcal{L}_{\rm eff}(\overset{(-)}{\nu}_e e^- \to \overset{(-)}{\nu}_e e^-) = -\frac{G_F}{\sqrt{2}}[\overline{\nu_e}\gamma^\mu(1-\gamma^5)\nu_e][\overline{e}\gamma_\mu((1+g_V)-(1+g_A)\gamma^5)e],$$

which has the form of the NC Lagrangian in Eq. 1.76 but for the unit factors added to the couplings $g^\ell_{V(A)}$ in the second square brackets.
The differential cross section can be evaluated starting from the Lagrangians defined above [76] and after some kinematics calculation can be evaluated as a function of the electron recoil energy, T_e, giving

$$\frac{d\sigma_{\nu_\ell - e}}{dT_e}(E_\nu, T_e) = \frac{G_F^2 m_e}{2\pi}\left[(g_V^{\nu_\ell}+g_A^{\nu_\ell})^2 + (g_V^{\nu_\ell}-g_A^{\nu_\ell})^2\left(1-\frac{T_e}{E_\nu}\right)^2 - ((g_V^{\nu_\ell})^2-(g_A^{\nu_\ell})^2)\frac{m_e T_e}{E_\nu^2}\right], \tag{1.78}$$

where m_e is the electron mass.
In the latter equation, the couplings $g_V^{\nu_\ell}$ and $g_A^{\nu_\ell}$ represent the vector and axial coupling between a neutrino ν_ℓ and an electron, respectively. To ensure the cross section to have the same form for all neutrino flavors, the couplings are defined such that they already include contributions from the charged current diagram, which affects the cross section for electron neutrino scattering off electrons. Thus, at tree-level, the SM values of these couplings are

$$g_V^{\nu_e e} = 2\sin^2\theta_W + 1/2\,, \qquad g_A^{\nu_e e} = 1/2\,, \tag{1.79}$$

$$g_V^{\nu_{\mu,\tau} e} = 2\sin^2\theta_W - 1/2\,, \qquad g_A^{\nu_{\mu,\tau} e} = -1/2\,. \tag{1.80}$$

For antineutrinos one must only substitute $g_A^{\nu_\ell e} \to g_A^{\overline{\nu}_\ell e} = -g_A^{\nu_\ell e}$ inside the cross section in Eq. 1.78. The couplings defined in Eq.1.79 and Eq. 1.80 are valid at the tree-level. To achieve more accurate calculations for the cross sections, it is essential to incorporate contributions from radiative corrections adopting the

formalism described in Sec. 1.2.3, which gives

$$g_V^{\nu_\ell\, e} = \rho\left(-\frac{1}{2} + 2\hat{s}_0^2\right) + \square_{WW} + 2\varnothing_{\nu_\ell W} + \rho(\boxtimes_{ZZ}^{eL} - \boxtimes_{ZZ}^{eR}), \tag{1.81}$$

$$g_A^{\nu_\ell\, e} = \rho\left(-\frac{1}{2} + \boxtimes_{ZZ}^{eL} + \boxtimes_{ZZ}^{eR}\right) + \square_{WW}, \tag{1.82}$$

and numerically correspond to

$$g_V^{\nu_e e} = 0.9521, \qquad g_A^{\nu_e e} = 0.4938, \tag{1.83}$$

$$g_V^{\nu_\mu e} = -0.0397, \qquad g_A^{\nu_\mu e} = -0.5062, \tag{1.84}$$

$$g_V^{\nu_\tau e} = -0.0353, \qquad g_A^{\nu_\tau e} = -0.5062. \tag{1.85}$$

Similarly to what was observed in the case of CEνNS, we notice that the couplings have acquired a flavor dependence, due to the neutrino charge radius radiative correction. The typical momentum transfer in this process is much smaller compared to that of a CEνNS interaction, and the momentum dependence of the radiative correction is negligible in the energy range of interest in this thesis.

In Fig. 1.10, the integrated cross section

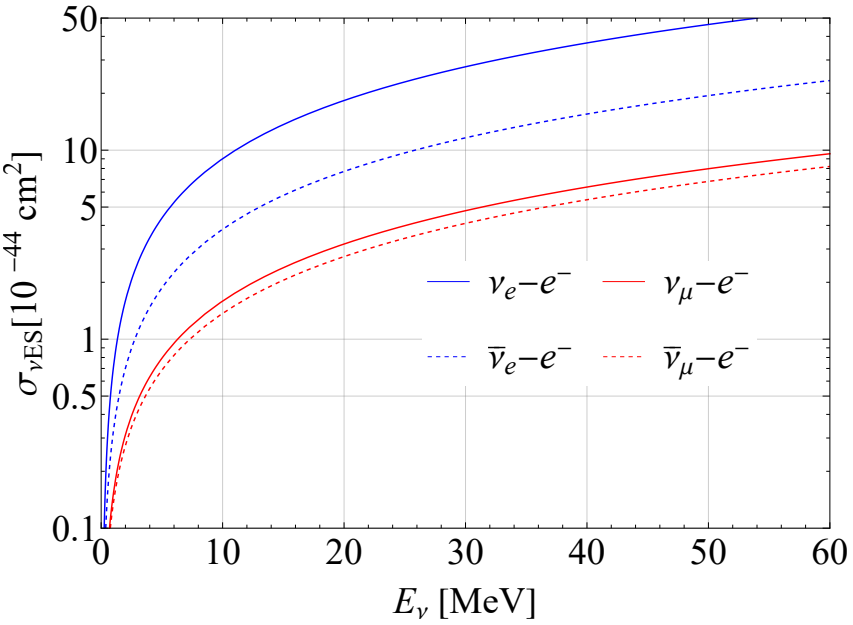

Figure 1.10: Neutrino electron cross section as a function of the neutrino energy for electronic and muonic neutrinos (solid lines) and antineutrinos (dashed lines). The ν_e cross section is bigger because the interaction can be mediated by both Z^0 and W bosons.

$$\sigma_{\nu\text{ES}}(E_\nu) = \int_0^{T_e^{\max}(E_\nu)} \frac{d\sigma_{\nu_\ell - e}^{\text{ES}}}{dT_e}(E_\nu, T_e)\, dT_e \tag{1.86}$$

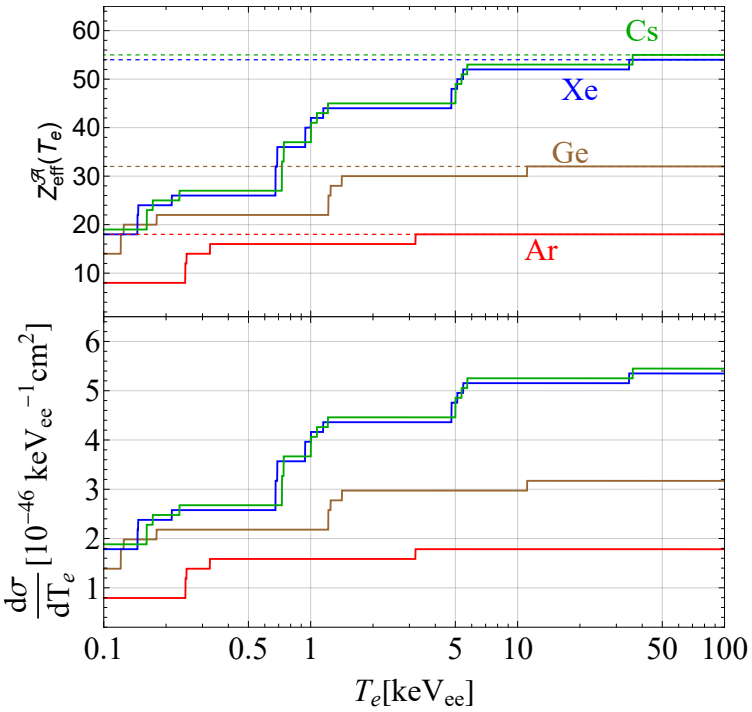

Figure 1.11: Upper panel: $Z^{\mathcal{A}}_{\rm eff}$ as a function of the electron recoil energy for different target materials (solid lines), compared with the number of electrons in the atom (dashed horizontal). Lower panel: Neutrino-electron scattering cross section, for different target materials, under the FEA+$Z_{\rm eff}$ approach. In both cases, the edges reflect the atomic structure of the material.

is shown for the neutrino and antineutrino elastic scattering off electrons, considering both electronic and muonic flavors including radiative corrections. Here $T_e^{\rm max}$ is the maximum recoil energy kinetically achievable given a certain neutrino energy, and is

$$T_e^{\rm max}(E_\nu) \simeq \frac{2E_\nu^2}{m_e + 2E_\nu}\,. \tag{1.87}$$

1.3.1 ν Scattering Off Atomic Electrons

The formalism described so far is valid only when considering the scattering off free electrons, the so-called free-electron approximation (FEA). In reality, neutrinos interact with the bound electrons in the atoms, $\mathcal{A}$, possibly ionizing them. A widely adopted formalism which accounts for the effects of the atomic structure of the target material is the effective atomic number ($Z_{\rm eff}$) approach [77, 78]. The $Z^{\mathcal{A}}_{\rm eff}$ term parameterizes the number of atomic electrons that can be ionized given an energy threshold T_e and is reported in App. A for different atoms. Within this

framework, the neutrino cross section for scattering with an atom containing Z electrons is now given by

$$\frac{d\sigma_{\nu_\ell-\mathcal{A}}}{dT_e} = Z_{\rm eff}^{\mathcal{A}}(T_e)\frac{G_F^2 m_e}{2\pi}\left[(g_V^{\nu_\ell}+g_A^{\nu_\ell})^2+(g_V^{\nu_\ell}-g_A^{\nu_\ell})^2\left(1-\frac{T_e}{E_\nu}\right)^2-((g_V^{\nu_\ell})^2-(g_A^{\nu_\ell})^2)\frac{m_e T_e}{E_\nu^2}\right]. \tag{1.88}$$

This thesis adopts the FEA+$Z_{\rm eff}$ approach to describe the electroweak interaction of neutrinos with atom $\mathcal{A}$. The upper panel of Fig. 1.11 illustrates $Z_{\rm eff}^{\mathcal{A}}$ as a function of T_e for various materials pertinent to our study, while the neutrino-atom cross section is reported in the lower panel. It is important to note that more accurate methods have been developed to provide a better description of neutrino interactions with atomic electrons. Among these methods, the sophisticated multiconfiguration relativistic random phase approximation (MCRRPA) [79, 80] and the many-body relativistic random phase approximation (RPPA) are available in the literature. However, it has been shown that they provide results similar to those obtained with the FEA+$Z_{\rm eff}$ approach [81].

2 Detailed Calculation of Neutrino Backgrounds for the DarkSide-20k Dark Matter Experiment

Opening

Arguably, one of the most important problems in fundamental physics today concerns the nature of dark matter (DM). This exotic form of matter permeates the universe, inspiring extensive theoretical and experimental research. This chapter aims to motivate the direct detection of DM, within the context of the DarkSide-20k experiment. The irreducible neutrino signal is known to be one of the major backgrounds which limits the discovery potential of DM candidates in a direct search experiment. Using the formalism developed in Chap. 1, the neutrino interaction rate expected from CEνNS and νES in DarkSide-20k will be evaluated. The DarkSide-20k sensitivity to low mass dark matter candidates based on a Collaboration study [9] will also be discussed.

2.1 The Dark Matter Problem

The study of DM is one of the most active and intriguing fields in modern physics. Its presence is inferred from a variety of probes as a result of its gravitational effects. Specifically, DM provides an explanation for the shape of the galaxy rotation curves [82], galaxy cluster dynamics observations [83], the formation and distribution of cosmic structures [84] and the primordial light element abundances [85, 86]. Moreover, cosmological data show that it has been present throughout the evolution of the universe [87].

In this framework, the experimental quest for non-gravitational signatures of dark matter has ramped up over the past decades. By combining our knowledge of the cosmological and astrophysical data, one can make quantitative statements about

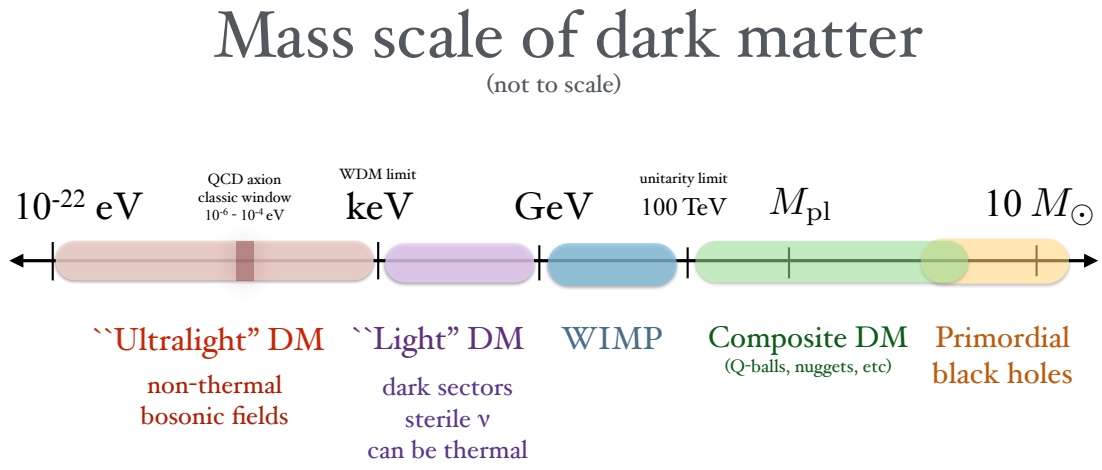

Figure 2.1: The mass range of possible DM candidates, including both particle candidates and primordial black holes. The mass ranges are only approximate and are meant to indicate general considerations. Figure taken from [88].

general DM properties. Dark matter has to be

- dark, meaning that its interaction is not included in the SM framework. Astrophysical observations imply that dark matter is not luminous, and cosmological evidence requires that a matter component interacting only by gravity must be present.
- Cold, or better say, non-relativistic, otherwise, the matter fluctuations structures can not form and can not match the distribution of structures we see today.
- Stable, or almost stable, since its lifetime should be much greater than the age of the universe, or it would have decayed by now.

Many dark matter candidates exist and must be consistent with the aforementioned broad range of observations on astrophysical and cosmological scales, while also satisfying laboratory bounds. Several hypotheses on the main constituent of dark matter are broadly studied [88–90], with a mass range that spans from $\sim 10^{-22}$eV to several $M_\odot$, where $M_\odot$ is the mass of our sun. A very simple schematic of different candidates is shown in Fig. 2.1 across an extensive mass range. For a review of the past and current status of DM searches, exploiting indirect and complementary techniques, as well as a discussion on alternatives to dark matter, see Ref. [90].

Among the different candidates for dark matter, this thesis will focus on Weakly

Interacting Massive Particles (WIMPs) [90, 91], widely studied particles predicted by many new physics scenarios and characterized by an extremely small cross section with ordinary matter, which makes their detection particularly challenging.

2.2 WIMP Paradigm

According to the WIMP paradigm, the dark matter we observe today was produced in the very early universe, as a thermal relic of the Big Bang [92]. In the standard framework describing the evolution of the universe [93], its early stages were characterized by a hot and dense plasma of particles assumed to be in thermal equilibrium, such that WIMPs (χ) can interact with SM particles, i.e. leptons, quarks or electroweak bosons, according to

$$\chi + \overline{\chi} \leftrightarrow \mathrm{SM} + \overline{\mathrm{SM}}. \tag{2.1}$$

This process, at high temperatures, proceeds in both directions, but as the temperature of the universe decreases below the WIMP mass m_χ the number of DM particles becomes exponentially suppressed by the Boltzmann factor $e^{-m_\chi/k_B T}$, with k_B the Boltzmann constant and T the temperature of the universe [90]. As the universe expands, the DM annihilation process becomes irrelevant, and we assist the so-called "freeze out" which gives rise to the relic abundance of DM particles we observe today.
WIMPs are assumed to be distributed in our galaxy according to the so-called standard halo model (SHM) [94, 95] with a constant density of $\rho_{\mathrm{DM}} \simeq 0.3\ \mathrm{GeV/cm^3}$. The lack of concrete evidence of direct DM detection so far motivates the search for lighter WIMPs, below 10 GeV, so-called light DM (LDM) candidates.
In the following, we will show how to obtain the differential event rate for a spin-independent (SI) DM-nucleus interaction of interest in this thesis. Spin-independent interactions are generated predominantly by scalar terms in a four-Fermi effective Lagrangian of the type [91]

$$\mathcal{L} \supset \alpha_q^s \chi\overline{\chi} q\bar{q}, \tag{2.2}$$

which describes interactions of a quark species q with the dark matter field χ, coupled via α_q^s. In this case, the differential spin-independent DM-nucleus cross section, under the simplified assumption of equal WIMP coupling with protons

and neutrons, can be written as [91]

$$\frac{d\sigma_{\rm SI}^{\chi-\mathcal{N}}}{dT_{\rm nr}} = \frac{m_N}{2\mu_{\chi-p}^2 v^2}\sigma_{\rm SI}^p (Z+N)^2 |F(T_{\rm nr})|^2. \tag{2.3}$$

Here, v is the velocity of the non-relativistic WIMP while $\sigma_{\rm SI}^p$ parameterizes the DM-nucleon cross section and is expected to be approximately at the level of weak interaction for TeV-scale WIMPs [90, 91]. Moreover

$$\mu_{\chi-p} = \frac{m_\chi m_p}{m_\chi + m_p} \tag{2.4}$$

is the reduced DM-nucleon mass[1]. In Eq. 2.3 we recognize the usual A^2 proportionality, similar to CEνNS, which means that in this simple scenario, all the nucleons respond coherently to the interaction. This implies that the WIMP cross section is bigger for heavy nuclei, but similarly to the CEνNS phenomenology, the nuclear form factor $F(T_{\rm nr})$ is responsible for a reduction in the expected number of events. We can clearly see that the WIMP interaction is very similar to that of CEνNS also because the single outcome of the interaction is a very small nuclear recoil energy $T_{\rm nr}$. It is worth mentioning that in direct WIMP searches, the form factor is usually parameterized according to the Helm function (Eq. 1.44) using the Lewin-Smith [96] prescription for R_0. The latter defines R_0 to be

$$R_0 = \sqrt{c(A)^2 + \frac{7}{3}\pi^2 a^2 - 5s^2}, \tag{2.5}$$

with $s = 0.9$ fm, $a = 0.52$ fm and $c(A)$ given by

$$c(A) = (1.23\ A^{1/3} - 0.6)\ \text{fm}. \tag{2.6}$$

In order to obtain the expected WIMP rate in a detector, we need to convolve the cross section with the expected DM flux at Earth from the SHM, which depends on the $f_1(v)$ velocity distribution and is given by [91, 94]

$$\frac{dR}{dT_{\rm nr}} = \frac{\rho_{\rm DM}}{2\mu_{\chi-p}^2 m_\chi}\sigma_{\rm SI}^p (Z+N)^2 |F(T_{\rm nr})|^2 \int_{v_{\rm min}}^{\infty} \frac{f_1(v)}{v} dv, \tag{2.7}$$

[1]The isospin limit is usually assumed in this calculation, meaning that the small mass difference between the proton and neutron is neglected.

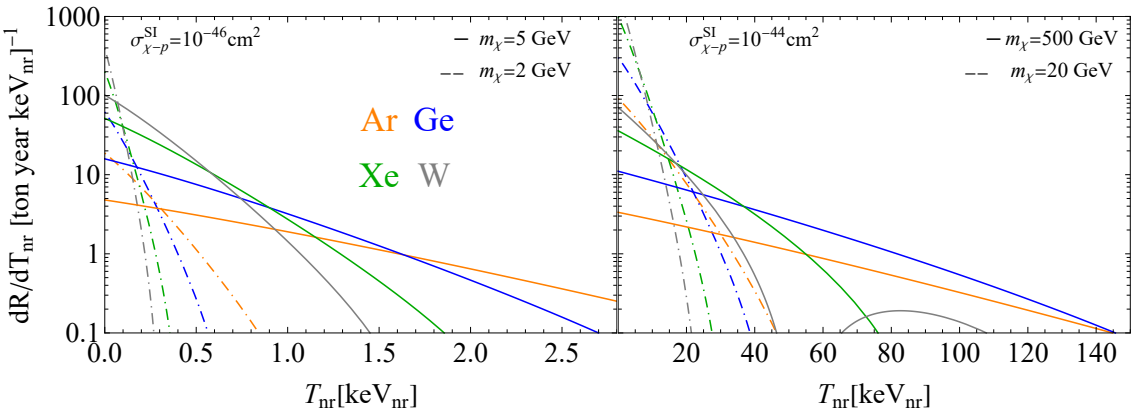

Figure 2.2: WIMP rate expected at Earth according to standard halo model for different target materials, as a function of the nuclear recoil energy.

where $v_{\min}$, is the minimum velocity for a given $T_{\rm nr}$ and is

$$v_{\min} = \sqrt{\frac{m_N T_{\rm nr}}{2\mu^2_{\chi-\mathcal{N}}}}, \tag{2.8}$$

with $\mu^2_{\chi-\mathcal{N}}$ the WIMP-nucleus reduced mass. Fig. 2.2 shows the theoretical WIMP rate in two different regimes. As a general statement, as shown in Fig. 2.2, DM candidates with a high mass produce larger nuclear recoil energies compared to lighter DM particles. For this reason, a necessary requirement for a direct detection DM experiment to be sensitive to light WIMPs is to have a low detection threshold. Direct research for dark matter is conducted using underground detectors, which allow for significant suppression of experimental backgrounds, specifically cosmic rays. Different technologies are currently used, and noble liquid detectors are particularly relevant for this thesis.
See Ref. [97] for a comprehensive and up-to-date review of the current status of direct detection dark matter searches, with a focus on all detectors that are currently operational.

2.2.1 Direct Search for WIMPs with Noble Liquids Detectors

Noble liquids, such as argon and xenon, are widely used as target material in direct WIMP searches because of their excellent scintillation properties and intrinsic radiopurity. This feature, combined with the ease of scaling up to large mass at moderated cost, has made LXe and LAr popular targets and detectors

for rare physics searches; in fact, noble liquid detectors are also exploited in the context of CEνNS searches (see Chap. 3 and Chap. 4). Specifically, different ton-scale liquid xenon detectors are currently operating, among them XENONnT [98], PandaX [99] and LZ [73]. Moreover, a well-established complementarity exists between dark DM experiments and neutrino physics [100]. Remarkably, both PandaX [101] and XENONnT [102] recently reported the first measurement of CEνNS from solar neutrinos at about 2.7 σ CL, while intriguing constraints of neutrino properties have been obtained by XENONnT [74] and LZ [103]. In Chap. 7 we will use LZ data to put world-leading constraints on some neutrino properties. On the other hand, argon has the advantage that it is quite abundant in Earth's atmosphere, it is easy to purify by removing electronegative impurities, which makes it less expensive compared to other noble liquids. This characteristic makes the idea of building large detectors more feasible. The most abundant component in atmospheric argon (AAr) is the stable isotope $^{40}\mathrm{Ar}$, produced by the electron capture of $^{40}\mathrm{K}$ [104]. The production rate is proportional to the number of $^{40}\mathrm{K}$, therefore the majority of the production occurs underground and from there $^{40}\mathrm{Ar}$ diffuses into the atmosphere. Indeed, due to interactions of cosmic rays, atmospheric argon also contains three long-lived radioactive isotopes: $^{39}\mathrm{Ar}$, $^{37}\mathrm{Ar}$ and $^{42}\mathrm{Ar}$. Among these three isotopes, the pure β-emitter $^{39}\mathrm{Ar}$ is often the dominant source of background at low energies for argon-based detectors, limiting the sensitivity to rare events searches. This unstable isotope has an activity of $(1.01 \pm 0.08)\ \mathrm{Bq\ kg^{-1}}$ [105], an endpoint of 565 keV, and a half-life of 269 years. For this reason, the use of underground argon (UAr) with a significant reduction of $^{39}\mathrm{Ar}$ compared to AAr, represented a game changer for argon detectors. The DarkSide-50 Collaboration, at Gran Sasso National Laboratories, cleverly decided to fill the TPC with UAr, reaching an unprecedentedly low background level for an argon-based detector. For a review specifically on direct dark matter detection with liquid argon, see Ref. [106]. In the next sections, the DarkSide program will be detailed, with a particular focus on the DarkSide-20k and its physics reach.

2.3 The DarkSide Program and the DarkSide-20k Experiment

This section will present the DarkSide project, which leads the argon-based direct dark matter searches using a dual-phase time projection chamber (TPC). The

DarkSide TPC consists of an active volume filled with liquid argon, which is immersed in a uniform electric field, to drift ionization electrons towards a gaseous region on top of the detector, where charges are accelerated to stimulate light production by electroluminescence. One of the major advantages of the use of argon as a target material for rare event searches lies in its unique scintillation properties, which allow for the distinction between nuclear recoils (NR) and electron recoils (ER). Therefore, it is useful to delve into the operational principles of an argon detector, as its understanding will be valuable not only in the context of the DarkSide TPC, but also for comprehending the CEνNS CENNS-10 experiment discussed in Sec. 3.3. Scintillation from noble liquids arises in two distinct ways, involving de-excitation and recombination. The interaction of a particle with atoms excites the atoms, leading to the formation of weakly bound excited dimers, called excimers, within a few picoseconds [107]. These excimers then radiatively de-excite, producing vacuum ultraviolet (VUV) photons

$$\begin{aligned} \mathrm{Ar}^{*}+\mathrm{Ar} &\rightarrow \mathrm{Ar}_{2}^{*}, \\ \mathrm{Ar}_{2}^{*} &\rightarrow 2\mathrm{Ar}+\gamma, \end{aligned} \tag{2.9}$$

with a wavelength of $128\ \mathrm{nm}$. Likewise, the ionization track produced by the recoiling argon nucleus upon interaction is followed by the recombination of electron-ion pairs and the formation of excited dimers, leading to the emission of scintillation VUV photons. The scintillation light produced by the excited molecular states has both a "fast" component ($\tau_s \simeq 6\ \mathrm{ns}$) and a "slow" component ($\tau_t \simeq 1600\ \mathrm{ns}$). These components are due to electronic and nuclear recoils in different proportions, allowing the differentiation between the two through pulse shape discrimination (PSD). This is achieved using the parameter f_{90}, which quantifies the fraction of light emitted in the first 90 ns after the recoil, compared to the total collected light. Since nuclear recoil signals produce almost all their light within the first 90 ns while electronic recoils later, it is possible to discriminate between NR and ER. The f_{90} parameter is more efficient at higher NR energies, setting the energy threshold to approximately $\sim 20\ \mathrm{keV_{nr}}$. In order to detect VUV photons, the inner TPC walls need to be coated with a wavelength shifter that absorbs photons at $\lambda = 128\ \mathrm{nm}$ and re-emittes in the visible range at $\lambda = 420\ \mathrm{nm}$, allowing them to be detected by the photo-multiplier tubes (PMTs) in the case of the DarkSide-50 detector. PMTs collect both the prompt scintillation light produced in liquid (S1), and the delayed electro-luminescence light (S2) generated in gas, allowing for en-

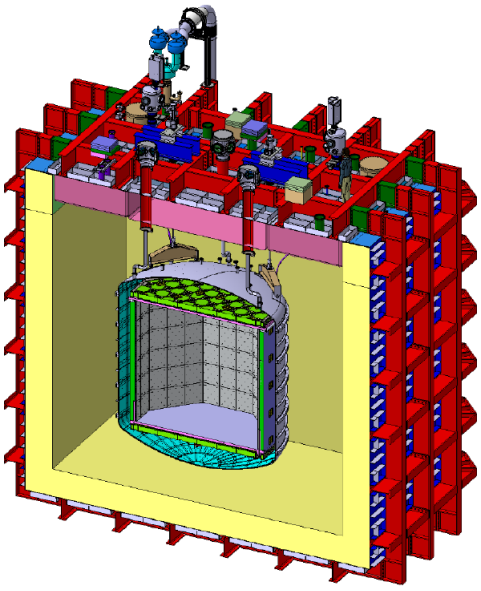

Figure 2.3: Cross-section of the DarkSide-20k detector showing the inner detector with the acrylic walls in green and the electrodes in pink. The stainless steel vessel is in grey and the Proto DUNE-like cryostat is in yellow and red. Figure taken from Ref. [9].

ergy measurement and 3D vertex reconstruction.

The DarkSide-50 detector operated with (46.4 ± 0.7) kg active mass of UAr and is now dismantled after its successful measurements started in 2013. The DarkSide-50 detector demonstrated in fact that the UAr has a $^{39}\mathrm{Ar}$ rate of $7.3 \times 10^{-4}\mathrm{Bq\ kg^{-1}}$, which is a factor of about 1400 below atmospheric levels [108] and allowed the collaboration to put very strict limits on DM candidates and BSM physics [109–113].

In light of its success, the DarkSide-50 experiment served as a prototype for the DarkSide-20k detector [114], whose schematic is shown in Fig. 2.3 and will be hosted by Gran Sasso National Laboratories in the same hall as its predecessor. The DarkSide-20k collaboration plans to extract UAr from CO_2 wells in Cortez, CO (US), through the Urania plant and to distil it in Sardinia at the ARIA plant, which is responsible for argon purification (further separation of isotopes $^{39}\mathrm{Ar}$ from $^{40}\mathrm{Ar}$ and chemical distillation) [12, 115]. The DarkSide-20k TPC, will be filled with 49.7 ton of UAr and shaped as a prism with an octagonal base, with a vertical drift length of 348 cm and an octagonal inscribed circle diameter of 350 cm. To ensure the extraction of electrons, the active volume is immersed in a uniform electric field generated by applying a voltage potential of 73.4 kV between the anode and the cathode made of transparent acrylic (PMMA) coated with a conductive material (Clevios). The S2 electroluminescence signal develops in a

multiplication region filled with gaseous argon, 7 mm thick between the liquid level and the anode, giving about 25 photo-electrons per ionization electron extracted in the gas pocket [9].
To ensure the best possible collection of both scintillation and ionization-induced photons, the inner TPC walls are coated with tetraphenyl butadiene to shift the VUV photons to visible wavelength for which photodetection efficiency is maximal. Two planes of cryogenic Silicon Photo Multipliers (SiPMs) cover the top and bottom faces of the TPC to detect the light signals. The ∼200k SiPMs are gathered in the so-called Photo Detector Modules (PDMs) [116] which consist of $5 \times 5\ \mathrm{cm}^2$ arrays. If neutrons scatter in the TPC and produce a WIMP-like signal, they are likely to be captured in the 15 cm thick acrylic TPC walls. Neutrons captured in this way release γ-rays which are detected in the TPC and/or the 32 ton UAr veto surrounding it. The TPC and this UAr veto are housed in a stainless steel (SS) vessel and read by 480 photo detector channels. This SS vessel is immersed in a bath of 650 tons of atmospheric argon (AAr), acting as a shield and an outer veto detector for muons and associated products. The AAr is contained in a ProtoDUNE-like membrane cryostat [117]. A dedicated material campaign carefully selected the materials with the lowest radioactivity level possible to reduce the background, and in this context an extensive simulation of all the background is crucial. Neutrinos represent an irreducible background, as they cannot be shielded and their signal cannot be distinguished from that of dark matter. However, due to the advancements in the knowledge of neutrino interactions, using the formalism described in Chap. 1 it is possible to carefully evaluate the expected rate of neutrino elastic scattering off nuclei and electrons for the DarkSide-20k experiment, as will be discussed in the following.

2.4 Astroparticle Neutrino Sources

The impact of the neutrino background in direct dark matter experiments is typically expressed through the so-called “neutrino floor” [120, 121]. This concept defines the region in the WIMP mass and cross-section parameter space where the WIMP signal becomes statistically indistinguishable, at a given confidence level, from the signal produced by neutrino interactions. The neutrino floor, or better say neutrino fog, has recently been revisited in Ref. [122]. The neutrino fog marks the point at which any experiment will start to be limited by the neutrino back-

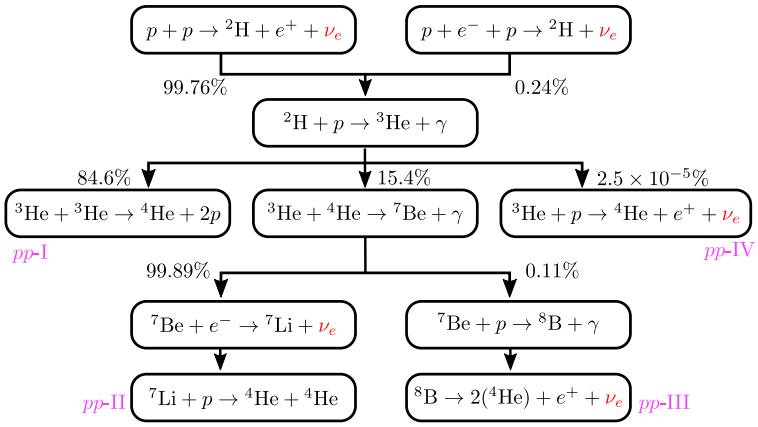

Figure 2.4: Reactions in the solar pp chain. Neutrinos (ν_e) produced in the five reactions in the top-down order are referred to as pp, pep, hep, ^{7}Be, ^{8}B neutrinos, respectively. The theoretical branching percentages are taken from Ref. [118]. Figure from Ref. [119].

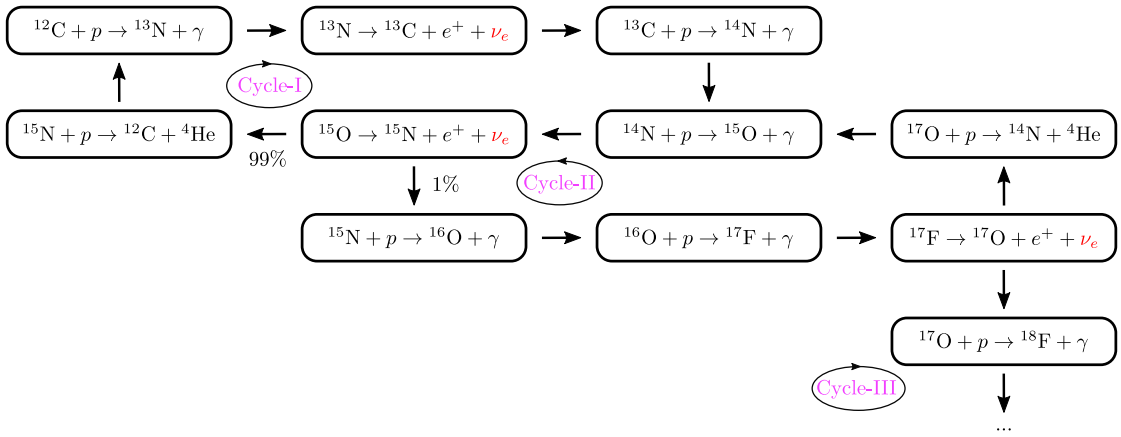

Figure 2.5: Reactions in the CNO cycle. Neutrinos (ν_e) are produced from decays of ^{13}N, ^{15}O, and ^{17}F in the first two cycles, Cycle-I and Cycle-II, with the latter suppressed relatively by $\sim 1\%$. The electron capture from oxigen and fluorine chains is not shown. Figure from Ref. [119].

ground. Still, it can be overcome by a deep knowledge of the neutrino signal, allowing its subtraction during statistical analyses.

This section will discuss the neutrino fluxes which will affect the sensitivity of direct detection experiments, in order to compute the expected rate for DarkSide-20k[2]. The main neutrino fluxes which originate from *astroparticle* sources could be divided into three categories: solar (Sec. 2.4.1), atmospheric (Sec. 2.4.2) and diffuse supernovae neutrinos (Sec. 2.4.3), where the respective origin is encoded in their name. The neutrino flux at Earth from each component mentioned above is reported in Fig. 2.6, while Tab. 2.1 lists all the neutrino flux components, with

[2]The results presented in this thesis, are intended to be an update of the calculation reported in Ref. [123] and recently in Ref. [124].

Channel	Flux	$E_{\rm av}$ [MeV]	$E_{\rm max}$ [MeV]	Flux at Earth	
				Total	Units
pp Chains	$\Phi_{\rm pp}$	0.267	0.423	$5.98 \pm 0.6\%$	$10^{10}{\rm cm}^{-2}{\rm s}^{-1}$
	$\Phi_{\rm B}$	6.735	16.34	$5.46 \pm 12\%$	$10^{6}{\rm cm}^{-2}{\rm s}^{-1}$
(β^+)	$\Phi_{\rm hep}$	9.628	18.784	$0.80 \pm 30\%$	$10^{4}{\rm cm}^{-2}{\rm s}^{-1}$
pp Chains	$\Phi_{\rm Be}$	0.863 (89.7%) 0.386 (10.3%)		$4.93 \pm 6\%$	$10^{9}{\rm cm}^{-2}{\rm s}^{-1}$
(EC)	$\Phi_{\rm pep}$	1.445		$1.44 \pm 1\%$	$10^{8}{\rm cm}^{-2}{\rm s}^{-1}$
CNO Cycle	$\Phi_{\rm N}$	0.706	1.198	$2.78 \pm 15\%$	$10^{8}{\rm cm}^{-2}{\rm s}^{-1}$
	$\Phi_{\rm O}$	0.996	1.732	$2.05 \pm 17\%$	
(β^+)	$\Phi_{\rm F}$	0.998	1.736	$5.29 \pm 20\%$	$10^{6}{\rm cm}^{-2}{\rm s}^{-1}$
CNO Cycle	$\Phi_{\rm eN}$	2.220		$2.20 \pm 15\%$	$10^{5}{\rm cm}^{-2}{\rm s}^{-1}$
	$\Phi_{\rm eO}$	2.754		$0.81 \pm 17\%$	
(EC)	$\Phi_{\rm eF}$	2.758		$3.11 \pm 20\%$	$10^{3}\ {\rm cm}^{-2}\ {\rm s}^{-1}$
Atm	$\Phi^{\rm atm}_{\nu_e+\bar{\nu}_e}$ $\Phi^{\rm atm}_{\nu_\mu+\bar{\nu}_\mu}$		944	3.68±20% 7.04±20%	$10^{0}{\rm cm}^{-2}{\rm s}^{-1}$
DSNB	$\Phi^{\rm DSNB}$		82.5	8.74±50%	$10^{1}\ {\rm cm}^{-2}\ {\rm s}^{-1}$
Geo-ν	$\Phi^{\rm geo}_{\bar{\nu}_e}$		4.4	$8.65 \pm 20\%$	$10^{7}\ {\rm cm}^{-2}\ {\rm s}^{-1}$

Table 2.1: Table collecting the flux prediction for solar neutrinos, atmospheric neutrinos, diffuse supernova and geoneutrinos used in this thesis. The table shows the average energy for the solar neutrino flux component, $E_{\rm av}$, and the maximum energy, $E_{\rm max}$. The total solar neutrino flux is based on the calculation from Ref. [128] from the standard solar model GS98 [129]. The normalization on the atmospheric neutrino [130], the diffuse supernova neutrino [131] and the geoneutrino [125] fluxes are also reported.

their respective absolute normalizations. The geoneutrino flux [125, 126] is also reported for completeness, to assess its impact on the total neutrino budget of DarkSide-20k. Note that in this study, the contribution of reactor neutrinos has been neglected. This contribution varies significantly based on the experiment's proximity to nuclear reactors and the reactors' power output. Therefore, it must be independently estimated during the experiment's data collection period [127].

2.4.1 Solar Neutrinos

According to the standard solar model [129] solar neutrinos are produced during the fusion of protons to helium nuclei taking place in the solar core

$$4p + 2e^- \rightarrow^4 {\rm He} + 2\nu_e + 26.73\ {\rm MeV}. \tag{2.10}$$

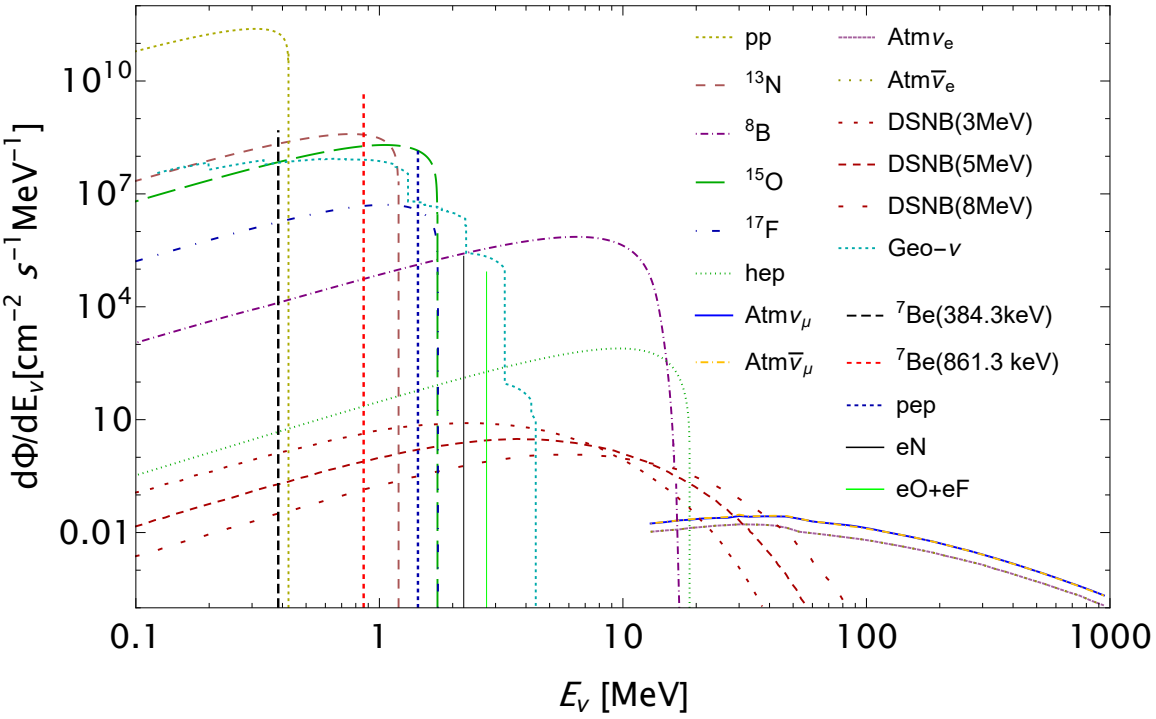

Figure 2.6: Neutrino flux at Earth from the solar pp chain and CNO cycle [128], atmospheric neutrinos [130], and diffuse supernovae neutrino [131]. The average geo-neutrino flux [125] is also reported for completeness. The absolute normalization for each component is reported in Tab. 2.1.

The dominant fusion process in the Sun is the pp chain. In contrast, the CNO cycle contributes only a subdominant fraction of the total solar energy, relying on the presence of heavier elements as well as the core's metallicity[3]. Both chains are schematized in Figs. 2.4 and 2.5, and the respective fluxes are indicated in Fig. 2.6. The majority of neutrinos originate in the pp process and have a continuous energy spectrum with 0.423 MeV endpoint. The pp chain is also responsible for the mono-energetic ^{7}Be neutrinos, with 10% branching at 0.386 MeV (excited state) and ∼90% branching at 0.863 MeV (ground state) and the mono-energetic (1.44 MeV) pep neutrinos. ^{8}B neutrinos are produced but with lower flux and a continuous energy spectrum that extend up to about 16.3 MeV. The fluxes from the pp chain have been precisely measured with a global analysis in Ref. [132], while the CNO cycle neutrino flux has been measured by Borexino [133, 134]. On the other hand, hep neutrinos with an extremely low flux and 18.784 MeV endpoint energy, have not been experimentally observed yet.

The neutrino emission from the CNO cycle is dominated by the β^+ decay of ^{13}N and

[3]The metallicity of a star refers to the proportion of elements heavier than hydrogen and helium, typically measured by the [Fe/H] ratio [129].

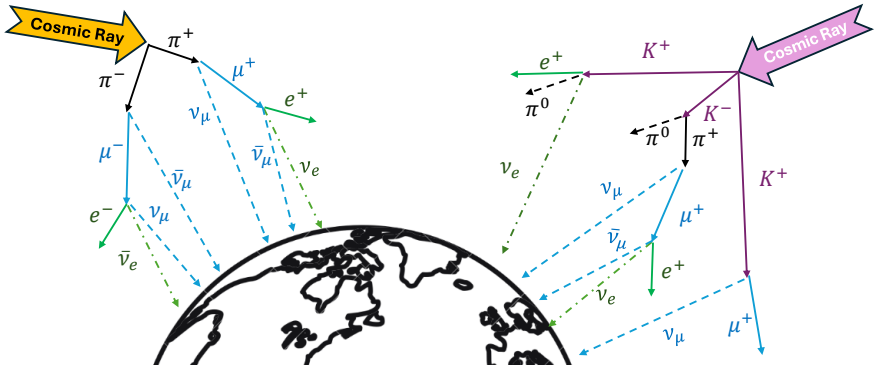

Figure 2.7: Schematic representation of the formation of atmospheric neutrinos. On the left is reported the decay chain involving $\pi^{\pm}$, while on the right the decay chain from $K^{\pm}$. The image is not in scale.

^{15}O, while ^{17}F decays contribute only at the 1% level. All three components are continuous spectra of similar shapes with endpoints below 1.8 MeV. In this thesis, to compute the expected neutrino flux, we also take into account the electron capture on N, O and F during the CNO chain [135], i.e.

$$^{13}\mathrm{N} + \mathrm{e}^- \rightarrow ^{13}\mathrm{C} + \nu_\mathrm{e}, \tag{2.11}$$

$$^{15}\mathrm{O} + \mathrm{e}^- \rightarrow ^{15}\mathrm{N} + \nu_\mathrm{e}, \tag{2.12}$$

$$^{17}\mathrm{F} + \mathrm{e}^- \rightarrow ^{17}\mathrm{O} + \nu_\mathrm{e}. \tag{2.13}$$

Such neutrinos have never been observed, but their contribution to the background budget of the experiment will be considered. Their fluxes are suppressed by about a factor of 10^{-4} compared to their β^+ decay neutrino fluxes [119] and are reported as mono-energetic lines in Fig. 2.6. The normalization of the absolute flux used in this thesis will follow Ref. [128], based on the standard solar model GS98 [129].

2.4.2 Atmospheric Neutrinos

Despite their name, the mechanism that originates atmospheric neutrinos has its foundation in astrophysical cosmic ray sources. The charged component of the primary cosmic rays hitting the atmosphere consists mainly of hadrons with a small fraction of electrons. The hadronic component itself is dominated mainly by protons and α-particles, with a subdominant component of heavier nuclei [17,

75]. The interaction of such energetic cosmic rays, $\mathcal{O}(\mathrm{GeV})$, with the nuclei in the outer layer atmosphere generates a cascade of hadrons, referred to as secondary cosmic rays, with a significant component of charged pions. The charged pions then decay and produce neutrinos. The decay channel is similar to that of interest for π-DAR neutrino sources (see Chap. 3), specifically [126, 130]

$$\pi^+ \to \nu_\mu + \mu^+, \qquad \pi^- \to \mu^- + \bar{\nu}_\mu, \tag{2.14}$$

$$\mu^+ \to e^+ + \nu_e + \bar{\nu}_\mu, \qquad \mu^- \to e^- + \bar{\nu}_e + \nu_\mu. \tag{2.15}$$

Atmospheric neutrinos can also be produced by kaon decays, i.e.

$$K^\pm \to \pi^0 + e^\pm + \nu_e(\bar{\nu}_e), \tag{2.16}$$

$$K^\pm \to \mu^\pm + \nu_\mu(\bar{\nu}_\mu), \tag{2.17}$$

$$K^\pm \to \pi^\pm + \pi^0, \tag{2.18}$$

whose decay of $\pi^\pm$ in turn produce neutrinos. A schematic representation of the decay channel which originates the atmospheric neutrino flux at Earth is shown in Fig. 2.7, while the normalization used for our calculation is based on Ref. [130]. The fluxes are shown in Fig. 2.6.

2.4.3 Diffuse supernova neutrino backgrounds

Another interesting and widely investigated source of neutrino is the diffuse supernova neutrino background (DSNB) [131, 136]. It refers to the flux from the past history of all supernova explosions in the universe. The DSNB flux is a convolution of the core-collapse supernova rate as a function of redshift with the neutrino spectrum per supernova. Even though it has never been observed yet, different prospects are underway to detect their signal [137], and for our purposes, it represent a source of background for dark matter searches. The rate of core-collapse events is calculated based on the star-formation rate and the initial mass function of stars. Then, the neutrino spectrum resulting from a core-collapse supernova resembles a Fermi-Dirac distribution, with temperatures spanning from 3 to 8 MeV, so in our calculation, we will consider spectra of 3, 5 and 8 MeV [131]. According to [131] a systematic uncertainty on the DSNB flux of 50% will be considered, and the fluxes are shown in Fig. 2.6.

2.5 Neutrino Background Rate In DarkSide-20k

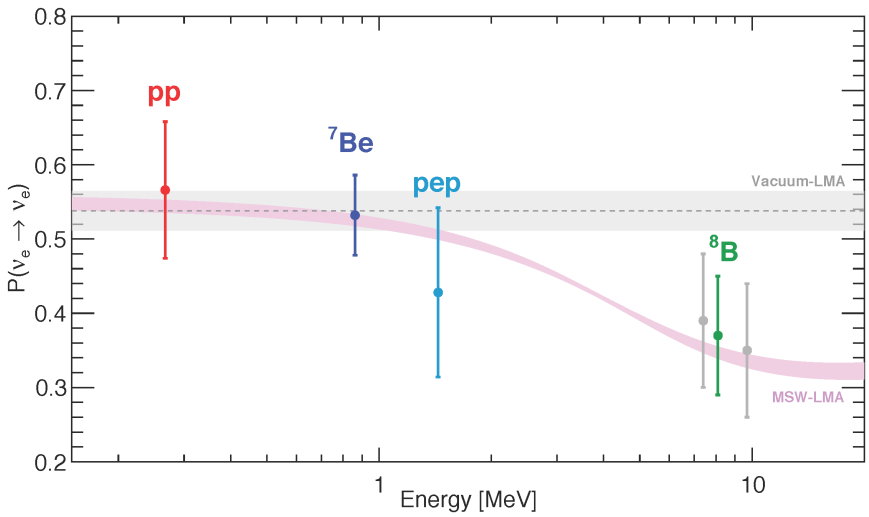

Figure 2.8: Electron neutrino survival probability $P(\nu_e \rightarrow \nu_e) \doteq P_{ee}$ as a function of neutrino energy. The pink band is the $\pm 1\ \sigma$ prediction of the MSW effect with oscillation parameters determined from Ref [138]. The grey band is the vacuum case. Data points represent the Borexino results. Figure from Ref. [71].

Having described the neutrino fluxes of interest, we can convolve them with the CEνNS and νES cross sections to calculate their expected rate of events. The cross section for both channels depends on the neutrino flavor, and so far we have overlooked a critical phenomenon which determines the solar neutrino flux at Earth, i.e. neutrino oscillations. Remarkably, solar neutrinos revealed the phenomenon of neutrino oscillation, which requires neutrinos to have mass [17, 75, 139], providing a solution to the well-known solar neutrino problem [140]. In fact, the reaction described in Sec. 2.4.1 shows that neutrinos produced in the Sun consist of ν_e, but due to neutrino oscillations, they are detected on Earth in different flavors, explaining the discrepancy with experimental observations. Indeed, measurements of the solar neutrino flux have been pivotal in advancing our understanding of neutrino oscillations. Moreover, measurements from solar neutrinos [19] revealed that the standard vacuum oscillation mechanism required further investigation and the Mikheyev-Smirnov-Wolfenstein (MSW) effect [141], was crucial to understanding that these oscillations are enhanced when neutrinos pass through matter. The traveling of neutrinos in the dense solar interior causes a significant portion of the electron neutrinos to change flavor before reaching the detectors on Earth. We adopted the MSW scheme to compute the neutrino oscillation from the Sun to our detector.

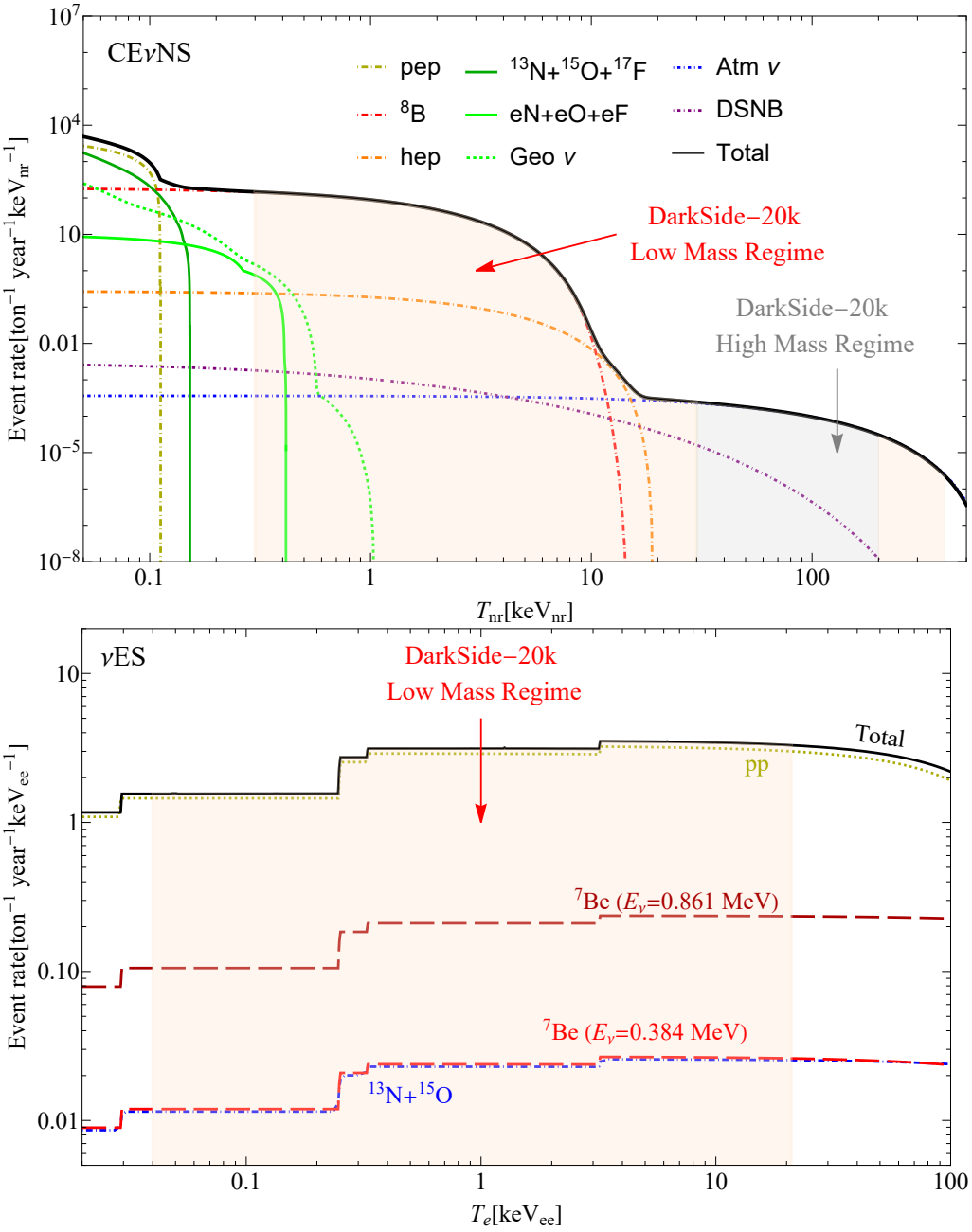

Figure 2.9: Event rate from CEνNS (upper panel) and νES (lower panel) expected in argon for various neutrino sources, whose flux is reported in Fig. 2.6. The orange band represent the recoil energy range for both CEνNS and νES of interest for the low mass analysis of DarkSide-20k, while the grey band represents approximately the nuclear recoil energy range for the DarkSide-20k high mass search.

Fig. 2.8 shows the survival probability of electron neutrinos, i.e. the probability that a neutrino produced in the Sun as an electron neutrino arrives at the Earth's surface with the same flavor, as a function of the neutrino energy. The pink band represents the MSW prediction, while the grey band represents the standard oscillation in vacuum. Intriguingly, all the experimental points from Borexino [71] are

in agreement with the MSW prediction.
Therefore, the total SM differential cross section, reported in Chap. 1, for scattering off nuclei (atoms) $\mathcal{N}$ ($\mathcal{A}$) from CEνNS (νES) as a function of the respective recoil energy, indicated for simplicity with T, is obtained by including the contribution from all neutrino flavours taking into account the oscillation probability in the 3-neutrino oscillation scheme. Namely, the cross section from solar neutrino is obtained as [142]

$$\frac{d\sigma_{\nu-\mathcal{N}(\mathcal{A})}}{dT} = P_{ee}(E_\nu)\frac{d\sigma_{\nu_e-\mathcal{N}(\mathcal{A})}}{dT} + \sum_{f=\mu,\tau} P_{ef}(E_\nu)\frac{d\sigma_{\nu_f-\mathcal{N}(\mathcal{A})}}{dT}, \tag{2.19}$$

where the transition probabilities, i.e. $P(\nu_e \to \nu_\mu) \doteq P_{e\mu}$ and $P(\nu_e \to \nu_\tau) \doteq P_{e\tau}$, are

$$P_{e\mu} = (1 - P_{ee})\cos^2\theta_{23}, \tag{2.20}$$

$$P_{e\tau} = (1 - P_{ee})\sin^2\theta_{23}, \tag{2.21}$$

where θ_{13} and θ_{23} are the mixing angles responsible for oscillations whose values are taken from Ref. [19].
Note that at low neutrino energies, which are relevant for νES, the survival probability can be approximated as $P_{ee} = \sin^4\theta_{13} + \cos^4\theta_{13}P^{2\nu}$ [142], where $P^{2\nu} \simeq 0.55$ [19, 143] is the ν_e survival probability in the 2-neutrino oscillation scheme.
We are neglecting oscillations from atmospheric, DSNB, and geo-neutrinos, as the uncertainty in their absolute normalization renders the impact of accounting for these oscillations negligible. The expected rate in the argon detector is obtained as a convolution of the cross section with the neutrino flux Φ, specifically

$$\frac{dR_{\nu-\mathcal{N}(\mathcal{A})}}{dT} = N(\mathrm{Ar})\int_{E_\nu^{\min}}^{E_\nu^{\max}} \frac{d\Phi}{dE_\nu}\frac{d\sigma_{\nu-\mathcal{N}(\mathcal{A})}}{dT}(E_\nu, T)dE_\nu, \tag{2.22}$$

where $N(\mathrm{Ar})$ is the number of Ar atoms in the detector, which is given by $N(\mathrm{Ar}) = N_\mathrm{A}M_\mathrm{det}/M_\mathrm{Ar}$, where N_A is the Avogadro number. M_det is the detector active mass, while M_Ar is the molar mass of argon $M_\mathrm{Ar} = 39.9623$ g/mol. $E_\nu^{\min} \simeq 1/2\left(T + \sqrt{T^2 + 2m_T T}\right)$ is the minimum neutrino energy allowed from the kinematics, where m_T is the target mass and T the energy deposit in the detector. Using the values in Tab. 1.1 to parameterize the nuclear structure of Ar and the SM value of the Weinberg angle, the rates obtained are shown in Fig. 2.9 for an exposure of 1 ton $\cdot$ year.

The contribution of neutrino background in DarkSide-20k can be classified into two main categories based on the WIMP candidate that the experiment wants to constrain:

- *High mass dark matter searches*: $\sim 10^{-2} - 10$ TeV [109]. High mass WIMPs can induce nuclear recoils larger than $\simeq 30$ $\mathrm{keV_{nr}}$ in Ar (right panel in Fig. 2.2), which allows for the utilization of Ar scintillation properties to maximize its background-rejection efficiency and enhance the ability to distinguish between NRs and ERs. A detailed selection of materials is mandatory to significantly reduce the neutron budget of the experiment, aiming to achieve *almost-zero*, specifically < 0.1 background events in the region of interest [109] in the whole exposure of 200 ton $\cdot$ year. Therefore, while neutrons can be moderated and reduced *a-priori*, neutrinos cannot be shielded. As it is clear from the upper panel of Fig. 2.9, only atmospheric and DSNB contribute for $T_{\mathrm{nr}} \gtrsim 30$ $\mathrm{keV_{nr}}$. In DarkSide-20k, about 3 neutrinos are expected within the full exposure of 200 ton $\cdot$ year, which will limit the sensitivity to high mass DM candidates, but would notably allow pointing toward the first identification of CEνNS events from atmospheric neutrinos.

- *Low mass dark matter searches*: $\sim 1 - 10$ GeV [144]. Light dark matter candidates give an experimental signature at low recoil energies (left panel in Fig. 2.2). In this regime, the prompt S1 scintillation signal is subdominant compared to the ionization one, such that, in this case, the search is based on the S2-only signal. In the S2-only analysis the PSD loses its discrimination power, it is impossible to reconstruct the interaction vertex and the ability to discriminate between NR and ER is lost. While, this method allows for a substantial reduction in the experimental threshold, i.e. $\simeq 0.3$ $\mathrm{keV_{nr}}$ corresponding to about 3 ionized electron N_e, a detailed characterization of different background components is pivotal. For the goal of this search, therefore both CEνNS and νES contribute.

2.6 DarkSide-20k Sensitivity to Low-Mass Dark Matter Particles

This section outlines the findings from the DarkSide-20k collaboration regarding the sensitivity of the experiment to light dark matter candidates, as detailed in

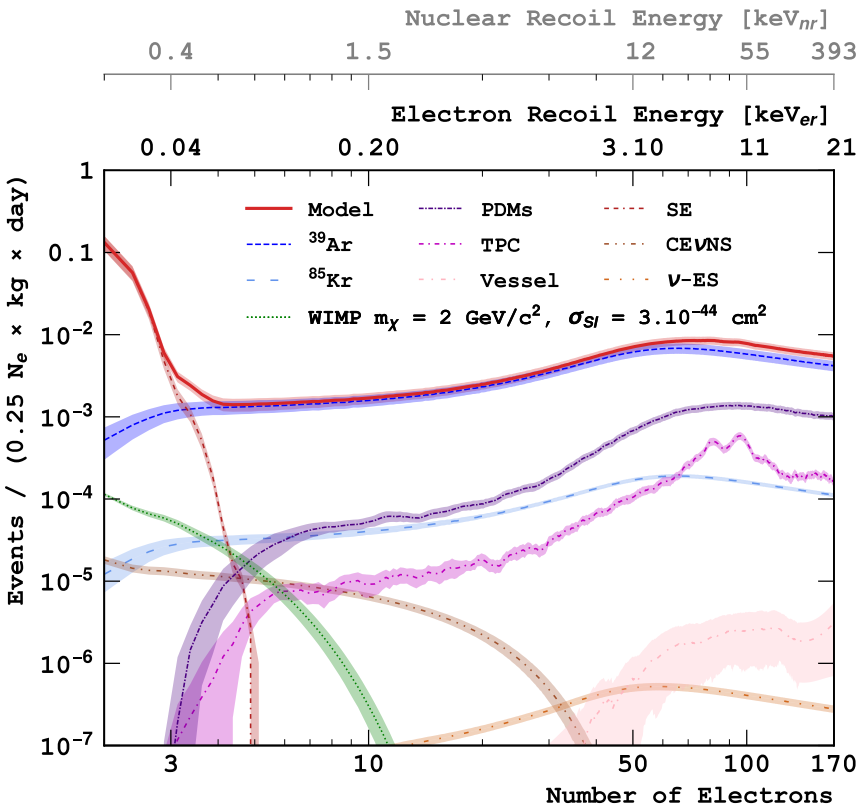

Figure 2.10: Pre-fit background spectra expected in DarkSide-20k in the low mass analysis, as a function of the number of photoelectrons N_e. The corresponding ER and NR energy scales are indicated at the top. The contribution from all the components is shown, together with their uncertainty. Figure from Ref. [9].

Ref. [9]. It also provides context for the neutrino background study conducted in this thesis. Fig. 2.10 shows the background rate, as a function of the photoelectrons N_e, from different components where the spectra have been convoluted with the detector response model (see Ref. [9] for more detail on the detector response model, and on the treatment of other backgrounds when scaling from DarkSide-50 to DarkSide-20k). From Fig. 2.10, it is evident that the intrinsic background in LAr is dominated by the β-decay of the ^{39}Ar isotope and ^{85}Kr present in the active volume of UAr. The former is assumed to be at the same level as in DarkSide-50 while the latter is expected to be reduced by a factor of 100 compared to the one of DarkSide-50, thanks to a new multiple distillation column system that has been added at the UAr extraction plant. The background is well-known for $N_e \gtrsim 4$, while for lower energies one has to deal with the single-electron problem, faced for the first time in Ar with the DarkSide-50 detector [144], which limits the sensitivity of the experiment. While the DarkSide-50 collaboration tried to characterize

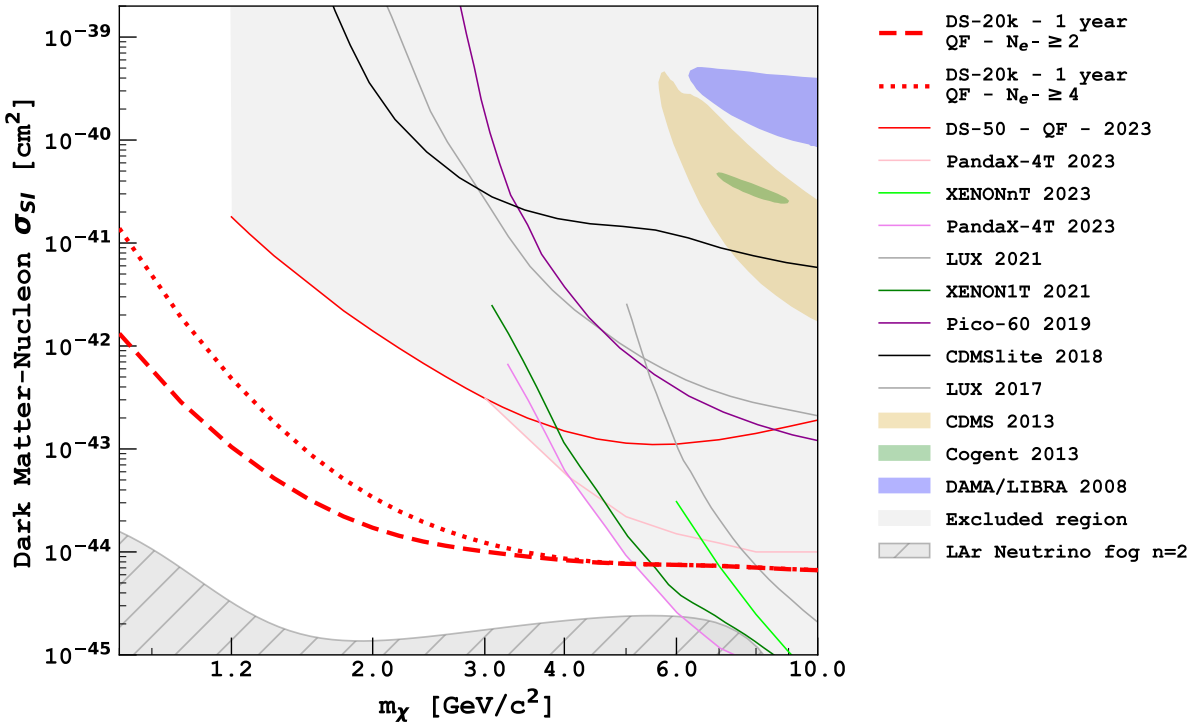

Figure 2.11: Expected DarkSide-20k 90% CL exclusion limits for spin-independent WIMP interaction (dotted: fit from $N_e = 4$, dashed: fit from $N_e = 2$). One year of data-taking is assumed, corresponding to a total exposure of 17.4 ton $\cdot$ year. They are compared to the published 90% CL limits from DarkSide-50 [111] and from other experiments [98, 99, 145–150], with currently excluded parameter space shaded in light grey, as well as claimed discovery from Refs [151–153]. The neutrino fog in LAr with index $n = 2$ [122] is also shown. A local dark matter density of 0.3 GeV/c^2/cm^3 is assumed. Figure from Ref. [9].

this background [154], its origin is still unknown, and remarkably a similar background has also been observed in xenon detectors [155–157]. This unexpected sharp rise in the observed energy spectrum is a common feature of low-threshold experiment and will be discussed separately in Chap. 5.

For comparison, Fig. 2.10 shows also the signal from a WIMP with 2 GeV mass and a spin independent cross section of $\sigma_{\rm SI} = 3 \cdot 10^{-44}$ cm^2. Due to its impressive mass and its low-energy threshold, the DarkSide-20k experiment expects to reach the strongest bounds on low mass dark matter candidates, as shown in Fig. 2.11. The DarkSide-20k 90% CL upper limit on spin idependent WIMP-nucleon cross section is reported in Fig. 2.11 according to the statistical analysis described in Ref. [9]. The results on the sensitivity are compared with the published 90% CL limits from DarkSide-50 [111] and from other experiments [98, 99, 145–150]. An improvement in sensitivity by up to a factor 40 over DarkSide-50 is achieved, even when

a conservative fit is performed restricting the range between $4 < N_e < 170$.

This increases to a factor 170 at 1.2 GeV/c^2 WIMP mass with the assumption that the single electron problem is solved and the background is known from $N_e \gtrsim 2$, reaching a $\sigma_{\rm SI}$ of 1×10^{-43} cm^2. In general, a sensitivity to $\sigma_{\rm SI}$ below 1×10^{-42} cm^2 is achieved for WIMP masses above 800 MeV/c^2, covering a large uncharted phase space with one year of data. As the sensitivity scales with the square root of the exposure, within 10 years of exposure, the sensitivity will improve by a factor 3 compared to one year, whatever the WIMP mass and the neutrino fog in LAr with index $n = 2$ [122] could be reached for WIMP masses around 5 GeV/c^2.

3 Legacy From The COHERENT Experiment

Opening

This chapter intends to offer an in-depth account of the CEνNS experiments conducted by the COHERENT collaboration, whose data will be extensively used in this thesis. Specifically, this chapter will delve into the details of the CsI detector, employed to detect CEνNS in 2017 and recently utilized to achieve the most accurate measurement so far in 2022, along with the CENNS-10 detector, which subsequently observed this process in argon in 2020. The detector details necessary to perform the analyses conducted in the rest of the thesis will be presented. Additionally, the COHERENT collaboration's future plans will be outlined and will aid in the sensitivity studies conducted in the next chapters.

3.1 The Spallation Neutron Source and The COHERENT Experiment

The primary actor in the CEνNS era has been the COHERENT experiment, which first observed this process in 2017 [158] using a cesium-iodine detector doped with Na (CsI[Na]). At the time of writing this thesis, the COHERENT collaboration stands as the primary experimental facility for definitively detecting CEνNS with high statistical significance using various target materials. The observation of CEνNS with argon [159] in 2020 further boosted the experimental research, and recently the COHERENT collaboration reported a 3.9σ CEνNS observation with a germanium detector [160]. The COHERENT Collaboration has not publicly released official data for the germanium observation; therefore, this measurement will not be considered in the analysis presented in this thesis. Moreover, the COHERENT collaboration is pioneering the measurement of ν_e charged-current cross

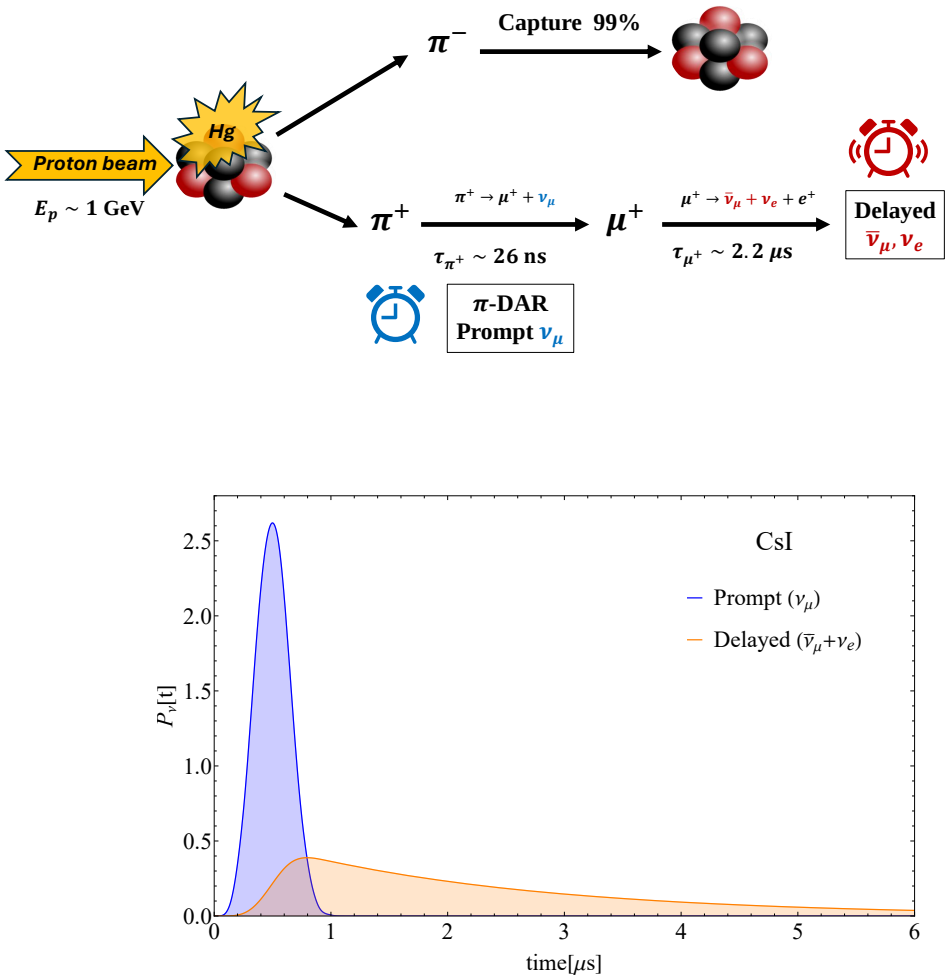

Figure 3.1: Upper panel: schematic representation of the process leading to neutrino production via πDAR at the SNS. Lower panel: arrival time distribution of neutrinos at the CsI[Na] detector normalized to unity [163].

sections [161] and other neutrino inelastic scattering channels [162], providing a wide and multi-purpose experimental program. This is achieved by taking advantage of neutrinos within the energy range of approximately 10-50 MeV, generated at the spallation neutron source (SNS) located at the Oak Ridge National Laboratory (ORNL) in Tennessee. The SNS is currently the most intense terrestrial source of neutrinos in the 10's of MeV energy range[1]. Such neutrinos are produced through the decay-at-rest (DAR) of pions $\pi^{\pm}$, the so-called π-DAR neutrino source. The SNS works according to the following steps [167]. H^- ions are initially stripped of their electrons using a thin foil. Afterwards, the remaining protons are injected into a linear accelerator and then circulated within a stor-

[1]Other similar facilities will hopefully be available in the near future. Among them the European Spallation Source (ESS) in Lund, Sweden [164], COHERENT Captain Mills (CCM) [165] and the China Spallation Neutron Source (CSNS) [166].

age ring, where they form packets of protons with energy reaching the order of GeV. Over slightly more than a millisecond, proton pulses accumulate before the beam is extracted and directed toward a liquid mercury target. This entire cycle repeats about 60 times per second, resulting in an output of roughly 10^{16} protons on target (POT) per second at 1.4 MW [158]. At the time of the latest CsI data release [163], the SNS employed a superconducting linear accelerator to accelerate the hydrogen ions to a kinetic energy of $E_p = 0.984$ GeV.

Upon impacting the mercury target, protons interact with individual nucleons, as their de Broglie wavelength is ∼0.1 fm, much smaller than the dimension of the nucleus. Kinetic energy is transferred from a proton to the nucleon through elastic collisions, resulting in an intranuclear cascade [168, 169]. During this cascade of nucleons, lasting about 10^{-22} s, neutrons are removed from the target nucleus which is left in an excited state and loses its remaining energy in approximately 10^{-16} s, primarily through neutron evaporation [170, 171]. In this process, 20-30 neutrons are approximately emitted per proton-Hg collision [172]. These neutrons then constitute a background for CEνNS research with an emission time directly associated with the proton beam. Let's now analyse in detail how neutrinos are produced. The scheme of this process is visible in the upper panel of Fig. 3.1. During the nuclear cascade, pions are also produced and stopped inside the target. About 99% of the π^- are captured by the Hg target, while most of the π^+, with an average lifetime of $\tau_\pi \simeq 26$ ns, decay at rest emitting a μ^+ and a ν_μ

$$\pi^+ \rightarrow \mu^+ + \nu_\mu. \tag{3.1}$$

The muon, which has a lifetime of $\tau_\mu \simeq 2.2$ μs, then decays into

$$\mu^+ \rightarrow e^+ + \nu_e + \overline{\nu}_\mu. \tag{3.2}$$

Thus, there is a first prompt emission of muonic neutrinos and a subsequent delayed emission of electronic neutrinos and muonic antineutrinos. The arrival time probability describes the arrival of neutrinos in the detector and can be well approximated by a Gaussian of mean a and width b, convoluted with the π^+ and μ^+ neutrino decay lifetimes τ_π and τ_μ respectively. The arrival time distributions can

be hence parameterized as

$$P_{\nu_\mu}(t) = \frac{1}{\sqrt{2\pi}b}\int_{t_0}^{t} e^{-\frac{(T-a)^2}{2b^2}}\frac{1}{\tau_\pi}e^{-\frac{t-T}{\tau_\pi}}dT, \tag{3.3}$$

$$P_{\bar{\nu}_e,\nu_\mu}(t) = \int_{t_0'}^{t} P_{\nu_\mu}(T')\frac{1}{\tau_\mu}e^{-\frac{t-T'}{\tau_\mu}}dT'. \tag{3.4}$$

The parameters t_0, t_0', a and b, are tuned to match the characteristics of the neutrino beam during the data taking of the experiment. Moreover, it is also possible to rely on the arrival time distribution obtained from Geant4 simulation [173]. As an example, the lower panel of Fig. 3.1 shows the simulation of the arrival

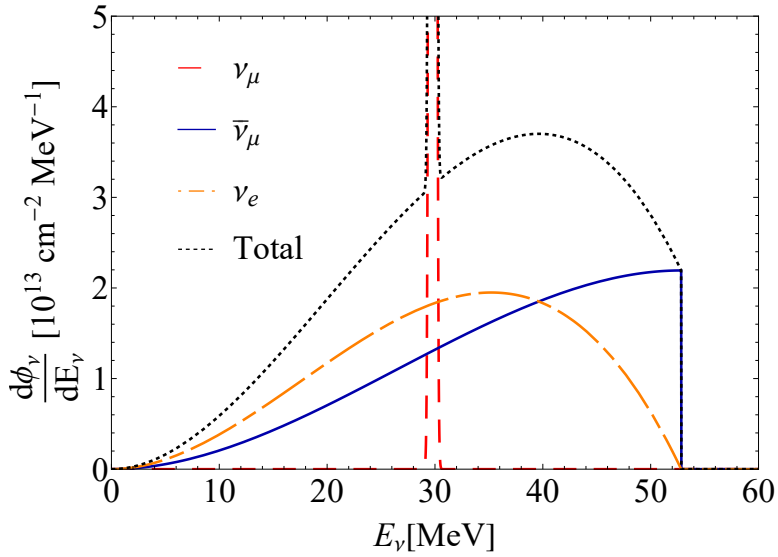

Figure 3.2: Neutrino flux divided by flavor: muon neutrinos (red) described as a narrow Gaussian with mean E_{ν_μ}, muon antineutrinos (blue), electron neutrinos (orange). The flux is calculated considering the COHERENT CsI detector setup with $N_{\mathrm{POT}} = 3.198 \cdot 10^{23}$, $r = 0.0848$, and $L = 19.3$ m [163].

time of neutrinos at the CsI[Na] detector extracted from the latest CsI data release [163], where we can clearly identify a prompt and a delayed neutrino emission. The spectral difference between prompt and delayed neutrinos enhances the constraining power and is highly effective for background rejection. Specifically, the fast ν_μ component originating from the two-body decay of the π^+, consists of a monochromatic component with an energy of $E_{\nu_\mu} = 29.792$ MeV. The delayed component, on the other hand, includes the flux of two neutrinos ν_e, $\bar{\nu}_\mu$, which have a continuous spectrum with a maximum corresponding to half the mass of the muon generating this three-body decay, thus $E_{\mathrm{end}} = m_\mu/2 = 52.8$ MeV. The

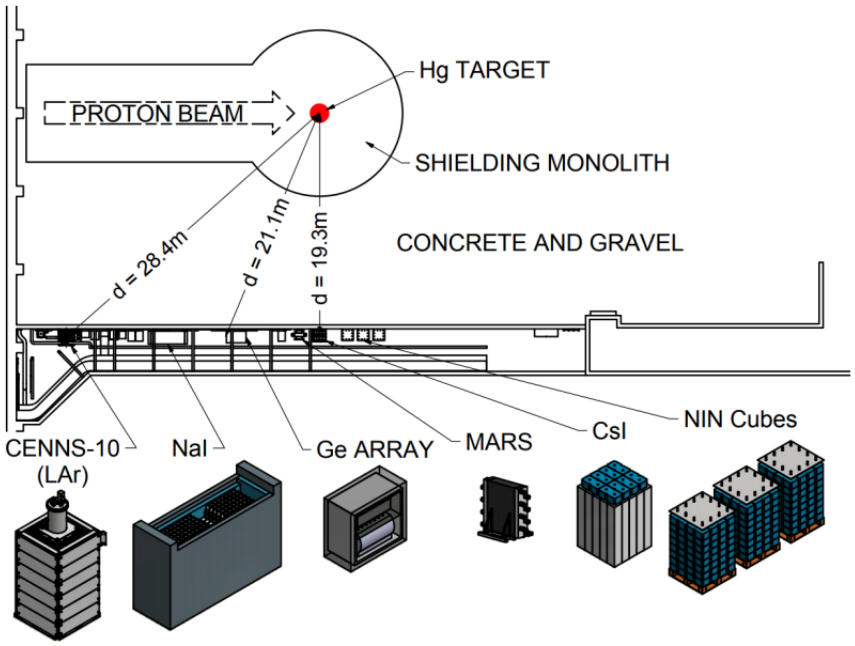

Figure 3.3: Detectors of Neutrino Alley [174] and their location for the COHERENT experiment, updated to 2020. The CsI[Na] detector and CENNS-10, sensitive to CEνNS, stopped taking data in 2019 and 2021, respectively. The 185 kg $\mathrm{NaI[Tl]}$ detector is not sensitive to CEνNS but to charge current interaction on ^{127}I. MARS [175] is a plastic scintillator measuring neutron background. Note that the actual distance of the LAr detector is 27.5 m.

distributions just described can be formally written as[2]

$$\frac{d\phi_{\nu_\mu}}{dE_\nu} = \frac{rN_{\mathrm{POT}}}{4\pi L^2}\delta\left(E_\nu - \frac{m_\pi^2 - m_\mu^2}{2m_\pi}\right), \tag{3.5a}$$

$$\frac{d\phi_{\bar{\nu}_\mu}}{dE_\nu} = \frac{rN_{\mathrm{POT}}}{4\pi L^2}\frac{64E_\nu^2}{m_\mu^3}\left(\frac{3}{4} - \frac{E_\nu}{m_\mu}\right), \qquad (E_\nu \leq m_\mu/2) \tag{3.5b}$$

$$\frac{d\phi_{\nu_e}}{dE_\nu} = \frac{rN_{\mathrm{POT}}}{4\pi L^2}\frac{192E_\nu^2}{m_\mu^3}\left(\frac{1}{2} - \frac{E_\nu}{m_\mu}\right), \qquad (E_\nu \leq m_\mu/2) \tag{3.5c}$$

where δ represents is the Dirac delta function, $m_\pi = 139.57039(18)$ MeV and $m_\mu = 105.6583755(23)$ MeV [19] are the masses of the pion and muon respectively, N_{POT} is the number of protons striking the target, r is the number of π^+ created per proton in the target and depends on the proton beam energy, while L is the distance between the target and the detector. Figure 3.2 displays the neutrino flux for the CsI detector, divided into the different neutrino flavors component. Finally, the detectors are located in a corridor near the mercury target (between 19 m and 28 m away), the so-called "Neutrino Alley", shown in Figure 3.3. In the following

[2]The ν_μ component can also be parameterized as a narrow Gaussian with mean E_{ν_μ}.

sections, we will have a closer look at the main detectors developed by COHERENT, describing the experimental data of interest for this thesis work as well as the main backgrounds involved.

3.1.1 Backgrounds for the CEνNS Search at COHERENT

Several backgrounds must be considered for the CEνNS experiments being conducted at the SNS facility. The backgrounds for COHERENT at SNS are divided into two categories: beam-unrelated backgrounds and beam-related backgrounds. The first category, also known as "steady state background" (SSB), includes all the events observed by the detector even when the beam is off. This background, being the most important and largest, primarily accounts for radioactivity from the detector itself, the walls of the facility, and cosmic rays and affects each detector differently. Impurities or unstable isotopes inside the detector contribute to the SSB. Specifically, regarding the argon detector, the unstable $^{39}\mathrm{Ar}$ isotope represents a significant background which limits the sensitivity to rare-events search, as discussed in Chap. 2 in the context of the DarkSide-20k program. However, a precise characterization of the SSB is possible during the period of beam off and is very beneficial for background rejection.
On the other hand, beam-related backgrounds are more difficult to characterize because they must be studied during the period of beam on. Thus, measurements are made with dedicated detectors designed solely to study background events. In this case, we can identify three categories of backgrounds

- beam-related prompt neutron background (PBRN),
- beam-related delayed neutron background (DBRN),
- neutrino-induced neutrons (NIN),

where the first two are usually referred to as beam-related neutrons (BRNs) and are produced during the neutron spallation.
The BRN is hence originated by the SNS target and reaches the detector simultaneously with the prompt neutrinos in the case of PBRN and the delayed neutrinos in the case of DBRN. The DBRN background is often neglected because it is quite small, but it will still be considered in the analyses conducted in this thesis. The NIN background, on the other hand, is produced by the interaction of neutrinos with the detector's shielding, particularly with $^{208}\mathrm{Pb}$. These neutrons are produced

through both charged current interactions according to

$$\nu_e + {}^{208}\mathrm{Pb} \rightarrow {}^{208}\mathrm{Bi}^* + e \rightarrow {}^{208-y}\mathrm{Bi} + x \times \gamma + y \times n, \tag{3.6}$$

and neutral current interactions

$$\nu_\ell + {}^{208}\mathrm{Pb} \rightarrow {}^{208}\mathrm{Pb}^* + \nu'_\ell \rightarrow {}^{208-y}\mathrm{Pb} + x \times \gamma + y \times n, \tag{3.7}$$

where ν_ℓ represents a neutrino of any flavor, and x and y represent the multiplicity of photons (γ) and neutrons (n), respectively. The NIN cross-section can be calculated theoretically [176, 177] with good precision using Monte Carlo event generators for neutrino-nucleus interactions at energies of tens of MeV and below, such as MARLEY [178]. However, experimental measurements [162] show significant disagreement with the theory. In particular, the measured NIN cross-section on ^{208}Pb is $0.29^{+0.17}_{-0.16}$ times the value predicted by MARLEY, although this issue is still under investigation.

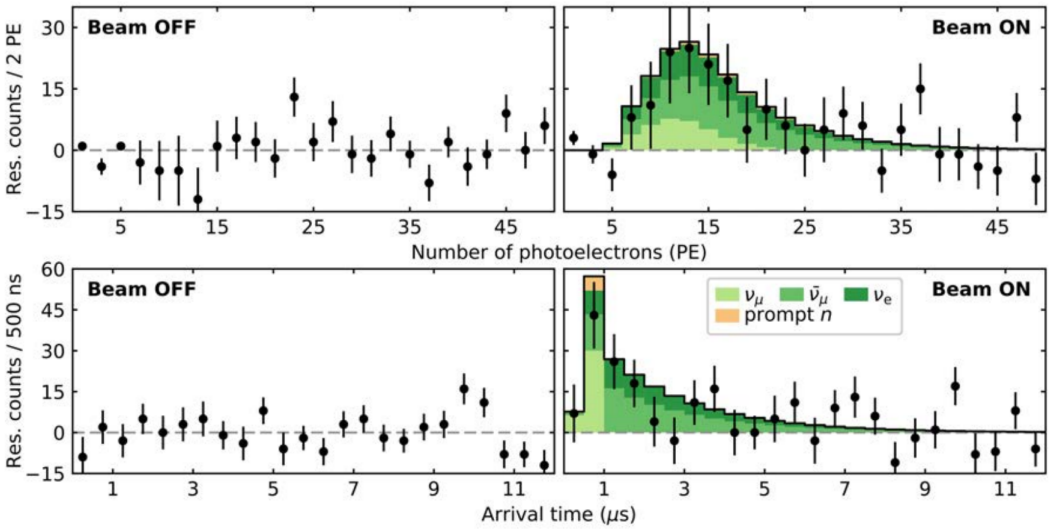

Figure 3.4: Residual counts representing the first observation of CEνNS on the CsI[Na] detector [158]. Upper panel: residual counts as a function of the recoil energy expressed in detected photoelectron. Lower panel: residual counts as a function of the trigger time. Environmental background contributes to both signal groups equally, vanishing upon subtraction. Error bars show statistical uncertainty. The data shown here include 153.5 days of SNS downtime ("BEAM OFF") and 308.1 days of neutrino production ("BEAM ON").

3.2 The COHERENT CsI Detector

The detector that has achieved the highest statistical significance of a CEνNS signal is the CsI[Na] detector, which utilizes a low-background CsI crystal with a mass of 14.6 kg. The addition of the Na dopant is very beneficial to increase the scintillation output after the nuclear recoil [179], and with a fractional mass of just $10^{-4} - 10^{-5}$, playing no significant role as a target. This detector allowed the first observation of CEνNS [158] at a confidence level of 6.7 σ compared to the background-only hypothesis. Intriguingly, a good agreement was found with the Standard Model expectations, observing 134 ± 22 events compared to the predicted 173 ± 48 events. Figure 3.4 shows their result derived from fifteen months of data collection, manifesting the power of performing a timing analysis comparing "BEAM ON" data, where the signal is present with "BEAM OFF" data, used to characterize the background. To mitigate the backgrounds, the detector is sur-

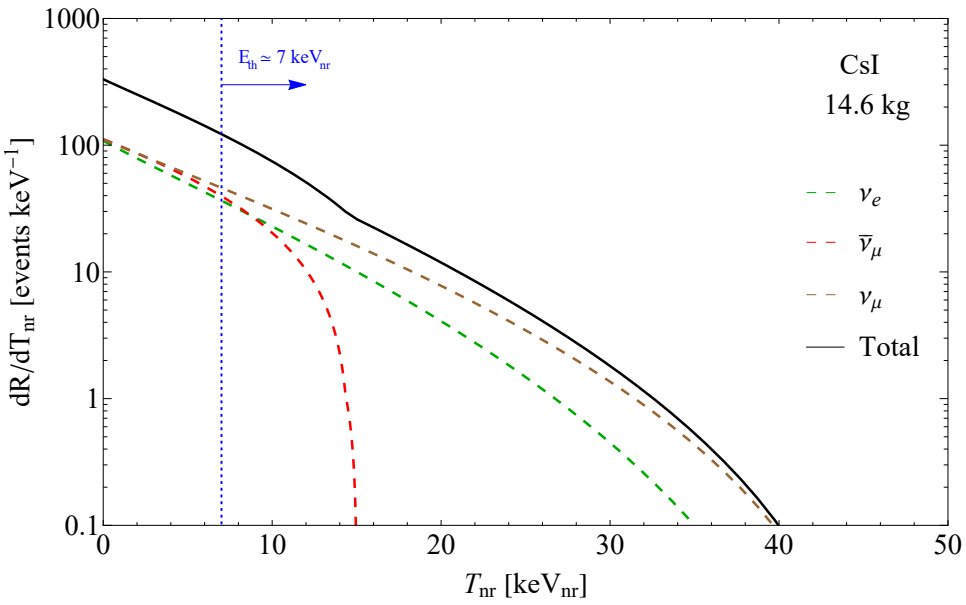

Figure 3.5: Theoretical CEνNS rates at the COHERENT CsI detector for different neutrino flavors as a function of the recoil energy. It represents the rate integrated over the exposure obtained with $L = 19.3\ m$, $N_{\rm POT} = 3.198 \cdot 10^{23}$, $r = 0.0848$ and a mass of 14.6 kg. The blue line represents the experimental threshold of the CsI detector of $E_{\rm th} \simeq 7\ {\rm keV_{nr}}$.

rounded by multiple layers of materials which shield from gamma and neutron backgrounds. Before ending its activity in 2019, the experiment provided additional data [163] corresponding to a total exposure of 13.99 GWhr of integrated beam power, considered in this thesis. Recalling that the beam power at the time of the CsI experiment was $P_{\rm beam} = 1.4\ {\rm MW}$, it is possible to convert the integrated

beam exposure in time units[3]

$$t_{\rm exp}^{\rm CsI} = \frac{13.99\ {\rm GWhr}}{1.4\ {\rm MW}} \simeq 1.14\ {\rm yr}. \tag{3.8}$$

Due to maintenance, beam stability, and other technical issues, the SNS operates for approximately 5000 hours per year, so the total exposure corresponds to about 2 SNS years. This dataset allowed to find $\sim 11.6\ \sigma$ evidence of the CEνNS signal, determining the flux-averaged cross section to be $165^{+30}_{-25} \times 10^{-40}\ {\rm cm}^2$ [163], consistent with the Standard Model, giving the most precise measurement of CEνNS yet. The theoretical CEνNS rate in the detector is obtained by convolving the cross section with the neutrino flux, and integrating over all possible neutrino energies. Specifically, the theoretical event rate for a neutrino with flavor ℓ is

$$\frac{dR_{\nu_\ell}}{dT_{\rm nr}} = N(\mathcal{N}) \int_{E_\nu^{min}}^{E_\nu^{max}} \frac{d\phi_{\nu_\alpha}}{dE_\nu} \frac{d\sigma_{\nu_\ell}^{\rm CsI}}{dT_{\rm nr}}(E_\nu, T_{\rm nr}) dE_\nu, \tag{3.9}$$

where the CsI cross section is defined as

$$\frac{d\sigma_{\nu_\ell}^{\rm CsI}}{dT_{\rm nr}} = \frac{d\sigma_{\nu_\ell}^{\rm Cs}}{dT_{\rm nr}} + \frac{d\sigma_{\nu_\ell}^{\rm I}}{dT_{\rm nr}}. \tag{3.10}$$

In Eq. 3.9 $N(\mathcal{N})$ is the number of $\mathcal{N}$ atoms in the detector, which is given by $N(\mathcal{N}) = N_{\rm A} M_{\rm det}/M_{\mathcal{N}}$, where $N_{\rm A}$ is the Avogadro number. $M_{\rm det}$ is the detector active mass, which correspond to $M_{\rm det} = 14.6$ kg for CsI, while $M_{\mathcal{N}}$ is the molar mass $M_{\rm CsI} = 259.8$ g/mol. $E_\nu^{\rm min} \simeq 1/2\left(T_{\rm nr} + \sqrt{T_{\rm nr}^2 + 2 m_{\mathcal{N}} T_{\rm nr}}\right)$ is the minimum neutrino energy allowed from the kinematics. Using the values in Tab. 1.1 and the SM value of the Weinberg angle, the rates obtained for the CsI detector are shown in Fig. 3.5. Those rates are not yet able to match the outcome of the detector, as experimental effects will play a crucial role and need to be taken into account. Specifically, what is actually measured is the scintillation light produced due to the nuclear recoils, which are known to generate just a fraction of that produced by an electron recoil of the same energy. When a particle interacts with the target nuclei, the energy can be deposited through excitation, ionization, and non-radiative transition (e.g. heat). The *quenching factor* (QF), $f_Q(T_{\rm nr})$, accounts for this effect and it is defined as the reduction of the ionization yield produced by

[3]Note that the same result can be obtained through the following relation $t_{\rm exp} = E_p N_{\rm POT}/P_{\rm beam}$, where E_p is the energy of the proton beam.

a nuclear recoil, with respect to an electron recoil T_e of the same energy

$$T_e = f_Q(T_{\rm nr})T_{\rm nr}. \tag{3.11}$$

The COHERENT collaboration measured the QF of the CsI crystal in the energy regime of interest [180], which is a function of the nuclear recoil energy and can be parameterized with a polynomial of the form

$$f_Q^{\rm CsI}(T_{\rm nr}) = 0.0554628 + 4.30681\left(\frac{T_{\rm nr}}{\rm MeV}\right) - 111.707\left(\frac{T_{\rm nr}}{\rm MeV}\right)^2 + 840.384\left(\frac{T_{\rm nr}}{\rm MeV}\right)^3, \tag{3.12}$$

with the values from the nominal scintillation model [163, 180]. The QF for the CsI detector (COH-CsI) is reported in Fig. 3.6 together with the $\pm 1\ \sigma$ uncertainty. The impact of the QF uncertainty on the CEνNS rate is of the order of 3% on the total number of events. The photomultiplier tubes (PMT) are able to detect

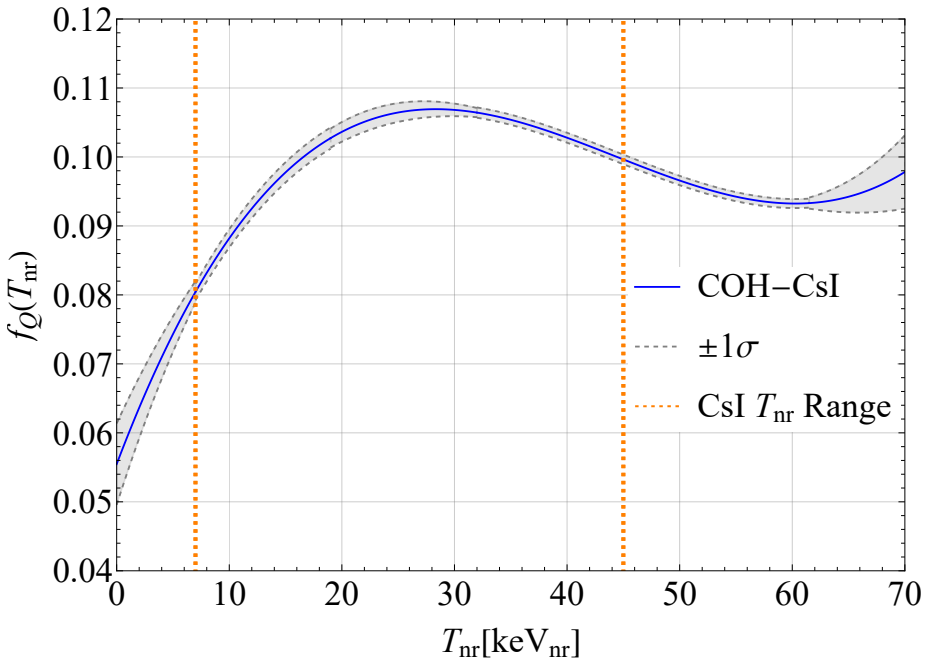

Figure 3.6: Nominal QF as reported by COHERENT [163] for the CsI detector (blue curve) together with the $\pm 1\ \sigma$ uncertainty. The vertical orange lines represent the experimental nuclear recoil range where the CEνNS signal is present.

the scintillation light produced inside the CsI detector, and the *light yield* (LY) defines the amount of photoelectron (PE) emitted for a given nuclear recoil. In the CsI analysis, it is equal to LY $= 13.35$ PE/keV$_{\rm ee}$, such that the number of

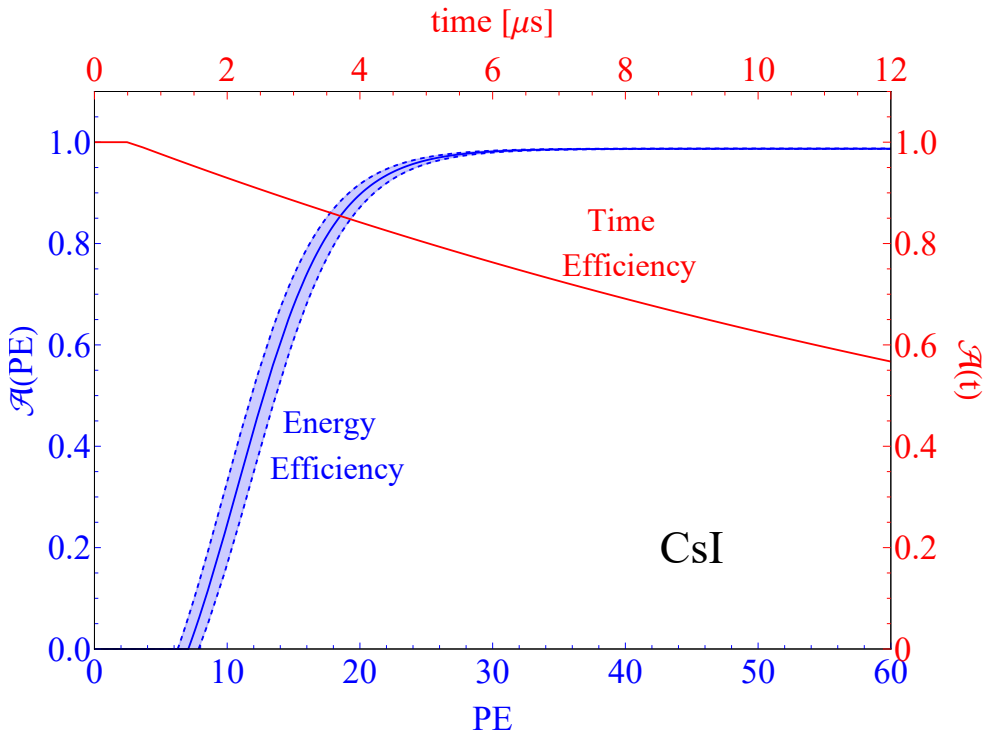

Figure 3.7: Energy dependent efficiency curve as a function of PE with the corresponding $\pm 1\ \sigma$ uncertainty (blue line), and the time efficiency curve as a function of the trigger time (red line). The $\pm 1\ \sigma$ uncertainty for the time efficiency is not present in the data release.

photoelectrons, $N_{\rm PE}$, emitted due to the nuclear recoil is

$$N_{\rm PE} = \text{LY}\ f_Q(T_{\rm nr})T_{\rm nr}. \tag{3.13}$$

Another ingredient that is needed to match the outcome of the experiment is the energy resolution function, also known as energy smearing. It describes how the true energy deposit PE' is reconstructed in terms of the observed recoil energy PE. The smearing was modelled with a gamma function

$$R(x) = \frac{(a(1+b))^{1+b}}{\Gamma(1+b)} x^b e^{-a(1+b)x} \tag{3.14}$$

which, empirically, fit well to simulated recoil distributions using $a = 1/\text{PE}$ and $b = 0.716 \times \text{PE}$ [163]. Another element relevant for a CEνNS detector is the energy acceptance, which determines also the experimental threshold. It is worth remarking that the experimental threshold should be, in principle, as small as possible to observe the lowest part of the CEνNS spectra, where more events are

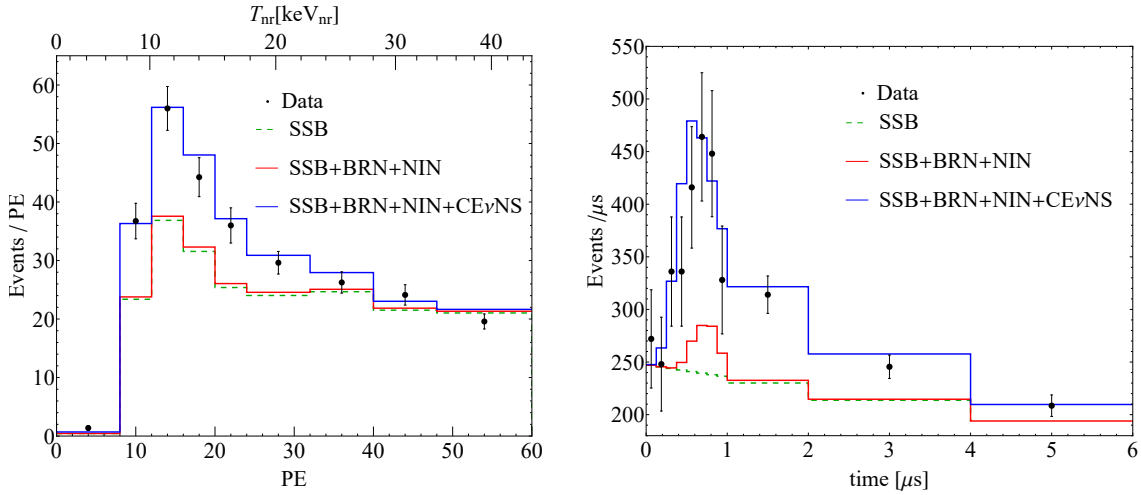

Figure 3.8: Pre-fit experimental data compared to the SSB, BRN, NIN backgrounds and the CEνNS prediction as a function of energy (left) and recording time (right) for the CsI data release. The rates have been obtained by integrating the predictions over time and energy, respectively.

expected and in the case of the CsI detector is $\sim 7\ \mathrm{keV_{nr}}$.

The energy-dependent $\mathcal{A}(\mathrm{PE})$ and the time-dependent $\mathcal{A}(t)$ efficiency curves are reported in Fig. 3.7 for the CsI detector. We are now able to write the expected CEνNS event number $N_i^{\mathrm{CE}\nu\mathrm{NS}}$ in each nuclear-recoil energy-bin i, which is given by

$$N_i^{\mathrm{CE}\nu\mathrm{NS}} = N(\mathcal{N}) \int_{T_{\mathrm{nr}}^i}^{T_{\mathrm{nr}}^{i+1}} dT_{\mathrm{nr}} \mathcal{A}(T_{\mathrm{nr}}) \int_0^{T'^{\mathrm{max}}_{\mathrm{nr}}} dT'_{\mathrm{nr}}\ R(T_{\mathrm{nr}}, T'_{\mathrm{nr}}) \int_{E_{\mathrm{min}}(T'_{\mathrm{nr}})}^{E_{\mathrm{max}}} dE_\nu \times \sum_{\nu=\nu_e,\nu_\mu,\bar{\nu}_\mu} \frac{d\phi_\nu}{dE_\nu}(E_\nu) \frac{d\sigma_{\nu-\mathcal{N}}}{dT_{\mathrm{nr}}}(E_\nu, T'_{\mathrm{nr}}). \tag{3.15}$$

Here T_{nr} is the reconstructed nuclear recoil kinetic energy while T'_{nr} is the true nuclear recoil kinetic energy. In order to exploit also the arrival time information, we calculated the CEνNS event number, $N_{ij}^{\mathrm{CE}\nu\mathrm{NS}}$, in each nuclear recoil energy bin i and time interval j with

$$N_{ij}^{\mathrm{CE}\nu\mathrm{NS}} = (N_i^{\mathrm{CE}\nu\mathrm{NS}})_{\nu_\mu} P_j^{(\nu_\mu)} + (N_i^{\mathrm{CE}\nu\mathrm{NS}})_{\nu_e,\bar{\nu}_\mu} P_j^{(\nu_e,\bar{\nu}_\mu)}, \tag{3.16}$$

where $P_j^{(\nu_\mu)}$ and $P_j^{(\nu_e,\bar{\nu}_\mu)}$ are obtained by integrating the arrival time distributions in Fig. 3.1 in the corresponding time intervals with the time-dependent efficiency function of Fig. 3.7. We are now able to compute the expected event rate in the CsI as a function of energy and time to compare with the experimental number

of events obtained from coincidence (C) data. Fig. 3.8 compares the SSB[4], BRN and NIN backgrounds and the CEνNS expected rate with the experimental data as a function of recorded energy and trigger time. The data clearly shows an excess of events which is well fitted "by eye" by the CEνNS prediction. It should be noticed that the data distribution is inherently two-dimensional, with each time bin containing an energy distribution of events. The data presented here have been obtained by integrating over time and energy respectively. The two-dimensional data utilized for the analysis can be found in App. B. Moreover, our calculation predicts $320 \pm 42(\text{sys.})$ events, compared to the 341 ± 42 of the collaboration, where the small difference might be explained by a different theoretical approach for radiative corrections and parameterization of the nuclear structure. Throughout the thesis, for certain new physics scenarios, we will also include the νES prediction. In this case, we evaluate the ES event number $N_i^{\rm ES}$ in the i-th bin as

$$N_i^{\rm ES}(\text{CsI}) = N(\mathcal{N}) \int_{T_{\rm e}^i}^{T_{\rm e}^{i+1}} dT_{\rm e}\, A(T_{\rm e}) \int_0^{T_{\rm e}'^{\rm max}} dT'_{\rm e}\, R(T_{\rm e}, T'_{\rm e}) \int_{E_{\rm min}(T'_{\rm e})}^{E_{\rm max}} dE_\nu \tag{3.17}$$

$$\sum_{\nu=\nu_e,\nu_\mu,\bar{\nu}_\mu} \frac{d\phi_\nu}{dE_\nu}(E_\nu) \frac{d\sigma^{\rm ES}_{\nu-\mathcal{A}}}{dT'_{\rm e}}(E_\nu, T'_{\rm e}), \tag{3.18}$$

where $N_i^{\rm ES}(\text{CsI}) = N_i^{\rm ES}(\text{Cs}) + N_i^{\rm ES}(\text{I})$, $E_{\rm min}(T'_{\rm e}) = (T'_{\rm e} + \sqrt{T'^2_{\rm e} + 2m_e T'_{\rm e}})/2$, and $T_{\rm e}'^{\rm max} = 2E_{\rm max}^2/(2E_{\rm max} + m_e)$. We performed the analysis of the COHERENT CsI data in the energy and time bins using the Poissonian least-squares function [19, 181]

$$\chi^2_{\rm CsI} = 2\sum_{i=1}^{9}\sum_{j=1}^{11}\left[\sum_{z=1}^{4}(1+\eta_z)N_{ij}^z - N_{ij}^{\rm exp} + N_{ij}^{\rm exp}\ln\left(\frac{N_{ij}^{\rm exp}}{\sum_{z=1}^4(1+\eta_z)N_{ij}^z}\right)\right] + \sum_{z=1}^{4}\left(\frac{\eta_z}{\sigma_z}\right)^2, \tag{3.19}$$

where the indices i and j denote the energy and time bins respectively, and the indices $z = 1, 2, 3, 4$ stand for CEνNS, BRN, NIN, and SSB respectively. In our notation, $N_{ij}^{\rm exp}$ is the experimental number of events from coincidence data, $N_{ij}^{\rm CE\nu NS}$ is the predicted number of CEνNS events from Eq. 3.16, that depends on the physics model under consideration, $N_{ij}^{\rm BRN}$ is the estimated BRN background, $N_{ij}^{\rm NIN}$ is the estimated NIN background, and $N_{ij}^{\rm SSB}$ is the SSB background obtained from AC data. We took into account the systematic uncertainties described in Ref. [163] with the nuisance parameters η_z and the corresponding uncertainties $\sigma_{\rm CE\nu NS} = 0.12$ which

[4]The SSB is derived from the anti-coincidence (AC) data and is included in the data release.

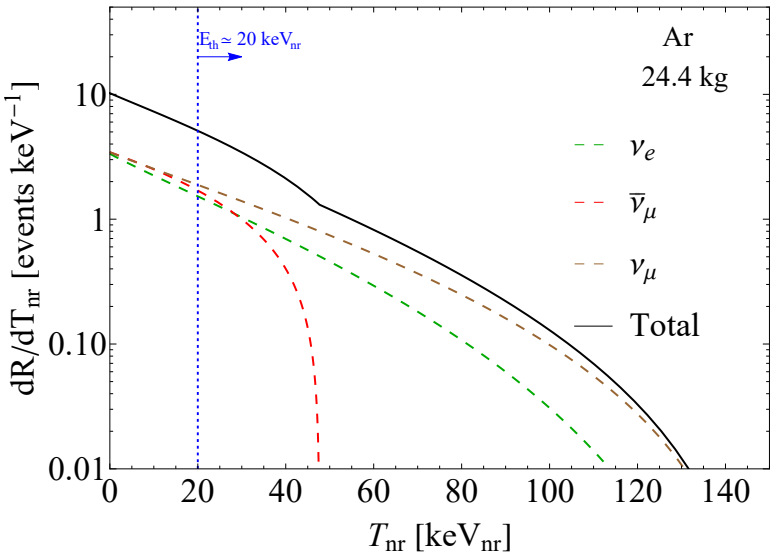

Figure 3.9: Theoretical CEνNS rates at the COHERENT Ar detector for different neutrino flavors as a function of the recoil energy. It represents the rate integrated over the exposure obtained with $L = 27.5\ m$, $N_{\rm POT} = 1.37 \cdot 10^{23}$, $r = 0.09$ and a mass of 24.4 kg. The threshold of the Ar detector is set approximately to $20\ \mathrm{keV_{nr}}$.

encompasses the systematic uncertainty of the signal rate considering the effects of the 10%, 3.8%, 4.1%, and 3.4% uncertainties of the neutrino flux, quenching factor, CEνNS efficiency, and neutron form factors, respectively. Moreover, the uncertainties associated to the backgrounds are $\sigma_{\rm BRN} = 0.25$, $\sigma_{\rm NIN} = 0.35$, and $\sigma_{\rm SSB} = 0.021$. When we include the νES channel, it is necessary to perform the substitution $N_{ij}^{\rm CE\nu NS} \to N_{ij}^{\rm CE\nu NS} + N_{ij}^{\nu \rm ES}$ removing the systematic uncertainty associated to the quenching factor and the nuclear structure.

3.3 The COHERENT CENNS-10 Detector

After the first measurement of CEνNS in 2017 with the CsI detector, CEνNS was observed for the first time in a single-phase liquid argon detector (LAr) in 2020 [159] filled with AAr. The CENNS-10 detector, containing 24.4 kg of argon, is located 27.5 meters from the SNS mercury target. The CENNS-10 experiment exploits PMTs and is sensitive only to the S1 signal produced in argon, and uses the f_{90} parameter to distinguish between NRs and ERs, as discussed in Chap. 2, which sets the threshold at about $20\ \mathrm{keV_{nr}}$. The data [159] analysed in this thesis correspond to $N_{\rm POT} = 1.37 \cdot 10^{23}$ and $r = 0.09$, i.e. a total exposure of $\simeq 0.49$ years corresponding to approximately 0.86 SNS years. The corresponding theoretical event rate is reported in Fig. 3.9 for the Ar detector for each neutrino flavor. As for

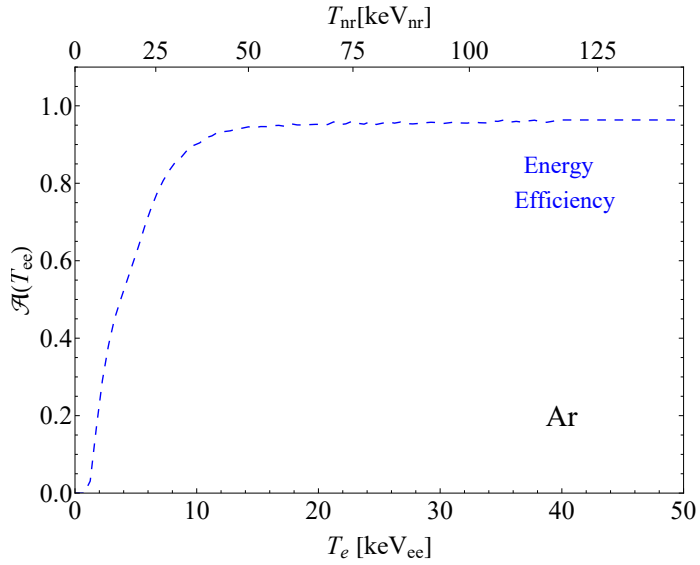

Figure 3.10: Energy acceptance for the Ar analysis as a function of the electron recoil energy (lower axis) and nuclear recoil energy (upper axis).

the CsI analysis, we need to account for various experimental features which are needed to describe the experimental data. The quenching factor is parameterized by a simple linear relation

$$f_Q^{\rm Ar}(T_{\rm nr}) = 0.00078\ T_{\rm nr} + 0.246 \quad \text{for} \quad {\rm T_{nr}} < 0.125\ {\rm keV_{nr}} \tag{3.20}$$

and it remains constant and equal to 0.3435 for $T_{\rm nr} > 0.125\ {\rm keV_{nr}}$, which provides a good fit to the available measurements on argon [182–185]. The time acceptance is set to 1 for the LAr analysis, while the time arrival time distribution is obtained with Eqs. 3.3 and 3.4 with $a = 0.44\ \mu s$, $b = 0.15\ \mu s$, $t_0 = 85\ ns$, $t_0' = 0$. The energy acceptance is reported in Fig. 3.10, while the energy resolution can be parameterized by a Gaussian with standard deviation σ_E

$$\frac{\sigma_E}{T_e} = \frac{a}{\sqrt{T_e({\rm keV_{ee}})}}, \tag{3.21}$$

with $a = 0.58$ as reported in [159]. We are now able to evaluate the two-dimensional distributions of CEνNS events and to compare them with the experimental backgrounds. Adopting our formalism, we predict $\sim 120 \pm 16$ CEνNS events. The one-dimensional distribution of the events integrated over energy and time is reported in Fig. 3.11. Since the SSB is the most significant background, the data shown here do not include SSB which has already been subtracted for visual purposes. We perform the Ar analysis by a least square function of the form

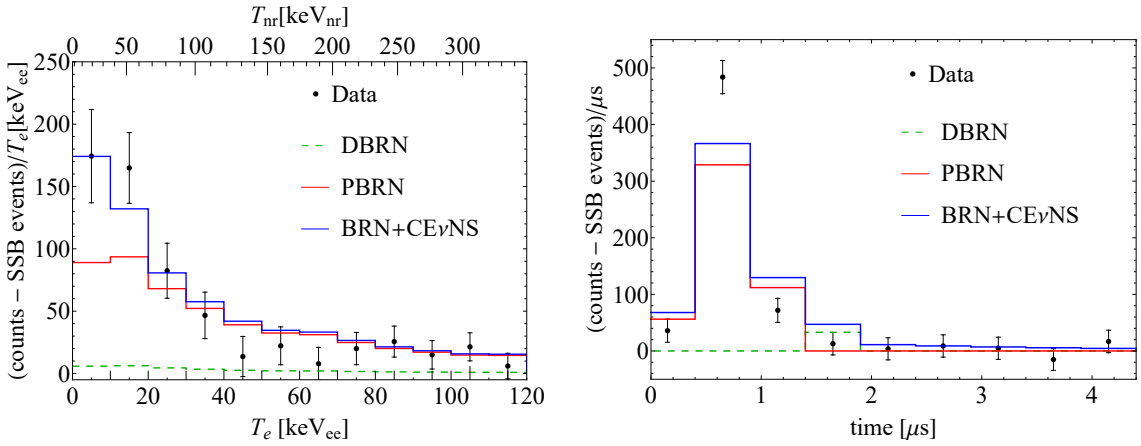

Figure 3.11: Pre-fit SSB subtracted events compared to the DBRN, PBRN backgrounds and the CEνNS prediction as a function of energy (left) and recording time (right) for the Ar data release. The rates have been obtained by integrating the predictions over time and energy respectively.

$$\chi^2_{\rm LAr} = \sum_{i=1}^{12}\sum_{j=1}^{10}\frac{1}{\sigma_{ij}^2}\Big[(1+\beta_0+\beta_1\Delta^{F_{90+}}_{\rm CE\nu NS}+\beta_2\Delta^{F_{90-}}_{\rm CE\nu NS}+\beta_3\Delta^{t_{trig}}_{\rm CE\nu NS})N^{\rm CE\nu NS}_{ij}+$$
$$(1+\beta_4)N^{\rm SSB}_{ij}+$$
$$(1+\beta_5+\beta_6\Delta^{E_+}_{\rm PBRN}+\beta_7\Delta^{E_-}_{\rm PBRN}+\beta_8\Delta^{t^+_{trig}}_{\rm PBRN}+\beta_9\Delta^{t^-_{trig}}_{\rm PBRN}+\beta_{10}\Delta^{t^W_{trig}}_{\rm PBRN})N^{\rm PBRN}_{ij}+$$
$$(1+\beta_{11})N^{\rm DBRN}_{ij}-N^{\rm exp}_{ij}\Big]^2+\sum_{k=0,4,5,11}\left(\frac{\beta_k}{\sigma_k}\right)^2+\sum_{k=1,2,3,6,7,8,9,10}(\beta_k)^2. \tag{3.22}$$

Here the indices i and j refer to the energy and time bins, respectively, while $N^{\rm exp}_{ij}$ is the number of events observed for each energy and time bin obtained from coincidence data. The parameters β_0, β_4, β_5, β_{11} are the nuisance parameters introduced to account for the normalization of CEνNS, SSB, PBRN, and DBRN with their respective uncertainties. Instead, the nuisance parameters β_1, β_2, β_3, β_6, β_7, β_8, β_9, β_{10} quantify the systematic uncertainty of the event rate for the theoretical predictions of CEνNS, SSB, PBRN, and DBRN, varying them within the corresponding uncertainty σ_k. The uncertainties σ_k are $\sigma_{\rm CE\nu NS} = 0.12$ that encompass the neutrino flux (10%), energy efficiency (3.6%), energy calibration (0.8%), the calibration of the pulse-shape discrimination parameter F90 (7.8%), QF (1%), and nuclear form factor (2%), $\sigma_{\rm PBRN} = 0.32$, $\sigma_{\rm DBRN} = 1$, and $\sigma_{\rm SSB} = 0.0079$.
Each systematic uncertainty comes from different sources: the distortion introduced by the f_{90} parameters, $t_{\rm trig}$ which defines the temporal distribution of events, and the parameter E, which defines the energy distribution of events. The distri-

butions introduced in Eq. 3.22 are defined as

$$\Delta_{\lambda}^{\xi_{\lambda}} = \frac{N_{ij}^{\lambda,\xi_{\lambda}} - N_{ij}^{\lambda,\mathrm{CV}}}{N_{ij}^{\lambda,\mathrm{CV}}}, \tag{3.23}$$

where $\lambda = \{\mathrm{CE}\nu\mathrm{NS}, \mathrm{PBRN}\}$ and ξ_{λ} represents each source of uncertainty ($F_{90}^{\pm}$, $t_{\mathrm{trig}}^{\pm}$, $E_{\pm}$) related to λ, and CV indicates the central value of the predicted $\mathrm{CE}\nu\mathrm{NS}$ and PBRN distributions. All this information is taken from Tables 2 and 3 of the data release [186]. The statistical uncertainty for each bin is given by

$$(\sigma_{ij})^2 = (\sigma_{ij}^{\mathrm{exp}})^2 + (\sigma_{ij}^{\mathrm{SSB}})^2, \tag{3.24}$$

where $\sigma_{ij}^{\mathrm{exp}} = \sqrt{N_{ij}^{\mathrm{exp}}}$ and $\sigma_{ij}^{\mathrm{SSB}} = \sqrt{N_{ij}^{\mathrm{SSB}}/5}$. The factor of 1/5 is due to the sampling time being 5 times longer for the SSB background compared to the signal time window as described in the data release [186]. In the COHERENT LAr analysis, we do not include νES events since the f_{90} data already ensure a successful discrimination of CEνNS- versus νES-induced signals in the detector.

3.4 COHERENT Experimental Program: Future Planning

The COHERENT collaboration is developing a comprehensive experimental program aimed at achieving precision tests of the SM with CEνNS [172, 187]. In this section, we will outline the key features of the upcoming COHERENT upgrades and experiments, providing relevant details. In the next chapters, we will present sensitivity studies to assess to which extent such experiments will be competitive in the future to various physics scenarios. The experimental program is highly related to the SNS improvements, which are already underway. At the moment, the protons are accelerated to a kinetic energy of $E_p = 1.01$ GeV [187] and a major upgrade of the SNS is planned for 2025 [188], when the proton beam energy will increase to 1.3 GeV. Moreover, the beam power P_{beam} will increase to 2 MW, compared to the current 1.4 MW. Recently, steady operations were achieved with a record 1.7 MW power [187].

The number of neutrinos per flavor produced for each proton-on-target will increase to a value of 0.123 [189], which is the value that will be used for our sensitivity studies. A second target station is planned for the 2030s, with a final

power of 2.8 MW, meaning that the future SNS upgrade will be able to get a much higher neutrino flux for each neutrino flavor with respect to the current configuration, providing substantial benefits for future CEνNS detectors. In addition, the systematic uncertainty on the neutrino flux will be strongly reduced thanks to a dedicated D_2O detector [173] and will approach 4.7(2)% statistical uncertainty after 2(5) SNS-years of operation. For a complete overview of the COHERENT planning, refer to Ref. [172].

3.4.1 The COH-Cryo-CsI Detectors

The so-called COH-Cryo-CsI I detector, scheduled for 2025 [172], will have a mass of about 10 kg and will exploit an undoped CsI crystal at cryogenic temperature (~ 40 K), which would permit to use SiPM arrays instead of PMTs in order to remove the Cherenkov radiation background emitted by the latter. Moreover, the undoped CsI crystals at cryogenic temperature have an increased light yield compared to CsI[Na] crystal at 300 K, namely about $\mathrm{LY} = 50$ PE/keV$_{\mathrm{ee}}$. The following upgrade will be the COH-Cryo-CsI II detector, planned in the 2030s, which will operate in similar conditions with a 700 kg undoped CsI detector. Both the COH-Cryo-CsI I and COH-Cryo-CsI II detectors will be able to lower the energy threshold to about ~ 0.5 keV$_{\mathrm{nr}}$, which is a fundamental requirement for CEνNS precision physics. In our analyses, we will consider a threshold of 6 PE, corresponding to about 0.8 keV$_{\mathrm{nr}}$, described by a stepping function. These conservative assumptions mitigate potential uncertainties in the knowledge of the acceptance shape near the threshold.

It is also worth noting that increased light yield, beyond lowering the threshold, will also improve both detector timing and energy resolution [187], which will be considered equal to unity in this study. For the sensitivity study, we will consider a quenching factor of $15 \pm 1.5\%$ as reported in Ref. [187] and as demonstrated in previous works [190]. We considered the same time timing distribution as in the current CsI analysis. We obtained about ~ 1005 CEνNS events for a 10 kg CsI crystal located 19 m from the SNS source in one SNS year, which is in good agreement with that reported by the collaboration [187], even though small differences might arise from a different approach in the evaluation of the CEνNS cross section, and a different treatment of experimental details, as threshold effects.

A thorough investigation to estimate the experimental backgrounds for this detector is not a simple task. The COHERENT collaboration is currently devel-

oping a detailed background model which includes events from intrinsic rates, afterglow effects in the detector, and external sources, by means of extensive simulations [187]. Luckily, the new detector at cryogenic temperatures is expected to achieve a lower background level compared to the CsI[Na] detector and thanks to the low-threshold, increased light yield and quenching factor, a signal-to-background ratio > 1 is expected such that the sensitivities are not strongly dependent on the actual background rate. For simplicity, we will consider an optimistic background-free experiment as we verified that we are able to reproduce the results reported in Ref. [187] for some benchmark models. For our sensitivity studies, we will adopt the Asimov dataset [191] to evaluate the test statistic with the most-likely dataset (i.e. setting all bin contents to their non-integer expectation values), which gives the median of the test statistic. For evaluating the statistical constraints on the parameters, we, therefore, perform a χ^2 analysis in the same form of Eq. 3.19, considering both energy and time distribution, setting to zero the backgrounds. The systematic uncertainty on the CEνNS signal is set to 6(3)% for COH-Cryo-CsI I(II).

3.4.2 The COH-LAr 750 Detector

The COH-Ar-750 detector represents the next phase of the COHERENT experiment for studying CEνNS in LAr. It will utilize a large cryostat filled with liquid argon (750 kg), surrounded by a 15 cm water shield that reduces events due to ambient gamma rays and a 10 cm lead shield that suppresses most of the beam-related neutrons [172]. The technology will remain basically the same as that of the CENNS-10 detector, hence we will use the same energy acceptance, QF, and energy resolution in the sensitivity studies. For this reason, the SSB is scaled with the mass of the detector, as well as the BRN backgrounds considering the same time and energy bins. A fiducialization could be in principle performed, to remove the backgrounds from the detector walls, but it is beyond the goal of this thesis. On the other hand, the COHERENT collaboration is considering using UAr, instead of AAr, which has a reduced percentage of ^{39}Ar, resulting in a significant reduction of background events. In this case, the impact of using the UAr is naively considered with a reduction of a factor 1400 [108] in the SSB. This simplified scenario assumes that the SSB is composed exclusively of ^{39}Ar, which is in any case a reasonable assumption as discussed in Ref. [159]. In this case, about 6498 CEνNS events are foreseen in one SNS year, thanks to the increased neutrino flux resulting

from the SNS upgrade. Hence, the sensitivity study on the physical parameter of interest is performed using the χ^2 distribution in Eq. 3.22, neglecting the spectral distortion parameters and setting the systematic uncertainty on the CEνNS signal to 6%. The systematic uncertainty on the SSB, PBRN and DBRN are the same as used in the CENNS-10 analysis.

4 The Hunt For CEνNS From Reactor Antineutrinos

Opening

Measuring the CEνNS process using $\bar{\nu}_e$ emitted from nuclear reactor power plants is one of the major challenges for the CEνNS community. As continuous and well-localized sources, they offer the advantage of providing high fluxes of low-energy antineutrinos, which allow for the study of the full coherency regime of the CEνNS interaction. However, this search is highly challenging due to the tiny recoil produced and the significant background that must be precisely characterized. Moreover, the need to lower the experimental threshold pioneers a new frontier in the study of low-energy physics and detector response. The goal of this chapter is to provide a detailed description of the elements needed to characterize the CEνNS signal produced at reactors, together with a complete overview of the world-wide searches. The focus will then be on the widely discussed observation of CEνNS at the Dresden-II reactor power plant, which relies on an unpredicted enhancement of the quenching factor at low energies. In this framework, based on our work [6], the Migdal effect will be investigated. This yet-to-be-observed quantum mechanical effect gained significant attention in this framework, as it was suggested as a potential explanation of the observed enhancement.

4.1 Reactor Antineutrino Spectra

The search for CEνNS from reactor $\bar{\nu}_e$ relies on a deep understanding of the reactor neutrino fluxes produced at nuclear power plants. The measurement of the $\bar{\nu}_e$ flux and the spectrum produced by a nuclear reactor has been a persistent challenge since the initial observation of the neutrino in 1956 by Reines and Cowan [18].

This section will refer to the recent results in Ref. [192] which provided an updated method to obtain the $\bar{\nu}_e$ neutrino flux in the energy range 0-12 MeVs, improving and methodically revising the so-called summation method often employed to obtain the neutrino spectrum. Reactor antineutrinos primarily arise from the β decay of neutron-rich by-products following the fission of uranium and plutonium in nuclear fuel. Commercial pressurized water reactors (PWR), which are of interest for this thesis work, are designed for large-scale electricity and release around 5% of the energy in the form of electron antineutrinos generated mainly through the fission of $^{235}\mathrm{U}$, $^{239}\mathrm{Pu}$, $^{241}\mathrm{Pu}$, and $^{238}\mathrm{U}$. The different fission fractions typically evolve with time (see Ref. [193] for a detailed discussion), but for our analysis, we will consider only average fission fractions equal to 0.559, 0.088, 0.291 and 0.062 for $^{235}\mathrm{U}$, $^{238}\mathrm{U}$, $^{239}\mathrm{Pu}$, and $^{241}\mathrm{Pu}$ respectively. On top of the neutrino flux produced by fission, an additional $\bar{\nu}_e$ contribution comes from the β decay of activation products of fuel and/or structural material. This contribution starts to play a role when the activated element has a significant capture cross-section and is present in a significant abundance. The activation element present in the fuel, of interest for PWR, is $^{238}\mathrm{U}$ and the neutron capture reaction is

$$n +^{238}\mathrm{U} \rightarrow^{239}\mathrm{U} + \gamma, \tag{4.1}$$

then the $^{239}\mathrm{U}$ undergo β^- decays with a lifetime $t_{1/2} = 23.45\ \mathrm{min}$ producing the instable $^{239}\mathrm{Np}$ ($t_{1/2} = 2.36\ \mathrm{days}$), which decays into $^{239}\mathrm{Pu}$ through β^- decay. This decay channel for producing neutrinos is usually referred to as $^{238}\mathrm{U}(n,\gamma)^{239}\mathrm{U}$. In Fig. 4.1 the reactor $\bar{\nu}_e$ spectra are reported from the different fission fragments as well as the contribution from the activation fuel (left panel), together with the total spectrum obtained by summing the various components weighting them for the corresponding abundances of a PWR (right panel). This spectrum will be referred to as CEA based on the affiliation of the authors [192]. In order to obtain the neutrino flux, the mean energy released by the fission is needed. We use an average energy of $\langle E\rangle_{\mathrm{fission}} \simeq 205.786\ \mathrm{MeV/fission}$ [194], such that the number of neutrinos emitted will be given by $P_W/\langle E\rangle_{\mathrm{fission}}$, where P_W is the reactor power, usually of the order of a few $\mathrm{GW_{th}}$[1]. The neutrino flux Φ at a distance d is given

[1]The suffix "th" indicates the thermal power produced by the reactor, which is the amount of thermal energy generated by the nuclear fission process within the reactor.

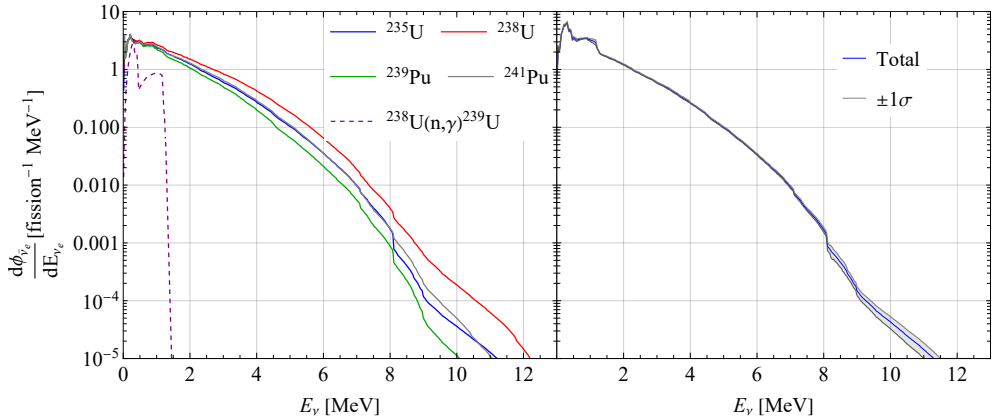

Figure 4.1: Left panel: PWR $\bar{\nu}_e$ spectrum resulting from thermal fission of ^{235}U, ^{238}U, ^{239}Pu, ^{241}Pu and neutron capture in ^{238}U. Right panel: total $\bar{\nu}_e$ spectrum obtained by weighting the fission fragments for their abundances and their respective ± 1 σ uncertainty. These neutrino spectra have been obtained following the information in Refs. [192, 193].

by[2]

$$\frac{d\Phi}{dE_\nu} = \frac{P_W}{\langle E \rangle_{\text{fission}}} \frac{1}{4\pi d^2} \frac{d\phi[\text{fission}^{-1}\text{MeV}^{-1}]}{dE_\nu}. \tag{4.2}$$

The method described previously serves as an illustrative purpose as it clearly provides all the components that constitute the reactor neutrino flux. However, in our work, we will also use other reactor flux models, which adopt different techniques to compute the $\bar{\nu}_e$ flux.

In particular, the neutrino spectra are built by combining the expected spectra for antineutrino energies above 2 MeV from either Ref. [195, 196] or Ref. [197], that we indicate as HM and EF, respectively, with the low-energy part determined by Ref. [198] and Refs. [199, 200], that we indicate as VE and K, respectively. Hereby, we derive three distinct combinations, which we denote as HMVE, EFK, and HMK. These spectra are obtained from the weighted average of the antineutrino fluxes from four main fission isotopes, namely ^{235}U, ^{239}Pu, ^{238}U and ^{241}Pu using the same relative abundances, as described before. In the K prediction [199, 200], the contribution at low energies from radiative neutron capture on ^{238}U is also taken into account. This contribution results in a higher spectrum for neutrino energies under approximately 1 MeV. In Fig. 4.2 we report the neutrino flux at 10 meters from a 3 GW_{th} PWR reactor, obtained by adopting the different parameterization discussed above. The total amount of neutrinos can be calculated

[2]Note that ϕ indicates the differential neutrino spectra in units of [fission MeV]$^{-1}$, while Φ describes the reactor flux in units of [MeV cm^2 s]$^{-1}$.

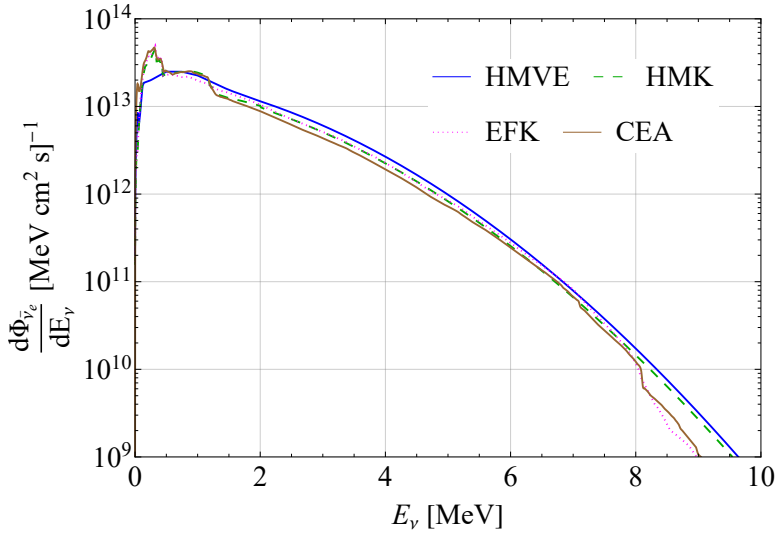

Figure 4.2: Neutrino flux expected at 10 meters from a 3 $\mathrm{GW_{th}}$ reactor obtained under different parameterizations for the neutrino flux: HM [195, 196]+VE [198] (solid blue), EF [197]+K [199, 200], HM+K and CEA [192].

by integrating over all neutrino energies, and is about $5.25 \times 10^{13}\ \bar{\nu}_e/\mathrm{cm}^2/\mathrm{s}$, consistent among the different parameterizations. It is worth noting that the use of such low-energy neutrinos makes the uncertainty in the nuclear structure almost completely irrelevant, as the nuclear form factors are usually close to unity in a CEνNS reactor experiment.

4.2 The Worldwide Reactor CEνNS Search and the NCC-1701 Observation

The search for CEνNS from reactor $\bar{\nu}_e$ has posed an exciting technological challenge to develop innovative detectors capable of spotting the extremely tiny nuclear recoils produced as a single outcome of the CEνNS interaction. There are different detectors currently under operation, but, due to the increased experimental challenge, many experiments obtained so far only upper limits on the CEνNS signal. Specifically, the CONNIE experiment [201] located ~ 30 m away from a 3.95 $\mathrm{GW_{th}}$ reactor core, exploits silicon detectors and reported so far only limits on the CEνNS signal [201–203] as well as very competitive constraints on new physics model [204, 205]. Similarly, the CONUS [206–208] and νGEN [209] experiments exploit germanium detectors located 17.1 and 11 meters away from 3.9 $\mathrm{GW_{th}}$ and 3.1 $\mathrm{GW_{th}}$ commercial reactors, respectively. Both the CONUS and νGEN Collaborations achieved extremely low experimental thresholds ($\sim 1\ \mathrm{keV_{nr}}$)

and background levels, being able to set very stringent upper limits on CEνNS taking advantage of their very high exposure of reactor ON and OFF data. Moreover, thanks to the high statistic and reduced background, the latest CONUS result [210] put a limit within a factor of two from the rate predicted by the Standard Model. In order to explore the regime of full coherency and to be sensitive to the lower part of the CEνNS spectrum where more events are expected, cryogenic detectors are under construction to further reduce the threshold. Among them, the NUCLEUS experiment [211, 212], which will be discussed in Chap. 5, in its first phase will make use of a gram-scale $\mathrm{CaWO_4}$ cryogenic detector, which benefits from a bigger CEνNS cross section compared to lighter elements, e.g. germanium or silicon, and a $\mathcal{O}(20)$ eV detector threshold, thanks to the excellent energy resolution. A similar technology is being developed by the Ricochet experiment at the ILL site, 8.8 m away from the core of the 58.3 $\mathrm{MW_{th}}$ research nuclear reactor, which is also aiming to measure CEνNS down to the sub-100 eV nuclear energy recoil regime [213–216].
Many other experimental programs are under development; among them, there are MINER [217], RED-100 [218], NEON [219], TEXONO [220], νBDX-DRIFT [221, 222], νIOLETA [223], NEWS-G3 and Bullkid [224]. Fig. 4.3 shows a world map that summarizes the main experimental efforts both at reactor (indicated with red dots) and stopped pion beams (green dots), the latter including also the Coherent Captain-Mills (CCM) [165], CSNS [166] and ESS facilities [164], the latter operating with the GanESS experiment [225]. Underground experiments sensitive to CEνNS are also indicated, specifically XENONnT [102], PandaX [101] and DarkSide-20k [114] which can exploit solar neutrinos, and RES-NOVA [35], which aims to detector CEνNS from supernovae neutrinos.

Within this worldwide search, the results reported in Ref. [226] from Collar *et al.* have gained significant attention and discussion, as they reported the first observation of CEνNS at the Dresden-II nuclear reactor power plant with significant implications for the physics that can be extracted within the SM and beyond [3, 227–229]. They used an ultra-low noise 2.924 kg p-type point-contact germanium detector, called NCC-1701, located 10.39 meters away from the Dresden-II PWR collecting about 96.4 days of effective exposure. Thanks to the low-energy threshold of such a detector, namely 0.2 $\mathrm{keV_{ee}}$, they presented an event spectrum with an excess of events that can be interpreted as a CEνNS signal when an increased quenching factor at low energies is considered. However, this observation

Figure 4.3: World map illustrating CEνNS experiments and facilities currently operating or under development. Red dots indicate reactor experiments, i.e. CONUS [206], νGeN [209], NUCLEUS [211, 212], Bullkid [224], CONNIE [201], νIOLETA [223], MINER [217], νBDX-DRIFT [221, 222], Dresden-II [226], Ricochet [213], NEON [219] and TEXONO [220], while green dots indicate Stopped Pion Source facilities, i.e. COHERENT [172], CCM [165], CSNS [166] and ESS [164] with the GanESS experiment [225]. Underground experiments sensitive to CEνNS are also indicated, specifically XENONnT [102], PandaX [101] and DarkSide-20k [114] which can exploit solar neutrinos, and RES-NOVA [35], which aims to detector CEνNS from supernovae neutrinos.

motivated several discussions within the CEνNS community, inspiring our study in Ref. [6] (see Sec. 4.3) where we explore effects which might enhance the observed spectrum at low energies.

For the Dresden-II analysis, the $\bar{\nu}_e$ flux has been normalized to the estimate reported in Ref. [226], which corresponds to $\Phi_{\rm est} = 4.8 \times 10^{13}\ {\rm cm}^{-2}{\rm s}^{-1}$, that has been determined considering a reactor power $P = 2.96\ {\rm GW_{th}}$ and a reactor-detector distance of $L = 10.39\ {\rm m}$ [226] adopting the HMVE parameterization. In the energy region of interest of Dresden-II, $0.2\,{\rm keV_{ee}} < T_{\rm e} < 1.5\,{\rm keV_{ee}}$, the background comes from the elastic scattering of epithermal neutrons and the electron capture in ^{71}Ge. The epithermal neutron contribution, which is the dominant one in the CEνNS recoil energy region, $T_{\rm e} \lesssim 0.5\,{\rm keV_{ee}}$, is described by an exponential function with decay constant $T_{\rm epith}$ plus a constant term $N_{\rm epith}$, while the electron capture peaks from ^{71}Ge, namely the L1-, L2- and M-shell peaks, are described each by a Gaussian function. The latter is parametrized by an amplitude A_i, the centroid T_i and the standard deviation σ_i, where $i =$ L1, L2 and M. Thus, the expected event rate

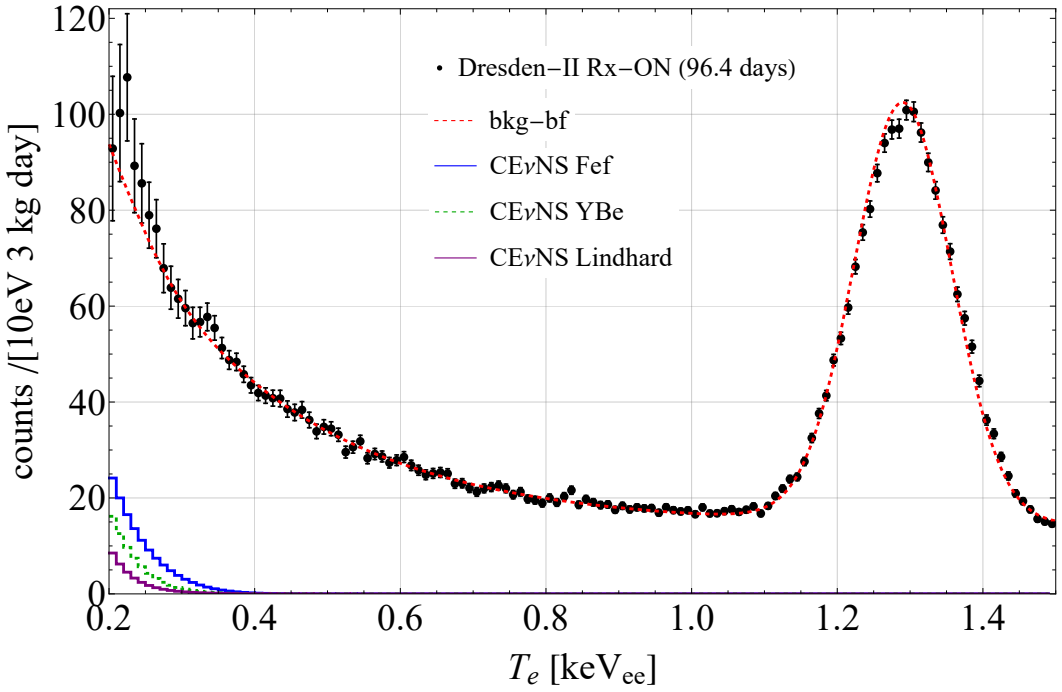

Figure 4.4: Dresden-II data from the data release [226] compared to the best-fit background model (dashed red) and the CEνNS prediction under different quenching factors hypothesis.

of background is given by

$$\frac{dN^{\rm bkg}}{dT_{\rm e}} = N_{\rm epith} + A_{\rm epith} e^{-T_{\rm e}/T_{\rm epith}} + \sum_{i={\rm L1,L2,M}} \frac{A_i}{\sqrt{2\pi}\sigma_i} e^{-\frac{(T_{\rm e}-T_i)^2}{2\sigma_i^2}} . \tag{4.3}$$

Following Ref. [226], the total amount of free parameters for the background prediction reduces to: $N_{\rm epith}$, $A_{\rm epith}$, $T_{\rm epith}$, $A_{\rm L1}$, $T_{\rm L1}$, $\sigma_{\rm L1}$ and $\beta_{\rm M/L1}$. In fact, the amplitude of the L2 shell contribution can be expressed in terms of the amplitude of the L1 shell ($A_{\rm L1}$), in particular $A_{\rm L2}/A_{\rm L1} = 0.008$, and $\sigma_{\rm L2} = \sigma_{\rm L1}$. The centroid of the L2 Gaussian can be safely set to the nominal value $T_{\rm L2} = 1.142$ keV. The standard deviation of the M-shell contribution can be fixed to the electronic noise uncertainty, which is $\sigma_n = 68.5$ eV for the Rx-ON (reactor operation period) data. The centroid of the M-shell Gaussian is fixed to its nominal value $T_{\rm M} = 0.158$ keV, being smaller than the experimental threshold whereas its amplitude is left free to vary in the fit with a constraint corresponding to the experimentally determined ratio $\beta_{\rm M/L1} = A_{\rm M}/A_{\rm L_1} = 0.16 \pm 0.03$. The best-fit background model to the data is shown in Fig. 4.4 (dashed red).

The expected CEνNS event-number $N_i^{\rm CE\nu NS}$ in each electron-recoil energy-bin i is

given by

$$N_i^{\mathrm{CE}\nu\mathrm{NS}}(\mathcal{N}) = N(\mathrm{Ge}) \int_{T_{\mathrm{e}}^i}^{T_{\mathrm{e}}^{i+1}} dT_{\mathrm{e}} \int_{T_{\mathrm{nr}}^{\prime\min}}^{T_{\mathrm{nr}}^{\prime\max}} dT'_{\mathrm{nr}}\, R(T_{\mathrm{e}}, T'_{\mathrm{e}}(T'_{\mathrm{nr}})) \times \int_{E_{\min}(T'_{\mathrm{nr}})}^{E_{\max}} dE \frac{d\Phi_{\overline{\nu}}}{dE}(E) \frac{d\sigma_{\overline{\nu}-\mathcal{N}}}{dT'_{\mathrm{nr}}}(E, T'_{\mathrm{nr}}), \tag{4.4}$$

where $\mathcal{N} = {}^A_Z\mathrm{Ge}$ with $A = 70, 72, 73, 74, 76$, with the corresponding natural abundances $f({}^A_Z\mathrm{Ge})$ of 0.2057, 0.2745, 0.0775, 0.3650, 0.0773 [230]. The expected CEνNS is obtained by weighting for the corresponding isotopic abundance, i.e. $N_i^{\mathrm{CE}\nu\mathrm{NS}}(\mathrm{Ge}) = \sum_A f({}^A_Z\mathrm{Ge}) N_i^{\mathrm{CE}\nu\mathrm{NS}}({}^A_Z\mathrm{Ge})$. Moreover, $N(\mathrm{Ge}) = 2.43 \times 10^{25}$ is the number of germanium atoms, $T_{\mathrm{nr}}^{\prime\min} \simeq 2.96$ eV is the minimum average ionization energy in Ge, $R(T_{\mathrm{e}}, T'_{\mathrm{e}}(T'_{\mathrm{nr}}))$ is the detector energy resolution function, $T'_{\mathrm{e}}(T'_{\mathrm{nr}}) = f_Q(T'_{\mathrm{nr}}) T'_{\mathrm{nr}}$ is the ionization energy where f_Q is the germanium quenching factor which will be addressed in Sec. 4.2.1. $d\Phi/dE_\nu$ is the neutrino flux defined in Eq. 4.2, and for our analyses, we will use the HMVE parameterizations consistently with the data release [226]. In Ref. [3] we showed that different parameterization provide very compatible results when physical parameters are extracted.

The detector energy-resolution function is described as a truncated Gaussian

$$R\left(T_{\mathrm{e}}, T'_{\mathrm{e}}(T'_{\mathrm{nr}})\right) = \left(\frac{2}{1 + \mathrm{Erf}\left(\frac{T'_{\mathrm{e}}(T'_{\mathrm{nr}})}{\sqrt{2}\sigma'_e}\right)}\right) \frac{1}{\sqrt{2\pi}\sigma'_e} e^{-\frac{\left(T_{\mathrm{e}} - T'_{\mathrm{e}}(T'_{\mathrm{nr}})\right)^2}{2{\sigma'_e}^2}}, \tag{4.5}$$

with a standard deviation equal to $\sigma'_e = \sqrt{\sigma_n^2 + \eta F_f T_{\mathrm{e}}}$, where the average energy of electron-hole formation is $\eta = 2.96$ eV and the Fano factor is $F_f = 0.11$ for Ge [226]. It is important to note that in Eq. (4.4) the experimental acceptance does not appear since the data points provided in the data release are already corrected for it. The details reported here, as well as analysis strategy methods, follow closely the prescription described in the supplemental material of Ref. [226], adopted also in other phenomenology studies [227].

To perform the analysis of the Dresden-II Ge data under the hypothesis of a CEνNS signal, we use the least-squares function

$$\chi^2_{\mathrm{Ge,CE}\nu\mathrm{NS}} = \sum_{i=1}^{130} \left(\frac{N_i^{\mathrm{bkg}} + \alpha N_i^{\mathrm{CE}\nu\mathrm{NS}} - N_i^{\mathrm{exp}}}{\sigma_{\mathrm{exp}}}\right)^2 + \left(\frac{\beta - \beta_{\mathrm{M/L1}}}{\sigma_{\beta_{\mathrm{M/L1}}}}\right)^2 + \left(\frac{\alpha - 1}{\sigma_\alpha}\right)^2, \tag{4.6}$$

where N_i^{bkg} and $N_i^{\mathrm{CE}\nu\mathrm{NS}}$ are the predictions in the i-th electron recoil energy bin for the background and the CEνNS signal, and N_i^{exp} is the experimental number of

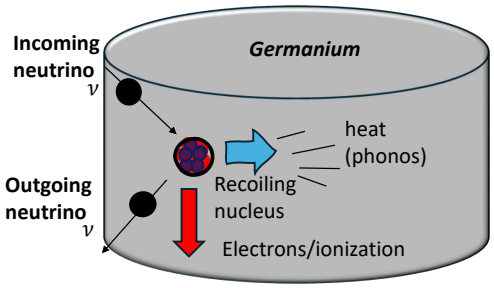

Figure 4.5: Schematic representation of the reduction of the ionization yield produced after the nuclear recoil, in this case, produced by the scattering of a neutrino off a germanium nucleus, due to the quenching effect. The ionized electrons produce the signal observed in the detector, while the heat is produced by inelastic collisions.

events in the i-th bin. The nuisance parameter α takes into account the uncertainty on the neutrino flux (with $\sigma_\alpha = 2\%$), while $\beta_{\mathrm{M/L1}}$ is a prior for the M- to L1-shells ratio, with $\beta_{\mathrm{M/L1}} = 0.16$ and $\sigma_{\beta_{\mathrm{M/L1}}} = 0.03$. The χ^2 in Eq. 4.6 will be used also to constrain different physics scenarios, modifying the expected $N_i^{\mathrm{CE}\nu\mathrm{NS}}$ according to the model considered in order to find the set of values which minimize the χ^2. When we consider the electron scattering channel, the signal will be $N_i^{\mathrm{CE}\nu\mathrm{NS}} \rightarrow N_i^{\mathrm{CE}\nu\mathrm{NS}} + N_i^{\mathrm{ES}}$, where N_i^{ES} is the expected number of electron scattering events occurring in the i-th bin and is given by

$$N_i^{\mathrm{ES}} = N(\mathrm{Ge}) \int_{T_{\mathrm{e}}^i}^{T_{\mathrm{e}}^{i+1}} dT_{\mathrm{e}} \int_{T_{\mathrm{e}}^{\prime\mathrm{min}}}^{T_{\mathrm{e}}^{\prime\mathrm{max}}} dT_{\mathrm{e}}^{\prime}\, R(T_{\mathrm{e}}, T_{\mathrm{e}}^{\prime}) \int_{E_{\mathrm{min}}(T_{\mathrm{e}}^{\prime})}^{E_{\mathrm{max}}} dE \frac{dN_{\overline{\nu}}}{dE}(E) \frac{d\sigma_{\overline{\nu}-\mathrm{Ge}}^{\mathrm{ES}}}{dT_{\mathrm{e}}^{\prime}}(E, T_{\mathrm{e}}^{\prime}), \quad (4.7)$$

with the difference that in the energy resolution, the quenching factor must be set to unity.

4.2.1 The Germanium Quenching Factor Puzzle

The QF, introduced in Sec. 3.2 and schematically shown in Fig. 4.5, is a crucial parameter for CEνNS experiments looking for the ionization signal produced at low recoil energies. Although QF measurements for CsI and Ar are quite constrained and well known at nuclear recoil energies $\gtrsim 10\ \mathrm{keV_{nr}}$, the germanium quenching factor is not very well known at low energies relevant for reactor searches. This has profound implications for understanding the experimental data. First of all,

we can make use of the standard Lindhard theory [231] to describe the behaviour of QF in a wide range of nuclear recoil energies. This theory predicts the amount of ionization due to the nuclear recoil under the following assumptions

- the contribution of the moving electrons is negligible;
- the electronic cloud follows immediately the nucleus;
- the energy transferred to ionized electrons is small compared to that transferred to recoiling ions;
- the effects of electronic and atomic collisions can be treated separately;
- the nuclear recoil energy is much smaller than the energy of the incident particle.

Under these assumptions, the quenching factor predicted by the Lindhard theory is given by

$$f_Q^{\text{Lind.}} = \frac{kg(\epsilon)}{1 + kg(\epsilon)}, \tag{4.8}$$

where $g(\epsilon) \simeq 3\,\epsilon^{0.15} + 0.7\,\epsilon^{0.6} + \epsilon$ with $\epsilon \simeq 11.5\,Z^{-7/3}\,T_{\text{nr}}$. The parameter k is found to be $k = 0.133\,Z^{2/3}A^{-1/3}$ which gives $k \simeq 0.158$ for Germanium. The Lindhard prediction shows a good agreement with experimental data for $T_{\text{nr}} \gtrsim 5$ keV$_{\text{nr}}$, which is the range for CEνNS experiments conducted at the SNS. On the other hand, there is an ongoing discussion regarding the behaviour of the Ge QF for lower energies. Indeed, the CEνNS observation by Dresden-II depends crucially on the two new QF measurements reported in Ref. [243]. The first one is determined from photo-neutron source measurements, so-called YBe [243], and the second one is derived from iron-filtered monochromatic neutrons, so-called Fef, that consists in a simple linear fit of the four data points for $T_{\text{nr}} \lesssim 1.35$ keV and is extended above this range with the standard Lindhard model with $k = 0.157$ [231]. However, these two QF determinations are in contrast with and significantly higher than the standard Lindhard prediction with the parameter $k = 0.157$ [231] and other independent experimental measurements. Moreover, CONUS data disfavours quenching parameters above $k = 0.27$ [207] and a recent low-energy determination of the QF finds a good agreement with the Lindhard theory with a parameter $k = 0.162 \pm 0.004$ (stat+sys) [236]. In Fig. 4.6 we compare the more relevant measurements of the germanium QF for $T_{\text{nr}} < 4$ keV$_{\text{nr}}$ at the moment of writing this thesis [232–238, 241, 242]. We also report the YBe

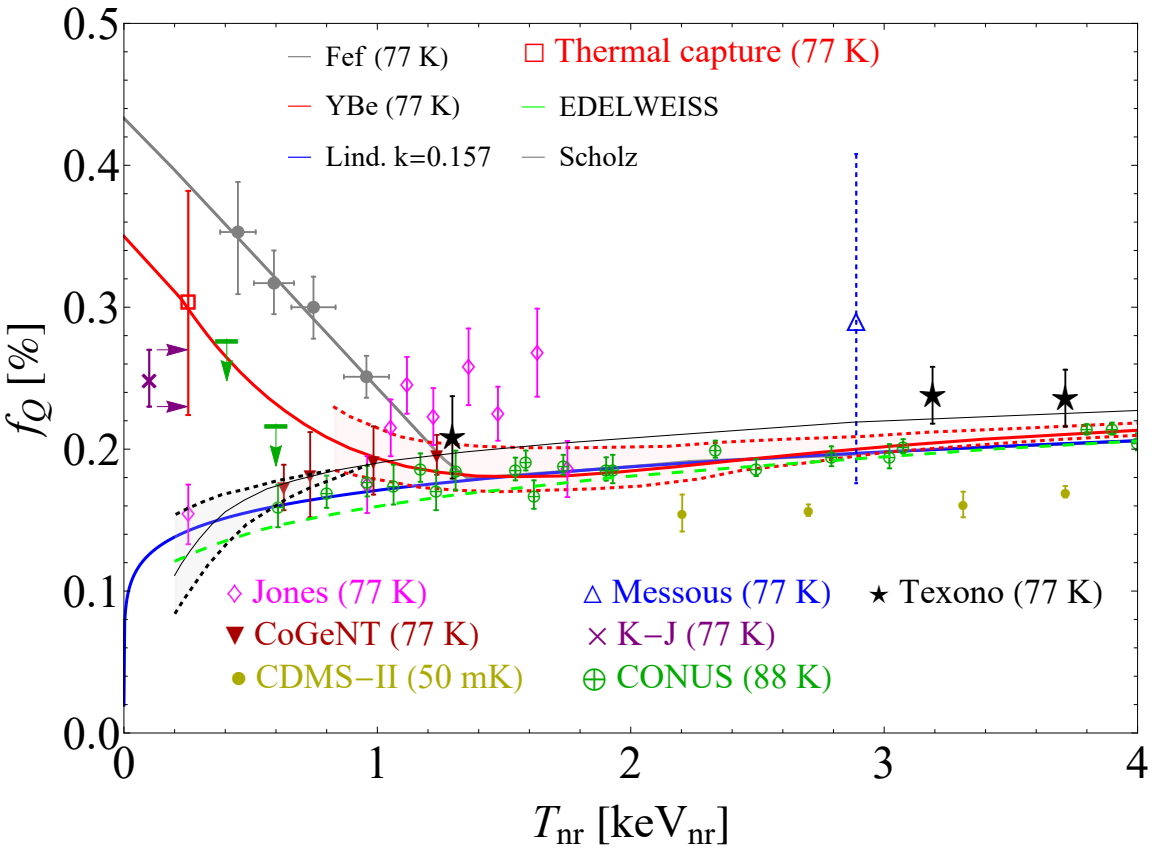

Figure 4.6: Summary plot representing the state-of-the-art measurements of the germanium quenching factor in the low-energy nuclear recoil range, i.e. $0.2 \lesssim T_{\rm nr}[{\rm keV_{nr}}] \lesssim 4$, of interest for CE$\nu$NS searches at reactor, from Jones *et al* [232, 233], CoGeNT [234], CDMS-II [235], CONUS [236], Messous [237], Texono [238], Scholz [239], Edelweiss [240] and a recent measurement from Kavner and Jovanovic (K-J) [241]. The purple arrows indicate that the latter measurement is to be intended at 0.254 keV$_{\rm nr}$. CONUS data have been obtained by considering different nominal neutron beam energies, and this plot presents the weighted average for data points at the same nuclear recoil energies. CONUS data below $T_{\rm nr}$ are reported at the 90% CL The best fit reported by the CONUS Collaboration yields $k = 0.162 \pm 0.004$. The work by Collar et al. [242] reports three different approaches to measure the ionization yield in germanium, i.e. photo-neutron source (YBe) indicated by the red band, iron-filtered low-energy neutron beam (Fef) and thermal neutron capture. As a comparison, the theoretical prediction from the standard Lindhard theory with $k = 0.157$ is also reported. See Fig. 1 of Ref. [235] for a complete summary of the quenching factor measurements at higher nuclear recoil energies.

and Fef QFs [242] which allowed the CEνNS evidence in Ref. [226]. Moreover, another recent measurement [241] (purple) performed at $T_{\rm nr} = 254$ eV$_{\rm nr}$ seems to support the evidence of an enhancement of the QF at low energies, even though there is a clear tension with previous measurements [232, 233] and the Lindhard prediction. Modifications to the Lindhard theory have been proposed to explain its enhancement at low energies [244, 245] by means of phenomenological parame-

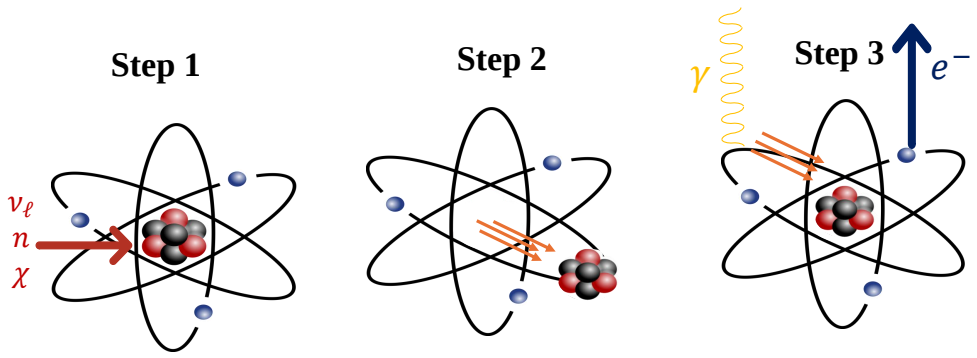

Figure 4.7: Simplified representation of the Migdal effect induced by nuclear recoil. An incoming neutral particle, e.g. neutrino (ν_ℓ), neutron (n) or dark matter (χ) interacts with the nucleus (step 1). The nucleus is displaced from its initial position, and the electronic cloud does not follow immediately the motion of the recoiling nucleus (step 2). To restore the equilibrium an electron can be emitted together with de-excitation light (step 3).

ters [246] to adjust the standard Lindhard prediction to accommodate Fef and YBe data. However, the approach exploited in these studies neglects the microscopic physics of the processes which are causing this ionization. One possible physical process which provides extra ionization on top of the standard nuclear recoil is the Migdal effect, which will be explored in detail in the next section.

4.3 Migdal Effect In Reactor CEνNS Searches

As discussed in the previous section, some data seem to be indicating a deviation from the QF Lindhard theory at low energies, resulting in extra ionization compared to the prediction, boosting theoretical investigations to explain this evidence. A suitable candidate is the Migdal effect, which refers to a phenomenon proposed by Migdal in the 1940s [247]. The Migdal effect predicts extra radiation being emitted from the atom after a nuclear process, i.e. α and β decays [248–250] or neutral particle scattering [247, 251]. Although the Migdal emission has been observed in α decay [252–254], β decay [255, 256], and β^+ decay [257], the first observation in the case of nuclear recoil is still missing at the time of writing this thesis. From a qualitative point of view we can imagine that atomic electrons do not immediately follow the motion of the recoiling nucleus, and, to restore

equilibrium, extra ionization can be injected into the detector, as schematically shown in Fig. 4.7. Many experimental programs are under development to unambiguously detect the electron produced by this process. Among these efforts, the MIGDAL Collaboration [258] has deployed an Optical Time Projection Chamber filled with a low-pressure gas based on CF_4, which reconstructs the topology of the emission to provide an *image* of the event. It is also relevant to mention that the authors in Ref. [259] reported the first direct search for the Migdal effect in liquid xenon using nuclear recoils produced by tagged neutron scatters. Intriguingly, they did not observe a signal consistent with predictions, pointing to the need to further investigate this effect both theoretically and experimentally. Moreover, the Migdal effect induced by dark matter (DM) particles has been recently taken into serious consideration in the context of dark matter searches [112, 260–266] as it enables to improve the constraints for DM candidates within the MeV range.

For our purposes, it is crucial to characterize the impact of the Migdal effect on top of the standard Lindhard theory to verify whether or not can be the source of enhancement observed by the Dresden-II Collaboration. We first calculate the Migdal rate using the formalism of Ibe *et al.* [260], which considers the target as composed of isolated atoms, which is clearly not a satisfying assumption for a semiconductor. In this section, we will only outline the key features of the Ibe *et al.* formalism, as it has already been previously adopted in the context of neutrino scattering [266, 267].[3]

This formalism relies on the dipole approximation that allows one to write the Migdal transition matrix element, M_{fi}, in the form

$$\begin{aligned} M_{fi} &= \langle \psi_f | e^{-im_e \vec{v} \cdot \sum_{i=1}^{Z} \vec{r}_i} | \psi_i \rangle \simeq \\ &\simeq -im_e \vec{v} \cdot \langle \psi_f | \sum_{i=1}^{Z} \vec{r}_i | \psi_i \rangle \\ &\equiv -im_e \vec{v} \cdot \vec{D}_{fi}, \end{aligned} \tag{4.9}$$

where $\vec{r}_i$ is the position operator of the Z electrons, $\vec{D}_{fi}$ is the dipole matrix element, m_e is the electron mass, $\vec{v}$ is the nuclear recoil velocity, while ψ_f and ψ_i are the wavefunctions of the final and the initial atomic states in the nucleus rest frame. The final state wavefunctions are boosted to the rest frame of the recoiling

[3]Note that the authors in Refs. [266, 267] provided some public codes to compute the CEνNS rate and the Migdal contribution using the formalism of Ibe *et al.* which have been used to validate our results.

nucleus by a Galilean transformation and are computed using the Dirac-Hartree-Fock method. Under these assumptions, the CEνNS differential cross section for the Migdal effect can be written as

$$\left(\frac{d\sigma_{\bar{\nu}_e\text{-}\mathcal{N}}}{dT_{\rm nr}}\right)^{\text{Ibe } et\ al.}_{\text{Migdal}} = \frac{G_{\rm F}^2 m_N}{\pi}\left(1-\frac{m_N T_{\rm nr}}{2E_\nu^2}\right)\mathcal{Q}_W^2\left|Z_{\rm ion}(q_e)\right|^2, \tag{4.10}$$

where $|Z_{\rm ion}(q_e)|$ is the ionization rate of an individual electron in the target with momentum q_e. It is defined as

$$|Z_{\rm ion}(q_e)|^2 = \frac{1}{2\pi}\sum_{n,\ell}\int dT_e \frac{d}{dT_e} p^c_{q_e}(n\ell \to T_e), \tag{4.11}$$

where $p^c_{q_e}(n\ell \to T_e)$ are the ionization probabilities for an atomic electron with quantum numbers n and ℓ that is ionized with a final energy T_e and are reported in Fig. 4.8. It should be noticed that very similar results are expected if one relies on

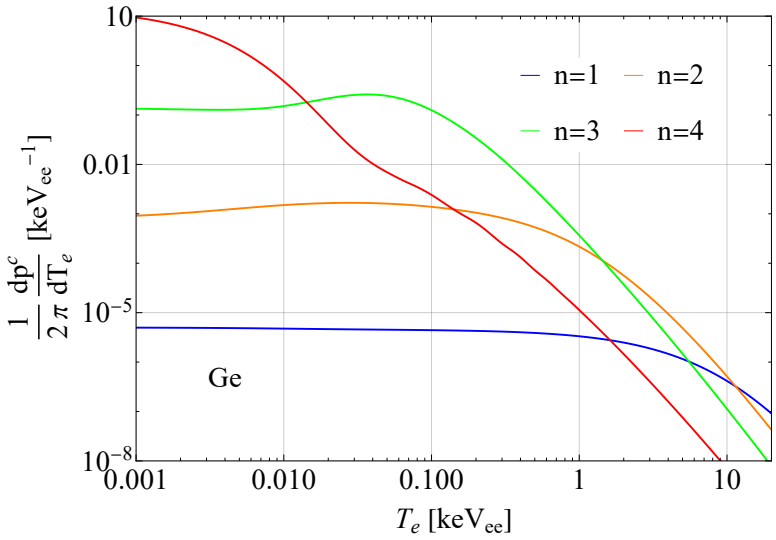

Figure 4.8: The differential ionization probabilities as a function of the emitted electron energy, T_e, for isolated Ge atoms. The contributions from different ℓ's quantum numbers are summed. The ionization probabilities are available in ancillary files of Ref. [260], and the integrated probabilities are given in Tab. II of the same reference.

the probabilities calculated in Ref. [258] with an independent approach. Indeed, the authors found a very good agreement with the results obtained with the Ibe *et al.* formalism that is also used in this thesis, demonstrating that the addition of sub-leading contributions to the ionization probabilities is not significant at low recoil energies for atomic germanium.

The double differential cross section under the Ibe *et al.* formalism, for the (n,ℓ)

state, as a function of both the electron and the nuclear recoil energy, is hence

$$\left(\frac{d^2\sigma_{\bar{\nu}_e\text{-}\mathcal{N}}}{dT_{\rm nr}dT_e}\right)^{\text{Ibe }et\ al.}_{n\ell} = \frac{G_{\rm F}^2 m_N}{\pi}\left(1-\frac{m_N T_{\rm nr}}{2E_\nu^2}\right)\mathcal{Q}_W^2\frac{1}{2\pi}\frac{d}{dT_e}p^c_{q_e}(n\ell\to T_e). \tag{4.12}$$

If the nuclear recoil is followed by a Migdal emission, the total energy deposit of the event in the detector is

$$E_{\rm det} = f_Q T_{\rm nr} + T_e + E_{n\ell}, \tag{4.13}$$

where the first term is the nuclear recoil energy deposit, while T_e and $E_{n\ell}$ account for the extra energy injected in the detector, $E_{n\ell}$ being the atomic de-excitation energy for Ge [260]. We evaluate the theoretical event rate as a function of the detected energy, which is given by

$$\left(\frac{dR}{dE_{\rm det}}\right)^{\text{Ibe }et\ al.}_{\text{Migdal}} = N(\text{Ge})\sum_{n,\ell}\int_{E_\nu^{\rm min}}^{E_\nu^{\rm max}} dE_\nu \frac{dN_{\bar{\nu}_e}}{dE_\nu}\int dT_e \int_{T_{\rm nr}^{\rm min}}^{T_{\rm nr}^{\rm max}} dT_{\rm nr}\left(\frac{d^2\sigma_{\bar{\nu}_e\text{-}\mathcal{N}}}{dT_{\rm nr}dT_e}\right)^{\text{Ibe }et\ al.}_{n\ell}\times \delta(E_{\rm det}-f_Q T_{\rm nr}-T_e-E_{n\ell}). \tag{4.14}$$

In this calculation, it is convenient to impose energy conservation using the Dirac δ, and $T_{\rm nr}$ is now constrained within the values $T_{\rm nr}^{\rm min}$ and $T_{\rm nr}^{\rm max}$ given by [268]

$$\frac{(T_e+E_{n\ell})^2}{2m_N} \le T_{\rm nr} \le \frac{(2E_\nu-(T_e+E_{n\ell}))^2}{2(m_N+2E_\nu)}. \tag{4.15}$$

The rate in Eq. (4.14) represents the Migdal contribution summed over all the possible (n,ℓ) atomic states and is shown in Fig. 4.11. On the other hand, to display the CEνNS rate in the same scale as a function of the ionization energy, we define $E_{\rm det} = f_Q T_{\rm nr}$ such that

$$\left(\frac{dR}{dE_{\rm det}}\right)^{\rm CE\nu NS} = N(\text{Ge})\int_{E_\nu^{\rm min}}^{E_\nu^{\rm max}} dE_\nu \frac{dN_{\bar{\nu}_e}}{dE_\nu}\frac{d\sigma_{\bar{\nu}_e\text{-}\mathcal{N}}}{dT_{\rm nr}}\left(f_Q + T_{\rm nr}\frac{df_Q}{dT_{\rm nr}}\right)^{-1}. \tag{4.16}$$

The last term in Eq. (4.16) is $dT_{\rm nr}/dE_{\rm det}$, which is needed to express the rate in terms of the electron-equivalent nuclear recoil energy. The total predicted event rate is thus given by the sum of Eq. (4.16) and Eq. (4.14).

4.4 Migdal Photo Absorption

The formalism described so far to compute the dipole matrix element for the Migdal rate relies on the assumption that the target atom is isolated. While this assumption is acceptable for noble elements, as for argon or xenon detectors [267], it is expected to be less valid in semiconductors, where solid-state effects might be relevant. However, developing a first-principle theory that goes beyond the isolated atom approximation is challenging because of the many-body effects that need to be taken into account. Remarkably, the formalism developed in Ref. [263] relates the photoabsorption cross section σ_γ to the dipole matrix element, necessary to compute the Migdal ionization rate, without requiring any many-body calculation. This scheme will be referred to as Migdal photoabsorption approximation (MPA). One of the major advantages of MPA is that the photoabsorption cross section is experimentally known, such that the Migdal rate suffers from very small uncertainties [263], well below the precision required in this work. MPA has been so far adopted in the context of dark matter searches, where the power of the formalism has been proved by comparing it to other computations for silicon and xenon [260, 261]. However, MPA has never been exploited in the context of neutrino scattering. In Ref. [6], for the first time, we apply this formalism in CEνNS searches and we compare its predictions with the formalism of Ibe *et al.* for germanium detectors. Explicitly, to derive the Migdal contribution to the CEνNS cross section under MPA, we recall that the Migdal transition matrix element under the dipole approximation, $|M_{fi}|^2$, is related to the ionization probability due to the Migdal effect. It is convenient to define the double differential cross section for $\bar{\nu}_e$ scattering off a nucleus $\mathcal{N}$ as

$$\left(\frac{d^2\sigma_{\bar{\nu}_e\text{-}\mathcal{N}}}{dT_{\rm nr}dE_r}\right)_{\rm Migdal} = \left(\frac{d\sigma_{\bar{\nu}_e\text{-}\mathcal{N}}}{dT_{\rm nr}}\right)|M_{fi}|^2, \tag{4.17}$$

where $T_{\rm nr}$ is the nuclear recoil energy, and the matrix element is a function of E_r, which in this notation is the energy deposit due to atomic excitation or ionization such that $E_{\rm det} = f_Q T_{\rm nr} + E_r$. The square of the transition matrix element in Eq. (4.17) can be recasted to

$$|M_{fi}|^2 = \left(\frac{m_e}{m_N}\right)^2 2m_N T_{\rm nr}\overline{D_{fi}^2}, \tag{4.18}$$

where we have used the fact that $m_N|\vec{v}| = \sqrt{2m_N T_{\rm nr}}$ is the momentum transfer of the recoiling nucleus, with $\vec{v}$ the nuclear recoil velocity. Here, $\overline{D^2_{fi}}$ is the average of the squared dipole matrix element. Under the MPA scheme, one has to relate $\overline{D^2_{fi}}$ with the photoabsorption cross section σ_γ through [263]

$$\overline{D^2_{fi}} = \frac{\sigma_\gamma(E_r)}{4\pi^2 \alpha_{\rm EM} E_r}, \tag{4.19}$$

where the photoabsorption cross section $\sigma^{\rm Ge}_\gamma(E_r)$ for Ge has been taken from Refs. [81, 269] for $E_r \geq 10$ eV$_{\rm ee}$. The double differential Migdal cross section as a function of E_r is given by

$$\left(\frac{d^2\sigma_{\bar{\nu}_e\text{-}\mathcal{N}}}{dT_{\rm nr} dE_r}\right)^{\rm MPA}_{\rm Migdal} = \frac{G_{\rm F}^2 m_N T}{\pi}\left(1 - \frac{m_N T_{\rm nr}}{2E_\nu^2}\right) Q_W^2 \frac{1}{2\pi^2 \alpha_{\rm EM}} \frac{m_e^2}{m_N} \frac{T_{\rm nr}}{E_r} \sigma^{\rm Ge}_\gamma(E_r). \tag{4.20}$$

We derive the differential Migdal cross section as a function of $E_{\rm det}$ by integrating over all possible nuclear recoils, i.e.

$$\left(\frac{d\sigma_{\bar{\nu}_e\text{-}\mathcal{N}}}{dE_{\rm det}}\right)^{\rm MPA}_{\rm Migdal} = \frac{G_{\rm F}^2}{\pi}\int_{T_{\rm nr}^{\rm min}}^{T_{\rm nr}^{\rm max}} dT_{\rm nr}\left(1 - \frac{MT_{\rm nr}}{2E_\nu^2}\right) Q_W^2 \frac{m_e^2}{2\pi^2\alpha_{\rm EM}} \times \frac{T_{\rm nr}}{E_{\rm det} - f_Q T_{\rm nr}} \sigma^{\rm Ge}_\gamma(E_{\rm det} - f_Q T_{\rm nr}). \tag{4.21}$$

In Fig. 4.9 we show the germanium photoabsorption cross section extracted from Ref. [269] as used in this thesis, along with the differential Migdal cross section as a function of $E_{\rm det}$ for $E_\nu = 3$ MeV. The two cross sections are reported at different energy scales indicated in the corresponding y axes. In Fig. 4.9, it is possible to see that the features that characterize the differential Migdal cross section within the MPA scheme are tightly connected with the photoabsorption peaks. On the other hand, in Fig. 4.10 we show the comparison between the differential Migdal cross section and the CEνNS one as a function of the observed energy $E_{\rm det}$, for a neutrino energy of $E_\nu = 6$ MeV and assuming the standard Lindhard quenching factor. We are now finally able to evaluate the theoretical Migdal event rate under MPA as a function of $E_{\rm det}$, which is obtained by integrating over all possible nuclear recoil energies. The results are shown in Fig. 4.11, which compares the Migdal ionization rate under MPA and Ibe *et al.* formalisms with the CEνNS rate as a function of the detected energy considering a 1 kg Ge detector located 10 m away from a 3 GW$_{\rm th}$ reactor power plant, whose $\bar{\nu}_e$ spectrum is given by the HMVE parameterization and adopting the Lindhard theory. This configuration re-

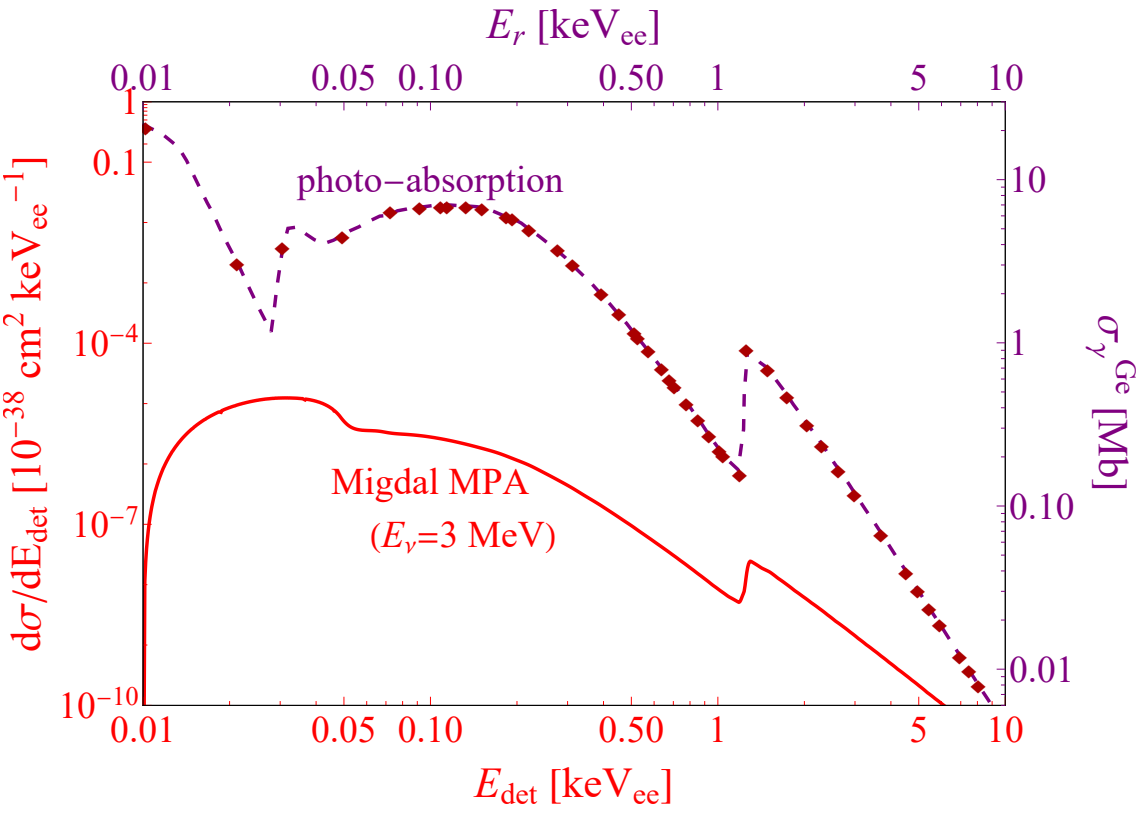

Figure 4.9: Photoabsorption cross section for Germanium taken from Ref. [269] (purple) and differential Migdal cross section for $E_\nu = 3$ MeV. The dots represent the photoabsorption cross section for each x-ray emission as listed in Ref. [269].

sembles current CEνNS reactor experiments, like Dresden-II, CONUS and νGEN. For the Ibe *et al.* rate in Fig. 4.11, we isolated the contributions from the different n shells, obtained by summing over all the different orbital angular momenta ℓ in the initial state. We found intriguingly that the two formalisms give practically identical results in the energy range considered. Moreover, in both cases, the Migdal contribution is completely subdominant with respect to the CEνNS one for energies below ~ 0.6 keV$_{ee}$, with the most significant contribution given by the $n = 2, 3$ shells. Above ~ 0.6 keV$_{ee}$ it starts to dominate[4], and it could provide the possibility to observe CEνNS above this threshold, even if being so small it would require extremely low levels of background.

It is worth discussing the validity of our formalism. It should be noticed that depending on the crystal scale that one is able to probe, other effects that account

[4]Note that a similar trend is also found in Ref. [267], where a comparison between the CEνNS rate and the Migdal contribution using the formalism of Ibe *et al.* has been evaluated for xenon and argon detectors in a reactor site.

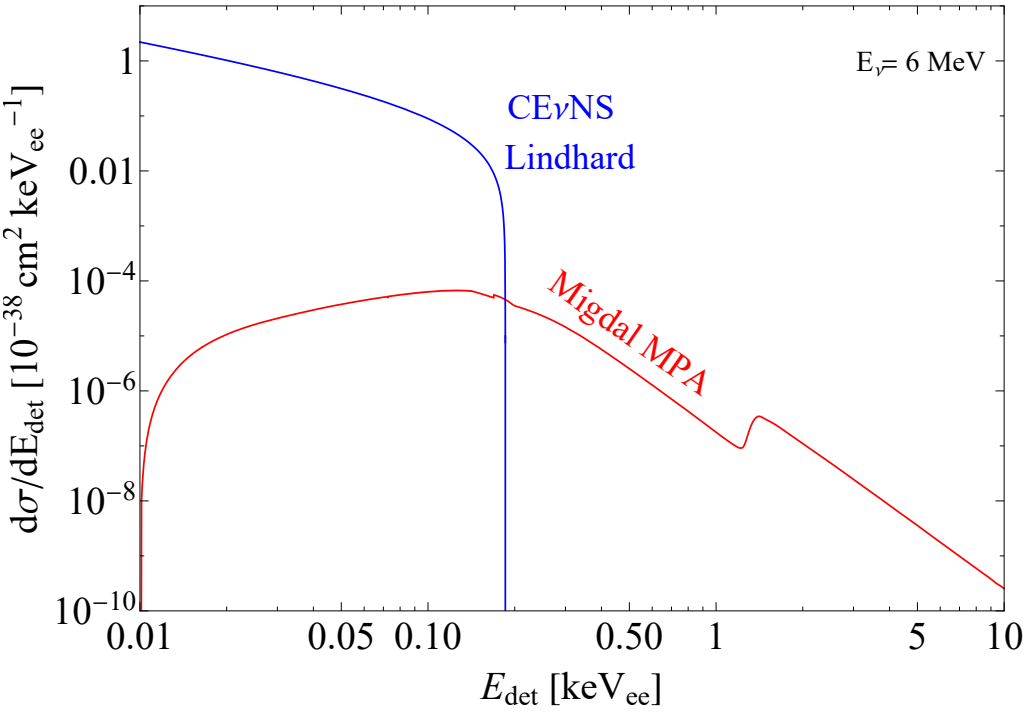

Figure 4.10: Comparison between the Migdal cross section (under the MPA scheme) and the CEνNS one as a function of the observed energy $E_{\rm det}$, assuming the standard Lindhard quenching factor and a neutrino energy of $E_\nu = 6$ MeV.

for the response of multiple atoms at once should be considered, as they have been proven to highly enhance the Migdal rate [270–273]. However, although the range of $T_{\rm nr}$ in Eq. (4.15) includes very small values, the main contribution in current Ge CEνNS reactor experiments comes from $T_{\rm nr}$ of the order of 1 keV. Thus, the momentum transfer is $|\vec{q}| \simeq \sqrt{2m_N T_{\rm nr}} \sim 10$ MeV with a corresponding de Broglie wavelength of about 20 fm. The latter is much smaller than the scale of the interparticle spacing in the crystal so, in this work, we can safely neglect these effects. We point here, that at lower ionization energies, multiple atom effects must be better taken into consideration. Moreover, it has been suggested that in germanium a larger amount of secondary nuclear recoils may be produced following a low-energy primary one [243]. This, in addition to possible more complex crystal response models [274–276], can significantly affect the microscopic description of the Migdal effect. However, the inclusion of these possible effects, which still needs to be investigated both theoretically and experimentally, is beyond the scope of our work.

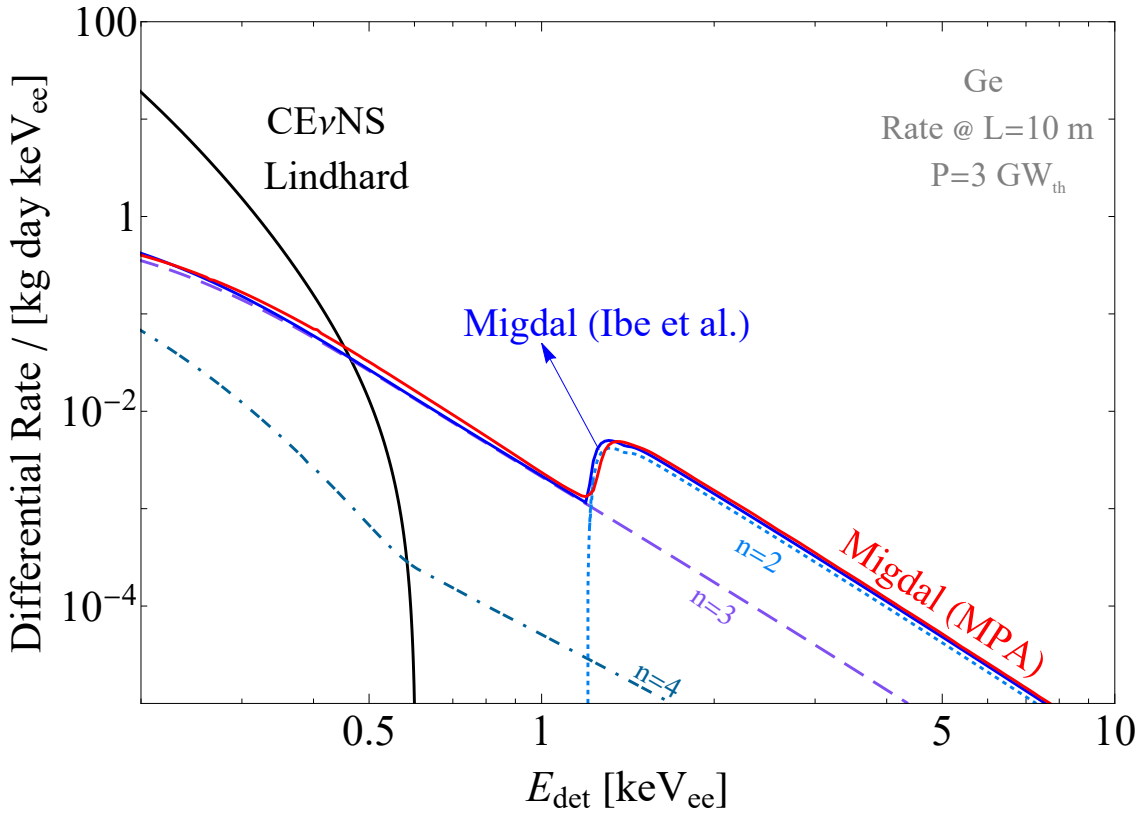

Figure 4.11: CEνNS theoretical differential rate for a Ge detector located $10\,\mathrm{m}$ away from a $3\,\mathrm{GW_{th}}$ reactor using the Lindhard QF (black solid line). We also show the Migdal rate obtained under the Ibe *et al.* formalism (solid blue line), highlighting also the contributions of the different $n = 2, 3, 4$ atomic shells (dashed curves), and the rate obtained with the MPA formalism (solid red line).

4.4.1 Impact of The Migdal Effect in The Dresden-II CEνNS Observation

In this section, we will study the implications of the Migdal effect on the Dresden-II science case. Here, as already stated in Sec. 4.2.1, the Migdal effect has been invoked as a possible explanation of the enhancement measured in the Fef and YBe quenching factors at low energies that in turn enabled the observation of CEνNS in the Dresden-II data. In the top panel of Fig. 4.12, we show the Dresden-II reactor ON (Rx-ON) data along with the standard CEνNS predictions obtained with three different QFs, namely Lindhard, Fef and YBe. To derive these spectra we used all the experimental information on the Dresden-II detector, including energy-smearing effects, following Refs. [3, 226, 227] and discussed in Sec. 4.2. In the bottom panel of Fig. 4.12 we show the same spectra for the three QFs but we compare them to the Dresden-II data residuals after background subtraction [226]. It is evident that only the Fef and marginally the YBe QFs fit the excess

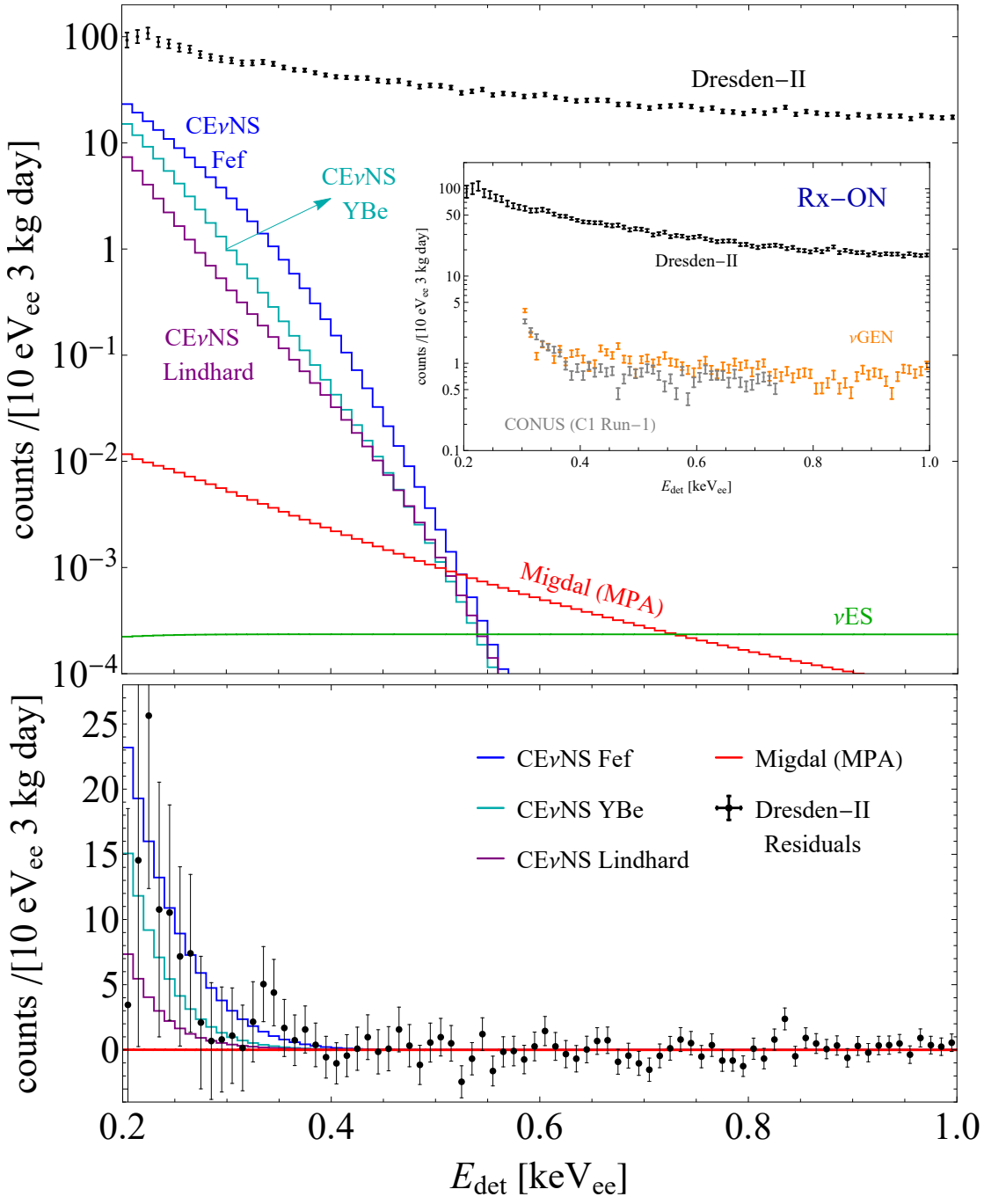

Figure 4.12: Expected number of CEνNS events in the Dresden-II detector obtained using different quenching factors, i.e. Fef (blue line), YBe (cyan line) and Lindhard (purple line). The Migdal contribution corresponds to the red curve, while the neutrino electron scattering contribution is given by the green line. In the top panel, we compare these curves with the Dresden-II reactor ON data, while in the bottom panel, we show the Dresden-II data residuals after background subtraction. The inset shows a comparison of Dresden-II reactor ON (Rx-ON) [226], νGEN [209] and CONUS (C1 Run-1) [207] data, all rescaled to the same units.

and lead to a statistically significant CEνNS observation for $E_{\rm det} \lesssim 0.3\,{\rm keV_{ee}}$. In the same figure, we also show the Migdal contribution using the MPA formalism. It is clear that adding the Migdal contribution to the CEνNS Lindhard prediction is not sufficient to explain the CEνNS Fef or YBe predictions, given that the former is completely negligible with respect to the CEνNS signal. Moreover, we find that the neutrino-electron scattering (νES) [3, 4] exceeds the Migdal rate for $E_{\rm det} \gtrsim 0.7\ {\rm keV_{ee}}$, as shown in the top panel of Fig. 4.12. Overall, both Migdal and νES rates are so small that with the current experimental precision can be overlooked in SM CEνNS searches. However, in some scenarios of physics beyond the SM, like non-standard properties of neutrinos, their contribution could be significantly enhanced and thus they need to be taken into account [3, 227] to derive meaningful limits.

In the inset of Fig. 4.12, for comparison purposes, we show a review of existing data from germanium detectors searching for CEνNS at a reactor site, i.e. Dresden-II [226], νGEN [209] and CONUS (C1 Run-1) [207][5]. Interestingly, despite the fact that CONUS and νGen have reached a much lower background level compared to Dresden-II, they have not detected CEνNS yet. Nevertheless, despite the low background level reached, the Migdal contribution is so small that it could be safely neglected also in experiments like νGEN and CONUS, which show a good agreement with the expected background. Similar conclusions are expected also for silicon detectors like CONNIE [202, 203] that operate in a similar energy range.

To conclude, we have shown that the Migdal contribution is orders-of-magnitude subdominant in the region of interest for reactor CEνNS searches with germanium detectors, independently of the formalism used to model the Migdal effect. Thus, the enhancement of the quenching factor at low energies found in Ref. [226] that enabled the observation of CEνNS at the Dresden-II site requires a different explanation than the standard Migdal effect.

[5] After the realization of our work, CONUS released updated measurements [210] with a lower background and threshold. However, this does not affect the conclusion of our work, and it strengthens the fact that they do not find an excess compatible with that reported in Ref. [226].

5 The NUCLEUS Experiment: Current Challenges and Physics Reach

Opening

The NUCLEUS project aims to measure the CEνNS cross section with high precision to probe the regime of full coherence of the CEνNS interaction. To do so, an extremely sensitive cryogenic detector will be deployed at the Chooz nuclear power plant in France, to exploit the high $\bar{\nu}_e$ flux from the reactor core. During my PhD, I worked at the Technical University of Munich to explore the physics potential of such a detector within the NUCLEUS Collaboration. The goal of this chapter is therefore to assess the main features of the NUCLEUS experimental program, to describe the main physics challenges which might be limiting the observation of CEνNS, and to describe the details needed to perform the sensitivity to electroweak parameters and BSM theories which will be presented in this thesis. Note that in the following studies, no private information will be used, hence the sensitivities presented here are not intended to be the official one from the Collaboration.

5.1 The Very Near Site Facility at Chooz

The NUCLEUS detector [211] will be housed at the so-called very near site (VNS) facility at the Chooz-B nuclear power plant, operated by Electricité de France. The VNS sits between two N4-type PWRs, separated by 160 meters and their respective cores are located approximately 7 meters above the Chooz ground level. Each reactor runs at a nominal power of 4.25 $\mathrm{GW_{th}}$ and is turned off to refuel approximately one month per year. Remarkably, since 2008, the Chooz power plant has already hosted the Double Chooz experiment, which provided very important re-

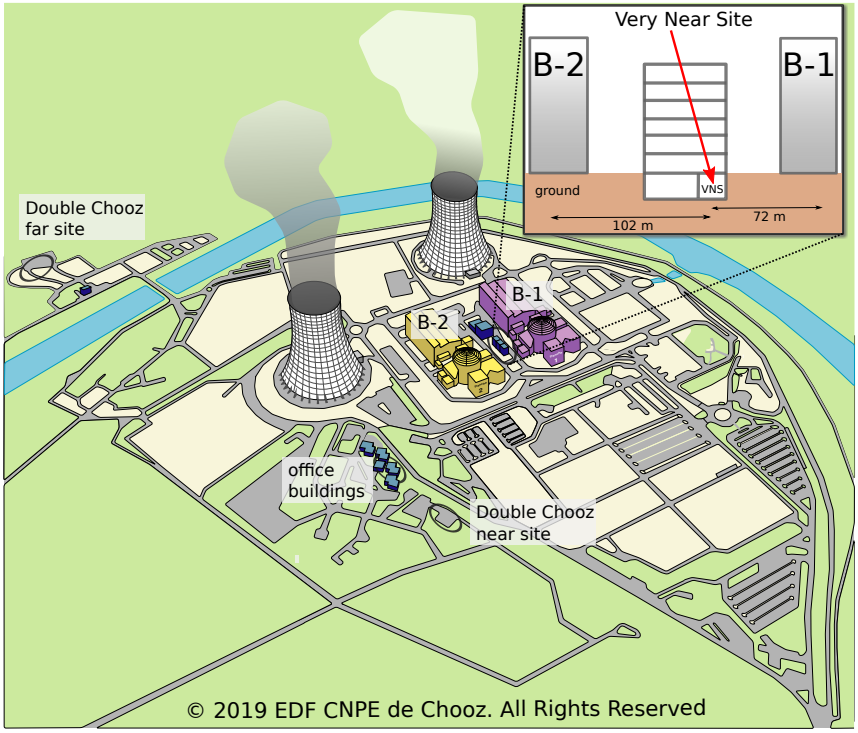

Figure 5.1: Sketch of the Chooz nuclear power plant and of the Very-Near-Site (VNS). The VNS is located 72 and 102 meters away the B1 and B2 reactors. The inset on the top right shows the office building between the reactor cores hosting the VNS. Figure from Ref. [211].

sults for neutrino oscillations [277–279].

The VNS, whose location is schematized in Fig. 5.1, is a 24 m^2 room, situated in the basement of a five-story office building, which allows having approximately three meters of water equivalent shielding. For this reason, special care must be taken when addressing the issue of cosmic ray background in the detector [211] and a cryogenic muon veto has been deployed to strongly mitigate muon-induced background events [280]. On the other hand, since the detector is located about 102 and 72 meters away from the two reactors, the reactor-related backgrounds are completely negligible.

For the NUCLEUS analyses, the CEA model described in Sec. 4.1 will be adopted to compute the expected neutrino flux. Moreover, the configuration is equivalent to considering an average reactor located at a distance $d \simeq 58.8$ m, with a power $3.4\ \mathrm{GW_{th}}$, where a duty cycle of 0.8 is considered. The expected flux obtained is shown in Fig. 5.2 with the $\pm 1\ \sigma$ uncertainty. This parameterization will be also used by the NUCLEUS Collaboration for extracting the physics reach of the experiment, and it gives an integrated neutrino flux of $(1.72 \pm 0.06) \times 10^{13}\ \nu/\mathrm{cm}^2/\mathrm{s}$.

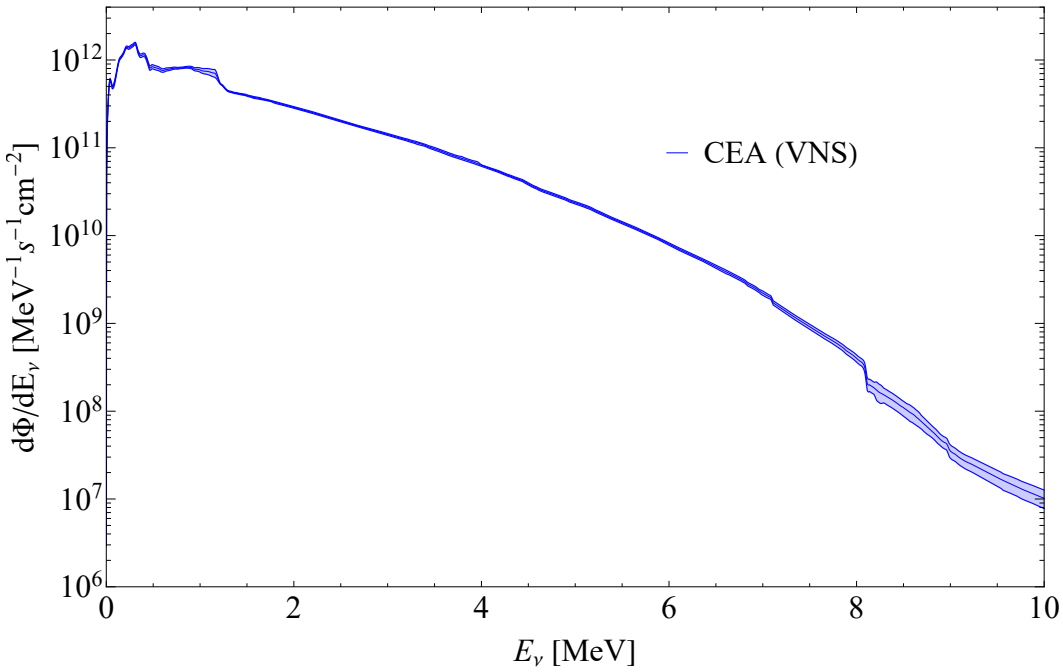

Figure 5.2: Reactor $\bar{\nu}_e$ flux, obtained using the method in [192], expected at the VNS for the NUCLEUS experiment. The shaded bands represent the expected ± 1 σ uncertainty. The integrated neutrino flux is $(1.72 \pm 0.06) \times 10^{13}$ $\nu/\mathrm{cm}^2/\mathrm{s}$.

5.2 The NUCLEUS Experiment

This section will focus on the characteristics which make the NUCLEUS detector very suitable for CEνNS searches. Specifically, the NUCLEUS experiment will take advantage of a cryogenic detector (~ 10 mK) with the goal of reaching an exceptionally low-energy threshold, i.e. about 20 $\mathrm{eV_{nr}}$, thanks to the excellent energy resolution achievable [281]. The NUCLEUS Collaboration planned to use a 10 gram-scale calcium tungstate $(\mathrm{CaWO_4})$ as a target material to detect CEνNS, and a sapphire $(\mathrm{Al_2O_3})$ detector to characterize the particle background. As we will discuss in Sec. 5.3, unexpected backgrounds arising at low energies might modify the strategy of the experiment, but in any case, the first stage of NUCLEUS will be referred to as NUCLEUS-10g which is indicative of the mass scale of the detector. To reach such low-energy thresholds, a transition-edge sensor, commonly referred to as TES, will be deposited on the target material. This sensor exploits the strongly temperature-dependent resistance of the superconducting phase transition to measure the passage of a particle through the active part of the detector. Once the neutrino undergoes a scattering in the absorber material, the nuclear displacement generates phonons, hence a temperature gradient, which are then absorbed by the TES and converted into a difference in the resistance of the sen-

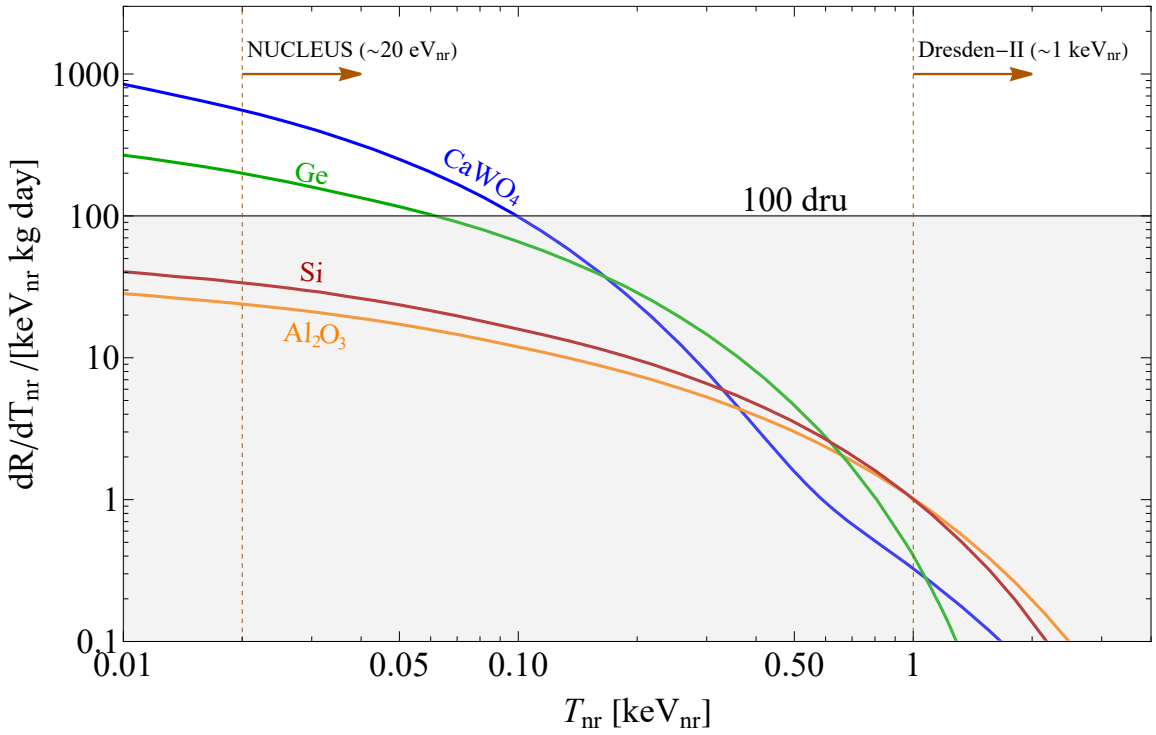

Figure 5.3: Theoretical event rate expected at the VNS for $CaWO_4$, Al_2O_3, Si and Ge. The target background level of 100 dru is also shown. The low threshold of the order of 20 eV_{nr} reachable by NUCLEUS will allow exploring the low-energy regime of CEνNS, compared to other reactor experiments, like Dresden-II where the threshold of about 1 keV_{nr} is shown for comparison.

sor. See Ref. [282] for a detailed description of the working principle of TESs and their application for NUCLEUS. Remarkably, TESs have been widely used by the CRESST collaboration in the context of dark matter searches [283, 284], COSINUS [285, 286] and will also be exploited by RES-NOVA [35, 287]. Relying on this technology, a 0.5 g prototype detector made of Al_2O_3 cubic crystal, achieved an unprecedented ultra-low threshold of $E_{\rm th} = 19.7 \pm 0.9$ eV [212], demonstrating the capability of probing such small recoil energies, to scale up the detector to increase the exposure.

Fig. 5.3 shows the theoretical event rate in units of dru ($keV\ kg\ day$) expected at the VNS for different target materials, i.e. $CaWO_4$, Al_2O_3, while Si and Ge are suitable candidates for the next stages of the NUCLEUS experiment. One of the advantages of probing such low-energetic regime is that the nuclear structure, which is not well-known for a heavy element as tungsten, does not affect the prediction and the experiment is sensitive to the normalization of the weak charge $\mathcal{Q}_W$. This allows for a clean extraction of electroweak parameters and makes the combination with CEνNS data from SNS source very compelling.

5.2.1 Future NUCLEUS Upgrades

A possible way to increase the active mass within the current NUCLEUS setup would be to increase the mass of the calcium tungstate cubes. Specifically, the configuration employing eighteen $(5\ \mathrm{mm})^3$ cubes allows reaching an active mass of 13.5 g. Increasing the size of the cubes to $(1\ \mathrm{cm})^3$ might be feasible and would allow the experiment to reach a total mass of 108 grams. On the other hand, scaling the cryogenic $\mathrm{CaWO_4}$ to higher mass, $\mathcal{O}(\mathrm{kg})$, is experimentally challenging. In fact, the TES readout is based on the use of superconducting quantum interference devices (SQUIDs), which are magnetically coupled to the TES circuit to probe its impedance [282]. Keeping the SQUID in the correct operating conditions is a difficult task that must be planned with care. While a dedicated SQUID for each absorber module is possible for the NUCLEUS-10g [211, 282], up-scaling to the NUCLEUS-1kg array keeping a good energy resolution require TES multiplexing and further readout techniques need to be developed. A possible way to increase the mass of a CEνNS cryogenic detector could rely on the use of different readout technology, which makes Kinetic Inductance Detectors (KIDs) [288, 289] very suitable, as scaling to a higher mass is more feasible. In this context, the BULLKID experiment [290, 291], designed primarily to detect dark matter, can also be used as a CEνNS detector. In fact, an excellent baseline energy resolution of $26 \pm 7\ \mathrm{eV_{nr}}$ [224] and an energy threshold of $160 \pm 16\ \mathrm{eV_{nr}}$ [291] have been demonstrated, making this detector suitable for rare events searches.

5.3 The Low-Energy Excess

The NUCLEUS experiment aims to reach an environmental background level of about 100 dru, as shown in Fig. 5.3 taking advantage of a dedicated shielding and veto systems [212, 280, 282]. This would allow the observation of CEνNS on top of background events during the reactor ON period.

Unfortunately, the quest to push the experimental threshold towards unprecedented low-energies unveiled new unexpected effects limiting the discovery potential to rare events. Indeed, several experiments have observed a sharply rising rate of events below the few hundred electronvolts, whose origin is still mysterious. Such unexpected background is often referred to as the low-energy excess (LEE). Its explanation in terms of new physics in the dark sector has been ruled out, since the intensity and properties of such LEEs are different for each

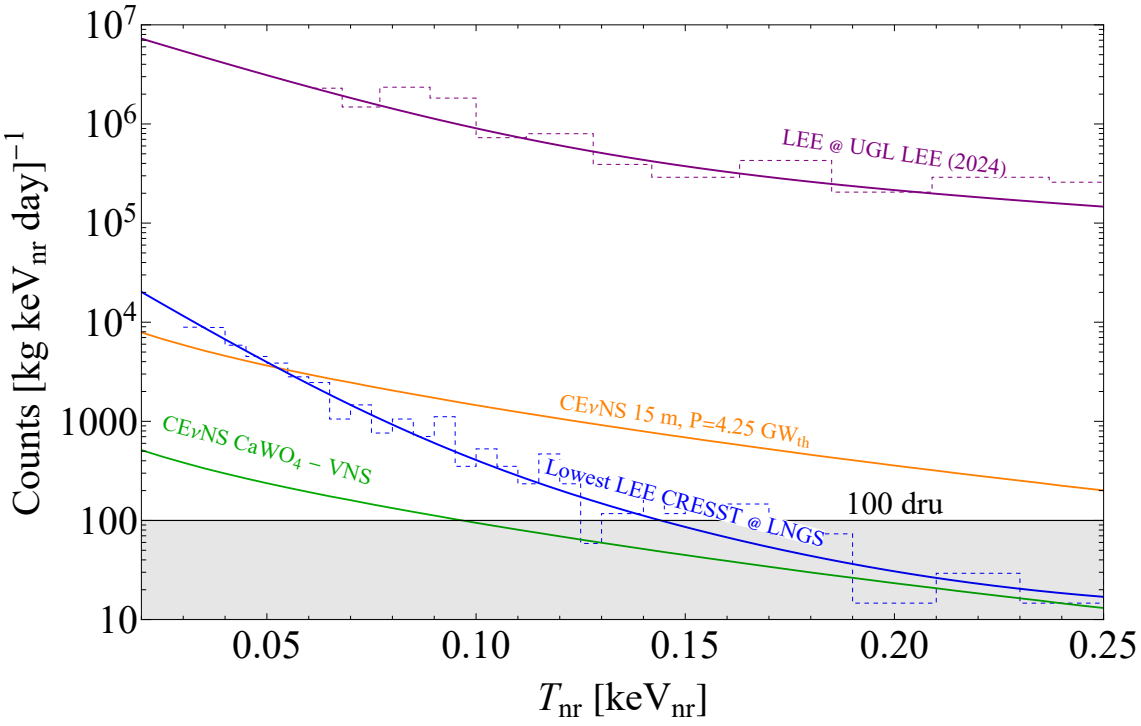

Figure 5.4: LEE from CRESST-III data [284, 299] on $CaWO_4$ scaled for exposure (dru units) and corrected for the energy acceptance, fitted with a double exponential as a function of nuclear recoil energy, compared with the best LEE observed by NUCLEUS [300]. The different excesses are compared with the CEνNS rate on $CaWO_4$ expected at the VNS (green) and at a distance of 15 m (orange), without accounting for the reactor duty cycle factor. See text for more details.

experiment and depend on the data-taking configuration. In particular, this excess manifests itself not only in solid-state cryogenic detectors [292], but also in noble liquids detectors [154, 293] even though it is unlikely that the physical process originating this emission is the same. For this reason, the community is making significant efforts to understand the characteristics of LEE and uncover its origin, both through theoretical studies [294] and by developing innovative data analysis frameworks that can distinguish between particle hits and LEE events in the detector [295]. Remarkably, due to the significant impact of this excess on the dark matter searches [283, 284, 296–298] and neutrino physics experiments [212, 217], a collective effort has been started to share the knowledge about the individual observations within the EXCESS Workshop. This dedicated series of events gathers different experts, providing a detailed summary of the state-of-the-art knowledge on the LEE [292]. The latest measurements from CRESST [301] on a double TES operating in a single active cube, have shown the ability to discriminate between the LEE events occurring in the proximity of the sensor, and the events occurring

inside the target crystal, but a huge amount of excess is still not under control. In addition, the data presented in Ref. [291] above ground from the KID technology do not show LEE. Even though it is not clear if the LEE is hidden in the background level, this might be pointing toward an understanding of the origin of the LEE. Moreover, given that different experimental measurements are pointing to the fact that the LEE is decaying with time [292], predicting the amount of LEE expected for NUCLEUS is not an easy task.

In this thesis, we will adopt two different LEE hypotheses:

- optimistic scenario. We consider a situtation in which the NUCLEUS experiment, with further research and development, will be able to achieve an LEE level comparable to that of CRESST-III [284]. CRESST-III dat currently holds the record for the lowest LEE level in underground experiments conducted at the LNGS with a 23.6 g $\mathrm{CaWO_4}$ detector. Their data release [299] consists of a total exposure of 5.689 $\mathrm{kg \cdot days}$ and have been scaled to dru units, accounting for exposure and energy efficiency;

- realistic scenario. A more realistic hypothesis assumes that the experimental realization at the VNS will reach a LEE level comparable to what was observed at the underground laboratory at TUM (so-called UGL). In this case, the shared events obtained with a 0.75 g $\mathrm{Al_2O_3}$ detector and reported in slide 11 of Ref. [300] will be used as a reference. Although this measurement was taken with an $\mathrm{Al_2O_3}$ detector, it serves as valuable indications of the physics that could be extracted using $\mathrm{CaWO_4}$, even in cases where a high LEE is observed. See Ref. [302] for a discussion of recent NUCLEUS results during the commissioning phase, including a detailed description of the NUCLEUS apparatus.

The LEE can be modelled with a double exponential as a function of energy, i.e.

$$\frac{dR^{\mathrm{LEE}}}{dT_{\mathrm{nr}}} = a + b\, e^{-T_{\mathrm{nr}}[\mathrm{keV_{nr}}]/c} + d\, e^{-T_{\mathrm{nr}}[\mathrm{keV_{nr}}]/e}, \tag{5.1}$$

and the best fit curve is shown in Fig. 5.4 for both the CRESST-III and UGL LEEs. Moreover, they have been extrapolated to 20 $\mathrm{eV_{nr}}$ using the best fit exponential. Fig. 5.4 shows a comparison of the expected LEE from the aforementioned CRESST-III and UGL data with the CEνNS expected rates.
Let's now discuss the different configurations. In case the experimental data will

show a LEE similar to the CRESST-III one, the CEνNS signal at VNS would be indistinguishable from the background unless a detailed characterization of the LEE is achievable during the reactor OFF period. Hence, a precise estimation of the systematic uncertainty associated with the background is needed, otherwise, the normalization of the LEE in the statistical analysis will completely hide the signal. In this thesis, we will refer to another configuration where the detector is hypothetically located 15 meters from one of the two reactors of the Chooz site. In this case, the CEνNS rate would be a factor ~ 15.4 higher. The higher signal would be crucial for a solid statistical analysis, where the systematic uncertainty on the normalization of the CRESST-III LEE would play a marginal role as the signal-to-noise ratio will be greater than 1 for $T_{\rm nr} \gtrsim 50\ \mathrm{eV_{nr}}$. In this case, the LEE would still need to be characterized during the period of reactor OFF, but can be safely subtracted in a likelihood analysis, allowing the normalization on the overall spectra to vary freely in a much wider range without significantly affecting the result. Note, however, that reactor-related background might start to play a role in the proximity of the reactor, hence this study can be considered as too optimistic. On the other hand, the observation of the UGL LEE would always completely hide the CEνNS signal. In the next section, we will describe the statistical method which can be adopted in the presence of an unknown background that cannot be subtracted, and we will assess the physics potential of NUCLEUS-10g in the presence of a LEE at the VNS.

5.4 Physics Reach of NUCLEUS-10g With and Without the LEE

In this sensitivity study, we will consider a detector made solely of 13.5 g of $\mathrm{CaWO_4}$, which is equivalent to considering two arrays of nine $(5\,\mathrm{mm})^3$ cubes each, while the particle background is assumed to be flat and equal to 100 dru. First of all, we will consider the optimistic scenario in which the excess is removed, achievable if its origin is known or with analysis discrimination methods [295], to assess the sensitivity to the CEνNS signal as a function of the exposure time. To do so, we performed a χ^2 analysis to get the significance of the signal compared

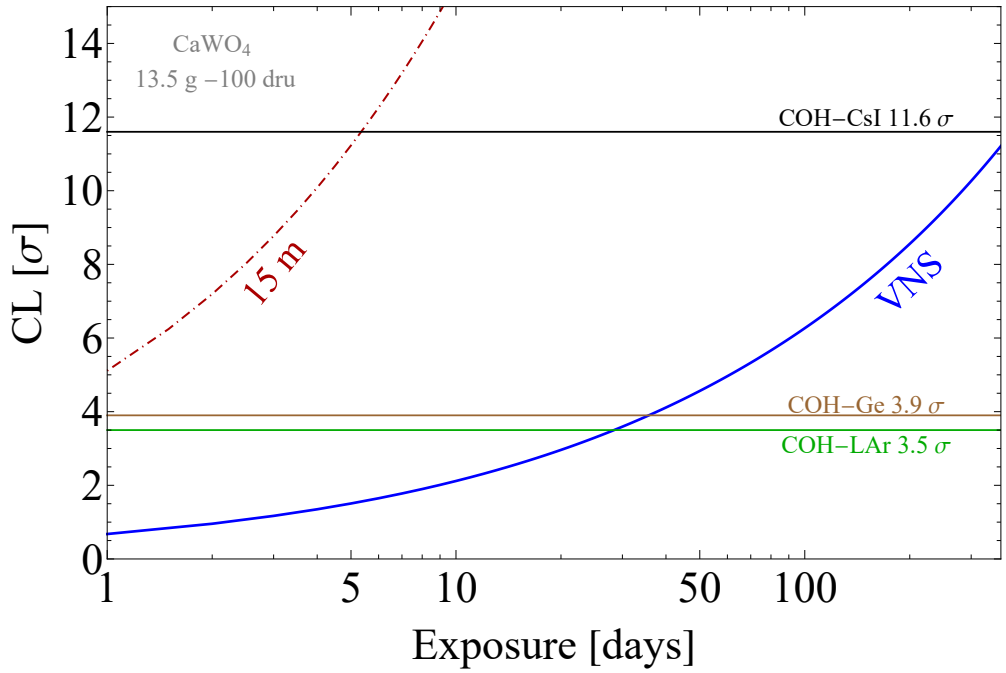

Figure 5.5: Statistical significance of CEνNS observation as a function of live time for 13.5 g of $CaWO_4$ at the VNS, considering a flat background of 100 dru and a threshold of 20 eV_{nr}. The sensitivity has been evaluated using the Asimov dataset. The comparison with the statistical significance of the CEνNS observations from the COHERENT collaboration on CsI [163], Ar [159] and recently on Ge [160] are shown.

to the background-only hypothesis

$$\chi^2_{CaWO_4} = 2\sum_i \left[\beta\, N_i^{bkg} - N_i^{exp} + N_i^{exp} \ln\left(\frac{N_i^{exp}}{\beta\, N_i^{bkg}}\right)\right] + \left(\frac{\beta-1}{\sigma_\beta}\right)^2, \tag{5.2}$$

where N_i^{exp} represents the Asimov dataset with the expected flat background and the expected CEνNS rate in the i-th bin with 5 eV width. The uncertainty in the normalization of the background, N_i^{bkg}, is encoded by the nuisance parameter β, whose uncertainty is fixed to $\sigma_\beta = 10\%$.

Fig. 5.5 shows the statistical significance of the CEνNS signal expected at VNS and at 15 m from the reactor core.

Remarkably, without the LEE, a statistical significance of about 10 σ is achieved at VNS in about 1 year of full-data taking[1], during which about 124 ± 6 CEνNS events are expected, while a great improvement is foreseen if the detector is placed 15 m from the reactor core with about 1913 ± 96 CEνNS events collected during one year of exposure. On the other hand, the extraction of the physical parameters

[1]Note that the results reported here for this configuration are less stringent than that reported in Ref. [211], but small differences are expected due to the different treatment of systematic uncertainties and a different threshold.

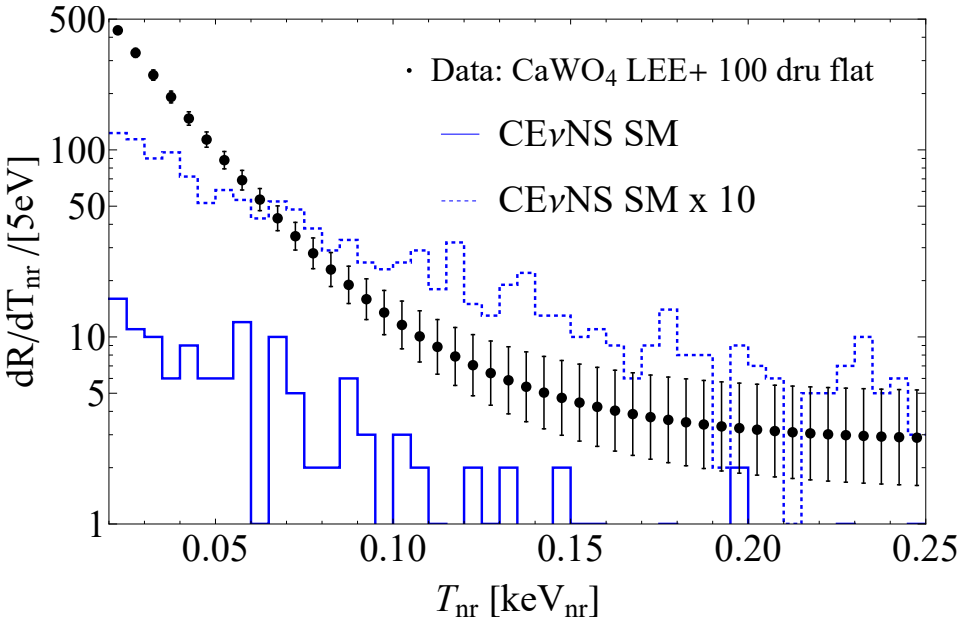

Figure 5.6: Comparison of the experimental outcome in the presence of the $\mathrm{CaWO_4}$ LEE on top of the flat 100 dru background, compared to Poissonian realizations of CEνNS counts in each bin according to the SM (blue) and a model hypothesis where the CEνNS cross section is ten times higher (blue dashed). This comparison serves as an example of the use of the Erickeck *et al.* method [303] to find an upper limit on the CEνNS signal in the presence of an unknown background. The Erickcek *et al.* method is capable of excluding the latter signal as it is too high. See text for more details.

is performed with a χ^2 function of the form

$$\chi^2_{\mathrm{CaWO_4}} = 2\sum_i \left[\alpha\, N_i^{\mathrm{CE\nu NS}} + \beta\, N_i^{\mathrm{bkg}} - N_i^{\mathrm{exp}} + N_i^{\mathrm{exp}} \ln\left(\frac{N_i^{\mathrm{exp}}}{\alpha\, N_i^{\mathrm{CE\nu NS}} + \beta\, N_i^{\mathrm{bkg}}}\right)\right] + \left(\frac{\alpha-1}{\sigma_\alpha}\right)^2 + \left(\frac{\beta-1}{\sigma_\beta}\right)^2, \tag{5.3}$$

where $N_i^{\mathrm{CE\nu NS}}$ is the expected number of events expected in the physics scenario of interest, while the systematic uncertainty on the normalization of the CEνNS signal is set to $\sigma_\alpha = 0.05$.

Let's now discuss the statistical procedure to follow in the presence of the LEE, where the standard χ^2 analysis, i.e. binned likelihood, which foresees a background subtraction cannot be employed. In the context of dark matter searches the maximum gap [304] and the optimum interval method [305], the latter usually referred to as the Yellin's method, have been developed, and they work quite well when the number of events is rather small. While the maximum gap method tends to be too conservative, Yellin's method became computationally very demanding when the event rate from the unknown source becomes big, as it is necessary to

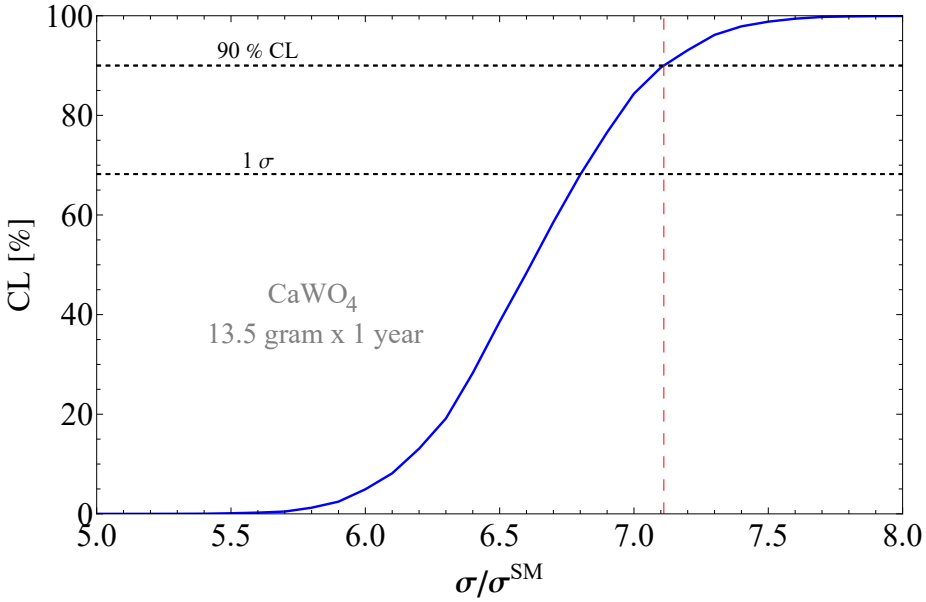

Figure 5.7: Limit on the CEνNS cross section obtained from $\mathrm{CaWO_4}$ mock Asimov data, with an exposure of 13.5 gram in 1 year exposure at the VNS. This limit has been obtained by adopting the Erickcek *et al.* method [303] in the presence of an unknown background.

work with unbinned data. For this reason, in this thesis, we will adopt the method derived by Erickeck *et al.* [303], which enables to work with binned data, and enables to exclude a signal hypothesis with an unknown background. While this method has been considered for Dark Matter limits [306], it has never been used in the context of neutrino scattering.

The first step of the Erickcek *et al.* method is to define the quantity

$$\chi^2_\sigma \equiv \sum_i \frac{(N_i(\sigma) - O_i)^2}{N_i(\sigma)} \, \Theta(N_i(\sigma) - O_i) \, , \tag{5.4}$$

where $\{O_i\}$ is the observed number of events in a certain energy bin, $N_i(\sigma)$ is the expected number of events for a given model hypothesis, and Θ is the Heaviside function such that only bins in which the predicted number is larger than the observed number are included in the sum. The idea of the Erickcek *et al.* method is to find the set of parameters for which a statistical realization of such model is excluded by the data at a given confidence level. To do so, one has to generate mock O_i data from a Poisson distribution from the mean number of counts N_i predicted by the model in each bin. Then the χ^2 value is calculated for each mock $\{O_i\}$, using Eq. 5.4. In order for the result to be statistically reliable, one has to compute many experimental realizations to get the mean value of the χ^2 for the specific set of parameters. We consider $N = 10^4$ statistical realization of the

mock data $\{O_i\}$ for each model hypothesis. To have a quantitative comparison, in Fig. 5.6 we show the experimental outcome in the presence of the $\mathrm{CaWO_4}$ LEE on top of the flat 100 dru background, compared to the Poissonian realizations of CEνNS counts in each bin according to the SM (blue) an model hypothesis where the CEνNS cross section is ten times higher (blue dashed). The Erickcek *et al.* method is capable of excluding the latter signal, as it is too high.

The number of cases in which the value of χ^2 is smaller than the original value of χ^2 is counted, and the confidence level is calculated using CL $=$ counts/(total number of trials). Another advantage of this model is that there is no need to assume any systematic uncertainty on the normalization of the background. The result of the analysis is shown in Fig. 5.7, which presents the upper limit on the CEνNS cross section that can be obtained in the presence of an unknown background. Specifically, the Asimov data of the CRESST-III LEE on top of a flat 100 dru background excludes a CEνNS cross section about seven times bigger than the SM. For comparison, the latest CONUS [210] data are able to exclude cross sections about a factor of two bigger than the SM, while CONNIE can put an upper limit of about a factor 60 [203]. This method will be adopted in Chap. 8 to evaluate the sensitivity of NUCLEUS to light mediators models in the presence of a LEE. This method can also be used to deal with other situations where the background is unknown, as in the case of the single electron problem in the DarkSide-50 experiment [154].

6 Insights Into Electroweak and Nuclear Physics

Opening

This chapter will present the constraints on the weak mixing angle at low energies derived from COHERENT CsI and LAr data, as well as measurements of the nuclear neutron distribution radius of the target material. Additionally, the results on the weak mixing angle from the Dresden-II reactor data will be discussed. Furthermore, the complementarity of CEνNS with other electroweak probes will be demonstrated, aiming to achieve a refined determination of the weak mixing angle at low energies through a global fit. Finally, the sensitivity to these quantities expected in future CEνNS detectors will be presented. Most of the results discussed here are based on Refs. [1, 5, 8].

6.1 Overview on the Weak Mixing Angle and Neutron Radius Measurements

In recent years, CEνNS has proven to be one of the most profitable tools to perform intriguing tests of nuclear physics and electroweak interactions [45, 51, 307–314]. Indeed, it has been shown [45, 307, 308, 310, 311, 315] that CEνNS can be exploited to extract information on the distribution of neutrons inside the nucleus, through the neutron rms radius, R_n. Such a quantity, introduced in Sec. 1.2.2, is of extreme interest in nuclear physics and astrophysics since it provides valuable information on the equation of state (EOS) of neutron-rich matter [316], which is at the basis of the formation, structure, and stability of atomic nuclei [317], whether stars collapse into neutron stars or black holes [318], as well as the understanding of gravitational wave events [319–323].

Despite its importance, R_n is experimentally poorly known, as the nuclear neu-

tron distribution can only be probed through strong or weak interactions. The former is usually model-dependent and influenced by non-perturbative effects [322], while the latter is typically limited by statistical uncertainties. However, the effects of weak neutral-current interactions are embodied in the weak charge of the nucleus and are well understood, making electroweak measurements systematically clean.

This lack of knowledge was behind the construction of the Lead Radius Experiment (PREX) at the Jefferson Laboratory in order to precisely determine the neutron radius of lead by exploiting parity violation electron scattering (PVES) on ^{208}Pb [323, 324]. Notably, they demonstrated the feasibility of measuring the neutron rms radius of ^{208}Pb at the percent level [323], being able to obtain the current most accurate determination of the neutron skin $\Delta R_{\rm np}$, i.e. the difference between R_n and the proton distribution rms radius R_p, of a heavy and neutron-rich nucleus like lead. More recently, the CREX experiment, the twin experiment of PREX that uses calcium, has reported a very precise determination of the neutron radius of ^{48}Ca [325].

On the other hand, COHERENT CsI data provide a compelling tool to probe the neutron nuclear structure of Cs and I. On the other hand, the determination of the cesium neutron radius using hadronic probes has historically been experimentally challenging due to its low melting point and tendency to spontaneously ignite in air. However, recently, a new direct measurement of the cesium neutron skin appeared [326], yielding $0.12 \pm 0.21\,\mathrm{fm}$. This result was obtained using proton-cesium elastic scattering at low momentum transfer at the Cooler Storage Ring (CSRe) at the Heavy Ion Research Facility in Lanzhou.

These achievements strengthen the importance of further exploiting electroweak probes to obtain direct, reliable and precise determinations of the neutron distribution radius. It is worth stressing that CEνNS provides a promising and long-lasting tool, especially as the community is putting a lot of effort into developing the future CEνNS program (see Sec. 4.2).

Here an important point should be highlighted. The extraction of the nuclear distribution from electroweak probes is usually dependent on the value of weak mixing angle at low energies, introduced in Sec. 1.1. This quantity is very sensitive to BSM models [327, 328], such as in the presence of dark Z bosons [2, 227, 314, 328, 329], and the determination of its value represents an important test of the SM. At the moment, the most precise determination of the weak mixing angle available in the low-energy sector comes from another electroweak probe,

the so-called Atomic Parity Violation (APV) experiments, also known as parity non-conservation (PNC) experiments, on cesium atoms [22, 330]. In particular, an APV experiment exploits an atomic transition which can happen only through the weak interaction, as it involves states with the same parity. By isolating such parity-violating transition it is possible to probe the weak mixing angle and the nuclear distributions. In the case of APV on cesium, the transition between 6S→7S states was exploited. The work in Refs. [308, 313], revisited in Ref. [5], demonstrated the complementarity of CEνNS and APV experiments to simultaneously extract information on the weak mixing angle and nuclear physics parameters. This approach was surpassed in Ref. [7] where we showed the complementarity of electroweak probes on Cs and Pb to simultaneously extract information on the Weinberg angle and the nuclear neutron radius. This complementarity, together with a description of the approach used, is briefly summarized in Sec. 6.5, while a more detailed discussion can be found in Ref. [124].

This thesis will discuss in detail the constraints obtained from CEνNS, specifically from COHERENT LAr (Sec. 6.2), COHERENT CsI (Sec. 6.3), Dresden-II (Sec. 6.4) and the expectation from future CEνNS experiments (Sec. 6.6). The accuracy of such determinations will be compared with the aforementioned results from the combined fit.

6.2 COHERENT LAr

This section presents the results on the weak mixing angle and nuclear physics obtained from the analysis of COHERENT LAr data [159]. The details of the data analysis strategy have been described in Sec. 3.3. Since the CEνNS cross section depends on both the weak mixing angle and on the nuclear neutron radius, one can choose to fix one of the two parameters to its standard prediction: $\sin^2\vartheta_W = 0.23863(5)$ for the weak mixing angle, and the reference value adopted in this thesis for the neutron radius of $^{40}\mathrm{Ar}$, based on nuclear shell models, which is $R_n(^{40}\mathrm{Ar}) = 3.55$ fm [41], as also reported in Table 1.1. In this way, by using the chi-square function in Eq. 3.22, one can measure the parameter of interest. After fixing the neutron radius to the chosen theoretical reference value, we can perform a measurement of the weak mixing angle at the experimental energy scale, namely $Q_{\mathrm{COH-LAr}} \simeq 50 - 60$ MeV. The result of the fit is shown in Fig. 6.1 (left panel) which shows the $\Delta\chi^2$ values, i.e. the difference between the χ^2_{min} in this fit and

the χ^2 obtained for a given value of the fitting parameter, as a function of $\sin^2\vartheta_W$. Numerically, the constraints on the weak mixing angle correspond to

$$\sin^2\vartheta_W(\mathrm{COH-Ar}) = 0.29 \pm 0.06(1\sigma), ^{+0.097}_{-0.11}\,(90\%\mathrm{CL}), ^{+0.12}_{-0.13}\,(2\sigma). \tag{6.1}$$

Even though a good agreement within the SM is found, the uncertainty on the extraction of $\sin^2\vartheta_W$ is too big to perform an accurate test of the SM. Similarly, COHERENT LAr data do not allow one to determine the neutron radius of argon-40, but only to set an upper bound, namely

$$R_n(^{40}\mathrm{Ar}) < 4.4(1\sigma), 6.7(2\sigma), 12.3(3\sigma)\ \mathrm{fm}, \tag{6.2}$$

which is shown in the right panel of Fig. 6.1. This limit was derived by imposing the condition $R_p(^{40}\mathrm{Ar}) < R_n(^{40}\mathrm{Ar})$, as nuclear models predict a positive neutron skin for argon [41]. Note that the results reported here are slightly different for both R_n and $\sin^2\vartheta_W$ compared to that in the previous study [51], which was dated before the official data release from the COHERENT Collaboration. In fact the analysis was performed without accounting for the time distribution of the data as well as the shape parameters that are now used in the χ^2 definition (Eq. 3.22).

The COHERENT Collaboration is planning another data release of the CENNS-10 detector with increased statistics [331], and the future COHERENT liquid argon detector, thanks to the increased mass and reduced backgrounds, will be able to significantly improve the extraction of both R_n and $\sin^2\vartheta_W$, as will be discussed in Sec. 6.6.

6.3 COHERENT CsI Constraints

This section will focus on the results obtained with the current CsI data set [163], following the data analysis strategy described in Sec. 3.2. As in the Ar analysis, it is possible to extract the rms neutron distribution radius, in order to obtain information on it. To do so, we fix the weak mixing angle to the SM low-energy value to let the average CsI neutron distribution radius $R_n(\mathrm{CsI})$ free to vary in the fit. Indeed, given the fact that the difference between the rms neutron radii of Cs and I is expected to be small compared to the current precision of experimental data, the choice to fit for an average value appears to be a fair approximation. Clearly, in this case, the contribution due to the neutron form factor to the total systematic

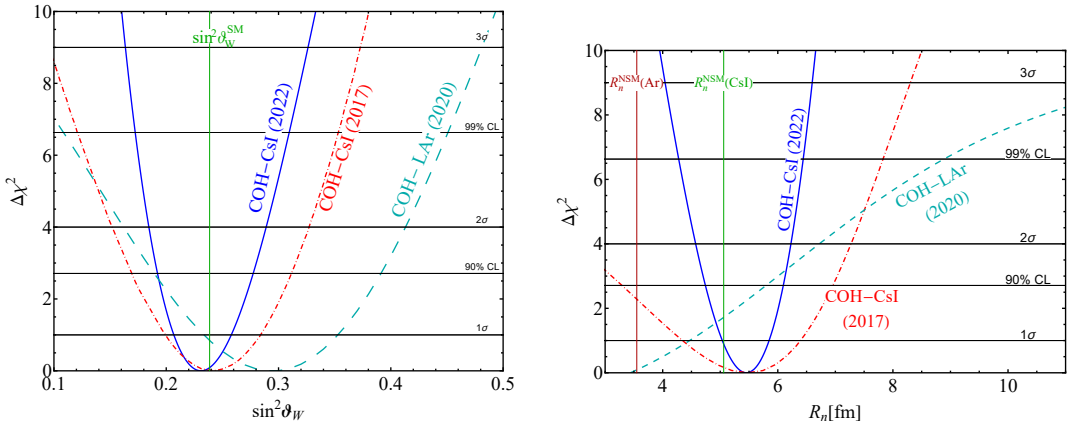

Figure 6.1: Left panel: marginalized $\Delta\chi^2$ curves for the fit of the weak mixing angle from COHERENT LAr data, COH-LAr (2020) and the latest COHERENT CsI data release,COH-CsI (2022). As a comparison, the constraint obtained in Ref. [51] from the first CsI data release [158] is also reported, together with the SM value of the weak mixing angle $\sin^2\vartheta_W^{\rm SM} \simeq 0.23863(5)$. Right panel: marginalized $\Delta\chi^2$ curves for the fit of the average CsI neutron nuclear radius $R_n(\mathrm{CsI})$ from the latest COHERENT CsI data release, compared to the constraints [51] obtained from the first CsI data release [158], and the $\Delta\chi^2$ profile for $R_n(\mathrm{Ar})$ from COHERENT LAr data. The average nuclear neutron radius from Cs and I from NSM [41] ($R_n^{\rm NSM}(\mathrm{CsI}) \simeq 5.06$ fm) and for Ar ($R_n^{\rm NSM}(\mathrm{Ar}) \simeq 3.55$ fm) are also shown.

uncertainty on $N_{ij}^{\rm CE\nu NS}$ is removed in the least-square function evaluation. The result of the fit is shown in the right panel of Fig. 6.1 and at the 1σ, 90% and 2σ CL we found

$$R_n(\mathrm{COH-CsI}) = 5.47 \pm 0.38(1\sigma), ^{+0.63}_{-0.72}\,(90\%\mathrm{CL}), ^{+0.76}_{-0.89}\,(2\sigma)\ \mathrm{fm}, \tag{6.3}$$

which is in agreement, within the uncertainty, with the NSM expected value for $R_n^{\rm NSM}(\mathrm{CsI})$ [41], despite the central value pointing toward larger neutron skin. The figure also reports the constraint of $R_n(\mathrm{CsI})$ obtained from the first CsI data release dated in 2017 [45, 158], showing a great improvement in the extraction of such a quantity given that the original accuracy was of the order of 20%, compared to $\sim 7\%$ obtained in this analysis. In addition, this result is almost 10% more precise than the previous determination of Ref. [308].

To better appreciate the sensitivity of CEνNS to R_n, Fig. 6.2 shows the impact of the nuclear structure to the theoretical prediction of the CEνNS event rates. In particular, we show the COHERENT excess counts, namely the background subtracted COHERENT data, as a function of both the photoelectrons (PE) and the corresponding nuclear recoil energy ($T_{\rm nr}$) and we compare them with the prediction obtained in case of full coherence, i.e., setting all nuclear form factors equal

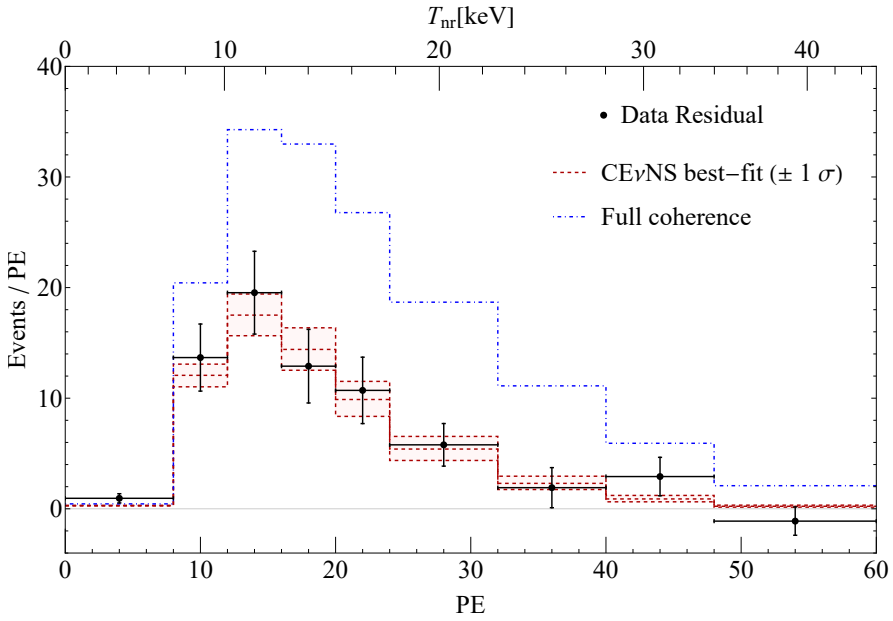

Figure 6.2: Background subtracted COHERENT CEνNS data versus the number of photoelectrons (PE) and the nuclear kinetic recoil energy ($T_{\rm nr}$). The histograms represent the theoretical prediction in the case of full coherence (blue dash-dotted line) and the best fit obtained leaving R_n free to vary (red dashed line). The red shadowed area represents the $\pm 1\sigma$ variation in the R_n value.

to unity, and with the best fit obtained leaving R_n free to vary, as described in this section. We find that COHERENT data shows a $\sim 6\ \sigma$ evidence of the nuclear structure suppression of the full coherence, making it an extremely powerful probe to determine nuclear parameters.

On the other hand, it is possible to rely on the theoretical prediction for the neutron radius, by fixing the average of the neutron Cs and I radius to the values in Tab. 1.1 to perform a fit to extract the weak mixing angle at the energy scale of the experiment, i.e. $Q_{\rm COH-CsI} \simeq 100$ MeV, using the least-square function in Eq. 3.19. The result is shown graphically in Fig. 6.1 (left panel) and at the 1σ, 90% and 2σ CL we found

$$\sin^2\vartheta_{\rm W}({\rm COH-CsI}) = 0.231^{+0.027}_{-0.024}(1\sigma)^{+0.046}_{-0.039}(90\%{\rm CL})^{+0.058}_{-0.047}\ (2\sigma). \tag{6.4}$$

This is in agreement with the expected SM running and the result recently presented in Ref. [314] when fitting the COHERENT CsI data with a different approach. Another derivation performed by the COHERENT Collaboration [163] reports $\sin^2\vartheta_{\rm W}({\rm CsI}) = 0.220^{+0.028}_{-0.026}$, which agrees rather well with our result although some small differences are expected due to the different description of the

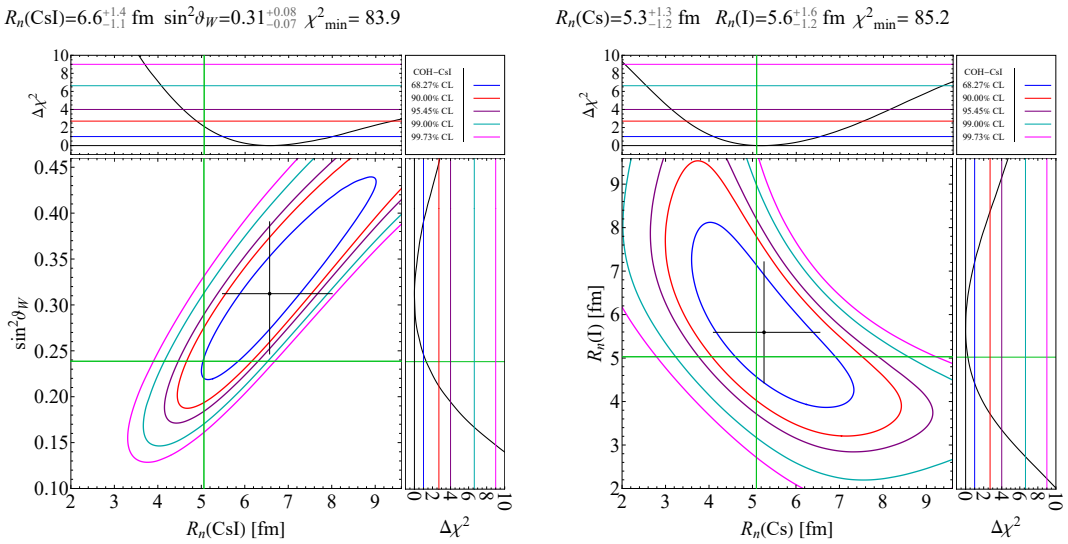

Figure 6.3: Constraints obtained from a simultaneous fit of the COHERENT CsI data on the weak mixing angle and the average rms CsI neutron radius (left) and on the plane of $R_n(^{133}\mathrm{Cs})$ and $R_n(^{127}\mathrm{I})$ (right) together with their marginalizations, at different CLs. The green lines indicate the theoretical low-energy value of the weak mixing angle and the NSM prediction for the corresponding rms neutron distribution radius.

nuclear structure, i.e. different choices of the reference values for the neutron nuclear radii, and a different approach to radiative corrections for neutrino-nucleus scattering. Moreover, we checked the impact of using a different quenching factor, by comparing our nominal results obtained using Refs. [163, 332] and the derivation in Ref. [190]. The latter lower QF decreases the total number of CEνNS events resulting in a larger $\sin^2\vartheta_W$ by about 10%. Also in this case, the extraction of $\sin^2\vartheta_W$ from the latest CsI data release is significantly stronger compared to previous determinations [51].

6.3.1 Simultaneous determination of $\sin^2\vartheta_W$ vs R_n(CsI)

In this section, we extend the analysis presented in Sec. 6.3, by letting both the weak mixing angle and the average CsI neutron radius vary freely in the fit such that the correlation between these two observables is properly taken into account. This allows one to obtain simultaneous information on both parameters, considering their degeneracy, and obtaining thus a more reliable result. The contours at different CLs of the allowed regions in the plane of the weak mixing angle and the average CsI neutron radius are reported in Fig. 6.3, using COHERENT CsI data. At

the 1σ CL we obtain

$$\mathrm{COH-CsI}: \quad \sin^2\vartheta_W = 0.31^{+0.08}_{-0.07}, \quad R_n(\mathrm{CsI}) = 6.6^{+1.4}_{-1.1}\ \mathrm{fm}. \tag{6.5}$$

The fit indicates a preference for values larger than expected for both parameters, with the expected value of the weak mixing angle and the average rms CsI neutron radius lying approximately $\sim 1\sigma$ and $\sim 1.3\sigma$ outside the marginalized allowed region, despite the large uncertainties. Indeed, the dataset is better fitted considering unusually large values for the weak mixing angle and the average rms neutron radius. In fact, it is interesting to note that the minimum χ^2 obtained when both $\sin^2\vartheta_{\mathrm{W}}$ and R_n are free to vary ($\chi^2_{\mathrm{min}} = 83.9$) improves compared to the case in which both parameters are fixed to their theoretical value, which yields $\chi^2_{\mathrm{min}} = 85.2$.

6.3.2 Simultaneous determination of R_n(I) vs R_n(Cs)

In this section, we describe the study of the correlation between $R_n(\mathrm{Cs}) - R_n(\mathrm{I})$ using the latest COHERENT CsI data. In fact, since COHERENT CsI result depends on both $R_n(^{133}\mathrm{Cs})$ and $R_n(^{127}\mathrm{I})$, it is interesting to fix the weak mixing angle to its SM value and to fit for both radii simultaneously. The result of the COHERENT CsI analysis is reported in the right panel of Fig. 6.3, where the contours at different CLs in the plane of $R_n(\mathrm{Cs})$ and $R_n(\mathrm{I})$ are shown. Namely, we get

$$\mathrm{COH-CsI}: \quad R_n(\mathrm{Cs}) = 5.3^{+1.3}_{-1.2}\ \mathrm{fm}, \quad R_n(\mathrm{I}) = 5.6^{+1.6}_{-1.2}\ \mathrm{fm}. \tag{6.6}$$

As expected, COHERENT CsI data alone does not allow for disentangling the two contributions. However, theoretical nuclear models predict the neutron skin of ^{133}Cs to be slightly larger than that of ^{131}I, being the former composed by two more neutrons. We thus redetermine these measurements after imposing the well-motivated constraint $R_n(\mathrm{I}) \leq R_n(\mathrm{Cs})$. In this case, the measurements performed in this section become

$$\mathrm{COH-CsI}\,[R_n(\mathrm{I}) \leq R_n(\mathrm{Cs})]: \quad R_n(\mathrm{Cs}) = 5.5^{+1.1}_{-0.4}\ \mathrm{fm}, \quad R_n(\mathrm{I}) = 5.4^{+0.4}_{-1.0}\ \mathrm{fm}, \tag{6.7}$$

which enables to reduce the uncertainty on the extraction of $R_n(\mathrm{Cs})$. The corresponding constraints on the plane of $R_n(^{133}\mathrm{Cs})$ and $R_n(^{127}\mathrm{I})$ together with their marginalizations, at different CLs can be found in Ref. [5].

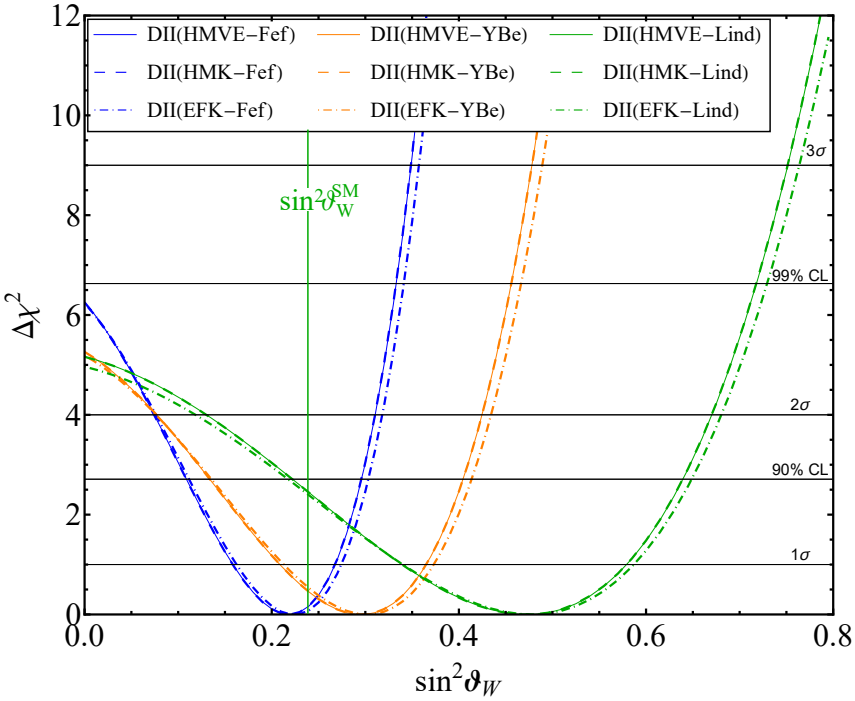

Figure 6.4: Marginal $\Delta\chi^2$'s for $\sin^2\vartheta_W$ obtained from the analysis of the Dresden-II data assuming the HMVE, HMK, or EFK reactor antineutrino flux and the Fef (blue), YBe (green) or Lindhard (green) quenching.

6.4 Dresden-II Results

This section will focus on the analysis of data from Dresden-II, as it is the only reactor experiment for which an official data release has been made public. As pointed out in Sec. 4.1, in the analysis of the Dresden-II data the form factor of both protons and neutrons is practically equal to unity, making the particular choice of the value of $R_n(\mathrm{Ge})$ completely irrelevant. For consistency, however, the analysis reported here employs the nuclear structure parameterization for germanium according to Tab. 1.1, but it is not possible to get relevant information on $R_n(\mathrm{Ge})$ from a fit to the data. Here, we show the result of a fit of the Dresden-II data aimed at the determination of the value of the weak mixing angle using three different antineutrino flux parameterizations, indicated as HMVE, HMK and EFK, and different germanium QF functional forms, i.e. Fef and YBe and Lindhard. The results of these fits are depicted in Fig. 6.4, where it is clear that the impact of the different antineutrino fluxes is minimal. On the contrary, the impact of the different QFs is non-negligible, being the YBe results shifted to larger values of the weak mixing angle and also less precise. On the other hand, the constraints obtained with Lindhard are completely out of scale and $\sim 2\sigma$ in tension with the

SM expectation, due to the fact that the Dresden-II excess cannot be reproduced assuming this QF parameterization and exotic values are found to accommodate the data. Focusing thus only on the HMVE flux, our numerical results are

$$\sin^2\vartheta_{\rm W}(\text{Dresden}-\text{II Fef}) = 0.219^{+0.06}_{-0.05}\,(1\sigma),^{+0.11}_{-0.08}\,(90\%),^{+0.14}_{-0.09}\,(2\sigma), \tag{6.8}$$

$$\sin^2\vartheta_{\rm W}(\text{Dresden}-\text{II YBe}) = 0.286^{+0.08}_{-0.07}\,(1\sigma),^{+0.16}_{-0.11}\,(90\%),^{+0.22}_{-0.13}\,(2\sigma), \tag{6.9}$$

$$\sin^2\vartheta_{\rm W}(\text{Dresden}-\text{II Lind}) = 0.48^{+0.11}_{-0.13}\,(1\sigma),^{+0.17}_{-0.25}\,(90\%),^{+0.20}_{-0.34}\,(2\sigma), \tag{6.10}$$

for the Fef, YBe and Lindhard quenching factors respectively. The fact that the results are dependent on the particular choice of the used QF, makes pivotal the need to clarify the germanium quenching factor puzzle (see Sec. 4.5). For completeness, Tab. 1 of Ref. [3] reports the statistical bounds on $\sin^2\vartheta_W$ obtained from the analysis of the Dresden-II data assuming the HMK and EFK neutrino fluxes and the Fef and YBe QFs.

6.5 Global Electroweak Fit at Low Energies

In this section, we will present the results of a global analysis conducted in Ref. [8] to obtain a refined determination of the mixing angle measurements at low energies, exploiting various electroweak probes, specifically COHERENT CsI, PVES on lead and APV measurements on both cesium and lead.

In fact, the weak mixing angle measurements performed in the previous sections using COHERENT and Dresden-II data are still far from the precision achieved by APV experiments on cesium. The extraction of $\sin^2\vartheta_{\rm W}$ from APV observables depends upon the nuclear distribution of both protons and neutrons. In fact, the APV interaction Hamiltonian ($\mathcal{H}$) for a single electron operator and under the assumption of non-relativistic nucleons is described by [124, 333]

$$\mathcal{H} = \frac{G_F}{2\sqrt{2}} Q_W \rho(r)\gamma_5, \tag{6.11}$$

where Q_W is the weak charge of the nucleus while $\rho(r)$ represents the nucleon density distribution. By looking at Eq. 6.11 it is thus clear that APV depends on the weak mixing angle through the weak charge, but also on the nuclear distributions and therefore their rms radii. In the following, we will make use of APV measurements on both $^{133}\mathrm{Cs}$ [22, 330] and $^{208}\mathrm{Pb}$ [334] atoms. Moreover, the nominal derivation of the weak mixing angle from APV(Cs), as reported in the PDG [19],

uses $\Delta R_{\rm np}(\rm Cs) = 0.13$ fm from antiprotonic atom x-ray data [335], which are known to be affected by considerable model dependencies. For this reason, the combination of APV(Cs) with COHERENT CsI data [5, 308, 313] is particularly interesting to break the degeneracy in the $\sin^2\vartheta_W - R_n(^{133}\rm Cs)$ plane for a data-driven extraction of the weak mixing angle where no assumption on $R_n(^{133}\rm Cs)$ is made. The $R_n - \sin^2\vartheta_W$ correlation is particularly relevant also in PVES. In fact, the experimental observable of a PVES measurement is the parity-violating asymmetry, $A^{\rm PV}$, which isolates the weak contribution to the electron-nucleus interaction. Assuming the so-called plane-wave Born approximation, i.e. neglecting the effect of Coulomb distortion on the electron wavefunction due to the potential generated by the nuclear charge distribution, the asymmetry takes the form [336, 337]

$$A^{\rm PV} = -\frac{G_F Q^2}{4\sqrt{2}\pi\alpha_{\rm EM}}\frac{Q_W}{Z}\frac{F_{\rm wk}(Q^2)}{F_{\rm ch}(Q^2)}, \tag{6.12}$$

where Q^2 is the four-momentum transfer squared. The dependence on the weak mixing angle is encoded in the weak charge Q_W, while $\frac{F_{\rm wk}(Q^2)}{F_{\rm ch}(Q^2)}$ is the ratio of the weak and charge form factors and encodes the effect of the nuclear structure. The PREX Collaboration [323, 324] exploited PVES on ^{208}Pb to obtain a precise measurement of $R_n(^{208}\rm Pb)$, by fixing $\sin^2\vartheta_{\rm W}$ to its SM expectation. Interestingly the PREX Collaboration reported a rather large value for the lead neutron skin with respect to the predictions from nuclear shell models. In our study [1], we demonstrated for the first time that the extracted value of the neutron radius of lead-208 ($^{208}\rm Pb$) depends on the value of the weak mixing angle at low energies. This finding suggests that the aforementioned discrepancy could be alleviated if the weak mixing angle is lower than the SM prediction at the energy scale of the experiment. Similarly to what has been discussed for cesium, the available measurement of APV on ^{208}Pb [338] can be used in combination with PREX to break the degeneracy among the two observables, as shown in Ref. [1].

To summarise, the usage of an extrapolated or imprecise value of the neutron radius of cesium or lead biases the extraction of $\sin^2\vartheta_{\rm W}$ and vice-versa, misinterpreting potential signs of BSM physics. It is thus of pivotal importance to exploit all available inputs on $\Delta R_{\rm np}$ and $\sin^2\vartheta_{\rm W}$ in a combined measurement, in order to take advantage of possible correlations and minimize external assumptions. For this reason, in Ref. [7], we performed a global fit using CEνNS on CsI, APV on Cs and Pb, and PVES from PREX-II. For more details on the PREX-II and APV(Pb) analyses refer to Refs. [1, 124]. The results from the global analysis will be shown

here for consistency, to show the state-of-the-art determination of the weak mixing angle at low energies. The Dresden-II results on $\sin^2\vartheta_{\rm W}$ have not been included in the fit due QF dependence of the results, while Ar constraints are too weak to be statistically relevant. CREX results [325] on ^{48}Ca, on the other hand, refer to a higher energy regime compared to PREX-II, and the use of such a lighter element compared to ^{133}Cs or ^{208}Pb, makes more complex the interpretation of a global fit.

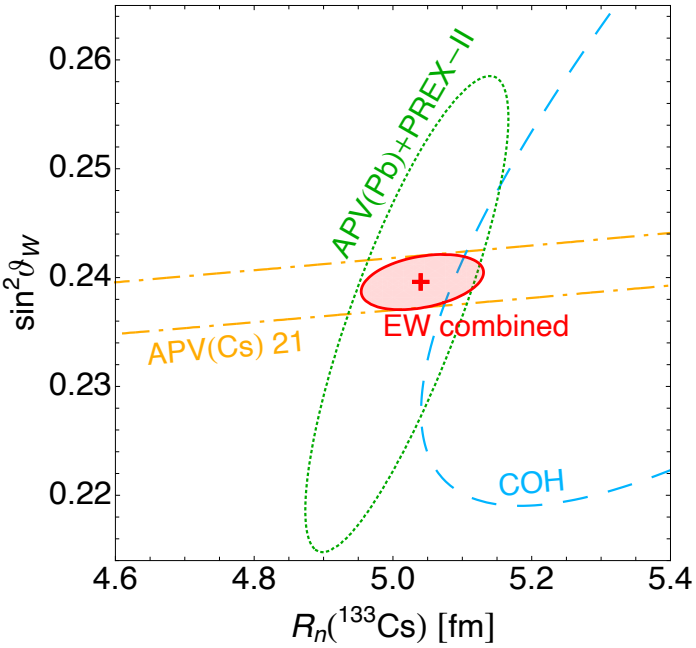

Figure 6.5: Individual and combined contours at 1σ CL of the available electroweak probes. Namely, APV(Cs) (orange dash-dotted line), APV(Pb)+PREX-II already converted into $R_n(\mathrm{Cs})$ (dotted green line), and COH CsI (light-blue dashed line). The red solid contour is the combination of all these EW probes, with the red cross indicating the best-fit values.

It is worth mentioning here that, in order to combine Cs and Pb probes, we relied on a practically model-independent correlation between the cesium and lead neutron skins predicted by a large sample of nuclear shell models, following the method developed in Ref. [328] and briefly summarised in Appendix A of Ref. [7], which allows one to translate a $R_n(\mathrm{Pb})$ determination into a measurement of $R_n(\mathrm{Cs})$. This allows us to obtain PREX+APV(Pb) constraints in the $\sin^2\vartheta_W - R_n(\mathrm{Cs})$ plane from the one obtained in Ref. [1], as shown in Fig. 6.5 at 1σ CL. In the same figure, it is possible to appreciate the good agreement between the different EW probes available nowadays, namely APV(Cs) 21[1], APV(Pb)+PREX-II, and COHERENT CsI. Since these probes show a different $\sin^2\vartheta_{\rm W}$-R_n correlation,

[1]The attribute "21" indicates that we are using the parity-non-conserving amplitude, $E_{\rm PNC}$

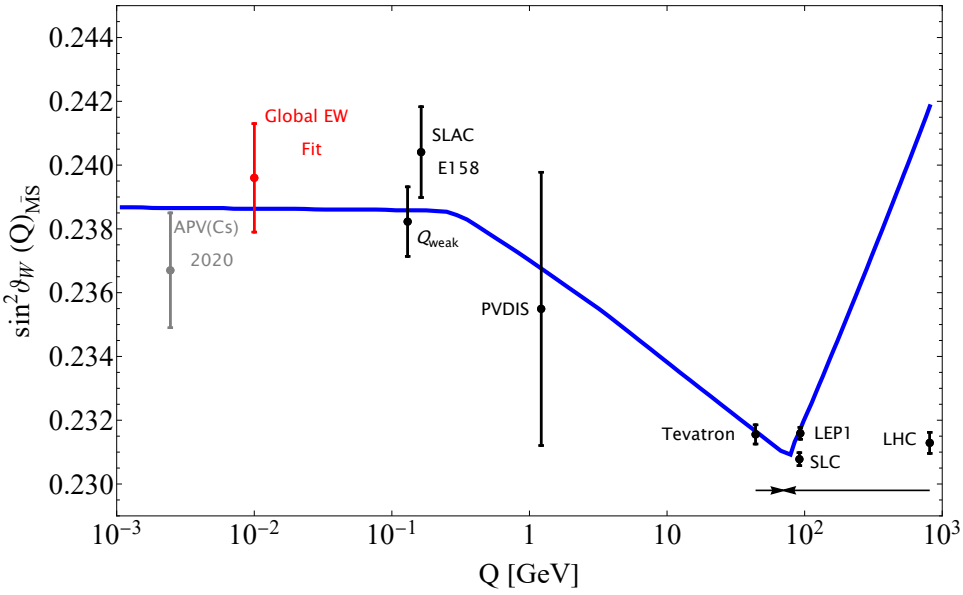

Figure 6.6: Running of the weak mixing angle in the SM (blue line) as a function of the energy scale Q. The black experimental determination represents the status of the art of the measurements at different energy scales [19, 23–26]. The red point shows the determinations from the combined analysis of APV(Cs), APV(Pb), PREX and COHERENT CsI measurements retrieved from our global electroweak fit, which supersedes the nominal APV(Cs) determination depicted in grey [22].

e.g. APV(Cs) is more sensitive to $\sin^2\vartheta_W$ while PREX is more sensitive to the neutron radius, they can be combined together to get a fully EW determination of $\sin^2\vartheta_W$ and $R_n(\mathrm{Cs})$, as shown by the red contour at 1 σ CL in Fig. 6.5. Numerically, they correspond to

$$\mathrm{EW-Combined}: \quad \sin^2\vartheta_W = 0.2396 \pm 0.0017, \quad R_n(\mathrm{Cs}) = 5.04 \pm 0.06 \text{ fm}. \tag{6.13}$$

Our combined analysis reveals that all results consistently point in the same direction to a value of the weak mixing angle compatible with the expected running and should surpass the previous PDG measurement, as shown in Fig. 6.6. Moreover, the marginalization of $R_n(\mathrm{Cs})$ is consistent with the recent measurement from proton-cesium elastic scattering [326] of $R_n(\mathrm{Cs}) = 4.94 \pm 0.21$ fm^2. This refined approach underscores the importance of combining diverse experimental

reported in Ref. [339] for the APV(Cs) calculation, which provides a different result compared to the PDG choice of using E_{PNC} from Ref. [23]. The results obtained with the PDG choice can be found in Ref [7].

[2]The latter radius has been obtained starting from the skin measured in Ref. [326] and using the rms proton radius of cesium $R_{\mathrm{p}}(\mathrm{Cs}) = 4.821(5)\,\mathrm{fm}$ [5, 47, 48] and the neutron radius $\langle r_{\mathrm{n}}^2\rangle \simeq \langle r_{\mathrm{p}}^2\rangle = 0.708\,\mathrm{fm}^2$ [51].

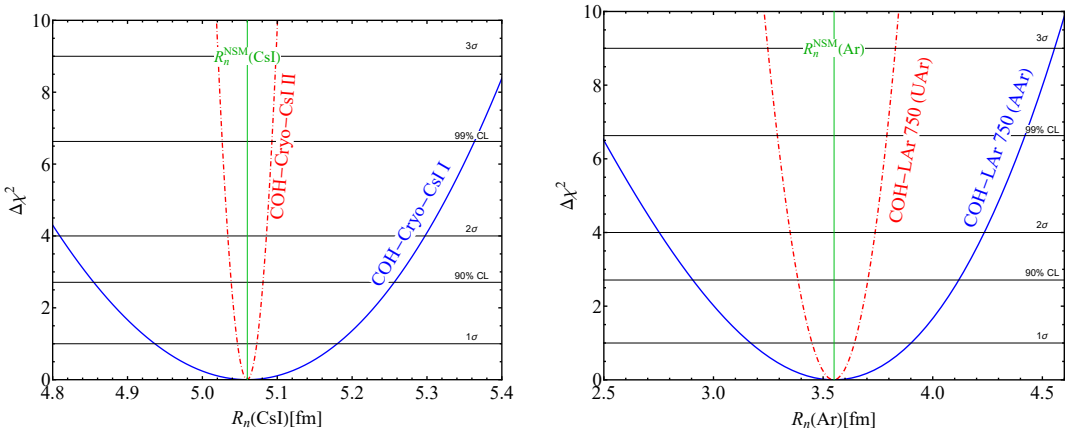

Figure 6.7: Left: sensitivity on the average rms neutron radius of CsI, expected for COH-Cryo-CsI I(II), with 10 (700) kg of active mass, in three SNS-year of data taking. The expected theoretical CsI-average NSM prediction is also shown. Right: sensitivity on the neutron rms radius of Ar evaluated from the COH-LAr-750 kg detector, under the hypothesis of AAr and UAr, compared to the expected value from NSM (green line).

data based on complementary physical effects to enhance our understanding of electroweak and nuclear physics.

6.6 Sensitivity Study for Future CEνNS Experiments

This section presents the sensitivities on $\sin^2\vartheta_W$ and R_n for the future COH-Cryo-CsI and COH-LAr-750 detectors planned by the COHERENT Collaboration, following the experimental details described in Sec. 3.4.1 and 3.4.2 respectively[3]. Additionally, the sensitivity to the weak mixing angle expected from a NUCLEUS-like 13.5 g $CaWO_4$ detector, as discussed in Chap. 5, will also be evaluated. Fig. 6.7 shows the expected sensitivity on the neutron radius of Cs (left panel) and Ar (right panel), achievable within three SNS-years of data taking obtained by fixing the weak mixing angle to its SM value. For the COH-Cryo-CsI science case, both the COH-Cryo-CsI I and the COH-Cryo-CsI II are considered, while the COH-Ar-750 analysis has been conducted assuming both AAr and UAr background hypotheses. We find that COH-Cryo-CsI I will be able to measure the neutron rms CsI radius with a precision of $\sigma(R_n(\text{CsI})) \simeq 0.12\,\text{fm}$ corresponding to a relative accuracy of about 2.4%. For the COH-CryoCsI II scenario we obtain a sensitivity projection for $R_n(\text{CsI})$ that corresponds to $\sigma(R_n(\text{CsI})) = 0.013\,\text{fm}$, meaning that COH-CryoCsI II will be able to reach a per-mille accuracy level, i.e., about 0.3%.

[3]The sensitivities reported here are part of a work in preparation which will update the results in Ref. [5], thanks to an improved description of the COH-Cryo-CsI detectors [187].

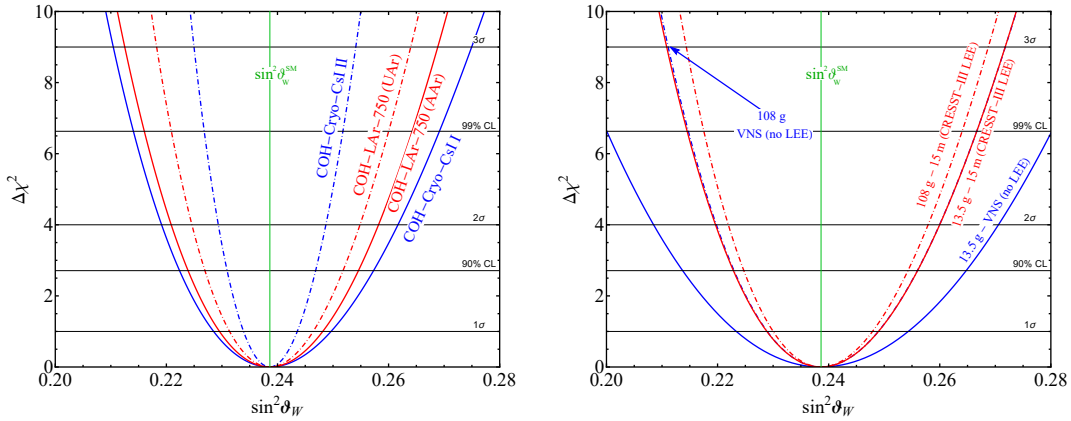

Figure 6.8: Left: expected sensitivity to the weak mixing angle obtained with the COH-Cryo I and II detectors, COH-LAr-750 with AAr and UAr assuming three SNS-years of data taking. Right: the blue lines show the expected sensitivity on the weak mixing angle expected for 13.5 g and 108 g of $\mathrm{CaWO_4}$, located at the VNS and assuming three years of data taking, without the low-energy excess. The sensitivity obtained with the same detectors located 15 m from the reactor core is shown in red under the hypothesis that the LEE is present.

It is worth noticing that, in this regime, the projected uncertainty on the neutron radius will become smaller than the difference between the Cs and I radius, expected to be $\sim 0.06\,\mathrm{fm}$. Thus, it will be of paramount importance to keep into account the different contributions of Cs and I by performing a simultaneous fit on these two quantities, as shown in Sec. 6.3.2, or to account for the correlation between the neutron radii of such nuclei, similarly to the discussion in Sec. 6.5. Moreover, a more accurate description of the nuclear form factors might play a significant role in this regime [42, 340].
Regarding the constraints from the COH-LAr-750 detector, it will be possible to reach a precision on the neutron radius of $^{40}\mathrm{Ar}$ of about $\simeq 0.36$ fm, i.e. about 10%, within three years of data taking in the case of AAr, which is reduced to $\sim 3\%$ in the presence of UAr which would represent the most precise direct measurement on the neutron radius of such element.

Moving to the weak mixing angle, the expected sensitivity is shown in Fig. 6.8 for the COH-Cryo-CsI I and II detectors as well as the COH-LAr-750 sensitivity under different assumptions for the $^{39}\mathrm{Ar}$ background (left panel), while the right panel shows the sensitivities for NUCLEUS-like detectors in different configurations. Specifically, the sensitivity study assumes a $\mathrm{CaWO_4}$ detector located at the VNS considering the LEE to be removed, assuming two different masses: 13.5 g and 108 g. Another configuration considered is the one where the detector is located 15 m away from the reactor core, which allows a signal-to-noise ratio good

enough to perform a likelihood analysis even in the presence of unknown LEE as discussed in Sec. 5.4. For the NUCLEUS analyses, 3 years of exposure have been considered, assuming a reactor duty cycle of 0.8.
Let us now discuss the results of the sensitivities. The determinations with COH-Cryo-CsI will allow one to reach a precision of about 5%, which will improve to $\simeq$2% with COH-Cryo-CsI II. The COH-LAr-750 detector will reach a precision of about 4(3)% with AAr(UAr). The NUCLEUS-like detector will be able to reach a precision of the order of 6% in the 13.5 g (VNS) configuration, which is comparable with the precision of the current CsI detector, which will be improved to about $\simeq 4\%$ in the 108 g (15 m) configuration.
Here an important point should be noticed about the sensitivity on $\sin^2\vartheta_{\mathrm{W}}$ and R_n. While the weak mixing angle impacts the rates approximately as a modification to the normalization of the overall spectrum, the neutron radius modifies its shape. As a result, the normalization of the neutrino flux, which is not precisely known and carries its own uncertainty, is strongly degenerate with any modification of $\sin^2\vartheta_{\mathrm{W}}$. This effect is shown graphically in the left panel of Fig. 6.9, which shows the comparison between the expected SM CEνNS spectrum of COH-Cryo-CsI I in one year of data taking (solid black), compared with the spectra expected with a ± 0.01 shift in the weak mixing angle (blue dashed) and the realization with a neutron radius 0.1 fm larger (green). The effect of the systematic uncertainty in the neutrino flux normalization is simulated via a 10% variation in the overall normalization of the CEνNS spectrum (solid red). It is therefore clear that the extraction of $\sin^2\vartheta_{\mathrm{W}}$ is degenerate with the systematic uncertainty associated with the neutrino flux.

To assess the impact of this effect, the right panel of Fig. 6.9 shows the $1\ \sigma$ precision on the determination on $\sin^2\vartheta_{\mathrm{W}}$, considering only one year of data taking, as a function of the systematic uncertainty on the normalization of the CEνNS signal, $\sigma_{\mathrm{CE}\nu\mathrm{NS}}$, which is dominated by the uncertainty on the neutrino flux. The uncertainties associated with the detector response model and nuclear structure have been neglected to highlight this effect. With few-% systematic uncertainty on the normalization of the CEνNS spectrum, the COH-Cryo-CsI II detector would be able to reach an uncertainty similar to that of APV with one year of data taking. Therefore, as discussed in Sec. 3.4, the $\mathrm{D_2O}$ detector [173] will be fundamental to achieve a precise measurement of the weak mixing angle at COHERENT via a precise measurement of the neutrino flux. Note that it is a common feature also for CEνNS detectors exploiting different nuclei and neutrino sources. Reactor neutri-

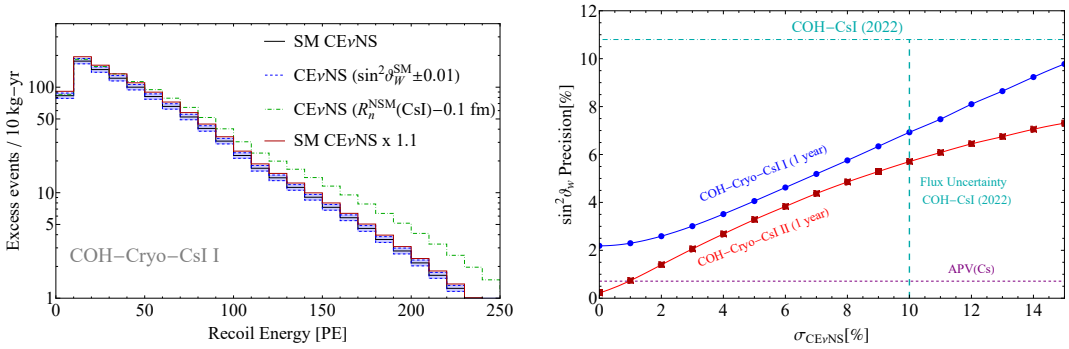

Figure 6.9: Left panel: SM CEνNS excess counts for the COH-Cryo-CsI I detector (solid black), compared with the spectra expected for a ± 0.01 shift in the weak mixing angle (blue dashed), the realization with a neutron radius 0.1 fm larger (green), and a CEνNS rate 10% higher due to the uncertainty on the neutrino flux. Right panel: relative precision on the $\sin^2\vartheta_W$ determination as a function of the systematic uncertainty on the CEνNS signal normalization, $\sigma_{CE\nu NS}$ for the COH-Cryo-CsI I and II detectors, compared with the relative uncertainty obtained by current CsI and APV(Cs) data.

nos are subject to the same degeneracy, which could be overcome with a thorough understanding of the neutrino flux at the nuclear reactor. On the other hand, the extraction of R_n is less sensitive to this effect because the spectral distortions mainly constrain the nuclear radius.

Note that the sensitivity projections on the weak mixing angle for the COH-Cryo-CsI I and LAr750 detectors have been reported also in Ref. [172] by the COHERENT Collaboration. The results presented here for the CsI detector are slightly different because of the updated description of the CsI cryogenic detector [187]. Moreover, the sensitivity to the weak mixing angle depends strongly on the values of R_n used to describe the loss of coherence for increasing recoil energies. The values from the NSM calculations adopted in our work differ from the significantly larger values used in the aforementioned works. See also Refs. [42, 341] for a sensitivity study on future CEνNS detectors.

6.7 Summary of Current and Future Constraints

Given the variety of results presented in the previous sections for both the neutron radius distribution and $\sin^2\vartheta_W$, here we will summarise all these results which will be compared with determinations from other electroweak probes.

Regarding the neutron radius R_n, Fig. 6.10 summarize the previous constraints from CsI crystal detectors [45, 308, 310] as well as the results discussed in this thesis, and shows the other available and currently world-leading measurements

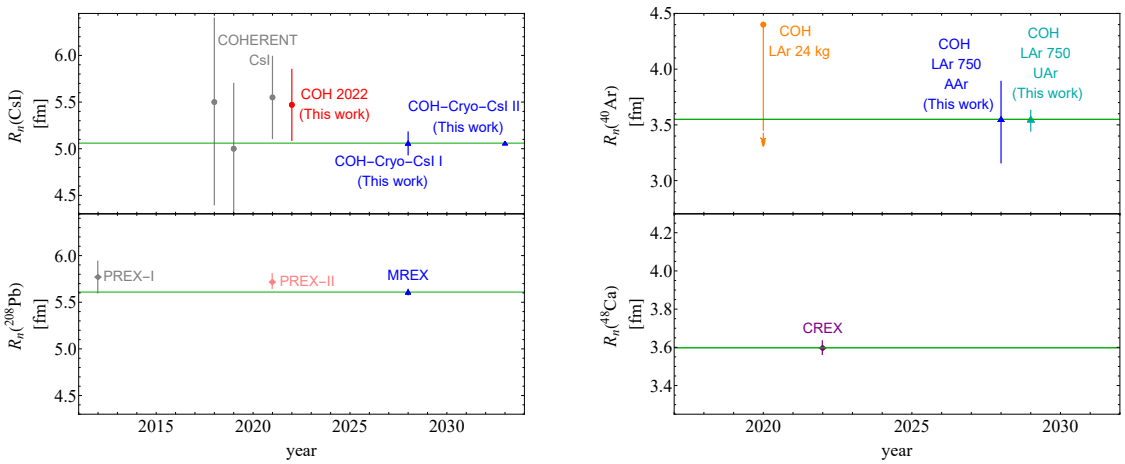

Figure 6.10: Current status and future projections for neutron distribution radii of different nuclei measured via electroweak probes. The upper plots show the current and foreseen measurements of $R_n(\mathrm{Cs})$ from CEνNS with CsI crystal detectors [45, 308, 310] (left) and of $R_n(\mathrm{Ar})$ from liquid Ar detectors [51, 172] (right), compared to the lower plots where the current and foreseen measurements from parity-violating electron scattering are shown, for the case of Pb [323, 324] (left) and Ca [325] (right). Note that the timescale of the experiments foreseen by COHERENT is not the official one from the Collaboration, and it might change in the future.

on heavy and neutron-rich nuclei from PVES, specifically for $^{208}\mathrm{Pb}$ [323, 324] as measured by PREX-I and PREX-II, respectively. It is worth noticing that the MREX experiment [342] also plans to measure the $^{208}\mathrm{Pb}$ neutron radius with an accuracy of about 0.5%. Talking about lighter nuclei, the right panel shows the available measurements on $^{40}\mathrm{Ar}$, discussed in this thesis, and $^{48}\mathrm{Ca}$ [325] from the CREX experiment exploiting again parity-violating electron scattering. The two nuclear systems are expected to have similar dimensions, even if argon is not as rich in neutrons as calcium. It is evident that even if the expected precision of the future COHERENT LAr detector is intriguing, it remains worse than the one achieved by CREX. On the contrary, the CREX experimental program does not foresee any future measurement, so, in principle, with next-to-next generation CEνNS LAr detector, there might be a chance to reach the current PVES precision. It is also worth mentioning that an intriguing $\sim 0.34\%$ precision on the weak radius of $^{12}\mathrm{C}$ and a $\sim 0.3\%$ determination on $\sin^2\vartheta_\mathrm{W}$ may be achieved at the MESA facility in the near future [124, 337]. These results depicted in Fig. 6.11, summarize the current status of the weak mixing angle measurements at low energies. It is worth noting that CEνNS from reactor antineutrinos has already demonstrated the ability to determine the weak mixing angle, although the current uncertainty is still too large to be depicted in Fig. 6.11. Similar uncertainties are expected to be achieved

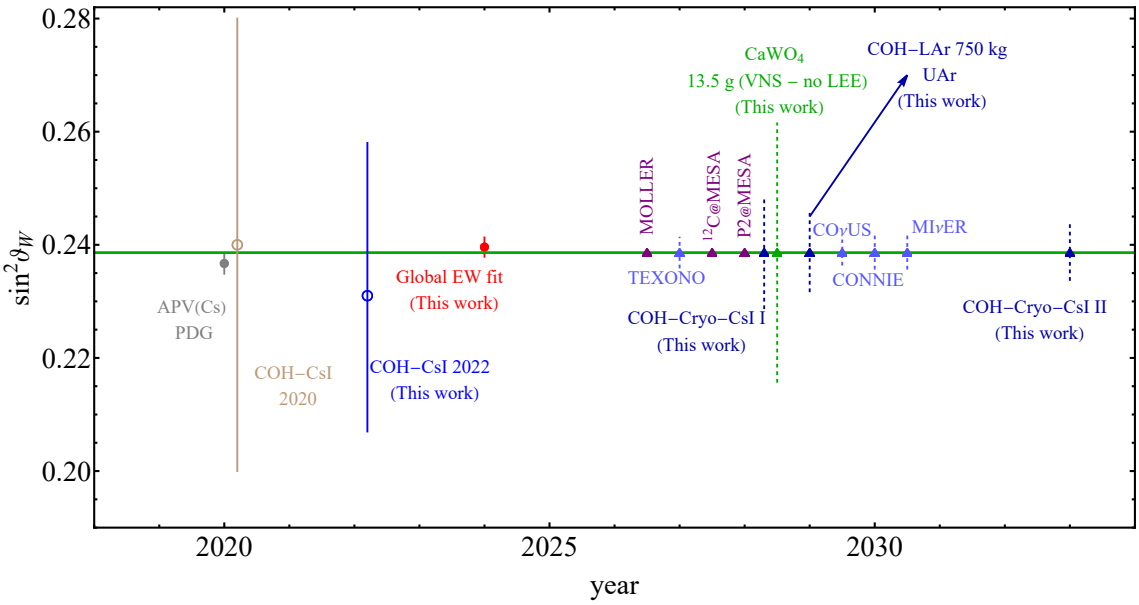

Figure 6.11: Current status and future projections for weak mixing angle measurements below $Q \lesssim 100$ MeV. The grey point shows the measurements from APV on cesium atoms [19]. The brown measurement refers to the COHERENT-only measurement (see Ref. [308]), while the dark blue and red points refer to the updated measurements reported in this work. The projections for future CEνNS experiments (COνUS [343], TEXONO [66], CONNIE [202], and MIνER [217]), shown by the light blue triangles and dashed error bars, are taken from Ref. [344]. The purple triangles are the projections for the future electron scattering experiment MOLLER [345], P2@MESA [342, 346] and ^{12}C@MESA [337]. The projections for the future COH-Cryo-CsI, COH-LAr-750 and the NUCLEUS-like detectors are also shown.

thanks to the detectors planned at the ESS [164] and at the CSNS [166].

7

Constraints on Neutrino Electromagnetic Properties in the Standard Model and Beyond

Opening

This chapter will focus on the so-called neutrino electromagnetic properties, which are of great interest in the neutrino and dark matter communities. Such properties describe possible photon-mediated neutrino interactions and their study represents a powerful tool to test the Standard Model picture, as well as beyond the Standard Model scenarios. In particular, we will present the current status of constraints on the neutrino charge radius, the neutrino magnetic moment and the neutrino electric charge from CEνNS and νES by the analysis of COHERENT, Dresden-II and LUX-ZEPLIN data. Most of the results have been taken from [3, 7] regarding the results from COHERENT and Dresden-II experiments and from Ref. [4] in the case of LUX-ZEPLIN data.

7.1 General Framework For ν Electromagnetic Properties

Since neutrinos do not carry electric charge, they can not couple to photons at tree level. However, such interactions can arise at the quantum level from loop diagrams of a higher order of the perturbative expansion of the interaction. The study of neutrino electromagnetic properties is a very active field of investigation, as they can be used to distinguish between Dirac and Majorana neutrinos [347–352] and also as insights of new physics that might exist beyond the SM. [353–355]. The one-photon neutrino electromagnetic interaction is shown in Fig. 7.1, where the electromagnetic vertex function Λ_μ is introduced and embodies the whole set of

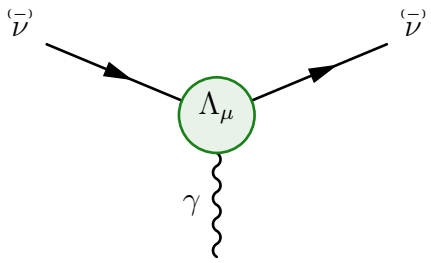

Figure 7.1: Diagram showing the effective one-photon coupling of a neutrino with a photon. The electromagnetic vertex function Λ_μ encompasses all the possible neutrino electromagnetic interactions [76].

neutrino electromagnetic characteristics. Λ_μ is a $\mathcal{N} \times \mathcal{N}$ matrix in spinor space and can be decomposed in terms of linearly independent products of Dirac matrices and the available kinematical variables of the process. The dimension of the matrix depends on the BSM theory considered. In the flavor basis, diagonal terms refer to electromagnetic interactions which left unchanged the neutrino flavor, while off-diagonal terms are responsible for a change in the neutrino flavor. In the most general case consistent with Lorentz and electromagnetic gauge invariance, the vertex function $\Lambda_\mu(q)$ is defined in terms of four form factors [76, 350–352, 356], namely

$$\Lambda_\mu(q) = \mathbb{f}_Q(q^2)\gamma_\mu - \mathbb{f}_M(q^2)i\sigma_{\mu\nu}q^\nu + \mathbb{f}_E(q^2)\sigma_{\mu\nu}q^\nu\gamma_5 + \mathbb{f}_A(q^2)(q^2\gamma_\mu - q_\mu \not{q})\gamma_5,$$

where $\mathbb{f}_Q$, $\mathbb{f}_M$, $\mathbb{f}_E$ and $\mathbb{f}_A$ are the real charge, dipole magnetic and electric, and anapole neutrino form factors. See Refs. [76, 356] for a detailed overview of neutrino electromagnetic properties and their phenomenology. In the following, we will explore the neutrino properties relevant to this thesis and the constraints we obtained by exploiting the CEνNS and νES channels.

7.1.1 Neutrino Magnetic Moment

The neutrino magnetic moment (MM), associated to the magnetic $\mathbb{f}_M$ form factor, is the most investigated neutrino electromagnetic property both theoretically and experimentally. Indeed, its existence is predicted by many BSM theories, especially those that include right-handed neutrinos, see the reviews in Refs. [76, 357]. In the SM, neutrinos are considered massless, and therefore neutrino MMs are vanishing. Nevertheless, from the fact that neutrinos oscillate, we know that

the SM must be extended to give masses to the neutrinos. In the minimal extension of the SM in which neutrinos acquire Dirac masses through the introduction of right-handed neutrinos, the neutrino MM is given by [76, 347–351, 357, 358]

$$\mu_\nu = \frac{3e_0 G_F}{8\sqrt{2}\pi^2} m_\nu \simeq 3.2 \times 10^{-19} \left(\frac{m_\nu}{\text{eV}}\right) \mu_B, \tag{7.1}$$

where μ_B is the Bohr magneton and m_ν is the neutrino mass. Taking into account the current upper limit on the neutrino mass [19], this value is less than $\mu_\nu \sim 10^{-18}\mu_B$, which is too small to be observed experimentally. Nevertheless, given that in some BSM scenarios the neutrino MM is predicted to be larger [357], a positive observation would represent a clear signature of physics beyond the minimally extended SM.

The differential CEνNS cross section that takes into account the contribution of the neutrino magnetic moment is obtained by adding to the SM cross section in Eq. 1.64 the MM component, namely

$$\frac{d\sigma^{\text{MM}}_{\nu_\ell\text{-}\mathcal{N}}}{dT_{\text{nr}}}(E_\nu, T_{\text{nr}}) = \frac{\pi\alpha^2}{m_e^2}\left(\frac{1}{T_{\text{nr}}} - \frac{1}{E_\nu}\right) Z^2 F_p^2(|\vec{q}|^2) \left|\frac{\mu_{\nu_\ell}}{\mu_{\text{B}}}\right|^2, \tag{7.2}$$

where μ_{ν_ℓ} is the effective MM of the flavor neutrino ν_ℓ in elastic scattering [76]. In the case of neutrino-electron scattering, we will adopt the FEA+Z_{eff} scheme discussed in Sec. 1.3, corrected for the presence of the BSM physics under investigation. Specifically, the cross section in Eq. 1.88 in the presence of neutrino magnetic moments receives a contribution equal to

$$\frac{d\sigma^{\text{ES, MM}}_{\nu_\ell\text{-}\mathcal{A}}}{dT_{\text{e}}}(E_\nu, T_{\text{e}}) = Z^{\mathcal{A}}_{\text{eff}}(T_{\text{e}}) \frac{\pi\alpha^2}{m_e^2}\left(\frac{1}{T_{\text{e}}} - \frac{1}{E_\nu}\right) \left|\frac{\mu_{\nu_\ell}}{\mu_{\text{B}}}\right|^2. \tag{7.3}$$

It is important to emphasize that both the CEνNS and νES cross sections are inversely proportional to the recoil energy, which leads to a significant enhancement in the expected event rate. For this reason, a low-threshold experiment has the potential to be highly sensitive to such new physics effects. It is also worth commenting that the cross section obtained in Eq. 7.3 is very similar to that obtained from ab initio calculation event for sub-keVs electron recoil energies [81] for different target materials.

Let us now discuss the constraints obtained with COHERENT CsI, LAr and Dresden-II data, following the discussion in Ref. [3]. Specifically, we studied the bounds on the neutrino MM, namely on $|\mu_{\nu_e}|$ and $|\mu_{\nu_\mu}|$ using the COHERENT data

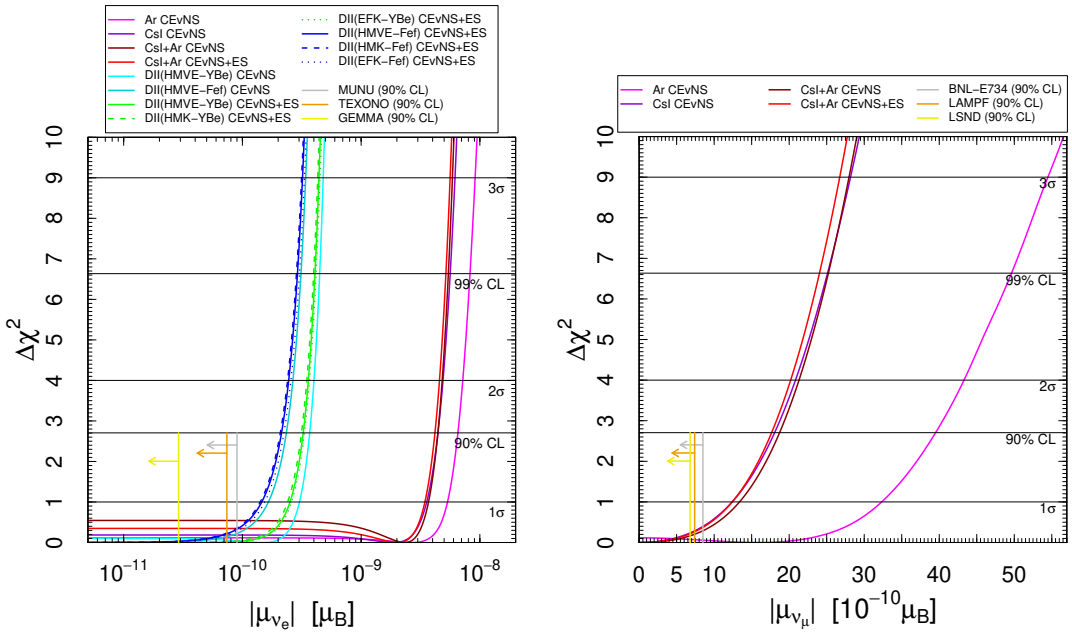

Figure 7.2: Marginal $\Delta\chi^2$'s for $|\mu_{\nu_e}|$ (left panel) and $|\mu_{\nu_\mu}|$ (right panel) obtained from: the separate analyses of the COHERENT Ar (magenta) and CsI (darkviolet) data with CEνNS interactions; the combined analyses of the COHERENT Ar and CsI data with CEνNS interactions only (dark red) and with CEνNS+ES interactions (red); the CEνNS-only analyses of Dresden-II data assuming the HMVE reactor antineutrino flux and the YBe (cyan) or Fef (dark cyan) quenching; the CEνNS+ES analyses of Dresden-II data assuming the HMVE, HMK, or EFK reactor antineutrino flux and the YBe (green) or Fef (blue) quenching. The short vertical gray, orange, and yellow lines show, respectively, the 90% CL upper bounds on: $|\mu_{\nu_e}|$ obtained in the MUNU [359], TEXONO [66], and GEMMA [68] experiments on the left panel; $|\mu_{\nu_\mu}|$ obtained in the BNL-E734 [360], LAMPF [361], and LSND [362] experiments on the right panel.

and $|\mu_{\nu_e}|$ only using the Dresden-II data. The results of our analysis for the neutrino MM are shown in Tab. 7.1 and Tab. 7.2 for COHERENT CsI and Ar data set and for the Dresden-II data[1], respectively. In both cases, we separate the scenarios in which ES is not considered, from those in which the ES contribution is added in the COHERENT CsI and the Dresden-II data set analyses. In the latter case, the different antineutrino fluxes are considered, as well as the YBe and Fef QF parameterizations. The constraints obtained with the Lindhard QF have not been considered since the corresponding CEνNS signal is not able to accommodate experimental data, and exotic results might arise. In fact, the residual excess counts might be explained by new physics, giving results in clear tension with those obtained with the Fef and YBe QFs.

By comparing Tab. 7.1 and Tab. 7.2, it is clear that the Dresden-II data allow us to

[1]The tables reported here do not include all the limits reported in Ref. [3]. Refer to the latter reference for a complete overview.

	1σ	90%	2σ	3σ	1σ	90%	2σ	3σ
	CsI (CEvNS)				**CsI (CEvNS+ES)**			
$\lvert\mu_{\nu_e}\rvert$	< 36	< 44	< 49	< 62	< 32	< 41	< 46	< 58
$\lvert\mu_{\nu_\mu}\rvert$	< 12	< 18	< 21	< 28	< 11	< 17	< 19	< 27
	Ar (CEvNS)							
$\lvert\mu_{\nu_e}\rvert$	< 53	< 65	< 72	< 91				
$\lvert\mu_{\nu_\mu}\rvert$	< 32	< 39	< 43	< 54				
	CsI (CEvNS) + Ar (CEvNS)				**CsI (CEvNS+ES) + Ar (CEvNS)**			
$\lvert\mu_{\nu_e}\rvert$	< 37	< 44	< 48	< 59	< 34	< 42	< 46	< 56
$\lvert\mu_{\nu_\mu}\rvert$	< 13	< 19	< 21	< 28	< 12	< 18	< 20	< 27

Table 7.1: Bounds on the neutrino magnetic moments in units of $10^{-10}\ \mu_B$ obtained from the analysis of the COHERENT CsI and Ar data. We show the results of the analyses of CsI data with CEνNS only interactions and with CEνNS+ES interactions.

significantly reduce the bound on $|\mu_{\nu_e}|$ with respect to COHERENT by more than one order of magnitude. Also in this case, the different antineutrino fluxes result in a negligible difference, while the two QFs produce a much more noticeable effect, with the Fef QF limits being almost a factor of two more precise. Finally, the inclusion of ES results in a marginal improvement of the Dresden-II limits of about 10%. At 90% CL, the bounds on the neutrino MM are

$$|\mu_{\nu_e}| < 2.13 \times 10^{-10}\,\mu_B \quad \text{Dresden} - \text{II}\,(\text{CE}\nu\text{NS} + \text{ES}), \tag{7.4}$$

$$|\mu_{\nu_\mu}| < 18 \times 10^{-10}\,\mu_B \quad \text{CsI}\,(\text{CE}\nu\text{NS} + \text{ES}) + \text{Ar}\,(\text{CE}\nu\text{NS}), \tag{7.5}$$

where for the Dresden-II data the Fef QF and HMVE neutrino flux parameterizations have been considered. These limits can be compared with the bounds obtained in accelerator experiments with $\nu_\mu - e$ scattering (see Table IV of Ref. [76]). The most stringent is the LSND bound $|\mu_{\nu_\mu}| < 6.8 \times 10^{-10}\,\mu_B$ at 90% CL [362], and that on $|\mu_{\nu_e}|$ established in reactor neutrino experiments, namely $|\mu_{\nu_e}| < 2.9 \times 10^{-11}\,\mu_B$ [19, 76].

In Fig. 7.2 we show the marginal $\Delta\chi^2$'s for $|\mu_{\nu_e}|$ and $|\mu_{\nu_\mu}|$ obtained from the COHERENT Ar and CsI data as well as their combination with the CEνNS-only analyses of Dresden-II data assuming the HMVE reactor antineutrino flux and the YBe or Fef QF. We also show the impact of the ES contribution assuming the HMVE, HMK, or EFK reactor antineutrino flux and the YBe or Fef QF. For comparison, we also show the 90% CL upper bounds on $|\mu_{\nu_e}|$ obtained in the MUNU [359], TEXONO [66], and GEMMA [68] experiments; and $|\mu_{\nu_\mu}|$ obtained in the BNL-E734 [360], LAMPF [361], and LSND [362] experiments. Here we compare the results of our analyses with the works in Refs. [227, 245]. Similar bounds to those

	1σ	90%	2σ	3σ	Interaction
Dresden-II (HMVE-Fef)					
$\lvert\mu_{\nu_e}\rvert$	< 1.65	< 2.34	< 2.66	< 3.41	CEvNS
	< 1.45	< 2.13	< 2.45	< 3.20	CEvNS+ES
Dresden-II (HMVE-YBe)					
$\lvert\mu_{\nu_e}\rvert$	< 3.02	< 3.68	< 4.00	< 4.79	CEvNS
	< 2.51	< 3.25	< 3.58	< 4.41	CEvNS+ES

Table 7.2: Bounds on the electron neutrino magnetic moment $|\mu_{\nu_e}|$ in units of 10^{-10} μ_B obtained from the analysis of the Dresden-II data assuming the HMVE reactor antineutrino flux and the Fef or YBe quenching. We show the results obtained with CEνNS only interactions and with CEνNS+ES interactions.

found in this work for $|\mu_{\nu_e}|$ have been obtained, although with some differences among the various data analyses. Namely, in Ref. [245] a bound at 90% CL of $|\mu_{\nu_e}| < 2.7 \times 10^{-10}\,\mu_B$ is found when using a modified QF model and ignoring the ES contribution. Similarly to Ref. [363] only the CEνNS Dresden-II residuals after the subtraction of the background are fitted, with no background uncertainty propagated in the analysis. In Ref. [227], a bound at 90% CL of $|\mu_{\nu_e}| < 2.2 \times 10^{-10}\,\mu_B$ is found when using the Dresden-II data in combination with ES, also using the Fef QF. In this latter case, a very similar treatment of the Dresden-II data with respect to this work has been followed by the authors, with only minimal differences in the antineutrino flux treatment and least-squares function definition.

7.1.2 Neutrino Electric Charge

It is usually believed that neutrinos are neutral particles. However, in some BSM theories, they can acquire a small electric charge (EC), q_ν, usually referred to as millicharge [76]. The strongest bound on the neutrino EC is of the order of $q_\nu \leq 4 \times 10^{-35} e_0$ and comes from the neutrality of the universe [364] inferred from cosmological data. Other strong constraints are obtained by exploiting the observation of astrophysical objects, such as supernovae explosions or the rotation of magnetized stars [76]. It is nevertheless interesting to obtain a direct constraint exploiting the CEνNS and νES scattering processes.

Here, we want to constrain possible BSM effects that could contribute to the neutrino EC. Thus, we consider the general case in which neutrinos can have both diagonal and off-diagonal, also referred to as transition, EC in the flavor basis that can be generated by BSM physics. The differential CEνNS cross section therefore

reads [365]

$$\frac{d\sigma^{\rm EC}_{\nu_\ell\text{-}\mathcal{N}}}{dT_{\rm nr}}(E_\nu, T_{\rm nr}) = \frac{G_{\rm F}^2 m_T}{\pi}\left(1 - \frac{m_T T_{\rm nr}}{2E_\nu^2}\right)\left\{\left[(g_V^p - Q_{\ell\ell})\, Z F_p(|\vec{q}|^2) + g_V^n N F_n(|\vec{q}|^2)\right]^2 + Z^2 F_p^2(|\vec{q}|^2)\sum_{\ell'\neq\ell}|Q_{\ell\ell'}|^2\right\}, \tag{7.6}$$

where the quantity $Q_{\ell\ell'}$

$$Q_{\ell\ell'} = \frac{2\sqrt{2}\pi\alpha}{G_{\rm F} q^2}\, q_{\nu_{\ell\ell'}}, \tag{7.7}$$

defines the strength of the neutrino electric charge, $q_{\ell\ell}$ for diagonal EC and $q_{\ell\ell'}$ for transition EC in units of the elementary charge e_0 . Specifically, the vector neutrino coupling, which already accounts for the radiative corrections as described in Chap. 1, receives another contribution from the diagonal EC $\ell\ell$-term, while the off-diagonal, or flavor changing $\ell\ell'$-terms give an incoherent contribution.

In the case of $\bar{\nu}_\ell$-$\mathcal{N}$ scattering, we have $g_V^{p,n} \to -g_V^{p,n}$ and $q_{\nu_{\ell\ell'}} \to q_{\bar{\nu}_{\ell\ell'}} = -q_{\nu_{\ell\ell'}}$. Therefore, the EC of flavor neutrinos and antineutrinos contribute with the same sign to the shift of the vector coupling in the CEνNS cross section. Regarding neutrino-electron elastic scattering, in the presence of a neutrino EC, the cross section is [365]

$$\left(\frac{d\sigma^{\rm ES,EC}_{\nu_\ell-\mathcal{A}}}{dT_{\rm e}}\right)_{\rm SM+Q} = \left(\frac{d\sigma^{\rm ES,EC}_{\nu_\ell-\mathcal{A}}}{dT_{\rm e}}\right)_{\rm SM+Q_{\ell\ell}} + \sum_{\ell'\neq\ell}\left(\frac{d\sigma^{\rm ES,EC}_{\nu_\ell-\mathcal{A}}}{dT_{\rm e}}\right)_{Q_{\ell\ell'}}, \tag{7.8}$$

where $(d\sigma^{\rm ES,EC}_{\nu_\ell-\mathcal{A}}/dT_{\rm e})_{\rm SM+Q_{\ell\ell}}$ is given by Eq. (1.88) with

$$g_V^{\nu_\ell} \to g_V^{\nu_\ell} + Q_{\ell\ell}, \tag{7.9}$$

and

$$\left(\frac{d\sigma^{\rm ES,EC}_{\nu_\ell-\mathcal{A}}}{dT_{\rm e}}\right)_{Q_{\ell\ell'}} = Z^{\mathcal{A}}_{\rm eff}(T_e)\,\frac{\pi\alpha^2}{m_e T_{\rm e}^2}\left[1 + \left(1 - \frac{T_{\rm e}}{E}\right)^2 - \frac{m_e T_{\rm e}}{E^2}\right]|q_{\nu_{\ell\ell'}}|^2, \tag{7.10}$$

for $\ell' \neq \ell$. There are five electric charges that can be determined with the COHERENT CEνNS data: the two diagonal EC $q_{\nu_{ee}}$ and $q_{\nu_{\mu\mu}}$, and the absolute values of the three transition EC $q_{\nu_{e\mu}} = q^*_{\nu_{\mu e}}$, $q_{\nu_{e\tau}}$, and $q_{\nu_{\mu\tau}}$. Using the Dresden-II data instead, only $q_{\nu_{ee}}$, $|q_{\nu_{e\mu}}|$, $|q_{\nu_{e\tau}}|$ can be tested. Given the extremely low momentum transfer and low-energy thresholds of reactor experiments, the q^2 dependence in

	1σ	90%	2σ	3σ
		CsI (CEvNS)		
$q_{\nu_{ee}}$	$(-1.6, 45.2) \times 10^{-8}$	$(-1.6, 5.8) \times 10^{-7}$	$(-1.9, 6.2) \times 10^{-7}$	$(-2.6, 7.0) \times 10^{-7}$
$q_{\nu_{\mu\mu}}$	$(-8.0, 136.0) \times 10^{-9}$	$(-3.2, 25.2) \times 10^{-8}$	$(-4.4, 30.8) \times 10^{-8}$	$(-8.4, 43.2) \times 10^{-8}$
$\lvert q_{\nu_{e\mu}}\rvert$	$< 1.8 \times 10^{-7}$	$< 2.3 \times 10^{-7}$	$< 2.5 \times 10^{-7}$	$< 2.9 \times 10^{-7}$
$\lvert q_{\nu_{e\tau}}\rvert$	$(1.5, 4.0) \times 10^{-7}$	$< 4.3 \times 10^{-7}$	$< 4.6 \times 10^{-7}$	$< 5.2 \times 10^{-7}$
$\lvert q_{\nu_{\mu\tau}}\rvert$	$< 1.8 \times 10^{-7}$	$< 2.3 \times 10^{-7}$	$< 2.5 \times 10^{-7}$	$< 3.0 \times 10^{-7}$
		CsI (CEvNS+ES)		
$q_{\nu_{ee}}$	$(-3.6, 3.6) \times 10^{-10}$	$(-5.0, 5.0) \times 10^{-10}$	$(-5.6, 5.6) \times 10^{-10}$	$(-7.5, 7.5) \times 10^{-10}$
$q_{\nu_{\mu\mu}}$	$(-1.2, 1.2) \times 10^{-10}$	$(-1.9, 1.9) \times 10^{-10}$	$(-2.2, 2.2) \times 10^{-10}$	$(-3.2, 3.2) \times 10^{-10}$
$\lvert q_{\nu_{e\mu}}\rvert$	$< 1.2 \times 10^{-10}$	$< 1.8 \times 10^{-10}$	$< 2.2 \times 10^{-10}$	$< 3.1 \times 10^{-10}$
$\lvert q_{\nu_{e\tau}}\rvert$	$< 3.5 \times 10^{-10}$	$< 5.0 \times 10^{-10}$	$< 5.6 \times 10^{-10}$	$< 7.5 \times 10^{-10}$
$\lvert q_{\nu_{\mu\tau}}\rvert$	$< 1.2 \times 10^{-10}$	$< 1.9 \times 10^{-10}$	$< 2.2 \times 10^{-10}$	$< 3.2 \times 10^{-10}$
		Ar (CEvNS)		
$q_{\nu_{ee}}$	$(-1.3, 1.7) \times 10^{-7}$	$(-1.7, 3.2) \times 10^{-7}$	$(-2.0, 3.5) \times 10^{-7}$	$(-2.7, 4.4) \times 10^{-7}$
$q_{\nu_{\mu\mu}}$	$(-4.4, 10.0) \times 10^{-8}$	$(-6.8, 21.6) \times 10^{-8}$	$(-8.0, 24.4) \times 10^{-8}$	$(-1.2, 3.0) \times 10^{-7}$
$\lvert q_{\nu_{e\mu}}\rvert$	$< 1.0 \times 10^{-7}$	$< 1.4 \times 10^{-7}$	$< 1.5 \times 10^{-7}$	$< 1.8 \times 10^{-7}$
$\lvert q_{\nu_{e\tau}}\rvert$	$< 2.0 \times 10^{-7}$	$< 2.5 \times 10^{-7}$	$< 2.8 \times 10^{-7}$	$< 3.6 \times 10^{-7}$
$\lvert q_{\nu_{\mu\tau}}\rvert$	$< 1.1 \times 10^{-7}$	$< 1.5 \times 10^{-7}$	$< 1.7 \times 10^{-7}$	$< 2.1 \times 10^{-7}$
		CsI (CEvNS) + Ar (CEvNS)		
$q_{\nu_{ee}}$	$(-12.4, 8.0) \times 10^{-8}$	$(-1.6, 1.7) \times 10^{-7}$	$(-1.7, 2.2) \times 10^{-7}$	$(-2.2, 3.5) \times 10^{-7}$
$q_{\nu_{\mu\mu}}$	$(-1.2, 7.6) \times 10^{-8}$	$(-3.2, 11.2) \times 10^{-8}$	$(-4.0, 12.8) \times 10^{-8}$	$(-6.8, 18.4) \times 10^{-8}$
$\lvert q_{\nu_{e\mu}}\rvert$	$< 1.1 \times 10^{-7}$	$< 1.4 \times 10^{-7}$	$< 1.5 \times 10^{-7}$	$< 1.9 \times 10^{-7}$
$\lvert q_{\nu_{e\tau}}\rvert$	$< 2.4 \times 10^{-7}$	$< 2.9 \times 10^{-7}$	$< 3.1 \times 10^{-7}$	$< 3.7 \times 10^{-7}$
$\lvert q_{\nu_{\mu\tau}}\rvert$	$< 1.2 \times 10^{-7}$	$< 1.5 \times 10^{-7}$	$< 1.6 \times 10^{-7}$	$< 2.0 \times 10^{-7}$
		CsI (CEvNS+ES) + Ar (CEvNS)		
$q_{\nu_{ee}}$	$(-3.5, 3.5) \times 10^{-10}$	$(-5.0, 5.0) \times 10^{-10}$	$(-5.6, 5.6) \times 10^{-10}$	$(-7.5, 7.5) \times 10^{-10}$
$q_{\nu_{\mu\mu}}$	$(-1.2, 1.2) \times 10^{-10}$	$(-1.9, 1.9) \times 10^{-10}$	$(-2.2, 2.2) \times 10^{-10}$	$(-3.2, 3.2) \times 10^{-10}$
$\lvert q_{\nu_{e\mu}}\rvert$	$< 1.2 \times 10^{-10}$	$< 1.8 \times 10^{-10}$	$< 2.2 \times 10^{-10}$	$< 3.1 \times 10^{-10}$
$\lvert q_{\nu_{e\tau}}\rvert$	$< 3.6 \times 10^{-10}$	$< 5.0 \times 10^{-10}$	$< 5.6 \times 10^{-10}$	$< 7.5 \times 10^{-10}$
$\lvert q_{\nu_{\mu\tau}}\rvert$	$< 1.2 \times 10^{-10}$	$< 1.9 \times 10^{-10}$	$< 2.2 \times 10^{-10}$	$< 3.2 \times 10^{-10}$

Table 7.3: Bounds on the neutrino electric charges in units of the elementary charge e_0 obtained from the analysis of the COHERENT CsI and Ar data. We show the results of the analyses of CsI data with CEνNS only interactions and with CEνNS+ES interactions.

the denominator of Eq. 7.7 helps to set more stringent constraints using the data of Dresden-II with respect to COHERENT, as it will be shown in the following. The results of our analyses are shown in Tab. 7.3 and Tab. 7.4 for the COHERENT CsI and Ar data set and for the Dresden-II data, respectively. Focusing on the results shown in Tab. 7.3, the contribution of Ar data is dominant in the combined COHERENT analysis of the neutrino electric charges, although the CsI data set has more statistics. It follows from the enhancement of the neutrino electric charge effect in CEνNS at low q^2, because of the denominator in Eq. 7.7. However, the expected enhancement due to the different CsI and Ar masses, is mitigated by the different sizes of the energy bins: in the Ar experiment the first bin includes energies from the threshold, of about 5 $\mathrm{keV_{nr}}$, to about 36 $\mathrm{keV_{nr}}$, whereas the first CsI energy bin has a much smaller size. Therefore, the enhancement of the EC

	1σ	90%	2σ	3σ
Dresden-II (HMVE-Fef CEvNS)				
$q_{\nu_{ee}}$	$(-1.5, 10.1) \times 10^{-10}$	$(-3.4, 12.5) \times 10^{-10}$	$(-4.3, 13.6) \times 10^{-10}$	$(-6.5, 16.0) \times 10^{-10}$
$\lvert q_{\nu_{e\mu}}\rvert$, $\lvert q_{\nu_{e\tau}}\rvert$	$< 6.0 \times 10^{-10}$	$< 8.2 \times 10^{-10}$	$< 9.1 \times 10^{-10}$	$< 1.1 \times 10^{-9}$
Dresden-II (HMVE-Fef CEvNS+ES)				
$q_{\nu_{ee}}$	$(-7.3, 7.6) \times 10^{-12}$	$(-9.3, 9.5) \times 10^{-12}$	$(-1.0, 1.0) \times 10^{-11}$	$(-1.2, 1.3) \times 10^{-11}$
$\lvert q_{\nu_{e\mu}}\rvert$, $\lvert q_{\nu_{e\tau}}\rvert$	$< 7.4 \times 10^{-12}$	$< 9.4 \times 10^{-12}$	$< 1.0 \times 10^{-11}$	$< 1.3 \times 10^{-11}$
Dresden-II (HMVE-YBe CEvNS)				
$q_{\nu_{ee}}$	$(-4.8, 12.4) \times 10^{-10}$	$(-6.6, 15.2) \times 10^{-10}$	$(-7.5, 16.3) \times 10^{-10}$	$(-9.8, 18.9) \times 10^{-10}$
$\lvert q_{\nu_{e\mu}}\rvert$, $\lvert q_{\nu_{e\tau}}\rvert$	$< 8.9 \times 10^{-10}$	$< 1.1 \times 10^{-9}$	$< 1.2 \times 10^{-9}$	$< 1.4 \times 10^{-9}$
Dresden-II (HMVE-YBe CEvNS+ES)				
$q_{\nu_{ee}}$	$(-1.1, 1.1) \times 10^{-11}$	$(-1.2, 1.3) \times 10^{-11}$	$(-1.3, 1.3) \times 10^{-11}$	$(-1.5, 1.5) \times 10^{-11}$
$\lvert q_{\nu_{e\mu}}\rvert$, $\lvert q_{\nu_{e\tau}}\rvert$	$< 1.1 \times 10^{-11}$	$< 1.2 \times 10^{-11}$	$< 1.3 \times 10^{-11}$	$< 1.5 \times 10^{-11}$

Table 7.4: Bounds on the neutrino electric charges in units of the elementary charge e_0 obtained from the analysis of the Dresden-II data assuming the HMVE reactor antineutrino flux and the Fef or YBe quenching. For the HMVE reactor antineutrino flux we show the results obtained with CEνNS only interactions and with CEνNS+ES interactions.

effect occurs only in the first energy bin of the Ar experiment. Nevertheless, this enhancement is sufficient to achieve a slightly better performance of the Ar data in constraining the neutrino EC in spite of the larger uncertainties. In Tab. 7.3 we also explicitly show the impact of including the ES in the CsI analysis, also when combining it with Ar. Thanks to the presence of the q^2 term in the denominator of Eq. 7.7, a large improvement of more than 2 orders of magnitude with respect to the limits derived ignoring the ES contribution is obtained.

In Tab. 7.4 we show the bounds on the EC found using the Dresden-II data. As for the neutrino MM limits discussed above, the different flux parameterizations cause only negligible differences in the bounds. As already anticipated, the $|q^2|$ corresponding to ES is much smaller than the CEνNS $|q^2|$, resulting in improved sensitivity when the ES contribution is included with respect to CEνNS only. Namely, with CEνNS only there is an improvement with respect to COHERENT CEνNS only of about 2 orders of magnitude, while with CEνNS + ES the improvement is of about 4 orders of magnitude, as is also visible from Fig. 7.3. Specifically, it shows the marginal $\Delta\chi^2$'s for $|q_{\nu_{ee}}|$ obtained from the separate analyses of the COHERENT Ar and CsI data and their combinations, with CEνNS interactions only and with the ES contribution, as well as the CEνNS -only analyses of Dresden-II data assuming the HMVE reactor antineutrino flux and the YBe or Fef QF. Moreover, also the CEνNS + ES analysis of Dresden-II data assuming the HMVE, HMK, or EFK reactor antineutrino flux and the YBe or Fef QF is drawn. We also show the 90% CL upper bounds on $|q_{\nu_{ee}}|$ obtained, respectively, in Ref. [366] from TEXONO data [367], in Ref. [368] from the GEMMA [68] bound on $|\mu_{\nu_e}|$,

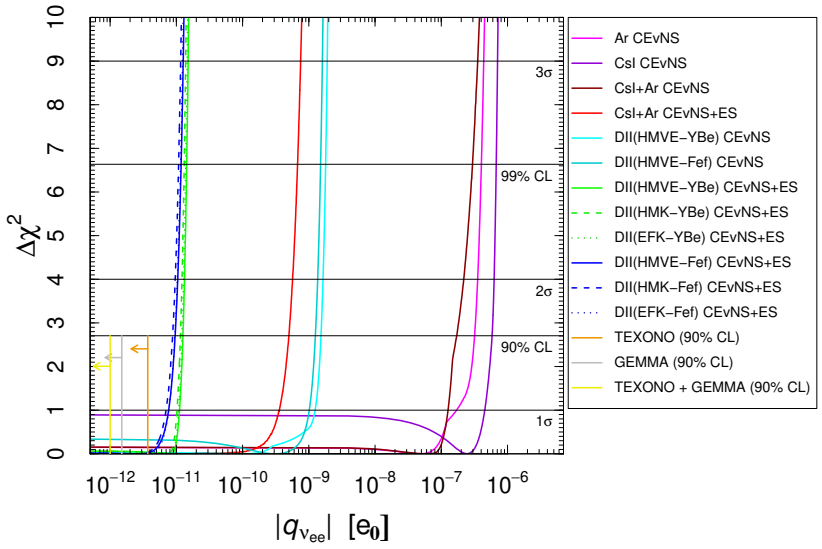

Figure 7.3: Marginal $\Delta\chi^2$'s for $|q_{\nu_{ee}}|$ obtained from: the separate analyses of the COHERENT Ar (magenta) and CsI (darkviolet) data with CEνNS interactions; the combined analyses of the COHERENT Ar and CsI data with CEνNS interactions only (dark red) and with CEνNS +ES interactions (red); the CEνNS -only analyses of Dresden-II data assuming the HMVE reactor antineutrino flux and the YBe (cyan) or Fef (dark cyan) quenching; the CEνNS +ES analyses of Dresden-II data assuming the HMVE, HMK, or EFK reactor antineutrino flux and the YBe (green) or Fef (blue) quenching. The short vertical orange, gray, and yellow lines show the 90% CL upper bounds on $|q_{\nu_{ee}}|$ obtained, respectively, in Ref. [366] from TEXONO data [367], in Ref. [368] from the GEMMA [68] bound on $|\mu_{\nu_e}|$, and in Ref. [369] from the combined analysis of the latter data.

and in Ref. [369] from the combined analysis of the latter data. Intriguingly, the bounds on $|q_{\nu_{ee}}|$ obtained from the combination of COHERENT with the Dresden-II CEνNS + ES data set are much more stringent than the COHERENT ones and the CEνNS only fit, namely at 90% CL and using the Fef quenching factor

$$-9.3 < q_{\nu_{ee}}[10^{-12}\, e_0] < 9.5. \tag{7.11}$$

This limit is competitive with respect to the other aforementioned bounds, that are at the level of $10^{-12}\, e_0$, the best laboratory limit being $|q_{\nu_{ee}}| < 1.0 \times 10^{-12}\, e$ [369]. However, when comparing these limits one has to keep in mind that the results in Ref. [369] have been derived using for the neutrino-electron cross section the MCRRPA theory [79, 80, 370]. The effect from many-body physics becomes relevant for data from Ge detectors at sub-keV sensitivities and allows them to achieve more stringent limits with respect to FEA in particular for the neutrino EC. Thus, the limits reported here can be considered conservative.

Finally, in Fig. 7.4 we show similar marginal $\Delta\chi^2$'s for $|q_{\nu_{\mu\mu}}|$ using COHER-

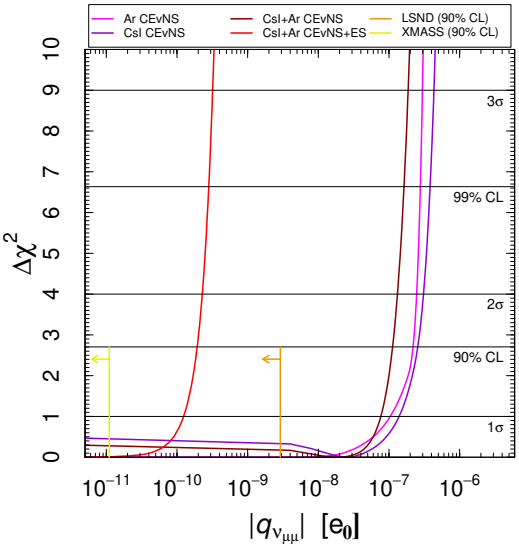

Figure 7.4: Marginal $\Delta\chi^2$'s for $|q_{\nu_{\mu\mu}}|$ obtained from: the separate analyses of the COHERENT Ar (magenta) and CsI (darkviolet) data with CEνNS interactions; the combined analyses of the COHERENT Ar and CsI data with CEνNS interactions only (dark red) and with CEνNS+ES interactions (red). The short vertical orange and yellow lines show the 90% CL upper bounds on $|q_{\nu_{\mu\mu}}|$ obtained, respectively, in Ref. [371] from the LSND [362] bound and in the XMASS-I experiment [372] from solar neutrino ES.

ENT data only. Here we also show the 90% CL upper bounds on $|q_{\nu_{\mu\mu}}|$ obtained, respectively, in Ref. [371] from the LSND [362] bound on $|q_{\nu_\mu}|$ and in the XMASS-I experiment [372] from solar neutrino νES[2]. Also in this case, the inclusion of the ES contribution significantly improves the bounds obtained for COHERENT, superseding the existing bounds from LSND. For a dedicated discussion on the off-diagonal constraints, as well as their $\Delta\chi^2$ profiles which are numerically reported in Tab. 7.4, see Ref. [3]. A detailed discussion of other bounds from dark matter experiment can be found Sec. 7.2.

7.1.3 Neutrino Charge Radius

From the previous discussions, it is now clear that even if neutrinos are neutral particles and cannot couple directly with photons, electromagnetic interactions are encoded in the electromagnetic vertex function defined in Eq. 7.1. Among them, there is a neutrino electromagnetic property which is predicted to be non-zero within the SM. It is the neutrino charge radius, introduced in Sec. 1.2.3, which is

[2]Also in the case of the XMASS-I limit, the electron-neutrino cross section is derived using an ab-initio multi-configuration relativistic random phase approximation [372] that allows them to set more stringent limits.

related to the charge form factor, $\mathbb{f}_Q(q^2)$, whose SM contribution can be related to that of the analpole moment $\mathbb{f}_A$ (see Ref. [76] for a theoretical discussion). In the following we will only focus on $\mathbb{f}_Q(q^2)$, which carries non-trivial information about the neutrino electric properties, even if the neutrino electric charge is null. In fact, a neutral particle can be characterized by a superposition of two different charge distributions of opposite signs described by a charge form factor which is non-zero only for momentum transfers different from zero, $q^2 \neq 0$ [76]. Expanding the form factor in a series of powers of q^2 we get

$$\mathbb{f}_Q(q^2) = \mathbb{f}_Q(0) + q^2 \frac{d\mathbb{f}_Q(q^2)}{dq^2}\bigg|_{q^2=0} + \dots . \tag{7.12}$$

In the "Breit frame", the charge form factor depends only on $|\vec{q}|$ and it can be interpreted as the Fourier transform of a spherically symmetric charge distribution, $\rho(r)$, so that [76]

$$\mathbb{f}_Q(q^2) = \int \rho(r) e^{-i\vec{q}\cdot\vec{r}} d^3r = \int \rho(r) \frac{\sin(qr)}{qr} d^3r \,. \tag{7.13}$$

From this interpretation, it is easy to understand that the first term in the expansion in Eq. 7.12, $\mathbb{f}_Q(0)$, has to be zero, since neutrinos are neutral, while the second term is identified as the neutrino charge radius, i.e. the radius of the electric charge distribution. By deriving the expression in Eq. 7.13 with respect to q^2 and taking the limit for $q^2 \to 0$, we obtain

$$\lim_{q^2\to 0} \frac{d\mathbb{f}_Q(q^2)}{dq^2} = \int \rho(r) \frac{r^2}{6} d^3r = \frac{\langle r^2 \rangle}{6} \,, \tag{7.14}$$

where $\langle r^2 \rangle$ is the neutrino charge radius which is defined as

$$\langle r^2 \rangle \equiv 6 \frac{d\mathbb{f}_Q(q^2)}{dq^2}\bigg|_{q^2=0} . \tag{7.15}$$

Let us note that $\langle r^2 \rangle$ has no defined sign because $\rho(r)$ is not a positively defined quantity.

Practically, the charge radius of a neutrino is generated by a loop insertion into the ν_ℓ line, where W boson(s) and charged lepton(s) ℓ can enter, as shown by the $WW\ell$ loop (left diagram) and the $\ell\ell W$ loop (right diagram) in Fig. 7.5. The contribution arising from these diagrams can be calculated and, according to Refs. [373–375], the NCR corresponds to a physical observable, being finite and gauge invari-

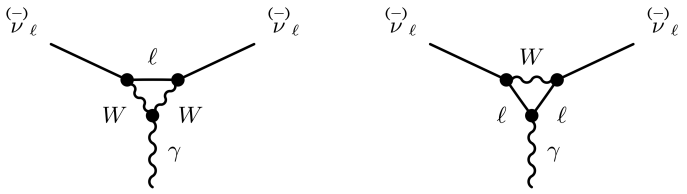

Figure 7.5: Diagrams describing the neutrino charge radius contributions to the photon-neutrino vertices.

ant. Recalling Eq. 1.65, the SM calculation for the NCR gives

$$\langle r^2_{\nu_\ell} \rangle_{\rm SM} = -\frac{G_F}{2\sqrt{2}\pi^2}\left[3 - 2\ln\left(\frac{m_\ell^2}{M_W^2}\right)\right], \tag{7.16}$$

where we can now recognise that the two terms appearing in the sum arise from the two diagrams mentioned above. Specifically, one constant term arises from the $WW\ell$ loop diagram, where the photon interacts with the W boson, and another is generated by the photon's interaction with the lepton ℓ. The latter generates an electroweak logarithm, which is divergent in the UV range, that is regularized at the lepton mass, m_ℓ, thus introducing a dependence of the NCR from the lepton flavor [60, 375]. As anticipated in Chap. 1, the neutrino charge radius has an impact on the scattering of neutrinos with charged particles through radiative corrections. In the case of CEνNS, it contributes only to the neutrino-proton coupling, and not to the neutron one, as visible in Eqs. 1.56 and 1.59. There, the NCR contribution modifies the proton coupling according to

$$g_V^p(\nu_\ell) \to \tilde{g}_V^p - \frac{\sqrt{2}\pi\alpha}{3G_F}\langle r^2_{\nu_\ell}\rangle^{\rm eff}, \tag{7.17}$$

where $\tilde{g}_V^p \simeq 0.0184$ is the neutrino-proton coupling without the contribution of the SM NCR, and we are already taking into account the effect of the NCR momentum-dependent radiative correction defined in Eqs. 1.69 and 1.72. In the case of $\bar{\nu}_\ell$-$\mathcal{N}$ scattering, it is sufficient to operate the substitutions: $g_V^{p,n} \to -g_V^{p,n}$ and $\langle r^2{}_{\nu_\ell}\rangle \to \langle r^2{}_{\bar{\nu}_\ell}\rangle = -\langle r^2{}_{\nu_\ell}\rangle$. Therefore, the NCR of neutrinos and antineutrinos contribute with the same sign to the shift of the weak mixing angle in the CEνNS cross-section.

Despite the fact that a measurement of the NCR would represent a fundamental test of the SM, the available data are still insufficient to provide a first determination. So far, only constraints have been placed on its value [3, 19, 67, 314, 376]. One has to keep in mind that when considering BSM effects that affect the NCR, it

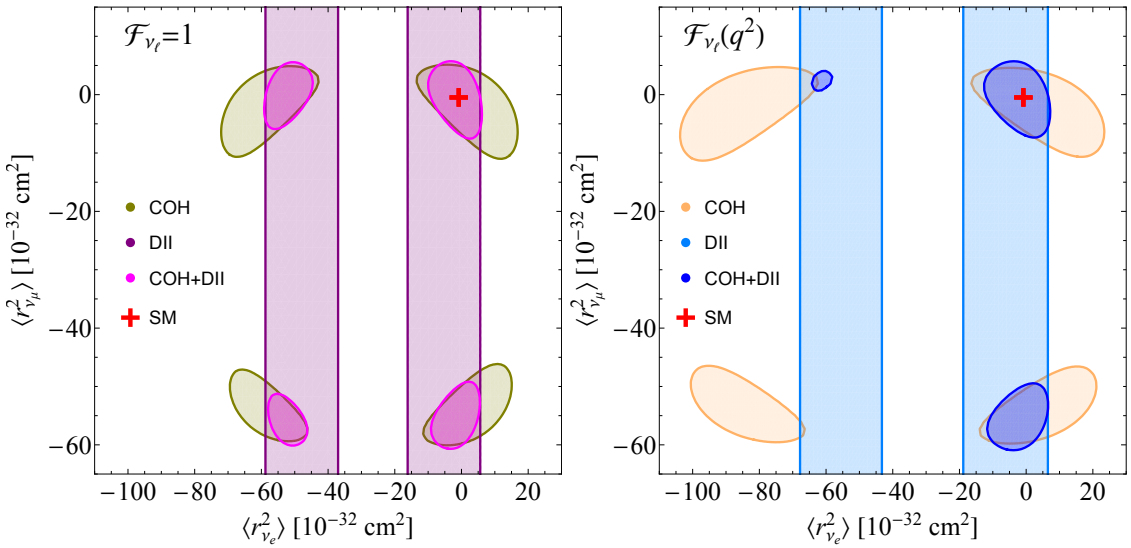

Figure 7.6: Allowed regions at 90% CL from the analysis of the latest COHERENT CsI and Ar data (COH), Dresden-II (DII) and their combination (COH+DII) in the $\langle r^2_{\nu_e}\rangle$ vs $\langle r^2_{\nu_\mu}\rangle$ plane in case of momentum-independent (left) and -dependent (right) neutrino charge radii correction. The red cross indicates the SM values in Eqs. 1.66 and 1.67.

is also possible to have so-called off-diagonal flavor-changing contributions, similar to those described for the neutrino electric charge, which are often referred to as transition charge radii. In Ref. [3] we computed limits on transition charge radii using available CEνNS data.
Nevertheless, in the following, we will focus only on diagonal NCRs to probe the values of the NCR in the SM. However, it is also likely that BSM physics generates off-diagonal neutrino charge radii that are much smaller than the diagonal ones and that can thus be neglected in a first approximation.

This section, based on the results in Ref. [6], will present the results of the analysis of the diagonal neutrino charge radii, $\langle r^2_{\nu_e}\rangle$ and $\langle r^2_{\nu_\mu}\rangle$, obtained using the latest COHERENT cesium iodide and argon dataset, both alone and in combination with the germanium NCC-1701 data from the Dresden-II nuclear reactor power plant[3]. To do so, we account for the energy-dependence of the radiative correction associated with the NCR by making use of the form factor $\mathcal{F}_{\nu_\ell}$ definition in Eq. 1.71 and shown in Fig. 1.8. Here we assume that possible BSM contributions affect only the value of the neutrino charge radius defined at zero-momentum transfer and the momentum dependence of the NCR radiative correction is the same as in the

[3]For simplicity, in this study we model the antineutrino spectra from the Dresden-II reactor considering only the HMVE parametrization, and use the Fef quenching factor.

SM. Therefore, the neutrino-proton coupling defined in Eq. 7.17 is modified by

$$g_V^p(\nu_\ell, T_{\rm nr}) \to \tilde{g}_V^p - \frac{\sqrt{2}\pi\alpha}{3G_F}\langle r^2_{\nu_\ell}\rangle \mathcal{F}_{\nu_\ell}(T_{\rm nr})\,, \tag{7.18}$$

where $\langle r^2_{\nu_\ell}\rangle$ is the physical value of the neutrino charge radius at zero-momentum transfer that we aim to measure through the data.

In particular, we focus on the comparison between the neutrino charge radii

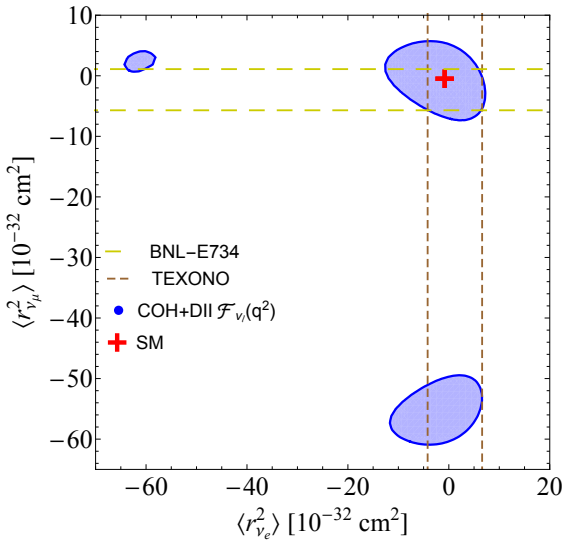

Figure 7.7: Allowed contours at 90% CL from the combined analysis of COHERENT and Dresden-II data in the $\langle r^2_{\nu_e}\rangle$ vs $\langle r^2_{\nu_\mu}\rangle$ plane (allowing only for diagonal NCR contributions). The red cross indicates the SM value of the neutrino charge radii as reported in Eqs. 1.66 and 1.67. We compare the results with the current best limits on $\langle r^2_{\nu_\mu}\rangle$ from BNL-E734 [376] (gold) and $\langle r^2_{\nu_e}\rangle$ from TEXONO [67] (brown).

results obtained from CEνNS data that are present in literature (see e.g. our previous work Ref. [3] for a strict comparison, but also Ref. [314]), which are obtained considering the NCR correction without any momentum dependence (i.e. $\mathcal{F}_{\nu_\ell} \equiv 1$), with our reanalysis in which we include the impact of a momentum-dependent form factor (i.e. $\mathcal{F}_{\nu_\ell}(T_{\rm nr})$). In the latter case, we are attempting to extract the physical value of the NCR at zero momentum transfer, whereas, neglecting the momentum dependence, one is measuring only an average effective neutrino charge radius relative to the typical momentum transfer of the experiment. The results from the analysis of COHERENT CsI, Ar and Dresden-II Ge data are shown in Fig. 7.6 at 90% CL, where the left plot shows the $\mathcal{F}_{\nu_\ell} = 1$ limit, while in the right plot a momentum-dependent charge radius form factor $\mathcal{F}_{\nu_\ell}(T_{\rm nr})$ has been used. Since reactors provide only a flux of electron antineutrinos, the analysis of the Dresden-II data results in two degenerate vertical bands, in cor-

respondence of the SM $\langle r^2_{\nu_e} \rangle$ value and for a large negative one, which produces a degenerate value of the CEνNS cross-section as defined in Eq. 1.64. Instead, the COHERENT CsI and Ar data analyses produce 4 closed contours, since they are also sensitive to the muonic flavor. These allowed regions correspond to the SM values of the electron and muon neutrino charge radii and to large negative charge radius values which produce a degenerate cross-section.

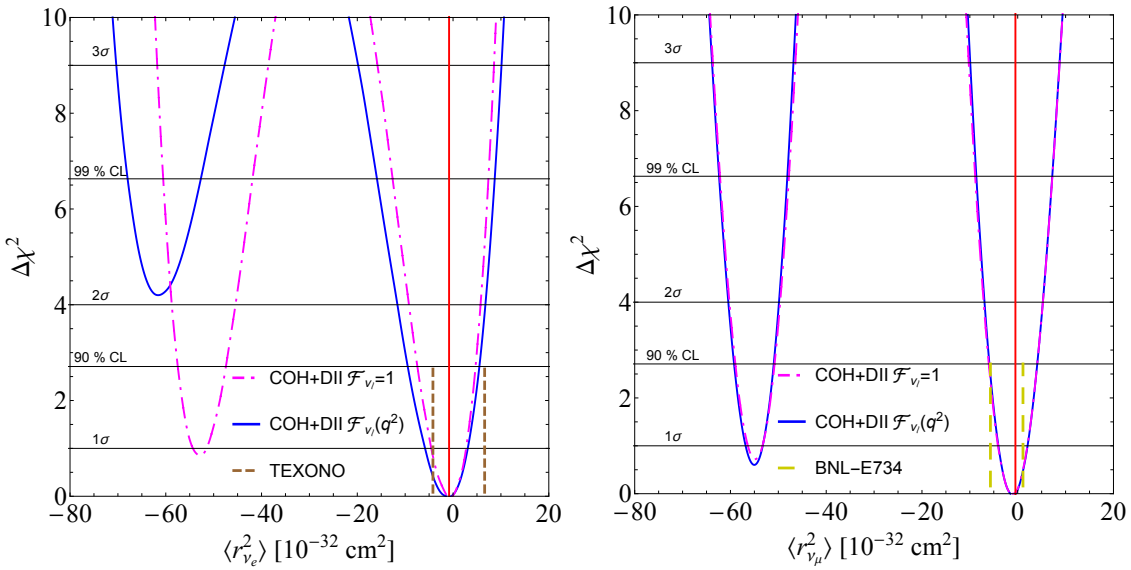

Figure 7.8: Marginal $\Delta\chi^2$'s for $\langle r^2_{\nu_e} \rangle$ (left) and $\langle r^2_{\nu_\mu} \rangle$ (right) obtained from the analysis of the COHERENT (CsI and Ar) data in combination with Dresden-II considering $\mathcal{F}_{\nu_\ell} = 1$ (dot-dashed magenta) and $\mathcal{F}_{\nu_\ell}(T_{\rm nr})$ (solid blue). The red line near the origin indicates the SM predictions. The short vertical dashed lines show the lower and upper 90% bounds on $\langle r^2_{\nu_e} \rangle$ obtained in the TEXONO [67] (left) experiment and on $\langle r^2_{\nu_\mu} \rangle$ obtained in the BNL-E734 [376] (right) experiment.

By comparing the two figures in Fig. 7.6 we observe that the effect of the NCR form factor leads, as expected, to a small shift of the Dresden-II bands, while the closed contours allowed by the COHERENT CsI and Ar data are more significantly affected. This can be understood considering that COHERENT and Dresden-II data refer to different momentum transfer regimes. Namely, the Dresden-II data come from a reactor experiment, which is operated at a much lower energy. Moreover, all of the obtained contours are slightly enlarged by the introduction of the form factor.

The main impact of accounting for the NCR form factor is that, by combining different measurements, it is possible to significantly reduce the allowed regions in the parameter space. Indeed, the different momentum transfer regimes relative to the various data, produce a reduced overlap between the allowed regions for non-

Process	Collaboration	Limit [10^{-32} cm^2]	CL	Ref.
Reactor $\bar{\nu}_e$-e	Krasnoyarsk	$\lvert\langle r^2_{\nu_e}\rangle\rvert < 7.3$	90%	[377]
	TEXONO	$-4.2 < \langle r^2_{\nu_e}\rangle < 6.6$	90%	[67]
Accelerator ν_e-e	LAMPF	$-7.12 < \langle r^2_{\nu_e}\rangle < 10.88$	90%	[361]
	LSND	$-5.94 < \langle r^2_{\nu_e}\rangle < 8.28$	90%	[362]
Accelerator ν_μ-e and $\bar{\nu}_\mu$-e	BNL-E734	$-5.7 < \langle r^2_{\nu_\mu}\rangle < 1.1$	90%	[360]
	CHARM-II	$\lvert\langle r^2_{\nu_\mu}\rangle\rvert < 1.2$	90%	[378]
CEνNS	CsI+LAr+DII	$-9.5 < \langle r^2_{\nu_e}\rangle < 5.5$	90%	[7]
CEνNS	CsI+LAr+DII	$-5.9 < \langle r^2_{\nu_\mu}\rangle\rvert < 4.1$	90%	[7]

Table 7.5: Experimental limits for the neutrino charge radii obtained from the combined analysis of COHERENT CsI, LAr and Dresden II (assuming the Fef quenching factor) [7] discussed in this thesis compared with existing bounds. Note that the results from TEXONO [67], LAMPF [361], LSND [362], BNL-E734 [360], CHARM-II [378] have been corrected by a factor of two due to a different convention [379].

SM values of $\langle r^2_{\nu_e}\rangle$, as shown in Fig. 7.7, where the current best limits from BNL-E734 [376] on $\langle r^2_{\nu_\mu}\rangle$ and TEXONO [67] on $\langle r^2_{\nu_e}\rangle$ are also shown. Interestingly, the SM predicted values for the neutrino charge radii fall within the allowed regions from all the experimental data.

Finally, in Fig. 7.8, we show the marginal $\Delta\chi^2$'s for $\langle r^2_{\nu_e}\rangle$ (left) and $\langle r^2_{\nu_\mu}\rangle$ (right) obtained from the combined COHERENT and Dresden-II data in the two NCR form factor regimes. As expected, recalling Eq. 1.71 and the NCR dependence on the recoil energy described in Fig. 1.8, the momentum dependence impacts primarily the constraints only for the electron flavor, leaving the results for the muon flavor practically unchanged. In particular, the presence of the NCR form factor decreases the significance of the allowed $\langle r^2_{\nu_e}\rangle$ values particularly different from the SM prediction. In particular, we obtain a competitive limit on $\langle r^2_{\nu_e}\rangle$ at 90% CL, namely

$$-9.5 < \langle r^2_{\nu_e}\rangle\,[10^{-32}\,\mathrm{cm}^2] < 5.5, \tag{7.19}$$

and on $\langle r^2_{\nu_\mu}\rangle$,

$$-59.2 < \langle r^2_{\nu_\mu}\rangle\,[10^{-32}\,\mathrm{cm}^2] < -51.0 \quad \text{and} \quad -5.9 < \langle r^2_{\nu_\mu}\rangle[10^{-32}\,\mathrm{cm}^2] < 4.1. \tag{7.20}$$

The numerical results obtained from our reanalysis are compared in Tab. 7.5, at 90% CL, with other leading existing laboratory bounds, while the reader can refer

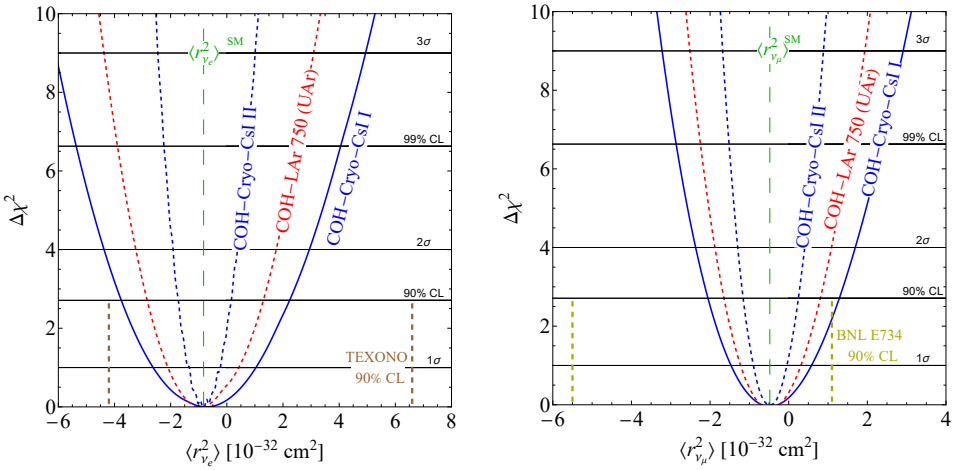

Figure 7.9: Marginal $\Delta\chi^2$'s for $\langle r^2_{\nu_e}\rangle$ (left), $\langle r^2_{\nu_\mu}\rangle$ (right) obtained from the sensitivity for the future COHERENT experiments assuming three SNS-year of data taking. The SM NCR predictions are reported, and for comparison, the current leading constraints from TEXONO [67] (left) and BNL-E734 [376] (right) are also reported.

to Tab. 1 of Ref. [7] for a complete summary of the constraints at different C.Ls. from COHERENT alone and in combination with Dresden-II data. Interestingly, we are able to improve the best upper bound limit for $\langle r^2_{\nu_e}\rangle$ previously set by TEXONO [67][4].

7.1.3.1 Toward A Neutrino Charge Radius Observation From Future CEνNS Data

This section will explore the sensitivity of future COHERENT experiments to the neutrino charge radius, based on a work in preparation, as well as the forecast for a NUCLEUS-like experiment assuming different configurations. We start by assessing the sensitivity of COH-Cryo-CsI (Sec. 3.4.1) and COH-LAr 750 (Sec. 3.4.2) detectors, allowing both $\langle r^2_{\nu_e}\rangle$ and $\langle r^2_{\nu_\mu}\rangle$ to be free to vary in the fit and assuming three SNS year of data taking. The expected precision on the neutrino charge radii will significantly benefit from the increased statistics, as shown in Fig. 7.9. Here we limit the sensitivity in the proximity of the expected SM value for the neutrino charge radii. We found that the next COHERENT upgrades will significantly improve the current constraints. Specifically, even with COH-Cryo-CsI I, it will be possible to reach the same level of accuracy or even surpass the limits set by TEXONO on $\langle r^2_{\nu_e}\rangle$ and by BNL on $\langle r^2_{\nu_\mu}\rangle$. In fact, the unique feature of COHERENT

[4]Both TEXONO and BNL-E734 results have been corrected by a factor of two due to a different convention, see Ref. [379]. Moreover, for the latter, we use the corrected value in Ref. [380].

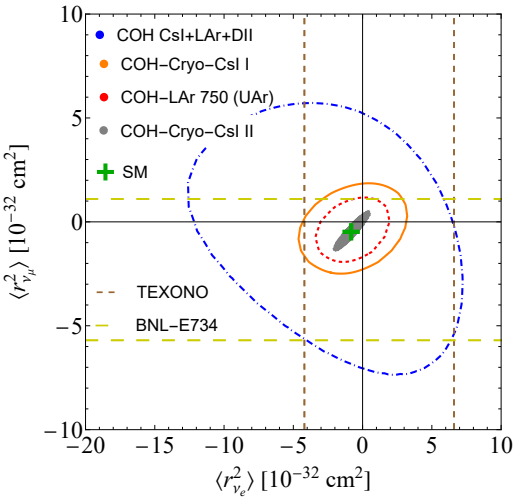

Figure 7.10: 90% CL allowed region in the $\langle r^2_{\nu_e}\rangle$ vs $\langle r^2_{\nu_\mu}\rangle$ plane obtained from the sensitivity for the future COHERENT experiments assuming three SNS-year of data taking. The SM NCR predictions are reported, and for comparison, the current constraints from the CsI+LAr+Dresden-II analysis, (Tab. 7.5), TEXONO [67] and BNL-E734 [376] are also reported.

is that it offers a distinctive way to simultaneously constrain both parameters, as shown in the lower panel of Fig. 7.10. Since the SNS ν_μ flux is higher compared to ν_e, the constraints are weaker for the latter. Moreover, the COH-LAr-750 detector will significantly benefit from the use of UAr instead of AAr, as shown in the upper left panel of Fig. 7.9. Despite the increase in statistical precision, the data from the next detectors will not be able to provide the first measurement of the NCR, according to our studies. Only the future COH-Cryo-CsI II detector will have sufficient precision to achieve about 1 σ significance for the simultaneous determination of the two NCRs in the event rate[5]. Specifically, the COH-Cryo-CsI constraints at 90% CL are

$$\mathrm{COH-Cryo-CsI\ I}: \quad -3.8 < \langle r^2_e\rangle\ [10^{-32}\mathrm{cm}^2] < 2.2, \tag{7.21}$$

$$-2.1 < \langle r^2_\mu\rangle\ [10^{-32}\mathrm{cm}^2] < 1.3, \tag{7.22}$$

$$\mathrm{COH-Cryo-CsI\ II}: \quad -1.73 < \langle r^2_e\rangle [10^{-32}\mathrm{cm}^2] < 0.16, \tag{7.23}$$

$$-1.16 < \langle r^2_\mu\rangle [10^{-32}\mathrm{cm}^2] < 0.25. \tag{7.24}$$

[5]The significance is evaluated as the difference of the χ^2 assuming the SM values for the NCRs and χ^2 from the null hypothesis, i.e. setting the NCRs to zero.

The COH-LAr 750 constraints, assuming UAr, are stronger (weaker) than COH-Cryo-CsI I (II) for both flavors.

These findings strengthen the need to perform complementarity analysis with reactor data, which are sensitive only to $\langle r^2_{\nu_e} \rangle$ in a different energy regime. In this context, Fig. 7.11 shows the expected sensitivity for a NUCLEUS-like experiment, obtained under different hypotheses for the signal and background as discussed in Chap. 5. In the scenario where the background is flat and equal to 100 dru, the 90% constraint reads

$$\text{NUCLEUS 13.5 g @VNS (no LEE)}: \quad -2.9 < \langle r^2_e \rangle [10^{-32}\text{cm}^2] < 1.4, \tag{7.25}$$

while increasing the mass at the VNS to 108 grams or considering the experiment located at 15 meters from the reactor core, assuming a background component with a CRESST-III level LEE, enables us to improve the constraints. At 90% CL they read

$$\text{NUCLEUS 108 g @VNS (no LEE)}: \quad -2.1 < \langle r^2_e \rangle [10^{-32}\text{cm}^2] < 0.6. \tag{7.26}$$

We found the sensitivity predictions to be very promising. This is because only $\langle r^2_{\nu_e} \rangle$ can be constrained with reactor data, such that the marginalization on the electron flavor is not affected by any correlation with the muonic flavor, unlike in the case of COHERENT.

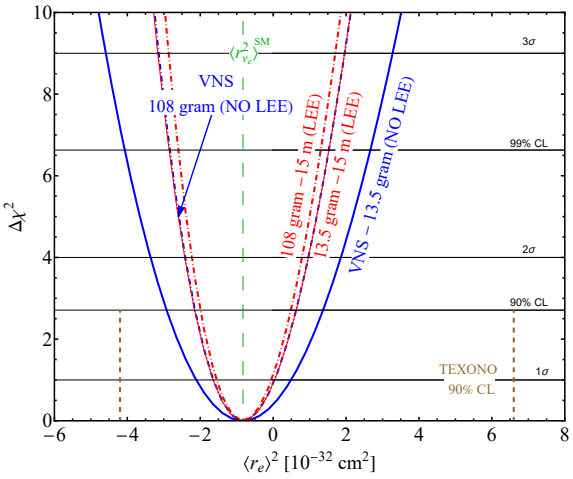

Figure 7.11: Marginal $\Delta\chi^2$'s for $\langle r^2_{\nu_e} \rangle$ obtained from the sensitivity for a NUCLEUS-like experiment assuming 3 years of data taking. The sensitivity is reported for 13.5 g and 108 g of $CaWO_4$ located at the VNS, as well as 15 meters from a 4.25 GW_{th} reactor core assuming the presence of the best LEE measured by CRESST-III (see Sec. 5.3). The SM NCR predictions are reported as well as the 90% CL constraints from TEXONO [67].

7.2 The LUX-ZEPLIN Dark Matter Experiment Science case

As already widely discussed, given that the presence of neutrino MMs and ECs manifest mainly at low recoil energies, experiments with low thresholds can set stronger constraints. Indeed, in Sec. 7.1.1 and 7.1.2 we showed that reactor CEνNS experiments, such as the Dresden-II one, are able to reach low thresholds leading to very stringent constraints. For this reason, a very strong complementarity exists between CEνNS and low-threshold dark matter detectors discussed in Chap. 2. The latter, being sensitive to solar neutrinos, represents a very profitable tool to study such neutrino electromagnetic properties. This section presents the results presented in our work [2], based on recent LUX-ZEPLIN (LZ) Collaboration data [73] searching for WIMPs. The LZ experiment is located at the Sanford Underground Research Facility in Lead, South Dakota. Its core is a dual-phase time TPC filled with about 10 tons of liquid xenon (LXe), of which 7 (5.5) tons of the active (fiducial) region. In liquid xenon, the interaction of a neutral particle with xenon nuclei inside the detector produces two detectable signals if the NR is above the $\sim$5 $\mathrm{keV_{nr}}$ threshold, namely scintillation photons (S1) in the detector bulk and a secondary scintillation signal (S2) produced by the ionized electrons that drift due to an electric field to the gas pocket on top of the detector, similarly to the DarkSide-20k technology (see Sec. 2.3). Both signals are captured by 494 photomultiplier tubes located at the top and the bottom of the TPC. The results reported correspond to 60.3 live days and given that the data are consistent with a background-only hypothesis, permit setting the most stringent limits on the spin-independent and spin-dependent WIMP-nucleon scattering cross section for masses greater than 9 GeV/c^2 [73], as well as new competitive limits on the spin-dependent WIMP-proton cross section.

Among the different background components that are kept into account in the data analysis, the solar νES inside the TPC gives a non-negligible contribution. Indeed, in the LZ analysis, the total number of such electron recoils (ERs) that is found after the combined fit of the background model plus a 30 GeV/c^2 WIMP signal is 27.2 ± 1.6 [73] and represents about 10% of the total background, giving room to put sensitive constraints on neutrino MM and EC. It is worth mentioning

that the MM measured for solar νES is an effective value given by

$$\mu_\nu^{2,\text{eff}} = \sum_j |\sum_k \mu_{jk} A_k(E_\nu, L)|^2, \tag{7.27}$$

where μ_{jk} is an element of the neutrino electromagnetic moments matrix and $A_k(E_\nu, L)$ is the amplitude of the k-mass state at the point of scattering [142]. Similarly, it is possible to define also an effective neutrino millicharge parameter q_ν^{eff} as a combination of the three flavor components. In the following analyses, we will separate the neutrino MM and EC contribution from the different flavors to extract the constrain on the parameter associated with a specific flavor. Here we are neglecting the possibility of transition neutrino electromagnetic properties to simplify the computation, as it would require the computation of three diagonal (ee, $\mu\mu$, $\tau\tau$) plus four off-diagonal terms ($e\mu$, $e\tau$, μe and $\mu\tau$) and would be computationally very expensive. This means that the results obtained here, in principle, could not be directly compared with reactor or COHERENT constraints in case off diagonal terms are considered.

To conclude, the XENONnT collaboration reported its first result based on the analysis of low-energy ER data collected with a dual-phase TPC filled with 4.37 tons of LXe fiducial mass and a total exposure of 1.16 ton · year [74]. The experiment obtained the lowest ER background level among current dark matter detectors in its energy range of interest. No excess above the background is found, allowing the collaboration to rule out the well-known XENON-1T excess [381], which motivated a considerable theoretical effort to interpret this anomaly [121, 382–384] which most probably produced by an unaccounted tritium background. Moreover, they also reported a limit on the neutrino magnetic moment that will be compared to that obtained in our work.

7.2.1 LZ Data Analysis Strategy

For the analysis of the LZ dataset, we obtained information on all the quantities used from Ref. [73] and the accompanying data release and supplemental material unless noted otherwise.

Since neutrinos are a mixture of mass eigenstates due to the phenomenon of oscillations, the cross section is calculated according to Eq. 2.19, and the total differential neutrino flux, Φ is given by the sum of all the different solar neutrino components described in Sec. 2.4.1. The most relevant for the sensitivity range

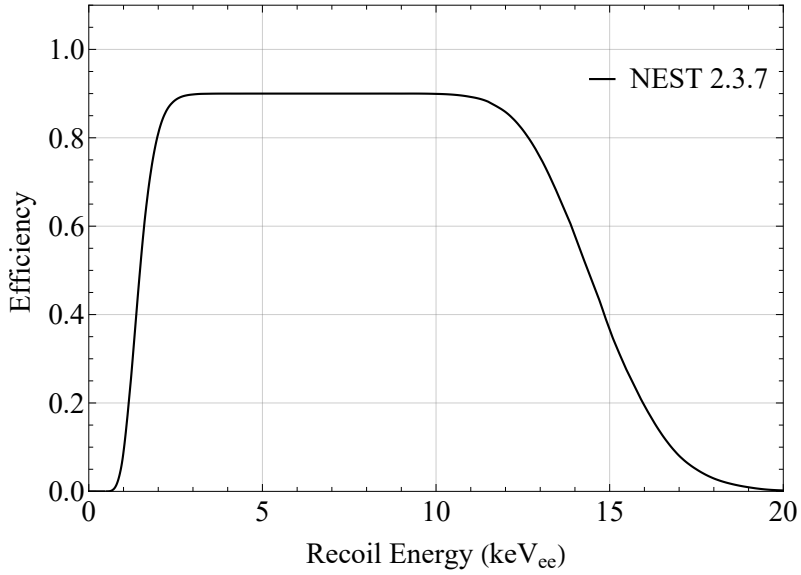

Figure 7.12: LZ signal efficiency as a function of the ER energy T_e, obtained from the NEST 2.3.7 software [385] using the details provided by the LZ collaboration.

of LZ are the continuous pp flux and the monochromatic ^{7}Be 861 keV line, even though there are many additional contributions from other mechanisms that are included in this analysis. In each ER energy bin i, the theoretical νES event number $N_i^{\nu\mathrm{ES}}$ is given by

$$N_i^{\nu\mathrm{ES}} = N(\mathrm{Xe}) \int_{T_\mathrm{e}^i}^{T_\mathrm{e}^{i+1}} dT_\mathrm{e}\, A(T_\mathrm{e}) \int_{E_\mathrm{min}(T_\mathrm{e})}^{E_\mathrm{max}} dE_\nu \frac{d\Phi}{dE_\nu} \frac{d\sigma_\nu}{dT_\mathrm{e}}(E_\nu, T_\mathrm{e}),$$

where $N(\mathrm{Xe})$ is the number of xenon targets contained in the detector, T_e is the ER kinetic energy, $A(T_\mathrm{e})$ is the energy-dependent detector efficiency, $E_\mathrm{min}(T_\mathrm{e}) = (T_\mathrm{e} + \sqrt{T_\mathrm{e}^2 + 2m_e T_\mathrm{e}})/2$, and $E_\mathrm{max} \sim 2$ MeV. The number of target xenon atoms in the detector is given by $N(\mathrm{Xe}) = N_\mathrm{A} M_\mathrm{det}/m_\mathrm{Xe}$, where N_A is the Avogadro number, $M_\mathrm{det} = 5.5$ ton is the detector fiducial mass and m_Xe is the average xenon molar mass. While the LZ collaboration provided the detector efficiency as a function of the NR energy T_nr, the energy observed in the detector is the ER energy T_e. For this reason, we derived the detector efficiency as a function of T_e using the NEST [385] 2.3.7 software, following the information provided by the LZ collaboration. The efficiency obtained and used in our analysis is shown in Fig. 7.12. Besides the solar νES, the background components that survive the selection in the region of interest come from different sources, the dominant one being the ERs from radioactive decay of impurities dispersed in the xenon, commonly referred to as β background. Together with a small ($< 1\%$) fraction due to ER from

γ rays originating in the detector components and cavern walls, this background represents about 79% of the total one. Other background sources include the naturally occurring isotopes of xenon, which also contribute to ER events, as well as isotopes that are activated cosmogenically, such as ^{127}Xe and ^{37}Ar. Moreover, the NR background has contributions from radiogenic neutrons and coherent elastic neutrino-nucleus scattering (CEνNS) from ^{8}B solar neutrinos. Finally, there is a small component of accidental backgrounds that is also kept into account. Overall, the LZ collaboration reports a background of 333 ± 17 events, of which 27.2 ± 1.6 are due to solar νES, see Table I in Ref. [73]. Moreover, thanks to the excellent energy resolution achieved by LZ, we verified that its inclusion does not significantly modify the limit obtained.

We performed the analysis of the LZ data using a Poissonian least-squares function [19, 181], given that in some energy bins the number of events is small, namely

$$\chi^2 = 2\sum_{i=1}^{51}[(1+\alpha)N_i^{\rm bkg} + (1+\beta)N_i^{\nu\rm ES} - N_i^{\rm exp} + N_i^{\rm exp}\ln\left(\frac{N_i^{\rm exp}}{(1+\alpha)N_i^{\rm bkg} + (1+\beta)N_i^{\nu\rm ES}}\right)] + \left(\frac{\alpha}{\sigma_\alpha}\right)^2 + \left(\frac{\beta}{\sigma_\beta}\right)^2, \tag{7.28}$$

where $N_i^{\rm bkg}$ is the number of residual background events found in the i-th bin fit by the LZ collaboration minus that due to solar νES (both extracted from Fig. 6 of Ref. [73]), $N_i^{\nu\rm ES}$ is the prediction in the i-th bin for the νES signal, and $N_i^{\rm exp}$ is the experimental number of events in the i-th bin, also extracted from Fig. 6 of Ref. [73]. The nuisance parameter α takes into account the uncertainty on the background (with $\sigma_\alpha = 5.1\%$)[6], while β keeps into account the uncertainty on the neutrino flux (with $\sigma_\beta = 7\%$)[7]. By using this procedure we ignore that a possible non-zero neutrino MM should also increase the CEνNS contribution from ^{8}B solar neutrinos. However, given that the latter contribution is only 0.15 ± 0.01 [73], we verified that we can safely neglect it. For the future, we note that a lower experimental energy threshold would increase the CEνNS contribution, thus contributing to further strengthening the MM and EC limits. We highlight that, differently from all the other background sources, the number of ^{37}Ar events

[6]We note that this procedure ignores the fact that the different background contributions have a different relative uncertainty. However, given that the total background is dominated by the β decays this approximation is valid.

[7]The flux uncertainty is about 7% for ^{7}Be and 0.6% for pp (see Tab. 2.1), we conservatively use the first one for both fluxes.

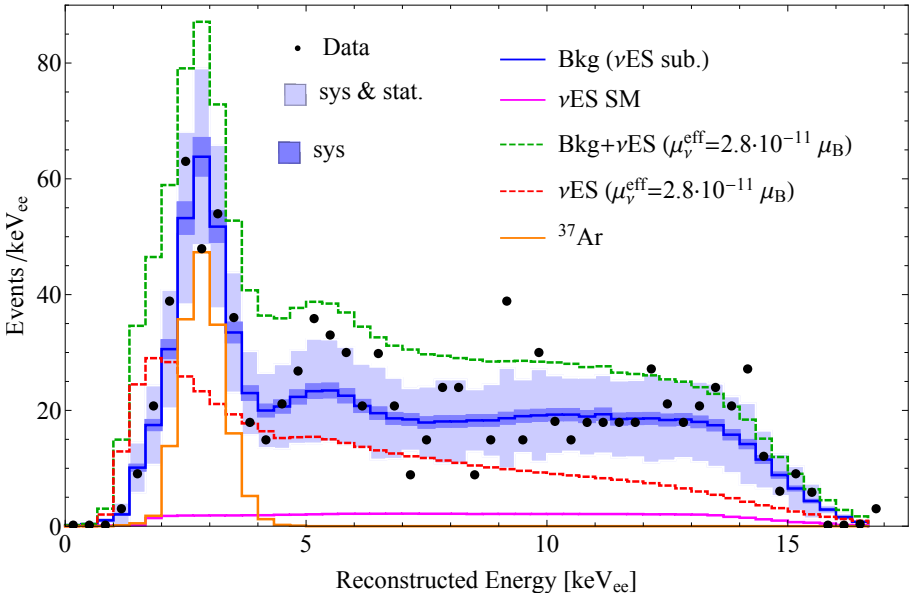

Figure 7.13: LZ energy spectrum (black points) as extracted from Fig. 6 of Ref. [73] with superimposed the sum of all background contributions minus the νES contribution (blue solid), the ^{37}Ar contribution (orange), the νES SM prediction (purple), and for illustration purposes the νES with $\mu_\nu^{\rm eff} = 2.8 \times 10^{-11}\ \mu_{\rm B}$, that corresponds to the 90% CL limit from BOREXINO [142], with (green dashed) and without (red dashed) the νES subtracted background. The dark blue and the light blue bands represent the systematic and systematic plus statistical uncertainties, respectively, used in this analysis.

is not well constrained theoretically. It is estimated by calculating the exposure of Xe to cosmic rays before it was brought underground, then correcting for the decay time before the data taking [386]. A flat constraint of 0 to three times (i.e., 288) the estimate of 96 events is imposed because of large uncertainties in the prediction. The fit to the data using this prior finds $52.5^{+9.6}_{-8.9}$ events. In order to keep into account this large uncertainty, we performed a second analysis in which we separate the ^{37}Ar contribution from the total background such that the least-squares function becomes

$$\begin{aligned}\chi^2_{^{37}\rm Ar} = 2\sum_{i=1}^{51}[&\alpha N_i^{\rm bkg} + \beta N_i^{\nu\rm ES} + \delta N_i^{^{37}\rm Ar} - N_i^{\rm exp} \\ &+ N_i^{\rm exp}\ln\left(\frac{N_i^{\rm exp}}{\alpha N_i^{\rm bkg} + \beta N_i^{\nu\rm ES} + \delta N_i^{^{37}\rm Ar}}\right)] \\ &+ \left(\frac{\alpha-1}{\sigma_\alpha}\right)^2 + \left(\frac{\beta-1}{\sigma_\beta}\right)^2 + \left(\frac{\delta-1}{\sigma_\delta}\right)^2,\end{aligned} \tag{7.29}$$

where $N_i^{\rm bkg}$ is the number of residual background events minus those due to νES and ^{37}Ar as found in the i-th electron recoil energy bin fit by the LZ collaboration,

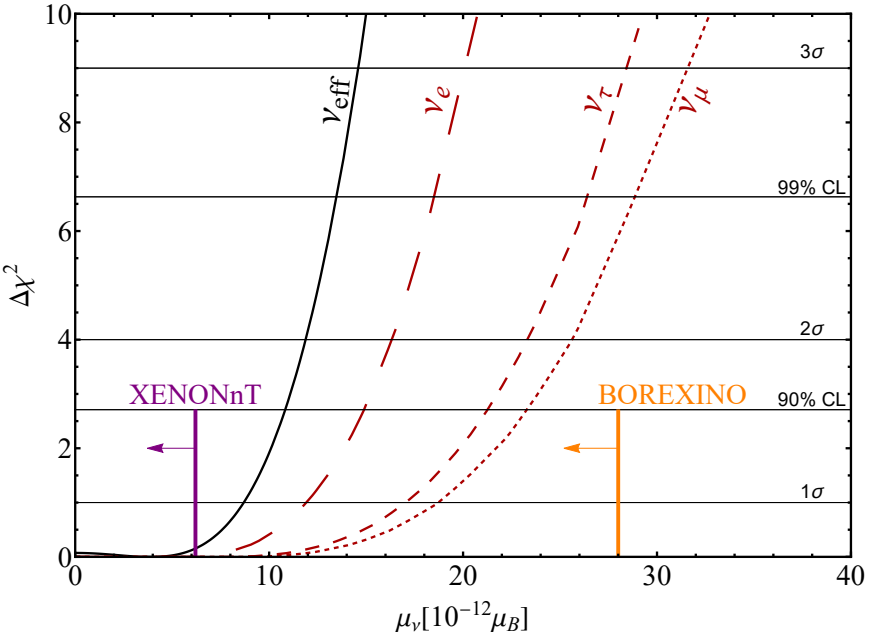

Figure 7.14: Marginal $\Delta\chi^2$s for $\mu_\nu^{\rm eff}$ obtained from the analysis of the LZ data with the χ^2 in Eq. 7.28 (black solid line) and the marginalized flavor components (dashed red lines). The solid purple (orange) line shows the 90% CL upper bound on the effective neutrino MM obtained in the XENONnT [74] (BOREXINO [142]) experiment.

and $N_i^{^{37}\rm Ar}$ is the number of ^{37}Ar background events found in the i-th bin fit by the LZ collaboration, scaled such that the integral is equal to 96 events, as estimated in Ref. [73]. We leave the latter free to vary in the fit with a Gaussian constraint given by the nuisance parameter δ, which takes into account the uncertainty on the ^{37}Ar background, with $\sigma_\delta = 100\%$. In this case, we set $\sigma_\alpha = 13\%$, which is the uncertainty on the expected number of background events provided in Ref. [73] when not considering the ^{37}Ar contribution. In Fig. 7.13 we show an example of the νES prediction in the presence of a possible neutrino MM for the LZ spectrum compared with the data, the SM νES prediction and the other background components, considering e.g. $\mu_\nu^{\rm eff} = 2.8 \times 10^{-11}\ \mu_{\rm B}$, which corresponds to the previous best limit at 90 % CL on the neutrino MM from Borexino [142].

7.2.2 LZ Constraints on the Neutrino Magnetic Moment

In Fig. 7.14 we show the marginal $\Delta\chi^2$s at different confidence levels, obtained using the χ^2 in Eq. 7.28, for both the effective MM and the marginalization over the three flavor components. The numerical values of the limits derived considering the three different flavors are reported in Tab. 7.6. At 90% CL, the bound on

	$\lvert\mu_\nu\rvert[\times 10^{-11}\mu_B]$	q_ν $[\times 10^{-13} e_0]$	
		FEA	EPA
ν_{eff}	< 1.1	[-3.0, 4.7]	[-1.5, 1.5]
ν_e	< 1.5	[-3.6, 6.5]	[-2.1, 2.0]
ν_μ	< 2.3	[-8.9, 8.8]	[-3.1, 3.1]
ν_τ	< 2.1	[-8.1, 8.1]	[-2.8, 2.8]

Table 7.6: Limits on the neutrino magnetic moment and neutrino millicharge at 90% CL obtained with a χ^2 analysis as defined in Eq. 7.28. For the neutrino millicharge, the limits are reported for both the FEA and the EPA formalism.

the effective neutrino MM we obtained is

$$\mu_\nu^{\text{eff}} \;<\; 1.1 \times 10^{-11}\,\mu_{\text{B}}, \tag{7.30}$$

with the minimum of the chi-square being $\chi^2_{\text{min}} = 100.0$, which corresponds to an integrated number of ∼50 νES events. It can be compared with the limit recently reported by the XENONnT collaboration corresponding to $\mu_\nu^{\text{eff}} < 6.4 \times 10^{-12}\,\mu_{\text{B}}$ [74], which is about a factor of 2 more stringent due to their lower background with respect to LZ. Further neutrino MM analyses exploiting XENONnT data can be found in Refs. [387–389]. These LZ and XENONnT limits, both obtained using a LXe double-phase TPC technology originally designed to search for dark matter and a similar analysis approach, are significantly tighter than the previous laboratory bounds, highlighting the potentiality that such a technique can offer thanks to the low-energy threshold and low level of background achieved.

Finally, we investigated the possibility of leaving the ^{37}Ar component free to vary in the fit using a prior similar to that implemented by the LZ collaboration, as defined in Eq. 7.29. Interestingly, the fit retrieves a number of ^{37}Ar events similar to that found by LZ, namely ~ 48 with $\chi^2_{\text{min}} = 99.6$. Thus, also in this case, the limits do not substantially change and for reference the bound on the effective neutrino MM at 90% CL becomes $\mu_\nu^{\text{eff}}(^{37}\text{Ar}) < 1.2 \times 10^{-11}\,\mu_{\text{B}}$. Fig. 7.16 (left) compares the results we obtained from LZ data with other leading constraints, including those from CEνNS presented in this thesis. We start by comparing our results with the obtained by the Super-Kamiokande collaboration of $3.6 \times 10^{-10}\mu_B$ (90% CL), derived by fitting day/night solar neutrino spectra above 5 MeV. With additional information from other solar neutrino and KamLAND experiments a limit of $1.1 \times 10^{-10}\mu_B$ (90% CL) was obtained [390]. The Borexino collaboration reported the previous best current limit on the effective MM by laboratory experiments of

$2.8 \times 10^{-11}\mu_B$ (90% CL) using the ER spectrum from solar neutrinos [142]. The best MM limit from reactor antineutrinos is $2.9 \times 10^{-11}\mu_B$ (90% CL) [68]. When considering non-laboratory experiments, the most stringent limits on the neutrino MM of up to $\sim 10^{-12}\mu_B$ come from astrophysical observations [391–393], which however are rather indirect. A complete historical record of limits on the neutrino MM can be found in Ref. [19] and a large collection of existing bounds is summarized in Fig. 7.16. It is possible to see that in our analysis of the LZ data we significantly improve the limits on the electron, muon and tau neutrino MM compared to the other laboratory bounds[8]. It is worth mentioning that after the publication of our work, the LZ collaboration released their official analysis [103], finding $\mu_\nu^{\text{eff}} < 1.36 \times 10^{-11}\ \mu_B$, which is very compatible with our results.
Remarkably, the results of our analysis have been considered in the latest version of the particle data group [31] together with the official LZ limits.

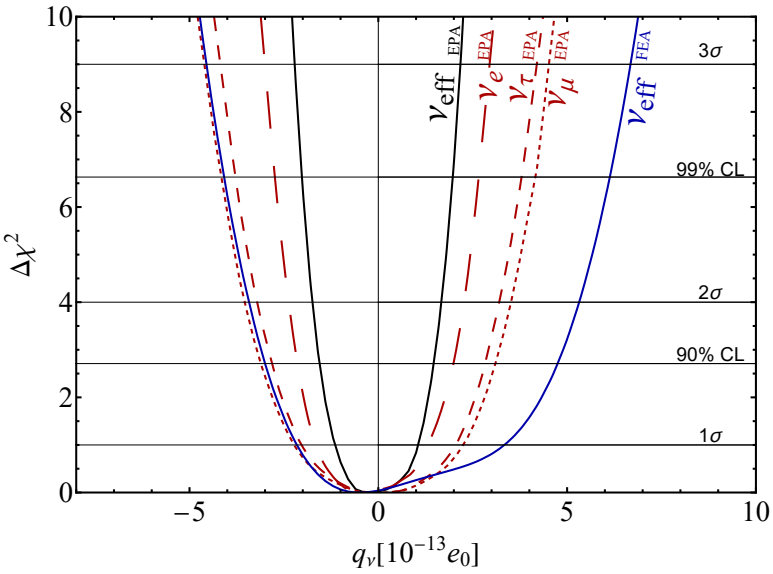

Figure 7.15: $\Delta\chi^2$ profiles of the effective (solid black) and flavor dependent (dashed red) neutrino millicharge obtained adopting the EPA formalism. As a comparison, the curve for the effective neutrino millicharge under the FEA approximation is also shown (solid blue).

[8]Let us note that one has to be careful when comparing laboratory bounds on the neutrino MMs to the ones from solar neutrinos. Indeed, due to the phenomenon of neutrino oscillations, the extracted constraints for MMs correspond to different combinations of the magnetic contributions relative to the mass eigenstates [365]. In this sense, the comparison in Fig. 7.16 (left) should be considered rather qualitative.

7.2.3 LZ Constraints on the Neutrino Electric Charge

Given that for low ER energies the momentum transfer is small, the analysis of the LZ data is expected to be particularly promising for millicharged neutrino searches. Moreover, in this analysis, we adopt a more accurate approach to compute the interaction of the millicharged neutrino with the atom. It is the so called equivalent photon approximation (EPA) which relates the ionization cross section to the photo-absorption one, and gives s a cross section more than one order of magnitude bigger than that obtained with the corrected FEA. Moreover, the EPA scheme provides a very similar result when compared to ab-initio RRPA approach [81, 394]. In this regard, we can consider the neutrino EC limit obtained within the FEA formalism as a conservative one. On the other hand, the EPA approach should lead to tighter constraints on the neutrino millicharge. In particular, the EPA cross section for a millicharged ultrarelativistic particle reads [81, 394]

$$\left.\frac{d\sigma_{\nu_\ell}}{dT_{\rm e}}\right|_{\rm EPA}^{\rm EC} = \frac{2\alpha}{\pi}\frac{\sigma_\gamma(T_e)}{T_e}\log\left[\frac{E_\nu}{m_\nu}\right] q_{\nu_\ell}^2, \tag{7.31}$$

where m_ν is the neutrino mass, and $\sigma_\gamma(T_e)$ is the photoelectric cross section by a real photon, which can be extracted from Ref. [269] for Xe. By looking at Eq. 7.31 it can be seen that the cross section in the EPA approximation is independent of the sign of the electric charge, differently from the case of the FEA approximation. We should underline that, although the EPA approach describes very well the cross section for ER energies below a few keVs, it is known to underestimate the scattering cross section for larger energies where the FEA formalism works better. For this reason, we will rely on the EPA scheme only when its cross section is larger than that of the corrected FEA, following the same procedure adopted in Ref. [395]. In the following, for simplicity, we will refer to this strategy as EPA. In Fig. 7.15 we present the limits on the neutrino EC obtained in this work within the FEA and EPA formalisms, using the χ^2 in Eq. 7.28. We note that the EPA cross section depends on the neutrino mass, as can be seen in Eq. 7.31, which is not yet precisely measured. We used a conservative value of $m_\nu = 1$ eV, which is close to the current laboratory upper bounds on the neutrino mass [19]. On the other hand, we verified that the limit is not significantly modified even when considering smaller values for m_ν. The 90% CL bounds on the effective millicharge are

$$\text{FEA}: \quad -3.0 < q_\nu^{\rm eff}\ [10^{-13}\ e_0] < 4.7, \tag{7.32}$$

$$\text{EPA}: \quad -1.5 < q_\nu^{\text{eff}}\ [10^{-13}\ e_0] < 1.5. \tag{7.33}$$

The values for the flavor-dependent neutrino millicharges are summarized in Tab. 7.6 both for the FEA and EPA analyses. It is clear that the limits obtained with the more realistic EPA formalism are much stronger than those obtained within FEA and hence, for simplicity, in Fig. 7.15 we showed only the effective EC limit for FEA. We note also that the limits obtained with FEA are comparable with those reported in Ref. [387], which exploits the ER energy efficiency derived in this work for the LZ analysis, and are less stringent than those obtained with XENONnT [387, 388]. On the other hand, the limits obtained adopting EPA when analyzing the LZ data are even stronger than the XENONnT limits obtained in Refs. [387, 388] that were determined using FEA.

For completeness, also in this case we investigated the impact of repeating the analysis leaving the ^{37}Ar component free to vary, similarly to what was done for the neutrino MM limits. In this case, the bounds on the effective neutrino millicharge become

$$\text{FEA}: \quad -3.3 < q_\nu^{\text{eff}}(^{37}\text{Ar})\ [10^{-13}\ e_0] < 5.0, \tag{7.34}$$

$$\text{EPA}: \quad -1.6 < q_\nu^{\text{eff}}(^{37}\text{Ar})\ [10^{-13}\ e_0] < 1.5. \tag{7.35}$$

As before, leaving the ^{37}Ar component free to vary does not impact significantly the results. Moreover, we foresee that, in the future, this should be even less problematic given that ^{37}Ar has a half-life of about 35 days and thus should be not present in future LZ data samples.

Fig. 7.16 shows a collection of existing bounds coming from different experiments. It can be seen that the limits derived using the LZ data and the more realistic EPA formalism significantly improve the previous best laboratory limits, that for the electron neutrino electric charge was obtained in Ref. [369] by combining TEXONO [66] and GEMMA [68] data, finding $|q_{\nu_e}| < 1.0 \times 10^{-12}\ e_0$. Also in this case we can compare our results with the official LZ limit for the neutrino electric charge obtained using a different approach to describe the interaction [103]: $q_\nu^{\text{eff}} < 2.24 \times 10^{-13} e_0$, which are a bit weaker compared to the results of our analysis. Also for the neutrino EC, the results of our analysis have been considered in the latest version of the particle data group [31] together with the official LZ limits.

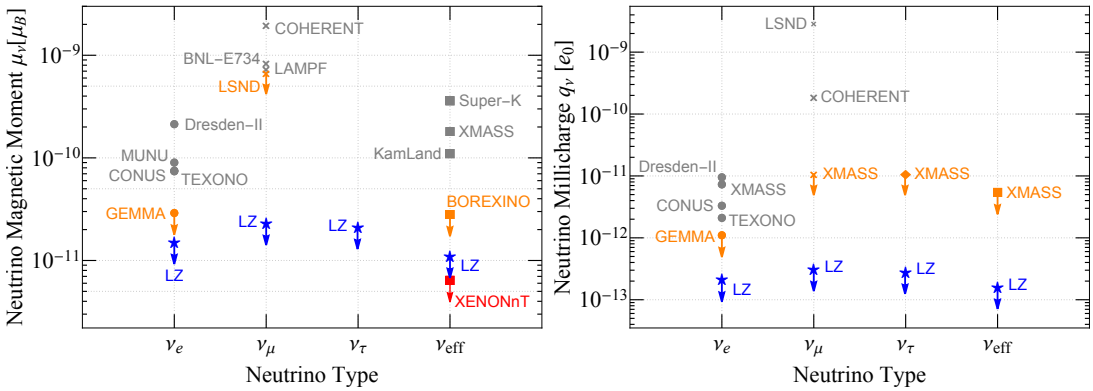

Figure 7.16: Summary of existing limits at 90% CL on the neutrino magnetic moment (left) and the neutrino millicharge (right) coming from a variety of experiments [19, 66, 68, 76, 142, 359–362, 372, 390, 396]. The limits are divided in flavor components μ_{ν_e} (q_{ν_e}) (dots), μ_{ν_μ} (q_{ν_μ}) (crosses), and μ_{ν_τ} (q_{ν_τ}) (diamonds) and also the ones on the effective magnetic moment μ_ν^{eff} (q_ν^{eff}) (squares) are shown. In orange, we highlighted the best limits before the LZ data release and in red the XENONnT limit on the MM [74]. The results derived from our analysis of the LZ data [4] are shown by the blue stars both for the effective parameter and divided in flavors.

8

Direct Search for New Neutral Boson Mediators

Opening

This chapter explores extensions of the SM through additional $U(1)'$ gauge groups, which generate new light vector mediators. The phenomenology of interactions involving a light scalar boson mediator will also be considered. Since the COHERENT CEνNS data are well-fitted with the cross section predicted by the SM, the analysis of the data yields constraints for the mass and coupling of the new boson mediator that depends on the charges of quarks and neutrinos in each model under consideration. We will compare these constraints with limits obtained from other experiments and examine their compatibility with the values required to explain the longstanding muon $g-2$ anomaly, particularly in models where the muon couples to the new boson mediator. Most of the results presented here are based on Ref. [4]. Additionally, the expected sensitivity to light mediators for future CEνNS experiments, based on ongoing work, will be discussed.

8.1 $U(1)'$ Models and the $(g-2)_\mu$ Anomaly

The search for extensions of the SM is of pivotal importance to enhance our understanding of the fundamental laws of nature, and one possible way is to look for new particles. If the SM is extended to include a new gauge symmetry $U(1)'$, we can study the interaction of the corresponding massive gauge boson with Standard Model fermions. Therefore, we also consider the BSM scenarios in which the new physics manifests through a novel interaction mediated by a light vector boson, usually called Z', or scalar boson, usually named ϕ. Historically, one of the strongest motivations behind the Z' searches was the possibility of explaining the long-standing tension between experimental measurements and the SM prediction

of the muon anomalous magnetic moment, so-called $(g-2)_\mu$ anomaly, in terms of such light mediator hypotheses. The muon magnetic moment, indicated as g_μ, is predicted to be equal to 2 at tree level, and radiative corrections are responsible for a deviation from this value, which originates an anomalous muon magnetic moment [397]. For this reason, the muon anomalous magnetic moment is usually parameterized in terms of $a_\mu = (g_\mu - 2)_\mu/2$, which accounts for the deviation of the value of the anomalous magnetic moment compared to its tree-level value. From the theoretical point of view, the SM prediction of the muon anomalous magnetic moment is defined as a sum of different contributions involving loop diagrams from QED, electroweak diagrams plus hadronic contributions. Therefore, a_μ has the potential to be sensitive to new physics effects which might arise at the loop level, but the calculation is also quite challenging (see e.g. Refs. [398, 399] for a review).

Here an intriguing anomaly has emerged: recently, the Fermilab Muon $g-2$ experiment [400] confirmed their previous measurement [400, 401] and the 2006 result by the Muon E821 experiment at Brookhaven National Laboratory [402], leading to the combined $\sim 5\sigma$ deviation from the SM g_μ prediction. Specifically, the discrepancy between the SM expectation ($a_\mu^{\rm SM}$) and the experimental measurement ($a_\mu^{\rm exp}$) gives

$$\Delta a_\mu = (24.9 \pm 4.8) \times 10^{-10}, \tag{8.1}$$

where $\Delta a_\mu = a_\mu^{\rm exp} - a_\mu^{\rm SM}$. Even if the $(g-2)_\mu$ anomaly has been notably considered as an indication of physics beyond the SM [403–432], recent developments from lattice calculation re-evaluated the hadronic vacuum polarization contribution to the muon anomalous magnetic moment [31, 433–435] pointing toward a mitigation of the tension. For this reason, the $(g-2)_\mu$ anomaly picture might change in the near future. Indeed, light mediator models [328, 436–444] have been invoked to solve the tension [403, 439]. Specifically, an additional neutral boson B with mass m_B, which interacts with muons with coupling g_B, contributes to the muon anomalous magnetic moment with [445]

$$\delta a_\mu^B = \frac{g_B^2}{8\pi^2} \int_0^1 dx \, \frac{Q(x)}{x^2 + (1-x)\, m_B^2/m_\mu^2} \tag{8.2}$$

where $Q(x)$ depends on the scalar or vector nature of the neutral boson B

$$Q(x) = \begin{cases} x^2\,(2-x) & \text{(scalar)}, \\ 2x^2\,(1-x) & \text{(vector)}. \end{cases} \tag{8.3}$$

The most appealing candidate models to solve the anomaly must present a direct interaction with the muonic flavor. In this sense, the COHERENT measurements of CEνNS provide a suitable setup to search for the mentioned signatures thanks to the presence of a ν_μ and $\bar{\nu}_\mu$ neutrino flux. The diagrams mediating the CEνNS process in the presence of a new mediator are shown in Fig. 8.1, with Z' vector interaction in the left panel and a scalar interaction mediated by ϕ in the right panel. Moreover, light mediator models have gained significant popularity also because

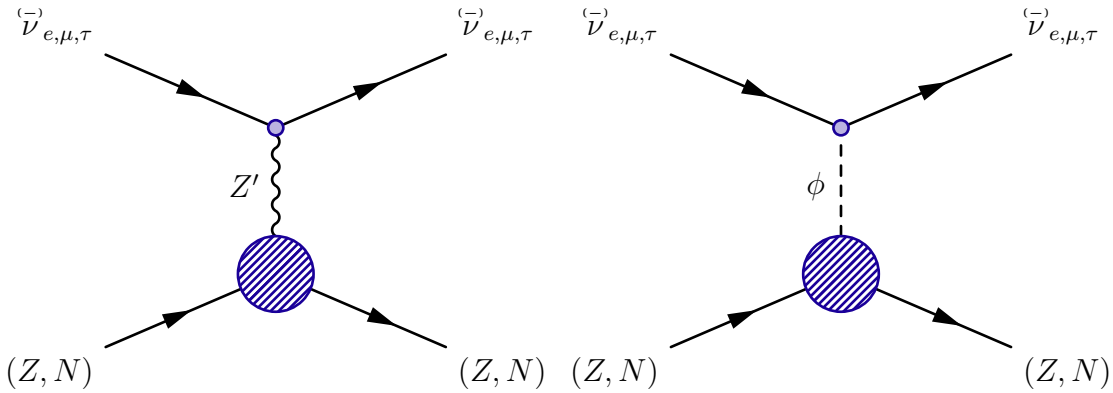

Figure 8.1: Feynman diagrams depicting the CEνNS process via a new mediator. The left panel shows the interaction mediated by a Z' vector boson, while the right panel represents the scalar interaction mediated by ϕ. The $U(1)$' charges of quarks and leptons in the vector mediator models considered are reported in Tab. 8.1.

they can alleviate the well-known cosmological Hubble tension [446] and might play a significant role in the process of supernovae explosion [447, 448], which makes it particularly relevant to test these model using available data. We will present the constraints obtained by analysing the COHERENT 2022 CsI data [163] and the COHERENT 2020 LAr data [159, 186] when considering the vector and scalar models. We will consider a smaller ensemble of models with respect to Ref. [2], where a more detailed discussion of Z' was provided. The constraints will be presented as exclusion limits in the mass and coupling of the light vector or scalar boson mediator parameter space and will be compared to the constraints coming from other experimental measurements.

8.1.1 Light Vector Z' Models

Here we are interested in the interaction vertex that describes the interaction of the Z' vector boson with the neutrino and quark fields, as schematically shown in the left panel of Fig. 8.1. The generic Lagrangian responsible for the interaction is

$$\mathcal{L}^V_{Z'} = -Z'_\mu \left[\sum_{\ell=e,\mu,\tau} g^{\nu_\ell V}_{Z'} \, \overline{\nu_{\ell L}} \gamma^\mu \nu_{\ell L} + \sum_{q=u,d} g^{qV}_{Z'} \, \overline{q} \gamma^\mu q \right], \tag{8.4}$$

where $g^{qV}_{Z'}$ and $g^{\nu_\ell V}_{Z'}$ are the coupling constants, whose structure depends upon the specific model considered and their strength is a free parameter of the model. The coupling constants are proportional to the charges Q'_q and Q'_ℓ of quarks and neutrinos under the new gauge symmetry: $g^{qV}_{Z'} = g_{Z'} Q'_q$ and $g^{\nu_\ell V}_{Z'} = g_{Z'} Q'_\ell$, where $g_{Z'}$ is the coupling constant of the symmetry group. Since both the SM and the Z' interactions are of vector type, they contribute coherently to the CEνNS cross section. Moreover, since the vector current is conserved, the proton and neutron coupling are given by the sums of the couplings of their valence quarks. Therefore, the total cross section is obtained by replacing the SM weak charge $Q^V_{\ell,\mathrm{SM}}$ with the new total weak charge (see App. C)

$$Q^V_{\ell,\mathrm{SM+V}} = Q^V_{\ell,\mathrm{SM}} + \frac{g^2_{Z'} Q'_\ell}{\sqrt{2} G_F \left(|\vec{q}|^2 + M^2_{Z'}\right)} \left[(2Q'_u + Q'_d) \, Z F_p(|\vec{q}|^2) + (Q'_u + 2Q'_d) \, N F_n(|\vec{q}|^2) \right], \tag{8.5}$$

with $|\vec{q}|^2 \simeq 2MT_{\mathrm{nr}}$. There are many models beyond the SM with an additional massive Z' vector boson associated with a new $U(1)'$ gauge symmetry [449]. A necessary requirement is that the theory is anomaly-free. However, it is possible to consider effective anomalous models that describe the interactions of SM fermions with the implicit requirement that the contributions of the non-standard fermions of the full theory cancel the anomalies. This is the case of the first model that we consider: a Z' boson which couples universally to all SM fermions [311, 450–455]. In this case $Q'_\ell = Q'_u = Q'_d = 1$, and the coupling is same for all the fermions. Other models that we consider are anomaly-free if the SM is extended with the introduction of three right-handed neutrinos (see, e.g., Ref. [456]), which are also beneficial for the generation of the neutrino masses [17, 19]. In this case, there is an infinite set of anomaly-free $U(1)'$ gauge groups generated by

$$G(c_1, c_2, c_3, c_e, c_\mu, c_\tau) = c_1 B_1 + c_2 B_2 + c_3 B_3 - c_e L_e - c_\mu L_\mu - c_\tau L_\tau, \tag{8.6}$$

Model	Q'_u	Q'_d	Q'_e	Q'_μ	Q'_τ
universal	1	1	1	1	1
$B-L$	$1/3$	$1/3$	-1	-1	-1
$B-3L_e$	$1/3$	$1/3$	-3	0	0
$B-3L_\mu$	$1/3$	$1/3$	0	-3	0
$B-2L_e-L_\mu$	$1/3$	$1/3$	-2	-1	0
$B-L_e-2L_\mu$	$1/3$	$1/3$	-1	-2	0
$B_y+L_\mu+L_\tau$	$1/3$	$1/3$	0	1	1
L_e-L_μ	0	0	1	-1	0
L_e-L_τ	0	0	1	0	-1
$L_\mu-L_\tau$	0	0	0	1	-1

Table 8.1: The $U(1)'$ charges of quarks and leptons in the vector mediator models considered in our work [2].

where B_1, B_2, and B_3 are the baryon numbers of the three generations and L_α are the lepton numbers for $\alpha = e, \mu, \tau$. We assume that for each generation the $U(1)'$ couplings of the right-handed neutrino are the same as that of the left-handed neutrino in order to have vectorial $U(1)'$ interactions. Therefore, we extend the SM gauge group $\mathrm{SU}(3)_C \otimes \mathrm{SU}(2)_L \otimes U(1)_Y$ to $\mathrm{SU}(3)_C \otimes \mathrm{SU}(2)_L \otimes U(1)_Y \otimes U(1)'$. The request for an anomaly-free theory leads to the condition [4]

$$c_1 + c_2 + c_3 - c_e - c_\mu - c_\tau = 0. \tag{8.7}$$

It is often assumed that the quark charges are universal, in order to avoid unobserved flavor-changing neutral currents in the quark sector. In this case, we have

$$G_B(c_B, c_e, c_\mu, c_\tau) = c_B B - c_e L_e - c_\mu L_\mu - c_\tau L_\tau, \tag{8.8}$$

with the constraint [457, 458]

$$3c_B - c_e - c_\mu - c_\tau = 0. \tag{8.9}$$

Here $B = B_1 + B_2 + B_3$ is the usual baryon number. In this work, we consider the models listed in Tab 8.1, and the expected event rate are shown in Fig. 8.2 for fixed values of the coupling $g_{Z'}$ and light mediator mass $m_{Z'}$. Remarkably, these

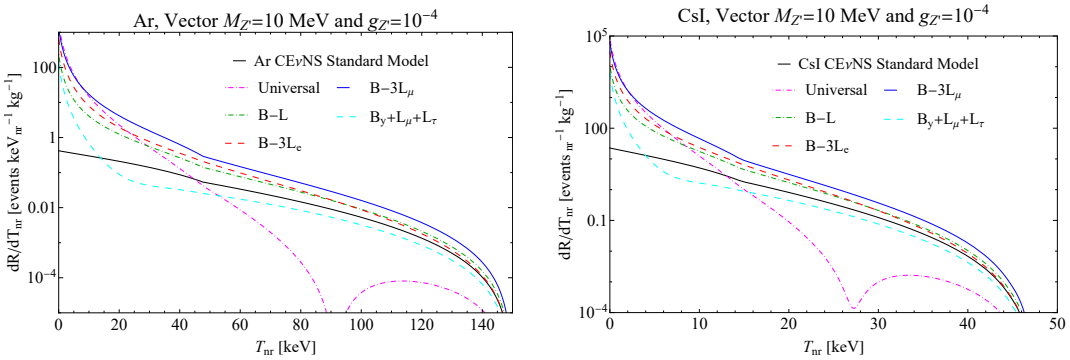

Figure 8.2: Predicted CEνNS differential event rates corresponding to the experimental configuration and data taking time of the COHERENT Ar and CsI detectors for different vector mediator models considered in this work.

models predict a considerable enhancement of the expected rate for small values of $T_{\rm nr}$ because of the propagator in Eq. 8.5. Moreover, in the case of the universal Z' model, there is a deep dip due to a cancellation between the negative SM and the positive Z' contributions to the weak charge in Eq. 8.5. This occurs only in the universal model because only in this case all the quark and lepton charges are positive and both ν_e and ν_μ interact with the Z'. Indeed, there is a cancellation for

$$T_{\rm nr} = -\frac{1}{2M}\left(\frac{3g_{Z'}^2}{\sqrt{2}G_F}\,\frac{ZF_p(|\vec{q}|^2)+NF_n(|\vec{q}|^2)}{g_V^p ZF_p(|\vec{q}|^2)+g_V^n NF_n(|\vec{q}|^2)}+M_{Z'}^2\right), \tag{8.10}$$

which occurs at $T_{\rm nr}\simeq 92$ keV for Ar and $T_{\rm nr}\simeq 27$ keV for CsI in Fig 8.2. Considering the last three models in Tab. 8.1, the Z' vector boson does not couple to quarks and there are no tree-level interactions that contribute to CEνNS , as shown in the Feynman diagram in the left panel of Fig. 8.3. However, there is kinetic mixing of the Z' and the photon at the one-loop level that induces a contribution to CEνNS through the photon interaction with quarks [443, 459–461]. The CEνNS cross section in these three models is [454, 459][1]

$$\left(\frac{d\sigma}{dT_{\rm nr}}\right)^{\nu_\ell-\mathcal{N}}_{L_\alpha-L_\beta}(E,T_{\rm nr}) = \frac{G_F^2 M}{\pi}\left(1-\frac{MT_{\rm nr}}{2E^2}\right) \tag{8.11}$$
$$\times\left\{\left[g_V^p(\nu_\ell)+\frac{\sqrt{2}\alpha_{\rm EM}g_{Z'}^2\left(\delta_{\ell\alpha}\varepsilon_{\beta\alpha}(|\vec{q}|)+\delta_{\ell\beta}\varepsilon_{\alpha\beta}(|\vec{q}|)\right)}{\pi G_F\left(|\vec{q}|^2+M_{Z'}^2\right)}\right]ZF_p(|\vec{q}|^2)+g_V^n NF_n(|\vec{q}|^2)\right\}^2,$$

where $\alpha_{\rm EM}$ is the electromagnetic fine-structure constant and $\varepsilon_{\beta\alpha}(|\vec{q}|)$ is the one-

[1]We correct here the sign of the Z' contribution with respect to that used in Ref. [454]. Let us also note that in the analysis in Ref. [461] the Z' contribution has the correct sign, but there is an additional factor $1/2$ that is incorrect, as shown in App. C.

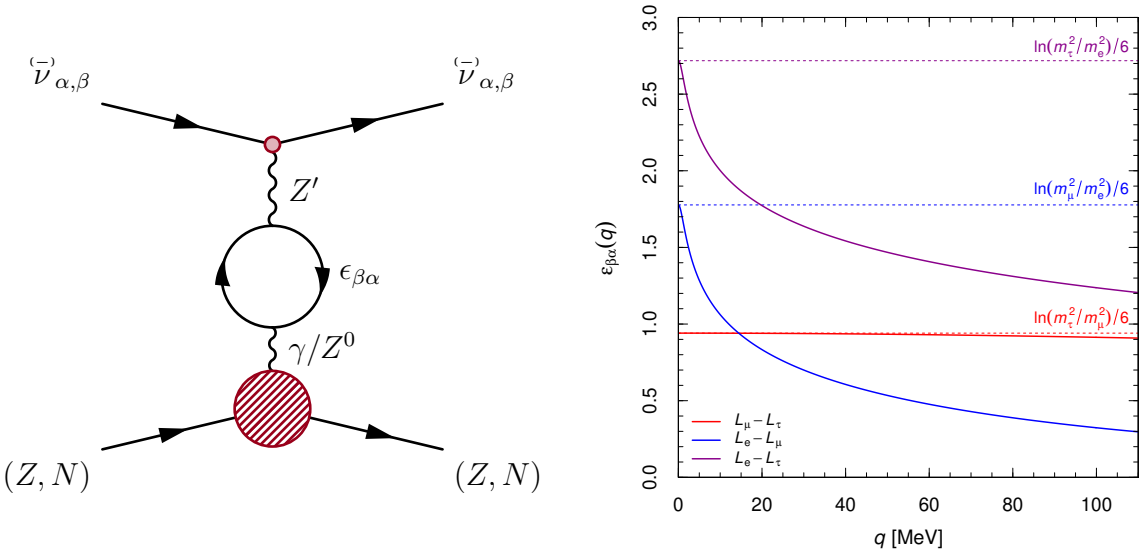

Figure 8.3: Left panel: Feynman diagram representing the CEνNS process mediated by a Z' model which interacts only with the α and β flavors. The interaction with the nucleus happens at the loop level through the kinetic mixing between the Z' boson and the SM Z^0 or γ. The loop kinetic mixing coupling $\varepsilon_{\beta\alpha}$ in Eq. 8.12 is shown in the right panel for each of the three $L_\alpha - L_\beta$ symmetries as a function of $q = |\vec{q}| \simeq \sqrt{2MT_{\rm nr}}$ in the range of the COHERENT CEνNS data.

loop kinetic mixing coupling, that is given by [443, 460, 461]

$$\varepsilon_{\beta\alpha}(|\vec{q}|) = \int_0^1 x(1-x)\ln\left(\frac{m_\beta^2 + x(1-x)|\vec{q}|^2}{m_\alpha^2 + x(1-x)|\vec{q}|^2}\right) dx\,, \tag{8.12}$$

where m_β and m_α are the charged lepton masses.

Note that the Z' contribution is invariant for $\alpha \leftrightarrows \beta$ since $L_\alpha - L_\beta$ and $L_\beta - L_\alpha$ are physically equivalent. Note also that the sign of the loop contribution of the i charged lepton to ν_ℓ scattering is given by $-Q'_i Q'_\ell$, where the minus comes from the negative electric charge of the charged lepton propagating in the loop. Therefore, the mass of the charged lepton with the same flavor ℓ of the scattering neutrino is always at the denominator of the logarithm in Eq. 8.12 and the mass of the other charged lepton taking part to the new symmetry is always at the numerator. The right panel of Fig. 8.3 shows the behaviour of $\varepsilon_{\beta\alpha}(|\vec{q}|)$ for each of the three $L_\alpha - L_\beta$ symmetries as a function of $|\vec{q}|$ in the range of the COHERENT CEνNS . One can see that only $\varepsilon_{\tau\mu}$ is almost constant, because $|\vec{q}| \ll m_\tau$ and $|\vec{q}| < m_\mu$. In this case, it is possible to approximate $\varepsilon_{\tau\mu} \simeq \ln(m_\tau^2/m_\mu^2)/6$, as done in Refs. [454, 455, 459]. On the other hand, for the symmetries $L_e - L_\mu$ and $L_e - L_\tau$ the $|\vec{q}|$ dependence of $\varepsilon_{\beta\alpha}$ on $|\vec{q}|$ must be taken into account, because $|\vec{q}| \gg m_e$. Fig. 8.4 illustrates the effects of the Z' contribution to the CEνNS differential event rates that are

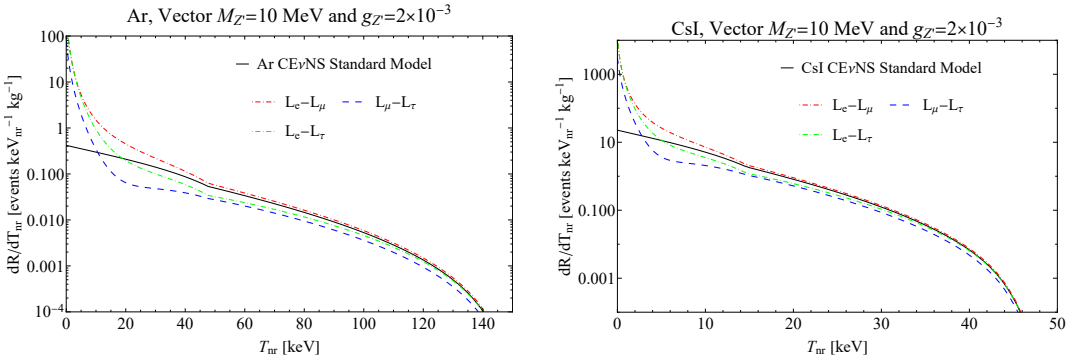

Figure 8.4: Predicted CEνNS differential event rates corresponding to the experimental configuration and data taking time of the COHERENT Ar and CsI detectors in the vector mediator models considered in this work.

predicted for the COHERENT Ar and CsI detectors in the $L_\alpha - L_\beta$ models. In these figures, we choose $g_{Z'} = 2 \times 10^{-3}$ and $M_{Z'} = 10$ MeV and we compared the model predictions with that of the SM.

In the case of the $L_\mu - L_\tau$ model the Z' contribution to $Q^V_{\mu,\mathrm{SM+V}}$ is positive and there can be a cancellation with the negative SM contribution.

8.1.2 Light Scalar Mediator

Non-standard neutrino interactions mediated by a scalar boson ϕ are possible if the SM fermion content is extended with the addition of right-handed neutrinos. The generic Lagrangian that describes the interaction of ϕ with neutrinos and quarks is

$$\mathcal{L}^S_\phi = -\phi \left[\sum_{\ell=e,\mu,\tau} g^{\nu_\ell}_\phi \, \overline{\nu_\ell} \, \nu_\ell + \sum_{q=u,d} g^q_\phi \, \overline{q} \, q \right], \tag{8.13}$$

where $\nu_\ell = \nu_{\ell L} + \nu_{\ell R}$ and $g^{\nu_\ell}_\phi$ and g^q_ϕ are the coupling constants. The contribution of the scalar boson interaction adds incoherently to the SM cross section [100, 312, 462–464]

$$\frac{d\sigma_{\nu_\ell\text{-}\mathcal{N}}}{dT_{\mathrm{nr}}} = \left(\frac{d\sigma_{\nu_\ell\text{-}\mathcal{N}}}{dT_{\mathrm{nr}}}\right)_{\mathrm{SM}} + \left(\frac{d\sigma_{\nu_\ell\text{-}\mathcal{N}}}{dT_{\mathrm{nr}}}\right)_{\mathrm{scalar}}, \tag{8.14}$$

with

$$\left(\frac{d\sigma_{\nu_\ell\text{-}\mathcal{N}}}{dT_{\mathrm{nr}}}\right)_{\mathrm{scalar}} = \frac{M^2 T_{\mathrm{nr}}}{4\pi E^2} \frac{(g^{\nu_\ell}_\phi)^2 \mathcal{Q}^2_\phi}{(|\vec{q}|^2 + M^2_\phi)^2}, \tag{8.15}$$

where $\mathcal{Q}_\phi$ is the scalar charge of the nucleus, given by

$$\mathcal{Q}_\phi = Z F_p(|\vec{q}|^2) \sum_{q=u,d} g^q_\phi \langle p|\bar{q}q|p\rangle + N F_n(|\vec{q}|^2) \sum_{q=u,d} g^q_\phi \langle n|\bar{q}q|n\rangle. \tag{8.16}$$

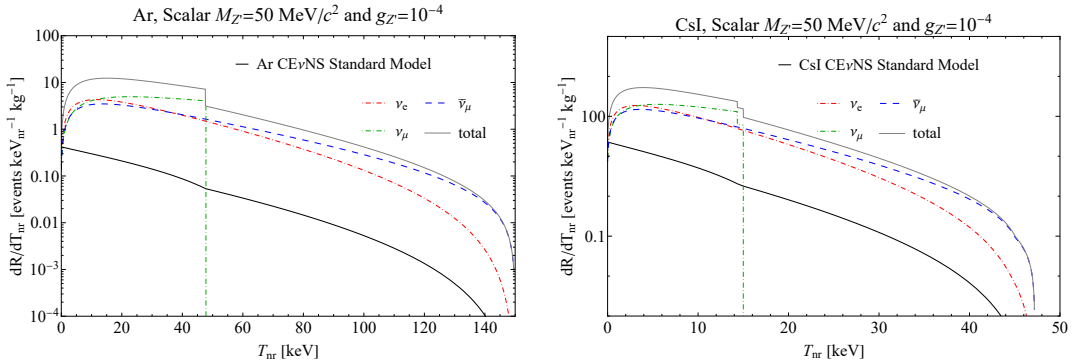

Figure 8.5: Predicted CEνNS differential event rates corresponding to the experimental configuration and data taking time of the COHERENT Ar and CsI detectors in the universal scalar mediator model.

It is sometimes written as [100, 312, 463, 464]

$$\mathcal{Q}_\phi = ZF_p(|\vec{q}|^2)\sum_{q=u,d} g_\phi^q \frac{m_p}{m_q} f_q^p + NF_n(|\vec{q}|^2)\sum_{q=u,d} g_\phi^q \frac{m_n}{m_q} f_q^n, \tag{8.17}$$

with the quark contributions to the nucleon masses

$$f_q^{\mathbb{N}} = \frac{m_q}{m_n}\langle \mathbb{N}|\bar{q}q|\mathbb{N}\rangle, \tag{8.18}$$

for $\mathbb{N} = p, n$. Since the scalar currents are not conserved, the scalar charges of the nucleons are not simply given by the sums of the charges of their valence quarks, as in the case of a vector boson mediator (see Eq. 8.5). The proton and neutron matrix elements of the scalar quark current must be calculated [465–468]. For simplicity, we consider equal couplings for the u and d quarks and equal couplings for ν_e and ν_μ

$$g_\phi^u = g_\phi^d = g_\phi^q \quad \text{and} \quad g_\phi^{\nu_e} = g_\phi^{\nu_\mu} = g_\phi^\nu. \tag{8.19}$$

Then, we have

$$\mathcal{Q}_\phi = g_\phi^q \left[ZF_p(|\vec{q}|^2)\langle p|\bar{u}u + \bar{d}d|p\rangle + NF_n(|\vec{q}|^2)\langle n|\bar{u}u + \bar{d}d|n\rangle\right]. \tag{8.20}$$

Considering the isospin approximation, we obtain[2]

$$\langle p|\bar{u}u + \bar{d}d|p\rangle = \langle n|\bar{u}u + \bar{d}d|n\rangle = \langle N|\bar{u}u + \bar{d}d|N\rangle = \frac{\sigma_{\pi N}}{\overline{m}_{ud}}, \tag{8.21}$$

[2]We neglect the small $|\vec{q}|$-dependent corrections discussed in Ref. [41].

where $\overline{m}_{ud} = (m_u + m_d)/2$ and $\sigma_{\pi N}$ is the pion-nucleon σ-term that has been determined in different ways in the literature (for a recent review see Ref. [469]). Recent values have been obtained from pionic atoms and pion-nucleon scattering [465, 470, 471] and from lattice calculations [466, 468]. Since there are large uncertainties on the values of $\sigma_{\pi N}$ and $\overline{m}_{ud}$, we choose a reference value for $\sigma_{\pi N}/\overline{m}_{ud}$ given by the ratio of the central value of $\sigma_{\pi N}$ determined in Ref. [465] ($\sigma_{\pi N} = 59.1\,\text{MeV}$) and the central PDG values [19] $m_u = 2.16\,\text{MeV}$ $m_d = 4.67\,\text{MeV}$, that gives

$$\left(\frac{\sigma_{\pi N}}{\overline{m}_{ud}}\right)_{\text{ref}} = 17.3, \tag{8.22}$$

that allows us to write the scalar cross section 8.15 as

$$\left(\frac{d\sigma_{\nu_\ell\text{-}\mathcal{N}}}{dT_{\text{nr}}}\right)_{\text{scalar}} = \frac{M^2 T_{\text{nr}}}{4\pi E^2} \frac{\tilde{g}_\phi^4}{(|\vec{q}|^2 + M_\phi^2)^2} \left(\frac{\sigma_{\pi N}}{\overline{m}_{ud}}\right)^2_{\text{ref}} \left[Z F_p(|\vec{q}|^2) + N F_n(|\vec{q}|^2)\right]^2, \tag{8.23}$$

with

$$\tilde{g}_\phi^2 = g_\phi^{\nu_\ell} g_\phi^q \frac{\sigma_{\pi N}/\overline{m}_{ud}}{(\sigma_{\pi N}/\overline{m}_{ud})_{\text{ref}}}. \tag{8.24}$$

In this way, the results of other calculations can be compared with our results by appropriate rescaling of $\tilde{g}_\phi$ according with the assumptions. We guess that $\tilde{g}_\phi$ is practically equal to g_ϕ in Ref. [307], where the expression 8.17 was used for the scalar charge of the nucleus, with the values of the $f_q^{\mathbb{N}}$'s given in Ref. [465], although the assumed values of the quark masses are not specified. Indeed, the values of the $f_q^{\mathbb{N}}$'s in Ref. [465] have been obtained from the value of $\sigma_{\pi N}$ using Eq. (13) of Ref. [472], which implies

$$\sum_{q=u,d} \frac{m_p}{m_q} f_q^p = \sum_{q=u,d} \frac{m_n}{m_q} f_q^n = \frac{\sigma_{\pi N}}{\overline{m}_{ud}}. \tag{8.25}$$

On the other hand, the approach in Refs. [100, 453, 473] considered different values for the proton and neutron matrix elements in Eq. 8.20: $\langle p|\bar{u}u + \bar{d}d|p\rangle = 15.1$ and $\langle n|\bar{u}u + \bar{d}d|n\rangle = 14$. These values correspond to a rather large 8% violation of the isospin symmetry. Let us also note that our treatment neglected the contribution of the strange and heavier quarks, whose contributions to the nucleon mass have very large uncertainties (see, e.g., Table 4 of Ref. [474]). If one wants to consider them, their contributions can be taken into account by rescaling appropriately $\tilde{g}_\phi$, assuming that the coupling of ϕ with all quarks is the same.

Fig. 8.5 illustrates the effect of the scalar boson mediator on the CEνNS differential event rates that are predicted for the COHERENT Ar and CsI detectors for

$\tilde{g}_\phi = 10^{-4}$ and $M_\phi = 50$ MeV. One can see that the total CEνNS rates are larger than the SM rates for all values of $T_{\rm nr}$, because the scalar boson cross section adds incoherently to the SM cross section, according to Eq. 8.14. In the two panels of Fig. 8.5 one can also notice that the total CEνNS rates represented by the grey lines have small discontinuities at $T_{\rm nr} = 47.7$ keV for Ar and $T_{\rm nr} \simeq 15$ keV for CsI. These values correspond to the maximum nuclear kinetic energy $T_{\rm nr}^{\rm max} = 2E_\nu^2/m_N$ for the monoenergetic ν_μ from pion decay ($E_\nu = 29.8$ MeV), as shown by the green-dashed lines that represent the ν_μ contributions. One can see that there is an effect also for the SM differential event rates, which change the slope at the same values of $T_{\rm nr}$. The effect for the scalar boson contribution is larger because it is enhanced by the $T_{\rm nr}$ in the numerator of the scalar cross section, see Eq. 8.15. Such a dependence causes also the decrease of the scalar contribution for very low values of $T_{\rm nr}$ that is visible in Fig. 8.5.

8.2 Constraints on Light Mediator Models

In this section, we present the results of the analyses of the COHERENT CsI and Ar data with the light-mediator models described in Sec. 8.1. Since the data are fitted well by the SM CEνNS prediction, we obtain constraints on the mass and coupling of the light mediator in each model. Let us note that the constraints that can be obtained with previous COHERENT CsI and Ar data have been presented in Refs. [450, 454, 461, 475–477] for the more popular universal, $B-L$, and $L_\mu - L_\tau$ models.

In the following subsections, we present the 2σ limits obtained from the COHERENT Ar and CsI data for the models discussed in Sec. 8.1 and we compare them with the constraints of other experiments by using the *darkcast* [478] code for recasting the limits in the different models under consideration. In particular, we compare the constraints on the light vector boson mediator obtained from the COHERENT data with the excluded regions obtained from searches of visible dark photon decays in beam dump (E141 [479], E137 [480], E774 [481], KEK [482], Orsay [483–485], ν-CAL I [486–489], CHARM [490, 491], NOMAD [492], and PS191 [493, 494]), fixed target (A1 [495] and APEX [496]), collider (BaBar [497], KLOE [498, 499], LHCb [500]), and rare-meson-decay (NA48/2 [501]) experiments, and searches of invisible dark photons decays in the NA64 [502] and BaBar [503] experiments. We also compare the constraints with the excluded

model	CsI+Ar	
	$g_{Z'}$(low $M_{Z'}$)	$\frac{g_{Z'}}{M_{Z'}}$(high $M_{Z'}$)
universal	2.07×10^{-5}	0.48×10^{-3}
$B-L$	4.42×10^{-5}	0.99×10^{-3}
$L_\mu - L_\tau$	103×10^{-5}	24.2×10^{-3}
	$\tilde{g}_\phi$(low M_ϕ)	$\frac{\tilde{g}_\phi}{M_\phi}$(high M_ϕ)
scalar	1.68×10^{-5}	0.30×10^{-3}

Table 8.2: The 2σ upper bounds on the coupling of the new boson mediator obtained from the combined analyses of the Ar and CsI COHERENT CEνNS data for low and high values of the boson mass for the selection of the models considered in this thesis. $g_{Z'}/M_{Z'}$ and $\tilde{g}_\phi/M_\phi$ are in units of GeV^{-1}. See Tab. II of Ref. [2] for the constraints on the models listed in Tab. 8.1.

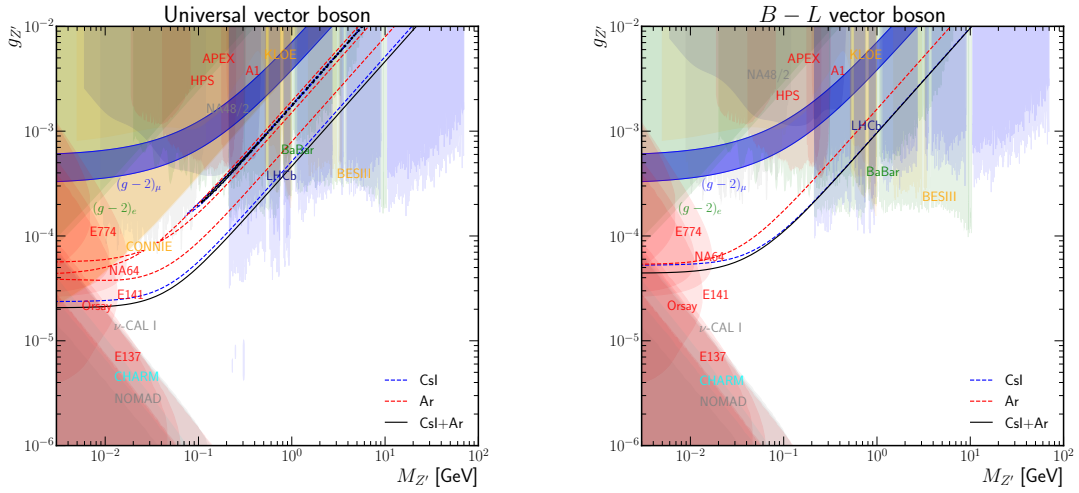

Figure 8.6: Excluded regions (2σ) in the $M_{Z'}$-$g_{Z'}$ plane for the universal vector mediator model (left panel), $B-L$ vector mediator (right panel).

regions obtained from the global analysis of oscillation data (OSC)[504].

8.2.1 Universal Z' model

Fig. 8.6 shows the 2σ limits that we obtained from the COHERENT Ar and CsI data for the universal Z' model [311, 450–455]. The black lines delimits the 2σ allowed regions obtained from the combined analysis of the CsI and Ar data, while the blue and red lines delimit the excluded regions obtained from the CsI and Ar data, respectively. Considering the combined analysis of the CsI and Ar data, one can see that in the low-mass region the black line, which represents the upper

boundary of the 2σ allowed region, flattens due to the fact that the contribution of the Z' boson mass to $Q^V_{\ell,\mathrm{SM+V}}$ is small. This happens for $M_{Z'} \ll 100$ MeV, because $g_{Z'}$ is small and the boundary does not depend on $M_{Z'}$ since $|\vec{q}| \gg M_{Z'}$ in the Z' boson propagator. On the other hand, for higher masses, the contribution of the Z' boson is suppressed by a large $M_{Z'}$, which is dominant in the propagator, and the boundary is given by a diagonal line proportional to $M_{Z'}$. The numerical values of the 2σ limits in these two simple cases are given in Table 8.2. In the upper-middle part of Fig. 8.6, for the universal model, one can see that a thin diagonal strip is present: this is generated by the degeneracy between the SM cross section and the light mediator contribution,$Q^V_{\ell,\mathrm{SM+V}} \simeq -Q^V_{\mathrm{SM}}$. Neglecting the form factors and the small proton SM contribution, one can find that the thin allowed strip corresponds to

$$(g^{\mathrm{univ}}_{Z'})_{\mathrm{strip}} \simeq \sqrt{\frac{N}{A}\frac{\sqrt{2}G_F M^2_{Z'}}{3}} \simeq 1.8 \times 10^{-3}\,\frac{M_{Z'}}{\mathrm{GeV}}, \tag{8.26}$$

taking into account that $(N/A)_{\mathrm{Ar}} \simeq (N/A)_{\mathrm{CsI}} \simeq 0.58$. Note that the existence of the allowed strip in the universal model is related to the possibility of having a cancellation of the CEνNS differential event rate as a consequence of the different signs of the SM and Z' contributions to $Q^V_{\ell,\mathrm{SM+V}}$ as shown in Eq. 8.10. Indeed, all the models that can have a cancellation of the CEνNS differential as discussed in Sec. 8.1 (i.e. the universal, $B_y + L_\mu + L_\tau$, $L_e - L_\tau$, and $L_\mu - L_\tau$ models) have an allowed strip. The cancellation occurs in the excluded parameter space between the lower allowed region and the thin allowed strip for

$$(g^{\mathrm{univ}}_{Z'})_{\mathrm{canc}} \simeq \sqrt{\frac{N}{A}\frac{\sqrt{2}G_F M^2_{Z'}}{6}} \simeq 1.3 \times 10^{-3}\,\frac{M_{Z'}}{\mathrm{GeV}}, \tag{8.27}$$

where we neglected the form factors and the small proton SM contribution. One can see from Fig. 8.6 that the limits obtained from the CsI data are stricter than those obtained from the Ar data and are close to those of the combined fit.

In Fig. 8.6 we compared the limits obtained from the COHERENT CEνNS data with those of non-CEνNS experiments and those of the CONNIE reactor CEνNS experiment [204]. Fig. 8.6 shows also the $(g-2)_\mu$ 2σ allowed band which can explain the anomalous magnetic moment of the muon in this model [401, 403]. One can see that the explanation of the $(g-2)_\mu$ anomaly with the universal model is excluded by the combination of the non-CEνNS exclusion limits in Fig. 8.6, by the CONNIE CEνNS bounds alone, and by the COHERENT CEνNS limits alone, which confirm and extend the CONNIE CEνNS bounds. Moreover, the COHER-

ENT CEνNS limits extend the total exclusion region by covering a previously not-excluded area for 20 MeV $\lesssim M_{Z'} \lesssim$ 200 MeV and $2 \times 10^{-5} \lesssim g_{Z'} \lesssim 10^{-4}$. The new COHERENT CE$\nu$NS limits are consistent with those obtained in Ref. [454] using the first COHERENT CsI data and slightly extend the COHERENT CEνNS exclusion region. It is worth mentioning that the inclusion of the electron scattering channel, which has not been included in this work, is responsible for a significant improvement of the constraints for $M_{Z'} \lesssim 0.1$ MeV [227, 314].

8.2.2 B-L model

The gauged $B - L$ model is the most popular Z' model (see, e.g., the reviews in Refs. [449, 505, 506]) and its effects in CEνNS have been studied in Refs. [307, 454, 455, 504, 507] using previous COHERENT data. The right panel of Fig. 8.6 shows the 2σ limits that we obtained from the COHERENT Ar and CsI data, compared with the limits obtained from other experiments and the $(g-2)_\mu$ 2σ allowed band in this model. One can see that the bounds obtained by experiments using only leptonic probes are the same as those for the universal model in Fig. 8.6, because of the same magnitudes of the lepton charges (see Tab. 8.1). The coupling $g_{Z'}$ is well constrained by the accelerator experiments for large values of $M_{Z'}$ and fixed target experiments for small values of $M_{Z'}$. Note also that the allowed region for $(g-2)_\mu$ is the same as that in the universal model, because the magnetic moment of the muon is not dependent on the couplings of quarks.

On the other hand, the CEνNS bounds are different from the universal model, because the Z' contribution to $Q^V_{\mu,\mathrm{SM+V}}$ is negative and adds to the negative SM contribution. Therefore, in Fig. 8.6 there are only the upper bounds shown by the blue-dashed, red-dashed, and black-solid lines that we obtained from the CsI, Ar, and combined analyses, respectively. These limits have the same behaviour as the corresponding ones discussed in Subsec. 8.2.1 for the universal model but are weaker because the quark charges are smaller by a factor of 3, as shown in Tab. 8.1. The numerical values of the limits for small and large values of $M_{Z'}$ are given in Table 8.2.

Fig. 8.6 shows that, as in the universal model, the COHERENT CEνNS limit confirms the exclusion of the explanation of the $(g-2)_\mu$ anomaly with the $B - L$ model and extends the total exclusion region of non-CEνNS experiments by covering a previously not-excluded area for 10 MeV $\lesssim M_{Z'} \lesssim$ 200 MeV and $5 \times 10^{-5} \lesssim g_{Z'} \lesssim 3 \times 10^{-4}$. Also in this case, the new COHERENT CEνNS limits are

consistent with those obtained in Ref. [454] using the first COHERENT CsI data and slightly extend the COHERENT CEνNS exclusion region.

8.2.3 $L_\mu - L_\tau$ model

The left panel of Fig. 8.7 shows the 2σ limits that we obtained from the COHERENT Ar and CsI data in the popular $L_\mu - L_\tau$ model [436, 454, 455, 459–461, 508, 509].

From Fig. 8.7, one can also see that there is an allowed diagonal strip that is the region of the parameters where $Q^V_{\ell,\mathrm{SM+V}} \simeq -Q^V_{\mathrm{SM}}$, which is due to the different signs of the SM and Z' contributions to $Q^V_{\ell,\mathrm{SM+V}}$, as discussed above. Since $\varepsilon_{\tau\mu} \simeq \ln(m_\tau^2/m_\mu^2)/6$, as discussed in Subsec. 8.1.1, the allowed diagonal strip corresponds to

$$(g_{Z'}^{L_\mu - L_\tau})_{\mathrm{strip}} \approx \sqrt{\frac{N}{Z}\frac{6\pi G_F M_{Z'}^2}{\sqrt{2}\alpha_{\mathrm{EM}}\ln(m_\tau^2/m_\mu^2)}} \approx 7\times 10^{-2}\,\frac{M_{Z'}}{\mathrm{GeV}}, \tag{8.28}$$

where we considered $N/Z \approx 1.3$. One can see from Fig. 8.7 that in the $L_\mu - L_\tau$ model there are several non-CEνNS constraints whose combination is more stringent than those given by the current COHERENT CEνNS data: CMS [510] ($Z \to Z'\mu\mu \to 4\mu$), BaBar [511] ($e^+e^- \to Z'\mu\mu \to 4\mu$), CCFR [512, 513] (neutrino trident production), and Borexino [509, 514, 515] (Z'-mediated solar neutrino interactions). These non-CEνNS constraints exclude the allowed diagonal strip corresponding to Eq. 8.28. On the other hand, they do not completely exclude the $(g-2)_\mu$ 2σ allowed band in this model, that is shown in Fig. 8.7. One can see that the part of this band for 10 MeV $\lesssim M_{Z'} \lesssim 200$ MeV and $3\times 10^{-4} \lesssim g_{Z'} \lesssim 10^{-3}$ eludes the exclusions, but will be covered by future COHERENT experiments as discussed in Sec. 8.3.

8.2.4 Scalar model

The right panel of Fig. 8.7 shows the 2σ limits that we obtained from the COHERENT Ar and CsI data in the scalar boson mediator model described in Subsec. 8.1.2. The figure shows also the $(g-2)_\mu$ 2σ allowed band in this model and the constraints obtained from the measurement of neutrons scattering on a ^{208}Pb target [516–518], the measurement of τ, mesons, and Z decays [519–524], and double-beta decay experiments [519, 525–527] (see also the summary in

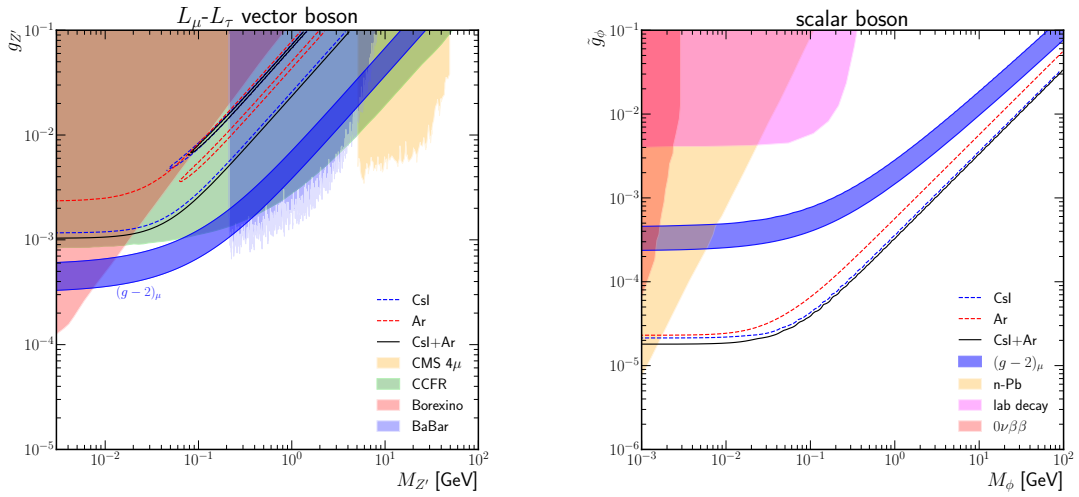

Figure 8.7: Excluded regions (2σ) in the $M_{Z'}$-$g_{Z'}$ plane for the $L_\mu - L_\tau$ vector mediator (left panel) and scalar model (right panel).

Ref. [473]). One can see from Fig. 8.7 that the COHERENT CEνNS constraints are much more stringent than the non-CEνNS bounds for $M_\phi \gtrsim 2$ MeV and they exclude the explanation of the $(g-2)_\mu$ anomaly in the scalar boson mediator model.

8.3 Projections on Light Mediator Models From Future CEνNS Detectors

The aim of this concluding section is to highlight the potential of the upcoming COH-Cryo-CsI and NUCLEUS detectors in constraining light mediator models. The studies presented will focus on the $L_\mu - L_\tau$ model for the COH-Cryo-CsI detectors, while the NUCLEUS sensitivities will address the universal[3] light mediator scenario. We anticipate that the Cryo-CsI constraints will surpass those from the Ar-750 detector, primarily due to the lower experimental threshold. A more detailed analysis regarding the COHERENT sensitivities, including a broader range of models and the Ar-750 constraints, will be presented in an upcoming publication. The sensitivities are obtained by considering 3 SNS-years of data taking for COH-Cryo-CsI and 3 years of exposure with 0.8 reactor duty cycle factor for a NUCLEUS-like detector located at the VNS.

The results are presented in Fig. 8.8. The left panel shows the constraints on the $L_\mu - L_\tau$ model, where, thanks to the increased statistics and the lower energy

[3]Since reactor data consist of $\bar{\nu}_e$, they cannot be used to probe the $L_\mu - L_\tau$ model.

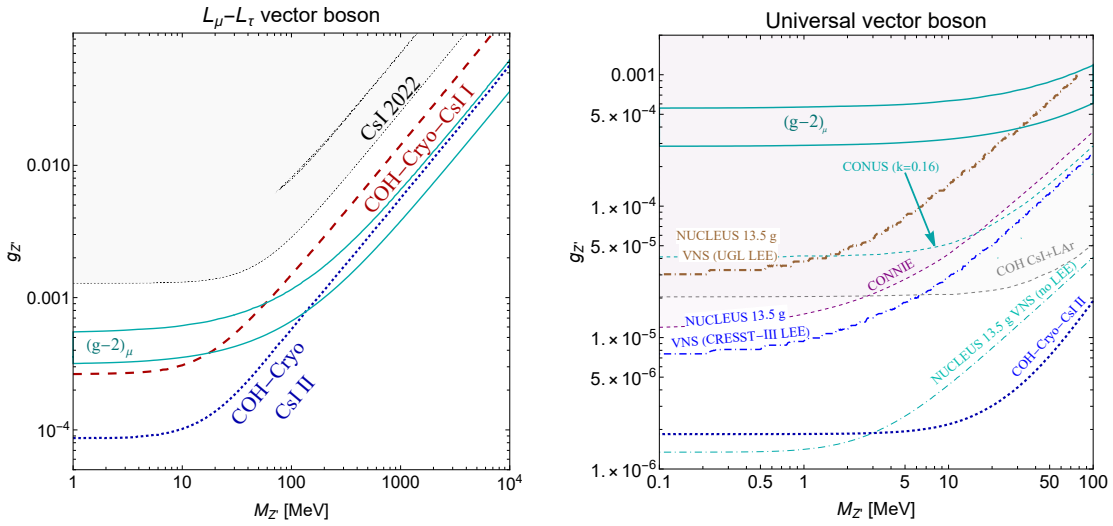

Figure 8.8: Excluded regions (2σ) in the $M_{Z'}$-$g_{Z'}$ plane for the $L_\mu - L_\tau$ vector mediator model (left panel) and for the universal light mediator model (right panel) expected in COH-Cryo-CsI detectors assuming three SNS-years, and in the NUCLEUS set-up assuming three years of exposure and 0.8 duty cycle factor.

threshold, the new Cryo-CsI detectors will substantially improve the constraints compared to the current CsI ones. Notably, the results from COH-Cryo-CsI I are in perfect agreement with the official COHERENT results reported in Ref. [187]. Looking forward, the future COH-Cryo-CsI II detectors will explore nearly the entire parameter space for explaining the $(g-2)_\mu$ anomaly in terms of a $L_\mu - L_\tau$ gauge boson for $M_{Z'} \lesssim 200$ MeV.

The right panel of Fig. 8.8 shows the expected sensitivity for the universal light mediator model under different physics cases. The sensitivities are compared with existing CEνNS constraints from COHERENT (Fig. 8.6), CONUS [208] and CONNIE [204]. For future perspectives with the CONUS experiment refer to Refs. [343, 528].

Since light vector mediator models predict an enhancement of the event rate at low energies, as shown e.g. Fig. 8.2, the NUCLEUS-like experiment located at the VNS will significantly benefit from the exceptionally low threshold of $20\ \mathrm{eV_{nr}}$ assumed in this study. Here we do not consider the situation where the NUCLEUS detector is located 15 meters from the reactor core, which would benefit from increased statistics. Specifically, if the LEE is not observed and a 100 dru flat background is reached at the VNS, the experiment will be able to probe a huge unexplored region of the parameter space, being even stronger than COH-Cryo-CsI II for $M_{Z'} \lesssim 3$ MeV. Let us now focus on the situation where the LEE is observed at the VNS such that the signal-to-background ratio would be $\ll 1$. In

this case, the standard χ^2 analysis cannot be performed in the presence of unknown background, and one should rely on statistical methods to put an upper limit without performing any background subtraction analysis. Here, the Erickceck *et al*. method [303] described in Chap. 5 comes into play. Intriguingly, if the NUCLEUS Collaboration reaches a LEE level compatible with CRESST-III, the experiment will be able to place a limit which would improve compared to existing CEνNS bounds for $M_{Z'} \lesssim 8\ \mathrm{MeV}$. Even the observation of a LEE about four orders of magnitude higher compared to the SM CEνNS, i.e. the UGL LEE described in Sec. 5.3, would permit to obtain a limit competitive compared to CEνNS existing bounds. These results demonstrate that NUCLEUS has the potential to explore new physics scenarios even in the presence of a consistent low-energy excess, by leveraging the low-detection threshold of the experiment.

Conclusions

This thesis investigated the phenomenology of neutrino interactions at low energies to examine electroweak physics and to search for signatures beyond the Standard Model. To do so, we exploited the promising avenue of coherent elastic neutrino-nucleus scattering (CEνNS), together with the well-established elastic neutrino-electron scattering (νES) process. As described in Chap. 1, a precise description of the CEνNS cross section, including radiative corrections and accurate nuclear form factor models, is essential for interpreting current data and will be even more critical for future high-precision detectors.

In particular, we discussed the COHERENT experiments, which marked a significant milestone in neutrino physics providing the first observation of CEνNS by employing neutrinos from the stopped pion decay-at-rest. The results from COHERENT not only validated the theoretical predictions but also set the stage for future experiments aiming to perform precision tests of the Standard Model with CEνNS.

In addition, we examined the rapidly growing field of reactor-based CEνNS searches, discussing the current state-of-the-art and presenting the main challenges. Specifically, we focused on the behavior of the germanium quenching factor at low energies, which remains a topic of ongoing debate and is crucial for interpreting the observations from the NCC-1701 detector at the Dresden-II power plant in terms of a CEνNS signal. By investigating the Migdal effect, we gained new insights into low-energy mechanisms that could leave observable imprints in the data. We demonstrated that the standard Migdal contribution is orders of magnitude subdominant in the region of interest for reactor CEνNS searches using germanium detectors, and it cannot explain the unexpected low-energy enhancement observed by Dresden-II regardless of the formalism employed to model the Migdal effect [6]. Within this worldwide search, the NUCLEUS project, with its ultra-low-threshold detectors, represents an innovative experiment for the precise measure-

ment of the CEνNS cross sections from reactor $\bar{\nu}_e$. In this thesis, we have given a description of the NUCLEUS detectors addressing the primary challenges that limit the experiment's sensitivity, particularly the unexpected low-energy-excess (LEE) which affects many low-threshold rare-event searches.
In addition, we have demonstrated the extensive physics potential of CEνNS measurements from available COHERENT data on CsI and LAr measurements, as well as Dresden-II data, to pose exciting determinations on the weak mixing angle and nuclear physics parameters [5]. In this sense, we found that the COHERENT CsI data shows about 6 σ evidence for the coherency loss due to nuclear structure, as shown in Fig. 6.2. In turn, this has been translated into a determination of the average rms neutron distribution radius of ^{133}Cs and ^{127}I at the $\sim$7% precision level. Interestingly, we have noticed that a common feature of electroweak probes is an intrinsic degeneracy between the weak mixing angle and the nuclear neutron radius in the cross section. Despite the tendency of this degeneracy to broaden the precision of the analysis of various experimental data, it is possible to break it by combining different probes. Specifically, we presented the result of a global fit including COHERENT CsI data in combination with atomic parity violation experiments on cesium and lead, as well as parity violation electron scattering data on lead, to obtain a refined extraction of these parameters through a data-driven approach. Fig. 6.5, shows the result of our global fit, and at 1σ confidence level we found [8]

$$\mathrm{EW-Combined}: \quad \sin^2\vartheta_W = 0.2396 \pm 0.0017, \quad R_n(\mathrm{Cs}) = 5.04 \pm 0.06 \text{ fm}.$$

These results are consistent with the Standard Model predictions for the weak mixing angle and align well with the neutron distribution radius estimated by nuclear shell models. The extraction of the weak mixing angle from this data-driven approach should surpass the value reported by the Particle Data Group. We also explored the sensitivity of future CEνNS experiments in constraining such parameters, finding that the next generation of COHERENT detectors might be able to enter the era of precision physics with CEνNS, offering complementary insights compared to other electroweak probes. We found that the future COHERENT Cryo-CsI detectors will be able to reach a percent level precision in the extraction of the weak mixing angle, as well as a sub percent level in the extraction of the neutron distribution radius of cesium and iodine. In addition, we foresee that the future COHERENT liquid argon detector will be able to provide a first determina-

tion of the neutron radius of $^{40}\mathrm{Ar}$ which will benefit from the use of underground argon to reduce intrinsic background. The complementarity with reactor CEνNS experiments was also investigated. Since precision physics requires a thorough understanding of the background, we considered the scenario where the LEE is removed by NUCLEUS, demonstrating that the experiment could achieve a measurement of the weak mixing angle with an accuracy of approximately 10%. Although this precision is less robust compared to the expected accuracy attainable with future COHERENT data, this extraction is unaffected by nuclear structure uncertainties and is conducted at an even lower and unexplored energy regime.
We also studied the electromagnetic properties of neutrinos, such as the neutrino magnetic moment, neutrino electric charge and neutrino charge radius. The latter is, remarkably, the only neutrino electromagnetic property predicted to be non-zero in the Standard Model. In this thesis, we discussed the need to properly account for the non-null momentum transfer of the experiments in the calculation of the neutrino charge radius radiative correction, with a significant impact in the interpretation of current and future neutrino scattering experiments aiming to extract this quantity. Building upon the formalism developed, we significantly reduce the allowed parameter space when combining available CEνNS data [7]. In particular, we obtained a competitive limit on $\langle r^2_{\nu_e} \rangle$ at 90% CL, namely

$$-9.5 < \langle r^2_{\nu_e} \rangle \, [10^{-32}\,\mathrm{cm}^2] < 5.5,$$

which is able to improve the best upper bound limit for $\langle r^2_{\nu_e} \rangle$ previously set by TEXONO. Unfortunately, the available CEνNS and νES data only allow setting constraints that are one order of magnitude larger than the SM prediction for the neutrino charge radii. However, we show that the next generation of detectors being developed by COHERENT will significantly improve the current constraints on both electronic and muonic flavors, while also demonstrating that NUCLEUS will play a crucial role in constraining the neutrino charge radius associated with the electronic flavor. In addition, we found that the next-to-next generation of the COHERENT cryogenic CsI detector will collect enough statistics to exclude the null hypothesis of no neutrino charge radius for both electronic and muonic flavors at approximately $1\ \sigma$ CL.
Moreover, while we discussed that neutrino-induced backgrounds from CEνNS and νES could pose a significant challenge for the detection of low-mass dark matter candidates in the DarkSide-20k dark matter experiment, we showed that

νES from solar neutrinos can also be the source of a signal in presence of some beyond the standard model neutrino properties. In fact, one of the main results obtained in this thesis was the examination of new physics scenarios predicting the existence of a neutrino magnetic moment and electric charge within the context of the LUX-ZEPLIN data, which allowed us to set some of the strongest laboratory limits available in the literature. Specifically, at the 90% CL we obtained

$$\mu_\nu^{\text{eff}} < 1.1 \cdot 10^{-11}\ \mu_B, \qquad |q_\nu^{\text{eff}}| < 1.5 \cdot 10^{-13}\ e_0.$$

Remarkably, such constraints have been considered in the latest version of the Particle Data Group [31] as being only one order of magnitude less stringent than the indirect constraints determined by the observation of astrophysical sources.
In conclusion, we also illustrated various scenarios beyond the Standard Model predicting the existence of light gauge boson mediators from a novel $U(1)'$ gauge symmetry, which could manifest as a signature in the experimental data. We presented different models, considering both vector and scalar mediators, and analysed the COHERENT data to set constraints on the strength of the new interaction and the mass of the additional mediator. In most of the considered models, the COHERENT data allowed us to extend existing bounds, particularly in the intermediate mass range, around a few hundred MeVs. In particular, we compared our results with the parameter space which would explain the famous muon anomalous magnetic moment discrepancy, which remains one of the most compelling measurements in modern physics. Thanks to the bounds obtained, the explanation of the $(g-2)_\mu$ anomaly in terms of an extra light mediator is rather unlikely. However, it is worth mentioning that the particular $L_\mu - L_\tau$ model, where the new gauge boson couples only to the μ and τ flavor, is still quite unconstrained for masses $M_Z' \sim [10 - 200]$ MeV but will be probed with future COHERENT experiments. In fact, extending these light mediator model studies to the future COHERENT and NUCLEUS detectors, we show that the former will play a major role in constraining the $L_\mu - L_\tau$ model. Furthermore, as shown in Fig. 8.8, we demonstrated that NUCLEUS, thanks to its low experimental threshold, will set relevant constraints on such a new physics model which predicts an increased number of events at low energies, even in the presence of the unknown LEE background, which might be orders of magnitude larger than the CEνNS signal.

Appendices

A

Z_{eff} tables

The effective electron charge of the target atom, $Z^{\mathcal{A}}_{\text{eff}}(T_e)$, for Ge A.4, I A.1, Xe A.2, Cs A.3.

$$
Z^{\text{I}}_{\text{eff}} = \begin{cases}
53, & T_e > 33.17 \text{ keV} \\
51, & 33.17 \text{ keV} \geq T_e > 5.19 \text{ keV} \\
49, & 5.19 \text{ keV} \geq T_e > 4.86 \text{ keV} \\
47, & 4.86 \text{ keV} \geq T_e > 4.56 \text{ keV} \\
43, & 4.56 \text{ keV} \geq T_e > 1.07 \text{ keV} \\
41, & 1.07 \text{ keV} \geq T_e > 0.93 \text{ keV} \\
39, & 0.93 \text{ keV} \geq T_e > 0.88 \text{ keV} \\
35, & 0.88 \text{ keV} \geq T_e > 0.63 \text{ keV} \\
31, & 0.63 \text{ keV} \geq T_e > 0.62 \text{ keV} \\
25, & 0.62 \text{ keV} \geq T_e > 0.19 \text{ keV} \\
23, & 0.19 \text{ keV} \geq T_e > 0.124 \text{ keV} \\
21, & 0.124 \text{ keV} \geq T_e > 0.123 \text{ keV} \\
17, & T_e < 0.123 \text{ keV}
\end{cases}
$$

Table A.1: The effective electron charge of the target atom, $Z^{\mathcal{A}}_{\text{eff}}(T_e)$, for I.

$$
Z_{\text{eff}}^{\text{Xe}} = \begin{cases}
54, & T_e > 34.561 \text{ keV} \\
52, & 34.561 \text{ keV} \geq T_e > 5.4528 \text{ keV} \\
50, & 5.4528 \text{ keV} \geq T_e > 5.1037 \text{ keV} \\
48, & 5.1037 \text{ keV} \geq T_e > 4.7822 \text{ keV} \\
44, & 4.7822 \text{ keV} \geq T_e > 1.1487 \text{ keV} \\
42, & 1.1487 \text{ keV} \geq T_e > 1.0021 \text{ keV} \\
40, & 1.0021 \text{ keV} \geq T_e > 0.9406 \text{ keV} \\
36, & 0.9406 \text{ keV} \geq T_e > 0.689 \text{ keV} \\
32, & 0.689 \text{ keV} \geq T_e > 0.6764 \text{ keV} \\
26, & 0.6764 \text{ keV} \geq T_e > 0.2132 \text{ keV} \\
24, & 0.2132 \text{ keV} \geq T_e > 0.1467 \text{ keV} \\
22, & 0.1467 \text{ keV} \geq T_e > 0.1455 \text{ keV} \\
18, & 0.1455 \text{ keV} \geq T_e > 0.0695 \text{ keV} \\
14, & 0.0695 \text{ keV} \geq T_e > 0.0675 \text{ keV} \\
10, & 0.0675 \text{ keV} \geq T_e > 0.0233 \text{ keV} \\
4, & 0.0233 \text{ keV} \geq T_e > 0.0134 \text{ keV} \\
2, & 0.0134 \text{ keV} \geq T_e > 0.0121 \text{ keV} \\
0, & T_e \leq 0.0121 \text{ keV}
\end{cases}
$$

Table A.2: The effective electron charge of the target atom, $Z_{\text{eff}}^{\text{Xe}}(T_e)$.

$$
Z_{\text{eff}}^{\text{Cs}} = \begin{cases}
55, & T_e > 35.99 \text{ keV} \\
53, & 35.99 \text{ keV} \geq T_e > 5.71 \text{ keV} \\
51, & 5.71 \text{ keV} \geq T_e > 5.36 \text{ keV} \\
49, & 5.36 \text{ keV} \geq T_e > 5.01 \text{ keV} \\
45, & 5.01 \text{ keV} \geq T_e > 1.21 \text{ keV} \\
43, & 1.21 \text{ keV} \geq T_e > 1.07 \text{ keV} \\
41, & 1.07 \text{ keV} \geq T_e > 1 \text{ keV} \\
37, & 1 \text{ keV} \geq T_e > 0.74 \text{ keV} \\
33, & 0.74 \text{ keV} \geq T_e > 0.73 \text{ keV} \\
27, & 0.73 \text{ keV} \geq T_e > 0.23 \text{ keV} \\
25, & 0.23 \text{ keV} \geq T_e > 0.17 \text{ keV} \\
23, & 0.17 \text{ keV} \geq T_e > 0.16 \text{ keV} \\
19 & T_e < 0.16 \text{ keV}
\end{cases}
$$

Table A.3: The effective electron charge of the target atom, $Z_{\text{eff}}^{\mathcal{A}}(T_e)$, for Cs.

$$
Z_{\text{eff}}^{\text{Ge}} = \begin{cases}
32, & T_e > 11.103 \text{ keV} \\
30, & 11.103 \text{ keV} \geq T_e > 1.4146 \text{ keV} \\
28, & 1.4146 \text{ keV} \geq T_e > 1.2481 \text{ keV} \\
26, & 1.2481 \text{ keV} \geq T_e > 1.217 \text{ keV} \\
22, & 1.217 \text{ keV} \geq T_e > 0.1801 \text{ keV} \\
20, & 0.1801 \text{ keV} \geq T_e > 0.1249 \text{ keV} \\
18, & 0.1249 \text{ keV} \geq T_e > 0.1208 \text{ keV} \\
14, & 0.1208 \text{ keV} \geq T_e > 0.0298 \text{ keV} \\
10, & 0.0298 \text{ keV} \geq T_e > 0.0292 \text{ keV} \\
4, & T_e \leq 0.0292 \text{ keV}
\end{cases}
$$

Table A.4: The effective electron charge of the target atom, $Z_{\text{eff}}^{\mathcal{A}}(T_e)$, for Ge.

B

2-D Distribution of COHERENT CsI Data

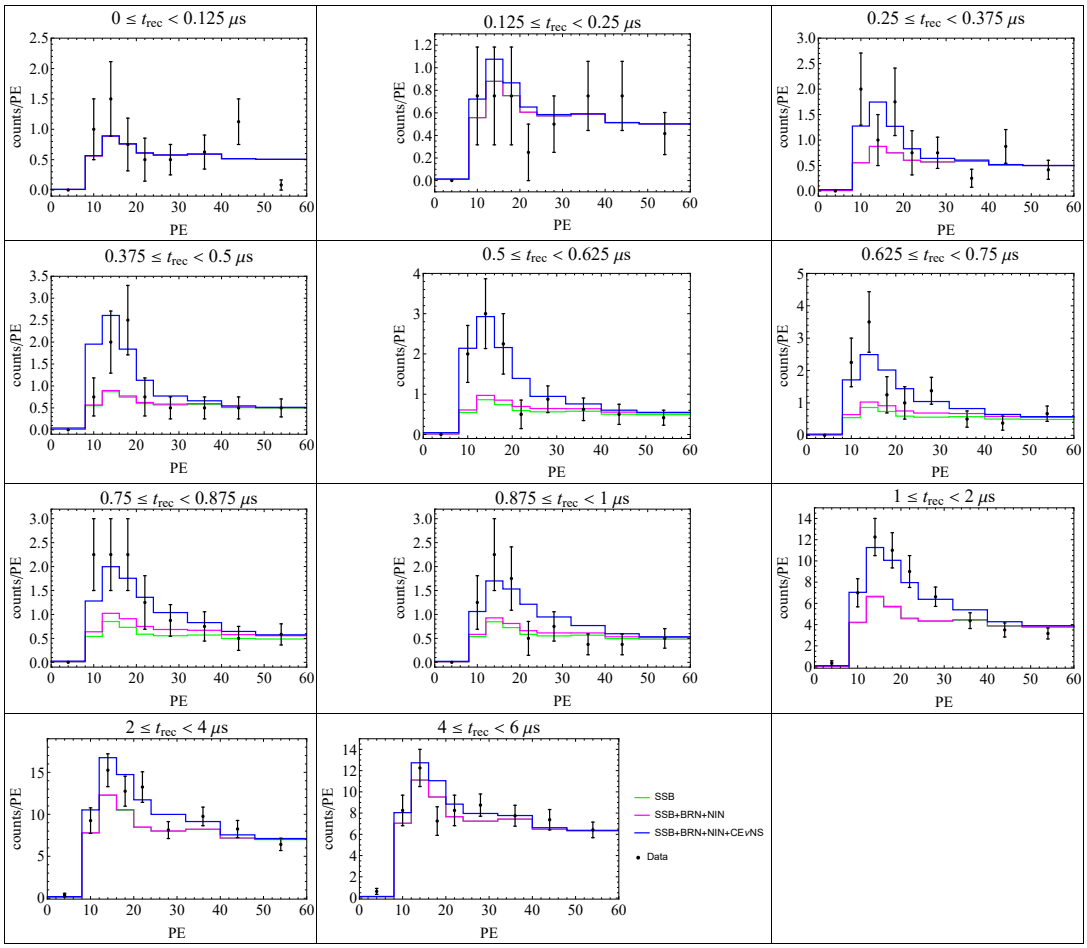

Figure B.1: 2-Dimensional distribution of events recorded by the CsI detector [163]. The data are compared with the SSB, BRN and NIN backgrounds, as well as the CEνNS prediction.

C

Comments on the Z' coupling

Let us start by considering the relevant vector part of the Standard Model neutral-current weak interaction Lagrangian (see, e.g., Refs. [17, 19])

$$\mathcal{L}_Z^V = -\frac{g}{2\cos\vartheta_{\mathrm{W}}} Z_\mu \left[2g_V^\nu \sum_{\ell=e,\mu,\tau} \overline{\nu_{\ell L}}\gamma^\mu \nu_{\ell L} + \sum_{q=u,d} g_V^q\, \overline{q}\gamma^\mu q \right], \tag{C.1}$$

with the tree-level couplings

$$g_V^\nu = \frac{1}{2}, \quad g_V^u = \frac{1}{2} - \frac{4}{3}\sin^2\vartheta_{\mathrm{W}}, \quad \text{and} \quad g_V^d = -\frac{1}{2} + \frac{2}{3}\sin^2\vartheta_{\mathrm{W}}. \tag{C.2}$$

Confronting Eq. (C.1) with the Lagrangian (8.4), one can see that the Z' vector interaction of left-handed neutrinos with quarks is obtained from the vector part of the Standard Model neutral-current interaction with the substitutions

$$\frac{g}{2\cos\vartheta_{\mathrm{W}}} 2g_V^\nu \to g_{Z'}^{\nu_\ell V}, \quad \frac{g}{2\cos\vartheta_{\mathrm{W}}} g_V^q \to g_{Z'}^{qV}, \quad \text{and} \quad m_Z \to m_{Z'}. \tag{C.3}$$

This correspondence is shown in Fig. C.1, where we depicted the two Feynman diagrams that describe the neutrino-quarks interactions that contribute to CEνNS at tree level. The total amplitude is given by the sum of the two diagrams

$$A \propto \frac{g^2}{4\cos^2\vartheta_{\mathrm{W}}} \frac{2g_V^\nu g_V^q}{q^2 - m_Z^2} + \frac{g_{Z'}^{\nu_\ell V} g_{Z'}^{qV}}{q^2 - m_{Z'}^2}. \tag{C.4}$$

Taking into account that $g_V^\nu = 1/2$ and

$$\frac{g^2}{4\cos^2\vartheta_{\mathrm{W}} m_Z^2} = \sqrt{2}G_{\mathrm{F}}, \tag{C.5}$$

for $q^2 \ll m_Z^2$ we obtain

$$A \propto g_V^q + \frac{g_{Z'}^{\nu_\ell V} g_{Z'}^{qV}}{\sqrt{2}G_{\mathrm{F}}\,(q^2 - m_{Z'}^2)}. \tag{C.6}$$

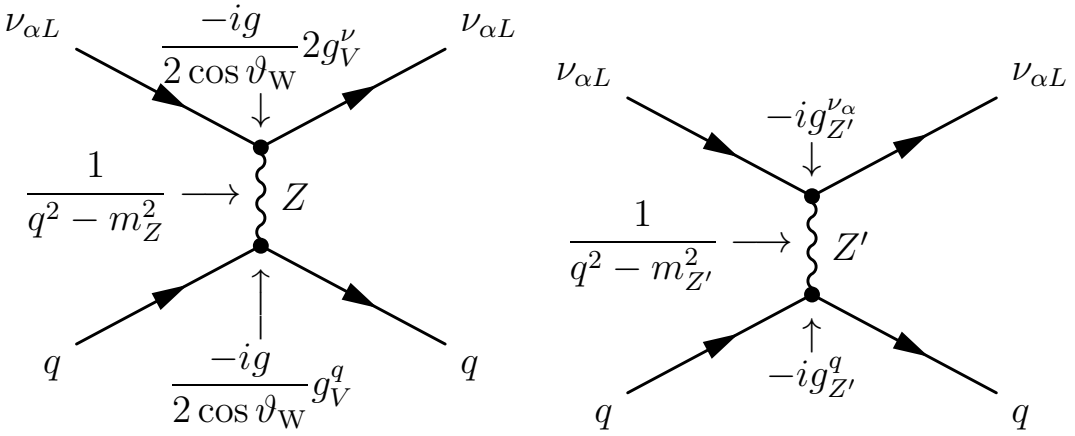

Figure C.1: Feynman diagrams describing the vector part of the Standard Model neutral-current interaction (left panel) and the Z' vector interaction of left-handed neutrinos with quarks (right panel).

This relation leads to Eq. (8.5), taking into account that the conservation of the vector current implies that

$$g_{Z'}^p = 2g_{Z'}^{uV} + g_{Z'}^{dV} \quad \text{and} \quad g_{Z'}^n = g_{Z'}^{uV} + 2g_{Z'}^{dV}\,. \tag{C.7}$$

In conclusion of this Appendix, let us note that the results of the analyses in Refs. [450, 451, 453, 476, 529, 530], where the Z' contribution to the weak charge in CEνNS is half of that in Eq. (8.5), must be reinterpreted by rescaling their Z' coupling $g_{Z'}$ by a factor $\sqrt{2}$.

Bibliography

[1] Mattia Atzori Corona et al. “Incorporating the weak mixing angle dependence to reconcile the neutron skin measurement on Pb208 by PREX-II”. In: *Phys. Rev. C* 105.5 (2022), p. 055503. DOI: 10.1103/PhysRevC.105.055503. arXiv: 2112.09717 [hep-ph] (cit. on pp. 1, 113, 123, 124).

[2] M. Atzori Corona et al. “Probing light mediators and $(g-2)_\mu$ through detection of coherent elastic neutrino nucleus scattering at COHERENT”. In: *JHEP* 05 (2022), p. 109. DOI: 10.1007/JHEP05(2022)109. arXiv: 2202.11002 [hep-ph] (cit. on pp. 1, 114, 153, 167, 169, 176).

[3] M. Atzori Corona et al. “Impact of the Dresden-II and COHERENT neutrino scattering data on neutrino electromagnetic properties and electroweak physics”. In: *JHEP* 09 (2022), p. 164. DOI: 10.1007/JHEP09(2022)164. arXiv: 2205.09484 [hep-ph] (cit. on pp. 1, 83, 86, 98, 100, 122, 133, 135, 136, 143, 145–147).

[4] M. Atzori Corona et al. “New constraint on neutrino magnetic moment and neutrino millicharge from LUX-ZEPLIN dark matter search results”. In: *Phys. Rev. D* 107.5 (2023), p. 053001. DOI: 10.1103/PhysRevD.107.053001. arXiv: 2207.05036 [hep-ph] (cit. on pp. 1, 7, 16, 100, 133, 163, 165, 169).

[5] M. Atzori Corona et al. “Nuclear neutron radius and weak mixing angle measurements from latest COHERENT CsI and atomic parity violation Cs data”. In: *Eur. Phys. J. C* 83.7 (2023), p. 683. DOI: 10.1140/epjc/s10052-023-11849-5. arXiv: 2303.09360 [nucl-ex] (cit. on pp. 1, 25, 113, 115, 120, 123, 125, 126, 184).

[6] M. Atzori Corona et al. “On the impact of the Migdal effect in reactor CEνNS experiments”. In: *Phys. Lett. B* 852 (2024), p. 138627. DOI: 10.

1016/j.physletb.2024.138627. arXiv: 2307.12911 [hep-ph] (cit. on pp. 1, 79, 84, 94, 146, 183).

[7] M. Atzori Corona et al. "Momentum dependent flavor radiative corrections to the coherent elastic neutrino-nucleus scattering for the neutrino charge-radius determination". In: *JHEP* 05 (2024), p. 271. DOI: 10.1007/JHEP05(2024)271. arXiv: 2402.16709 [hep-ph] (cit. on pp. 2, 7, 16, 27, 28, 115, 123–125, 133, 149, 150, 185).

[8] M. Atzori Corona et al. "Refined determination of the weak mixing angle at low energy". In: *Phys. Rev. D* 110.3 (2024), p. 033005. DOI: 10.1103/PhysRevD.110.033005. arXiv: 2405.09416 [hep-ph] (cit. on pp. 2, 113, 122, 184).

[9] F. Acerbi et al. "DarkSide-20k sensitivity to light dark matter particles". In: (July 2024). arXiv: 2407.05813 [hep-ex] (cit. on pp. 2, 37, 44, 45, 55, 56).

[10] Mattia Atzori Corona et al. "Pseudoscalar sterile neutrino self-interactions in light of Planck, SPT and ACT data". In: *JCAP* 06.06 (2022), p. 010. DOI: 10.1088/1475-7516/2022/06/010. arXiv: 2112.00037 [astro-ph.CO] (cit. on p. 2).

[11] P. Agnes et al. "Sensitivity projections for a dual-phase argon TPC optimized for light dark matter searches through the ionization channel". In: *Phys. Rev. D* 107.11 (2023), p. 112006. DOI: 10.1103/PhysRevD.107.112006. arXiv: 2209.01177 [physics.ins-det] (cit. on p. 2).

[12] E. Aaron et al. "Measurement of isotopic separation of argon with the prototype of the cryogenic distillation plant Aria for dark matter searches". In: *Eur. Phys. J. C* 83.5 (2023), p. 453. DOI: 10.1140/epjc/s10052-023-11430-0. arXiv: 2301.09639 [physics.ins-det] (cit. on pp. 2, 44).

[13] A. Elersich et al. "Study of cosmogenic activation above ground for the DarkSide-20k experiment". In: *Astropart. Phys.* 152 (2023), p. 102878. DOI: 10.1016/j.astropartphys.2023.102878. arXiv: 2301.12970 [astro-ph.IM] (cit. on p. 2).

[14] P. Agnes et al. "Constraints on directionality effect of nuclear recoils in a liquid argon time projection chamber". In: *Eur. Phys. J. C* 84.1 (2024), p. 24. DOI: 10.1140/epjc/s10052-023-12312-1. arXiv: 2307.15454 [physics.ins-det] (cit. on p. 2).

[15] F. Acerbi et al. “A new hybrid gadolinium nanoparticles-loaded polymeric material for neutron detection in rare event searches”. In: *JINST* 19.09 (2024), P09021. DOI: 10.1088/1748-0221/19/09/P09021. arXiv: 2404.18492 [physics.ins-det] (cit. on p. 2).

[16] F. Acerbi et al. “Benchmarking the design of the cryogenics system for the underground argon in DarkSide-20k”. In: (Aug. 2024). arXiv: 2408.14071 [physics.ins-det] (cit. on p. 2).

[17] Carlo Giunti and Chung W. Kim. *Fundamentals of Neutrino Physics and Astrophysics*. 2007. ISBN: 978-0-19-850871-7 (cit. on pp. 8, 14, 32, 49, 51, 168, 195).

[18] F. Reines and C. L. Cowan. “Detection of the free neutrino”. In: *Phys. Rev.* 92 (1953), pp. 830–831. DOI: 10.1103/PhysRev.92.830 (cit. on pp. 8, 13, 79).

[19] R. L. Workman et al. “Review of Particle Physics”. In: *PTEP* 2022 (2022), p. 083C01. DOI: 10.1093/ptep/ptac097 (cit. on pp. 8, 10, 11, 15, 25, 26, 51, 53, 63, 71, 122, 125, 131, 135, 137, 145, 156, 160, 161, 163, 168, 174, 195).

[20] Ahmed Tarek Abouelfadl Mohamed. “The Standard Model of Particle Physics”. In: *Measurement of Higgs Boson Production Cross Sections in the Diphoton Channel: with the full ATLAS Run-2 Data and Constraints on Anomalous Higgs Boson Interactions*. Cham: Springer International Publishing, 2020, pp. 3–35. ISBN: 978-3-030-59516-6. DOI: 10.1007/978-3-030-59516-6_1. URL: https://doi.org/10.1007/978-3-030-59516-6_1 (cit. on p. 8).

[21] Mark Thomson. *Modern particle physics*. New York: Cambridge University Press, 2013. ISBN: 978-1-107-03426-6. DOI: 10.1017/CBO9781139525367 (cit. on pp. 9, 10, 18).

[22] C. S. Wood et al. “Measurement of parity nonconservation and an anapole moment in cesium”. In: *Science* 275 (1997), pp. 1759–1763. DOI: 10.1126/science.275.5307.1759 (cit. on pp. 10, 11, 115, 122, 125).

[23] V. A. Dzuba et al. “Revisiting parity non-conservation in cesium”. In: *Phys. Rev. Lett.* 109 (2012), p. 203003. DOI: 10.1103/PhysRevLett.109.203003. arXiv: 1207.5864 [hep-ph] (cit. on pp. 10, 11, 125).

[24] P. L. Anthony et al. “Precision measurement of the weak mixing angle in Moller scattering”. In: *Phys. Rev. Lett.* 95 (2005), p. 081601. DOI: 10.1103/PhysRevLett.95.081601. arXiv: hep-ex/0504049 (cit. on pp. 10, 125).

[25] D. Wang et al. “Measurement of parity violation in electron–quark scattering”. In: *Nature* 506.7486 (2014), pp. 67–70. DOI: 10.1038/nature12964 (cit. on pp. 10, 125).

[26] D. Androić et al. “Precision measurement of the weak charge of the proton”. In: *Nature* 557.7704 (2018), pp. 207–211. DOI: 10.1038/s41586-018-0096-0. arXiv: 1905.08283 [nucl-ex] (cit. on pp. 10, 11, 125).

[27] Jens Erler and Michael J. Ramsey-Musolf. “The Weak mixing angle at low energies”. In: *Phys. Rev. D* 72 (2005), p. 073003. DOI: 10.1103/PhysRevD.72.073003. arXiv: hep-ph/0409169 (cit. on p. 11).

[28] Jens Erler and Rodolfo Ferro-Hernández. “Weak Mixing Angle in the Thomson Limit”. In: *JHEP* 03 (2018), p. 196. DOI: 10.1007/JHEP03(2018)196. arXiv: 1712.09146 [hep-ph] (cit. on p. 11).

[29] S. Schael et al. “Precision electroweak measurements on the Z resonance”. In: *Phys. Rept.* 427 (2006), pp. 257–454. DOI: 10.1016/j.physrep.2005.12.006. arXiv: hep-ex/0509008 (cit. on p. 11).

[30] K. S. Kumar et al. “Low Energy Measurements of the Weak Mixing Angle”. In: *Ann. Rev. Nucl. Part. Sci.* 63 (2013), pp. 237–267. DOI: 10.1146/annurev-nucl-102212-170556. arXiv: 1302.6263 [hep-ex] (cit. on p. 11).

[31] S. Navas et al. “Review of particle physics”. In: *Phys. Rev. D* 110.3 (2024), p. 030001. DOI: 10.1103/PhysRevD.110.030001 (cit. on pp. 11, 160, 162, 166, 186).

[32] B.M. Roberts, V.A. Dzuba, and V.V. Flambaum. “Parity and Time-Reversal Violation in Atomic Systems”. In: *Annual Review of Nuclear and Particle Science* 65.1 (Oct. 2015), pp. 63–86. ISSN: 1545-4134. DOI: 10.1146/annurev-nucl-102014-022331. URL: http://dx.doi.org/10.1146/annurev-nucl-102014-022331 (cit. on p. 11).

[33] Daniel Z. Freedman. “Coherent Neutrino Nucleus Scattering as a Probe of the Weak Neutral Current”. In: *Phys. Rev. D* 9 (1974), pp. 1389–1392. DOI: 10.1103/PhysRevD.9.1389 (cit. on p. 11).

[34] M. Cadeddu, F. Dordei, and C. Giunti. "A view of coherent elastic neutrino-nucleus scattering". In: *EPL* 143.3 (2023), p. 34001. DOI: 10.1209/0295-5075/ace7f0. arXiv: 2307.08842 [hep-ph] (cit. on p. 14).

[35] Luca Pattavina, Nahuel Ferreiro Iachellini, and Irene Tamborra. "Neutrino observatory based on archaeological lead". In: *Phys. Rev. D* 102.6 (2020), p. 063001. DOI: 10.1103/PhysRevD.102.063001. arXiv: 2004.06936 [astro-ph.HE] (cit. on pp. 14, 30, 83, 84, 104).

[36] L. Pattavina et al. "Production and characterisation of a $PbMoO_4$ cryogenic detector from archaeological Pb". In: *Eur. Phys. J. A* 56.2 (2020), p. 38. DOI: 10.1140/epja/s10050-020-00050-x. arXiv: 1906.09296 [physics.ins-det] (cit. on p. 14).

[37] L. Pattavina et al. "Radiopurity of an archaeological Roman lead cryogenic detector". In: *Eur. Phys. J. A* 55.8 (2019), p. 127. DOI: 10.1140/epja/i2019-12809-0. arXiv: 1904.04040 [physics.ins-det] (cit. on p. 14).

[38] Philipp Eller et al. "Online triggers for supernova and pre-supernova neutrino detection with cryogenic detectors". In: *JCAP* 10 (2022), p. 024. DOI: 10.1088/1475-7516/2022/10/024. arXiv: 2205.03350 [astro-ph.IM] (cit. on p. 14).

[39] Diego Aristizabal Sierra. *CEνNS Theory*. CEνNS Theory Lecture Magnificent CEνNS 2023, 22–29 Mar 2023. 2023 (cit. on p. 15).

[40] J. Barranco, O. G. Miranda, and T. I. Rashba. "Probing new physics with coherent neutrino scattering off nuclei". In: *JHEP* 12 (2005), p. 021. DOI: 10.1088/1126-6708/2005/12/021. arXiv: hep-ph/0508299 (cit. on p. 20).

[41] Martin Hoferichter, Javier Menéndez, and Achim Schwenk. "Coherent elastic neutrino-nucleus scattering: EFT analysis and nuclear responses". In: *Phys. Rev. D* 102.7 (2020), p. 074018. DOI: 10.1103/PhysRevD.102.074018. arXiv: 2007.08529 [hep-ph] (cit. on pp. 20, 23, 115–117, 173).

[42] D. Aristizabal Sierra. "Extraction of neutron density distributions from high-statistics coherent elastic neutrino-nucleus scattering data". In: *Phys. Lett. B* 845 (2023), p. 138140. DOI: 10.1016/j.physletb.2023.138140. arXiv: 2301.13249 [hep-ph] (cit. on pp. 20, 127, 129).

[43] D W L Sprung and J Martorell. “The symmetrized Fermi function and its transforms”. In: *Journal of Physics A: Mathematical and General* 30.18 (Sept. 1997), p. 6525. DOI: 10.1088/0305-4470/30/18/026. URL: https://dx.doi.org/10.1088/0305-4470/30/18/026 (cit. on p. 21).

[44] J. Piekarewicz et al. “Power of two: Assessing the impact of a second measurement of the weak-charge form factor of ^{208}Pb”. In: *Phys. Rev. C* 94.3 (2016), p. 034316. DOI: 10.1103/PhysRevC.94.034316. arXiv: 1604.07799 [nucl-th] (cit. on p. 21).

[45] M. Cadeddu et al. “Average CsI neutron density distribution from COHERENT data”. In: *Phys. Rev. Lett.* 120.7 (2018), p. 072501. DOI: 10.1103/PhysRevLett.120.072501. arXiv: 1710.02730 [hep-ph] (cit. on pp. 21, 113, 117, 129, 130).

[46] L. C. Maximon and R. A. Schrack. “The form factor of the Fermi model spatial distribution”. In: *J. Res. Natl. Bur. Stand. B* 70.1 (1966). DOI: 10.6028/jres.070b.007 (cit. on p. 21).

[47] G. Fricke et al. “Nuclear Ground State Charge Radii from Electromagnetic Interactions”. In: *Atom. Data Nucl. Data Tabl.* 60 (1995), pp. 177–285. DOI: 10.1006/adnd.1995.1007 (cit. on pp. 22, 23, 125).

[48] I. Angeli and K. P. Marinova. “Table of experimental nuclear ground state charge radii: An update”. In: *Atom. Data Nucl. Data Tabl.* 99.1 (2013), pp. 69–95. DOI: 10.1016/j.adt.2011.12.006 (cit. on pp. 22, 125).

[49] A. Ong, J. C. Berengut, and V. V. Flambaum. “The Effect of spin-orbit nuclear charge density corrections due to the anomalous magnetic moment on halonuclei”. In: *Phys. Rev. C* 82 (2010), p. 014320. DOI: 10.1103/PhysRevC.82.014320. arXiv: 1006.5508 [nucl-th] (cit. on p. 22).

[50] C. J. Horowitz et al. “Weak charge form factor and radius of 208Pb through parity violation in electron scattering”. In: *Phys. Rev. C* 85 (2012), p. 032501. DOI: 10.1103/PhysRevC.85.032501. arXiv: 1202.1468 [nucl-ex] (cit. on p. 22).

[51] M. Cadeddu et al. “Physics results from the first COHERENT observation of coherent elastic neutrino-nucleus scattering in argon and their combination with cesium-iodide data”. In: *Phys. Rev. D* 102.1 (2020), p. 015030. DOI: 10.1103/PhysRevD.102.015030. arXiv: 2005.01645 [hep-ph] (cit. on pp. 22, 113, 116, 117, 119, 125, 130).

[52] C. J. Horowitz and J. Piekarewicz. “Impact of spin-orbit currents on the electroweak skin of neutron-rich nuclei”. In: *Phys. Rev. C* 86 (2012), p. 045503. DOI: 10.1103/PhysRevC.86.045503. arXiv: 1208.2249 [nucl-th] (cit. on p. 22).

[53] Richard H. Helm. “Inelastic and Elastic Scattering of 187-Mev Electrons from Selected Even-Even Nuclei”. In: *Phys. Rev.* 104 (1956), pp. 1466–1475. DOI: 10.1103/PhysRev.104.1466 (cit. on p. 22).

[54] P.-G. Reinhard, W. Nazarewicz, and R. F. Garcia Ruiz. “Beyond the charge radius: The information content of the fourth radial moment”. In: *Phys. Rev. C* 101 (2 Feb. 2020), p. 021301. DOI: 10.1103/PhysRevC.101.021301. URL: https://link.aps.org/doi/10.1103/PhysRevC.101.021301 (cit. on p. 23).

[55] J. Friedrich and N. Voegler. “The salient features of charge density distributions of medium and heavy even-even nuclei determined from a systematic analysis of elastic electron scattering form factors”. In: *Nucl. Phys. A* 373 (1982), pp. 192–224. DOI: 10.1016/0375-9474(82)90147-6 (cit. on p. 23).

[56] Spencer Klein and Joakim Nystrand. “Exclusive vector meson production in relativistic heavy ion collisions”. In: *Phys. Rev. C* 60 (1999), p. 014903. DOI: 10.1103/PhysRevC.60.014903. arXiv: hep-ph/9902259 (cit. on p. 23).

[57] Baishan Hu et al. “Ab initio predictions link the neutron skin of ^{208}Pb to nuclear forces”. In: *Nature Phys.* 18.10 (2022), pp. 1196–1200. DOI: 10.1038/s41567-023-02324-9. arXiv: 2112.01125 [nucl-th] (cit. on p. 23).

[58] URL: %7Bhttps://pubchem.ncbi.nlm.nih.gov/ptable/atomic-mass/%7D (cit. on p. 23).

[59] W. J. Marciano and A. Sirlin. “Radiative corrections to neutrino-induced neutral-current phenomena in the $\mathrm{SU}(2)_L \times \mathrm{U}(1)$ theory”. In: *Phys. Rev. D* 22 (11 Dec. 1980), pp. 2695–2717. DOI: 10.1103/PhysRevD.22.2695. URL: https://link.aps.org/doi/10.1103/PhysRevD.22.2695 (cit. on p. 25).

[60] Jens Erler and Shufang Su. “The Weak Neutral Current”. In: *Prog. Part. Nucl. Phys.* 71 (2013), pp. 119–149. DOI: 10.1016/j.ppnp.2013.03.004. arXiv: 1303.5522 [hep-ph] (cit. on pp. 25, 32, 145).

[61] Jens Erler and Michael J. Ramsey-Musolf. “Weak mixing angle at low energies”. In: *Phys. Rev. D* 72 (7 Oct. 2005), p. 073003. DOI: 10.1103/PhysRevD.72.073003. URL: https://link.aps.org/doi/10.1103/PhysRevD.72.073003 (cit. on p. 25).

[62] William J. Marciano and Zohreh Parsa. “Neutrino electron scattering theory”. In: *J. Phys. G* 29 (2003), pp. 2629–2645. DOI: 10.1088/0954-3899/29/11/013. arXiv: hep-ph/0403168 (cit. on p. 28).

[63] L.M. Sehgal. “Differences in the coherent interactions of ve, vμ, and vτ”. In: *Physics Letters B* 162.4 (1985), pp. 370–372. ISSN: 0370-2693. DOI: https://doi.org/10.1016/0370-2693(85)90942-6. URL: https://www.sciencedirect.com/science/article/pii/0370269385909426 (cit. on p. 28).

[64] F. J. Hasert et al. “Search for Elastic ν_μ Electron Scattering”. In: *Phys. Lett. B* 46 (1973), pp. 121–124. DOI: 10.1016/0370-2693(73)90494-2 (cit. on p. 30).

[65] B. C. Canas et al. “The weak mixing angle from low energy neutrino measurements: a global update”. In: *Phys. Lett. B* 761 (2016), pp. 450–455. DOI: 10.1016/j.physletb.2016.08.047. arXiv: 1608.02671 [hep-ph] (cit. on p. 31).

[66] H. T. Wong et al. “A Search of Neutrino Magnetic Moments with a High-Purity Germanium Detector at the Kuo-Sheng Nuclear Power Station”. In: *Phys. Rev. D* 75 (2007), p. 012001. DOI: 10.1103/PhysRevD.75.012001. arXiv: hep-ex/0605006 (cit. on pp. 31, 131, 136, 137, 162, 163).

[67] M. Deniz et al. “Measurement of Nu(e)-bar -Electron Scattering Cross-Section with a CsI(Tl) Scintillating Crystal Array at the Kuo-Sheng Nuclear Power Reactor”. In: *Phys. Rev. D* 81 (2010), p. 072001. DOI: 10.1103/PhysRevD.81.072001. arXiv: 0911.1597 [hep-ex] (cit. on pp. 31, 145, 147–152).

[68] A. G. Beda et al. “The results of search for the neutrino magnetic moment in GEMMA experiment”. In: *Adv. High Energy Phys.* 2012 (2012), p. 350150. DOI: 10.1155/2012/350150 (cit. on pp. 31, 136, 137, 141, 142, 160, 162, 163).

[69] G. Bellini et al. “Measurement of the solar 8B neutrino rate with a liquid scintillator target and 3 MeV energy threshold in the Borexino detector”. In: *Phys. Rev. D* 82 (2010), p. 033006. DOI: 10.1103/PhysRevD.82.033006. arXiv: 0808.2868 [astro-ph] (cit. on p. 31).

[70] C. Arpesella et al. “Direct Measurement of the Be-7 Solar Neutrino Flux with 192 Days of Borexino Data”. In: *Phys. Rev. Lett.* 101 (2008), p. 091302. DOI: 10.1103/PhysRevLett.101.091302. arXiv: 0805.3843 [astro-ph] (cit. on p. 31).

[71] M. Agostini et al. “Comprehensive measurement of *pp*-chain solar neutrinos”. In: *Nature* 562.7728 (2018), pp. 505–510. DOI: 10.1038/s41586-018-0624-y (cit. on pp. 31, 51, 52).

[72] G. Bellini et al. “First evidence of pep solar neutrinos by direct detection in Borexino”. In: *Phys. Rev. Lett.* 108 (2012), p. 051302. DOI: 10.1103/PhysRevLett.108.051302. arXiv: 1110.3230 [hep-ex] (cit. on p. 31).

[73] J. Aalbers et al. “First Dark Matter Search Results from the LUX-ZEPLIN (LZ) Experiment”. In: *Phys. Rev. Lett.* 131.4 (2023), p. 041002. DOI: 10.1103/PhysRevLett.131.041002. arXiv: 2207.03764 [hep-ex] (cit. on pp. 31, 42, 153, 154, 156–158).

[74] E. Aprile et al. “Search for New Physics in Electronic Recoil Data from XENONnT”. In: *Phys. Rev. Lett.* 129.16 (2022), p. 161805. DOI: 10.1103/PhysRevLett.129.161805. arXiv: 2207.11330 [hep-ex] (cit. on pp. 31, 42, 154, 158, 159, 163).

[75] K. Zuber. *Neutrino physics*. 2004. ISBN: 978-0-7503-0750-5 (cit. on pp. 32, 49, 51).

[76] Carlo Giunti and Alexander Studenikin. “Neutrino electromagnetic interactions: a window to new physics”. In: *Rev. Mod. Phys.* 87 (2015), p. 531. DOI: 10.1103/RevModPhys.87.531. arXiv: 1403.6344 [hep-ph] (cit. on pp. 32, 134, 135, 137, 138, 144, 163).

[77] Konstantin A. Kouzakov and Alexander I. Studenikin. “Theory of neutrino-atom collisions: the history, present status and BSM physics”. In: *Adv. High Energy Phys.* 2014 (2014), p. 569409. DOI: 10.1155/2014/569409. arXiv: 1406.4999 [hep-ph] (cit. on p. 34).

[78] Jiunn-Wei Chen et al. “Low-energy electronic recoil in xenon detectors by solar neutrinos”. In: *Phys. Lett. B* 774 (2017), pp. 656–661. DOI: 10.1016/j.physletb.2017.10.029. arXiv: 1610.04177 [hep-ex] (cit. on p. 34).

[79] Jiunn-Wei Chen et al. “Atomic ionization of germanium by neutrinos from an ab initio approach”. In: *Phys. Lett. B* 731 (2014), pp. 159–162. DOI: 10.1016/j.physletb.2014.02.036. arXiv: 1311.5294 [hep-ph] (cit. on pp. 35, 142).

[80] Keh-Ning Huang. “Relativistic many-body theory of atomic transitions. The relativistic equation-of-motion approach”. In: *Phys. Rev. A* 26 (2 Aug. 1982), pp. 734–739. DOI: 10.1103/PhysRevA.26.734. URL: https://link.aps.org/doi/10.1103/PhysRevA.26.734 (cit. on pp. 35, 142).

[81] Jiunn-Wei Chen et al. “Constraining neutrino electromagnetic properties by germanium detectors”. In: *Phys. Rev. D* 91.1 (2015), p. 013005. DOI: 10.1103/PhysRevD.91.013005. arXiv: 1411.0574 [hep-ph] (cit. on pp. 35, 95, 135, 161).

[82] Edvige Corbelli and Paolo Salucci. “The Extended Rotation Curve and the Dark Matter Halo of M33”. In: *Mon. Not. Roy. Astron. Soc.* 311 (2000), pp. 441–447. DOI: 10.1046/j.1365-8711.2000.03075.x. arXiv: astro-ph/9909252 (cit. on p. 37).

[83] Douglas Clowe et al. “A direct empirical proof of the existence of dark matter”. In: *Astrophys. J. Lett.* 648 (2006), pp. L109–L113. DOI: 10.1086/508162. arXiv: astro-ph/0608407 (cit. on p. 37).

[84] P. J. E. Peebles and J. T. Yu. “Primeval adiabatic perturbation in an expanding universe”. In: *Astrophys. J.* 162 (1970), pp. 815–836. DOI: 10.1086/150713 (cit. on p. 37).

[85] R. A. Alpher, H. Bethe, and G. Gamow. “The origin of chemical elements”. In: *Phys. Rev.* 73 (1948), pp. 803–804. DOI: 10.1103/PhysRev.73.803 (cit. on p. 37).

[86] G. Gamow. “Expanding universe and the origin of elements”. In: *Phys. Rev.* 70 (1946), pp. 572–573. DOI: 10.1103/PhysRev.70.572.2 (cit. on p. 37).

[87] N. Aghanim et al. “Planck 2018 results. VI. Cosmological parameters”. In: *Astron. Astrophys.* 641 (2020). [Erratum: Astron.Astrophys. 652, C4 (2021)], A6. DOI: 10.1051/0004-6361/201833910. arXiv: 1807.06209 [astro-ph.CO] (cit. on p. 37).

[88] Tongyan Lin. "Dark matter models and direct detection". In: *PoS* 333 (2019), p. 009. DOI: 10.22323/1.333.0009. arXiv: 1904.07915 [hep-ph] (cit. on p. 38).

[89] Gianfranco Bertone and Dan Hooper. "History of dark matter". In: *Rev. Mod. Phys.* 90 (4 Oct. 2018), p. 045002. DOI: 10.1103/RevModPhys.90.045002. URL: https://link.aps.org/doi/10.1103/RevModPhys.90.045002 (cit. on p. 38).

[90] Marco Cirelli, Alessandro Strumia, and Jure Zupan. "Dark Matter". In: (June 2024). arXiv: 2406.01705 [hep-ph] (cit. on pp. 38–40).

[91] David G. Cerdeno and Anne M. Green. "Direct detection of WIMPs". In: (Feb. 2010), pp. 347–369. DOI: 10.1017/CBO9780511770739.018. arXiv: 1002.1912 [astro-ph.CO] (cit. on pp. 39, 40).

[92] Robert J. Scherrer and Michael S. Turner. "On the relic, cosmic abundance of stable, weakly interacting massive particles". In: *Phys. Rev. D* 33 (6 May 1986), pp. 1585–1589. DOI: 10.1103/PhysRevD.33.1585. URL: https://link.aps.org/doi/10.1103/PhysRevD.33.1585 (cit. on p. 39).

[93] Scott Dodelson. *Modern Cosmology*. Amsterdam: Academic Press, 2003. ISBN: 978-0-12-219141-1 (cit. on p. 39).

[94] Katherine Freese, Joshua Frieman, and Andrew Gould. "Signal modulation in cold-dark-matter detection". In: *Phys. Rev. D* 37 (12 June 1988), pp. 3388–3405. DOI: 10.1103/PhysRevD.37.3388. URL: https://link.aps.org/doi/10.1103/PhysRevD.37.3388 (cit. on pp. 39, 40).

[95] Andrzej K. Drukier, Katherine Freese, and David N. Spergel. "Detecting cold dark-matter candidates". In: *Phys. Rev. D* 33 (12 June 1986), pp. 3495–3508. DOI: 10.1103/PhysRevD.33.3495. URL: https://link.aps.org/doi/10.1103/PhysRevD.33.3495 (cit. on p. 39).

[96] J. D. Lewin and P. F. Smith. "Review of mathematics, numerical factors, and corrections for dark matter experiments based on elastic nuclear recoil". In: *Astropart. Phys.* 6 (1996), pp. 87–112. DOI: 10.1016/S0927-6505(96)00047-3 (cit. on p. 40).

[97] Marcin Misiaszek and Nicola Rossi. "Direct Detection of Dark Matter: A Critical Review". In: *Symmetry* 16.2 (2024), p. 201. DOI: 10.3390/sym16020201. arXiv: 2310.20472 [hep-ph] (cit. on p. 41).

[98] E. Aprile et al. “First Dark Matter Search with Nuclear Recoils from the XENONnT Experiment”. In: *Phys. Rev. Lett.* 131.4 (2023), p. 041003. DOI: 10.1103/PhysRevLett.131.041003. arXiv: 2303.14729 [hep-ex] (cit. on pp. 42, 56).

[99] Shuaijie Li et al. “Search for Light Dark Matter with Ionization Signals in the PandaX-4T Experiment”. In: *Phys. Rev. Lett.* 130.26 (2023), p. 261001. DOI: 10.1103/PhysRevLett.130.261001. arXiv: 2212.10067 [hep-ex] (cit. on pp. 42, 56).

[100] David G. Cerdeño et al. “Physics from solar neutrinos in dark matter direct detection experiments”. In: *JHEP* 05 (2016). [Erratum: JHEP 09, 048 (2016)], p. 118. DOI: 10.1007/JHEP09(2016)048. arXiv: 1604.01025 [hep-ph] (cit. on pp. 42, 172–174).

[101] Zihao Bo et al. “First Measurement of Solar ^{8}B Neutrino Flux through Coherent Elastic Neutrino-Nucleus Scattering in PandaX-4T”. In: (July 2024). arXiv: 2407.10892 [hep-ex] (cit. on pp. 42, 83, 84).

[102] E. Aprile et al. “First Measurement of Solar ^{8}B Neutrinos via Coherent Elastic Neutrino-Nucleus Scattering with XENONnT”. In: (Aug. 2024). arXiv: 2408.02877 [nucl-ex] (cit. on pp. 42, 83, 84).

[103] J. Aalbers et al. “Search for new physics in low-energy electron recoils from the first LZ exposure”. In: *Phys. Rev. D* 108.7 (2023), p. 072006. DOI: 10.1103/PhysRevD.108.072006. arXiv: 2307.15753 [hep-ex] (cit. on pp. 42, 160, 162).

[104] J. H. J. Poole and C. F. G. Delaney. “Origin of atmospheric argon and the radioactive decay constants of potassium-40”. In: (). DOI: 10.1038/167680b0 (cit. on p. 42).

[105] P. Benetti et al. “Measurement of the specific activity of ar-39 in natural argon”. In: *Nucl. Instrum. Meth. A* 574 (2007), pp. 83–88. DOI: 10.1016/j.nima.2007.01.106. arXiv: astro-ph/0603131 (cit. on p. 42).

[106] Giuseppe Matteucci and Giuliana Fiorillo. “Liquid Argon for Direct Dark Matter Detection”. In: (2024). DOI: 10.31526/jais.2024.523 (cit. on p. 42).

[107] V. Chepel and H. Araujo. “Liquid noble gas detectors for low energy particle physics”. In: *JINST* 8 (2013), R04001. DOI: 10.1088/1748-0221/8/04/R04001. arXiv: 1207.2292 [physics.ins-det] (cit. on p. 43).

[108] P. Agnes et al. “Results From the First Use of Low Radioactivity Argon in a Dark Matter Search”. In: *Phys. Rev. D* 93.8 (2016). [Addendum: Phys.Rev.D 95, 069901 (2017)], p. 081101. DOI: 10.1103/PhysRevD.93.081101. arXiv: 1510.00702 [astro-ph.CO] (cit. on pp. 44, 77).

[109] P. Agnes et al. “DarkSide-50 532-day Dark Matter Search with Low-Radioactivity Argon”. In: *Phys. Rev. D* 98.10 (2018), p. 102006. DOI: 10.1103/PhysRevD.98.102006. arXiv: 1802.07198 [astro-ph.CO] (cit. on pp. 44, 54).

[110] P. Agnes et al. “Constraints on Sub-GeV Dark-Matter–Electron Scattering from the DarkSide-50 Experiment”. In: *Phys. Rev. Lett.* 121.11 (2018), p. 111303. DOI: 10.1103/PhysRevLett.121.111303. arXiv: 1802.06998 [astro-ph.CO] (cit. on p. 44).

[111] P. Agnes et al. “Search for low-mass dark matter WIMPs with 12 ton-day exposure of DarkSide-50”. In: *Phys. Rev. D* 107.6 (2023), p. 063001. DOI: 10.1103/PhysRevD.107.063001. arXiv: 2207.11966 [hep-ex] (cit. on pp. 44, 56).

[112] P. Agnes et al. “Search for Dark-Matter–Nucleon Interactions via Migdal Effect with DarkSide-50”. In: *Phys. Rev. Lett.* 130.10 (2023), p. 101001. DOI: 10.1103/PhysRevLett.130.101001. arXiv: 2207.11967 [hep-ex] (cit. on pp. 44, 91).

[113] P. Agnes et al. “Search for Dark Matter Particle Interactions with Electron Final States with DarkSide-50”. In: *Phys. Rev. Lett.* 130.10 (2023), p. 101002. DOI: 10.1103/PhysRevLett.130.101002. arXiv: 2207.11968 [hep-ex] (cit. on p. 44).

[114] C. E. Aalseth et al. “DarkSide-20k: A 20 tonne two-phase LAr TPC for direct dark matter detection at LNGS”. In: *Eur. Phys. J. Plus* 133 (2018), p. 131. DOI: 10.1140/epjp/i2018-11973-4. arXiv: 1707.08145 [physics.ins-det] (cit. on pp. 44, 83, 84).

[115] P. Agnes et al. “Separating ^{39}Ar from ^{40}Ar by cryogenic distillation with Aria for dark-matter searches”. In: *Eur. Phys. J. C* 81.4 (2021), p. 359. DOI: 10.1140/epjc/s10052-021-09121-9. arXiv: 2101.08686 [physics.ins-det] (cit. on p. 44).

[116] Marco D'Incecco et al. "Development of a Novel Single-Channel, 24 cm^2, SiPM-Based, Cryogenic Photodetector". In: *IEEE Trans. Nucl. Sci.* 65.1 (2017), pp. 591–596. DOI: 10.1109/TNS.2017.2774779. arXiv: 1706.04220 [physics.ins-det] (cit. on p. 45).

[117] Babak Abi et al. "Deep Underground Neutrino Experiment (DUNE), Far Detector Technical Design Report, Volume I Introduction to DUNE". In: *JINST* 15.08 (2020), T08008. DOI: 10.1088/1748-0221/15/08/T08008. arXiv: 2002.02967 [physics.ins-det] (cit. on p. 45).

[118] W. C. Haxton, R. G. Hamish Robertson, and Aldo M. Serenelli. "Solar Neutrinos: Status and Prospects". In: *Ann. Rev. Astron. Astrophys.* 51 (2013), pp. 21–61. DOI: 10.1146/annurev-astro-081811-125539. arXiv: 1208.5723 [astro-ph.SR] (cit. on p. 46).

[119] Xun-Jie Xu, Zhe Wang, and Shaomin Chen. "Solar neutrino physics". In: *Prog. Part. Nucl. Phys.* 131 (2023), p. 104043. DOI: 10.1016/j.ppnp.2023.104043. arXiv: 2209.14832 [hep-ph] (cit. on pp. 46, 49).

[120] J. Billard, L. Strigari, and E. Figueroa-Feliciano. "Implication of neutrino backgrounds on the reach of next generation dark matter direct detection experiments". In: *Phys. Rev. D* 89.2 (2014), p. 023524. DOI: 10.1103/PhysRevD.89.023524. arXiv: 1307.5458 [hep-ph] (cit. on p. 45).

[121] C. Bœhm et al. "How high is the neutrino floor?" In: *JCAP* 01 (2019), p. 043. DOI: 10.1088/1475-7516/2019/01/043. arXiv: 1809.06385 [hep-ph] (cit. on pp. 45, 154).

[122] Ciaran A. J. O'Hare. "New Definition of the Neutrino Floor for Direct Dark Matter Searches". In: *Phys. Rev. Lett.* 127.25 (2021), p. 251802. DOI: 10.1103/PhysRevLett.127.251802. arXiv: 2109.03116 [hep-ph] (cit. on pp. 45, 56, 57).

[123] Matteo Cadeddu. "DarkSide-20k sensitivity, directional dark matter detection and the role of coherent elastic neutrino-nucleus scattering background". PhD thesis. Cagliari U., 2018 (cit. on p. 46).

[124] Nicola Cargioli. "Standard model physics and beyond in low energy neutrino scattering and parity violating electron interactions with nuclei". PhD thesis. Cagliari U., 2024 (cit. on pp. 46, 115, 122, 123, 130).

[125] S. Enomoto et al. "Neutrino geophysics with KamLAND and future prospects". In: (Aug. 2005). arXiv: hep-ph/0508049 (cit. on pp. 47, 48).

[126] Edoardo Vitagliano, Irene Tamborra, and Georg Raffelt. "Grand Unified Neutrino Spectrum at Earth: Sources and Spectral Components". In: *Rev. Mod. Phys.* 92 (2020), p. 45006. DOI: 10.1103/RevModPhys.92.045006. arXiv: 1910.11878 [astro-ph.HE] (cit. on pp. 47, 50).

[127] D. Aristizabal Sierra, Valentina De Romeri, and Christoph A. Ternes. "Reactor neutrino background in next-generation dark matter detectors". In: *Phys. Rev. D* 109.11 (2024), p. 115026. DOI: 10.1103/PhysRevD.109.115026. arXiv: 2402.06416 [hep-ph] (cit. on p. 47).

[128] Núria Vinyoles et al. "A new Generation of Standard Solar Models". In: *Astrophys. J.* 835.2 (2017), p. 202. DOI: 10.3847/1538-4357/835/2/202. arXiv: 1611.09867 [astro-ph.SR] (cit. on pp. 47–49).

[129] N. Grevesse and A. J. Sauval. "Standard Solar Composition". In: *Space Sci. Rev.* 85 (1998), pp. 161–174. DOI: 10.1023/A:1005161325181 (cit. on pp. 47–49).

[130] G. Battistoni et al. "The atmospheric neutrino flux below 100-MeV: The FLUKA results". In: *Astropart. Phys.* 23 (2005), pp. 526–534. DOI: 10.1016/j.astropartphys.2005.03.006 (cit. on pp. 47, 48, 50).

[131] John F. Beacom. "The Diffuse Supernova Neutrino Background". In: *Ann. Rev. Nucl. Part. Sci.* 60 (2010), pp. 439–462. DOI: 10.1146/annurev.nucl.010909.083331. arXiv: 1004.3311 [astro-ph.HE] (cit. on pp. 47, 48, 50).

[132] Johannes Bergstrom et al. "Updated determination of the solar neutrino fluxes from solar neutrino data". In: *JHEP* 03 (2016), p. 132. DOI: 10.1007/JHEP03(2016)132. arXiv: 1601.00972 [hep-ph] (cit. on p. 48).

[133] S. Appel et al. "Improved Measurement of Solar Neutrinos from the Carbon-Nitrogen-Oxygen Cycle by Borexino and Its Implications for the Standard Solar Model". In: *Phys. Rev. Lett.* 129.25 (2022), p. 252701. DOI: 10.1103/PhysRevLett.129.252701. arXiv: 2205.15975 [hep-ex] (cit. on p. 48).

[134] M. Agostini et al. "Experimental evidence of neutrinos produced in the CNO fusion cycle in the Sun". In: *Nature* 587 (2020), pp. 577–582. DOI: 10.1038/s41586-020-2934-0. arXiv: 2006.15115 [hep-ex] (cit. on p. 48).

[135] John N. Bahcall. “Line versus continuum solar neutrinos”. In: *Phys. Rev. D* 41 (10 May 1990), pp. 2964–2966. DOI: 10.1103/PhysRevD.41.2964. URL: https://link.aps.org/doi/10.1103/PhysRevD.41.2964 (cit. on p. 49).

[136] Anna M. Suliga. “Diffuse Supernova Neutrino Background”. In: *Handbook of Nuclear Physics*. Ed. by Isao Tanihata, Hiroshi Toki, and Toshitaka Kajino. 2022, pp. 1–18. DOI: 10.1007/978-981-15-8818-1_129-1. arXiv: 2207.09632 [astro-ph.HE] (cit. on p. 50).

[137] Angel Abusleme et al. “Prospects for detecting the diffuse supernova neutrino background with JUNO”. In: *JCAP* 10 (2022), p. 033. DOI: 10.1088/1475-7516/2022/10/033. arXiv: 2205.08830 [hep-ex] (cit. on p. 50).

[138] Ivan Esteban et al. “Updated fit to three neutrino mixing: exploring the accelerator-reactor complementarity”. In: *JHEP* 01 (2017), p. 087. DOI: 10.1007/JHEP01(2017)087. arXiv: 1611.01514 [hep-ph] (cit. on p. 51).

[139] Q. R. Ahmad et al. “Direct evidence for neutrino flavor transformation from neutral current interactions in the Sudbury Neutrino Observatory”. In: *Phys. Rev. Lett.* 89 (2002), p. 011301. DOI: 10.1103/PhysRevLett.89.011301. arXiv: nucl-ex/0204008 (cit. on p. 51).

[140] W. C. Haxton. “The solar neutrino problem”. In: *Ann. Rev. Astron. Astrophys.* 33 (1995). Ed. by G. Burbidge and A. Sandage, pp. 459–503. DOI: 10.1146/annurev.aa.33.090195.002331. arXiv: hep-ph/9503430 (cit. on p. 51).

[141] A. Yu. Smirnov. “The MSW effect and solar neutrinos”. In: *10th International Workshop on Neutrino Telescopes*. May 2003, pp. 23–43. arXiv: hep-ph/0305106 (cit. on p. 51).

[142] M. Agostini et al. “Limiting neutrino magnetic moments with Borexino Phase-II solar neutrino data”. In: *Phys. Rev. D* 96.9 (2017), p. 091103. DOI: 10.1103/PhysRevD.96.091103. arXiv: 1707.09355 [hep-ex] (cit. on pp. 53, 154, 157, 158, 160, 163).

[143] Jiunn-Wei Chen et al. “Low-energy electronic recoil in xenon detectors by solar neutrinos”. In: *Physics Letters B* 774 (Nov. 2017), pp. 656–661. DOI: 10.1016/j.physletb.2017.10.029. URL: https://doi.org/10.1016%5C%2Fj.physletb.2017.10.029 (cit. on p. 53).

[144] P. Agnes et al. “Low-Mass Dark Matter Search with the DarkSide-50 Experiment”. In: *Phys. Rev. Lett.* 121.8 (2018), p. 081307. DOI: 10.1103/PhysRevLett.121.081307. arXiv: 1802.06994 [astro-ph.HE] (cit. on pp. 54, 55).

[145] Wenbo Ma et al. “Search for Solar B8 Neutrinos in the PandaX-4T Experiment Using Neutrino-Nucleus Coherent Scattering”. In: *Phys. Rev. Lett.* 130.2 (2023), p. 021802. DOI: 10.1103/PhysRevLett.130.021802. arXiv: 2207.04883 [hep-ex] (cit. on p. 56).

[146] E. Aprile et al. “Search for Coherent Elastic Scattering of Solar ^{8}B Neutrinos in the XENON1T Dark Matter Experiment”. In: *Phys. Rev. Lett.* 126 (2021), p. 091301. DOI: 10.1103/PhysRevLett.126.091301. arXiv: 2012.02846 [hep-ex] (cit. on p. 56).

[147] D. S. Akerib et al. “Improving sensitivity to low-mass dark matter in LUX using a novel electrode background mitigation technique”. In: *Phys. Rev. D* 104.1 (2021), p. 012011. DOI: 10.1103/PhysRevD.104.012011. arXiv: 2011.09602 [hep-ex] (cit. on p. 56).

[148] D. S. Akerib et al. “Results from a search for dark matter in the complete LUX exposure”. In: *Phys. Rev. Lett.* 118.2 (2017), p. 021303. DOI: 10.1103/PhysRevLett.118.021303. arXiv: 1608.07648 [astro-ph.CO] (cit. on p. 56).

[149] R. Agnese et al. “Low-mass dark matter search with CDMSlite”. In: *Phys. Rev. D* 97.2 (2018), p. 022002. DOI: 10.1103/PhysRevD.97.022002. arXiv: 1707.01632 [astro-ph.CO] (cit. on p. 56).

[150] C. Amole et al. “Dark Matter Search Results from the Complete Exposure of the PICO-60 C_3F_8 Bubble Chamber”. In: *Phys. Rev. D* 100.2 (2019), p. 022001. DOI: 10.1103/PhysRevD.100.022001. arXiv: 1902.04031 [astro-ph.CO] (cit. on p. 56).

[151] R. Agnese et al. “Silicon Detector Dark Matter Results from the Final Exposure of CDMS II”. In: *Phys. Rev. Lett.* 111.25 (2013), p. 251301. DOI: 10.1103/PhysRevLett.111.251301. arXiv: 1304.4279 [hep-ex] (cit. on p. 56).

[152] C. E. Aalseth et al. “CoGeNT: A Search for Low-Mass Dark Matter using p-type Point Contact Germanium Detectors”. In: *Phys. Rev. D* 88 (2013), p. 012002. DOI: 10.1103/PhysRevD.88.012002. arXiv: 1208.5737 [astro-ph.CO] (cit. on p. 56).

[153] R. Bernabei et al. “Final model independent result of DAMA/LIBRA-phase1”. In: *Eur. Phys. J. C* 73 (2013), p. 2648. DOI: 10.1140/epjc/s10052-013-2648-7. arXiv: 1308.5109 [astro-ph.GA] (cit. on p. 56).

[154] P. Agnes et al. “A study of events with photoelectric emission in the DarkSide-50 liquid argon Time Projection Chamber”. In: *Astropart. Phys.* 140 (2022), p. 102704. DOI: 10.1016/j.astropartphys.2022.102704. arXiv: 2107.08015 [physics.ins-det] (cit. on pp. 56, 106, 112).

[155] B. et al Edwards. “Measurement of single electron emission in two-phase xenon”. In: *Astroparticle Physics* 30.2 (Sept. 2008), pp. 54–57. ISSN: 0927-6505. DOI: 10.1016/j.astropartphys.2008.06.006. URL: http://dx.doi.org/10.1016/j.astropartphys.2008.06.006 (cit. on p. 56).

[156] E. Aprile et al. “Observation and applications of single-electron charge signals in the XENON100 experiment”. In: *J. Phys. G* 41 (2014), p. 035201. DOI: 10.1088/0954-3899/41/3/035201. arXiv: 1311.1088 [physics.ins-det] (cit. on p. 56).

[157] D. Yu. Akimov et al. “Observation of delayed electron emission in a two-phase liquid xenon detector”. In: *JINST* 11.03 (2016), p. C03007. DOI: 10.1088/1748-0221/11/03/C03007 (cit. on p. 56).

[158] D. Akimov et al. “Observation of Coherent Elastic Neutrino-Nucleus Scattering”. In: *Science* 357.6356 (2017), pp. 1123–1126. DOI: 10.1126/science.aao0990. arXiv: 1708.01294 [nucl-ex] (cit. on pp. 59, 61, 65, 66, 117).

[159] D. Akimov et al. “First Measurement of Coherent Elastic Neutrino-Nucleus Scattering on Argon”. In: *Phys. Rev. Lett.* 126.1 (2021), p. 012002. DOI: 10.1103/PhysRevLett.126.012002. arXiv: 2003.10630 [nucl-ex] (cit. on pp. 59, 72, 73, 77, 109, 115, 167).

[160] S. Adamski et al. “First detection of coherent elastic neutrino-nucleus scattering on germanium”. In: (June 2024). arXiv: 2406.13806 [hep-ex] (cit. on pp. 59, 109).

[161] P. An et al. “Measurement of Electron-Neutrino Charged-Current Cross Sections on I127 with the COHERENT NaIνE Detector”. In: *Phys. Rev. Lett.* 131.22 (2023), p. 221801. DOI: 10.1103/PhysRevLett.131.221801. arXiv: 2305.19594 [nucl-ex] (cit. on p. 60).

[162] P. An et al. “Measurement of Pb208(νe,Xn) production with a stopped-pion neutrino source”. In: *Phys. Rev. D* 108.7 (2023), p. 072001. DOI: 10.1103/PhysRevD.108.072001. arXiv: 2212.11295 [hep-ex] (cit. on pp. 60, 65).

[163] D. Akimov et al. “Measurement of the Coherent Elastic Neutrino-Nucleus Scattering Cross Section on CsI by COHERENT”. In: *Phys. Rev. Lett.* 129.8 (2022), p. 081801. DOI: 10.1103/PhysRevLett.129.081801. arXiv: 2110.07730 [hep-ex] (cit. on pp. 60–62, 66–69, 71, 109, 116, 118, 119, 167, 193).

[164] H. Abele et al. “Particle Physics at the European Spallation Source”. In: *Phys. Rept.* 1023 (2023), pp. 1–84. DOI: 10.1016/j.physrep.2023.06.001. arXiv: 2211.10396 [physics.ins-det] (cit. on pp. 60, 83, 84, 131).

[165] R. G. Van de Water et al. “LANSCE-PSR Short-Pulse Upgrade for Improved Dark Sector Particle Searches with the Coherent Captain Mills Experiment”. In: *Snowmass 2021*. Apr. 2022. arXiv: 2204.01860 [physics.ins-det] (cit. on pp. 60, 83, 84).

[166] Chenguang Su, Qian Liu, and Tianjiao Liang. “CEνNS Experiment Proposal at CSNS †”. In: *Phys. Sci. Forum* 8.1 (2023), p. 19. DOI: 10.3390/psf2023008019. arXiv: 2303.13423 [physics.ins-det] (cit. on pp. 60, 83, 84, 131).

[167] Robert L. Kustom. “An Overview of the Spallation Neutron Source project”. In: *eConf* C000821 (2000). Ed. by A. W. Chao, TU101. arXiv: physics/0008212 (cit. on p. 60).

[168] J. Cugnon. “Cascade models and particle production: A comparison”. In: *NATO Advanced Study Institute on Particle Production in Highly Excited Matter*. 1992, pp. 271–293 (cit. on p. 61).

[169] A. Krása. “Spallation Reaction Physics”. In: 2010. URL: https://api.semanticscholar.org/CorpusID:28796927 (cit. on p. 61).

[170] A. Bolozdynya et al. “Opportunities for Neutrino Physics at the Spallation Neutron Source: A White Paper”. In: Nov. 2012. arXiv: 1211.5199 [hep-ex] (cit. on p. 61).

[171] Gary J. Russell. “Spallation Physics - An Overview”. Los Alamos National Laboratory Los Alamos, New Mexico, 1990 (cit. on p. 61).

[172] D. Akimov et al. “The COHERENT Experimental Program”. In: *Snowmass 2021*. Apr. 2022. arXiv: 2204.04575 [hep-ex] (cit. on pp. 61, 75–77, 84, 129, 130).

[173] D. Akimov et al. “A D_2O detector for flux normalization of a pion decay-at-rest neutrino source”. In: *JINST* 16.08 (2021), P08048. DOI: 10.1088/1748-0221/16/08/P08048. arXiv: 2104.09605 [physics.ins-det] (cit. on pp. 62, 76, 128).

[174] D. Akimov et al. “COHERENT 2018 at the Spallation Neutron Source”. In: (Mar. 2018). arXiv: 1803.09183 [physics.ins-det] (cit. on p. 63).

[175] D. Akimov et al. “Monitoring the SNS basement neutron background with the MARS detector”. In: *JINST* 17.03 (2022), P03021. DOI: 10.1088/1748-0221/17/03/P03021. arXiv: 2112.02768 [physics.ins-det] (cit. on p. 63).

[176] George M. Fuller, Wick C. Haxton, and Gail C. McLaughlin. “Prospects for detecting supernova neutrino flavor oscillations”. In: *Phys. Rev. D* 59 (8 Mar. 1999), p. 085005. DOI: 10.1103/PhysRevD.59.085005. URL: https://link.aps.org/doi/10.1103/PhysRevD.59.085005 (cit. on p. 65).

[177] J. Engel, G. C. McLaughlin, and C. Volpe. “What can be learned with a lead based supernova neutrino detector?” In: *Phys. Rev. D* 67 (2003), p. 013005. DOI: 10.1103/PhysRevD.67.013005. arXiv: hep-ph/0209267 (cit. on p. 65).

[178] Steven Gardiner. “Nuclear de-excitations in low-energy charged-current ν_e scattering on ^{40}Ar”. In: *Phys. Rev. C* 103 (4 Apr. 2021), p. 044604. DOI: 10.1103/PhysRevC.103.044604. URL: https://link.aps.org/doi/10.1103/PhysRevC.103.044604 (cit. on p. 65).

[179] J. I. Collar et al. “Coherent neutrino-nucleus scattering detection with a CsI[Na] scintillator at the SNS spallation source”. In: *Nucl. Instrum. Meth. A* 773 (2015), pp. 56–65. DOI: 10.1016/j.nima.2014.11.037. arXiv: 1407.7524 [physics.ins-det] (cit. on p. 66).

[180] D. Akimov et al. “COHERENT Collaboration data release from the measurements of CsI[Na] response to nuclear recoils”. In: (July 2023). arXiv: 2307.10208 [physics.ins-det] (cit. on p. 68).

[181] Steve Baker and Robert D. Cousins. “Clarification of the Use of Chi Square and Likelihood Functions in Fits to Histograms”. In: *Nucl. Instrum. Meth.* 221 (1984), pp. 437–442. DOI: 10.1016/0167-5087(84)90016-4 (cit. on pp. 71, 156).

[182] P. Agnes et al. “Measurement of the liquid argon energy response to nuclear and electronic recoils”. In: *Phys. Rev. D* 97.11 (2018), p. 112005. DOI: 10.1103/PhysRevD.97.112005. arXiv: 1801.06653 [physics.ins-det] (cit. on p. 73).

[183] H. Cao et al. “Measurement of Scintillation and Ionization Yield and Scintillation Pulse Shape from Nuclear Recoils in Liquid Argon”. In: *Phys. Rev. D* 91 (2015), p. 092007. DOI: 10.1103/PhysRevD.91.092007. arXiv: 1406.4825 [physics.ins-det] (cit. on p. 73).

[184] W. Creus et al. “Scintillation efficiency of liquid argon in low energy neutron-argon scattering”. In: *JINST* 10.08 (2015), P08002. DOI: 10.1088/1748-0221/10/08/P08002. arXiv: 1504.07878 [physics.ins-det] (cit. on p. 73).

[185] D. Gastler et al. “Measurement of scintillation efficiency for nuclear recoils in liquid argon”. In: *Phys. Rev. C* 85 (2012), p. 065811. DOI: 10.1103/PhysRevC.85.065811. arXiv: 1004.0373 [physics.ins-det] (cit. on p. 73).

[186] D. Akimov et al. “COHERENT Collaboration data release from the first detection of coherent elastic neutrino-nucleus scattering on argon”. In: (June 2020). DOI: 10.5281/zenodo.3903810. arXiv: 2006.12659 [nucl-ex] (cit. on pp. 75, 167).

[187] P. S. Barbeau et al. “Accessing new physics with an undoped, cryogenic CsI CEvNS detector for COHERENT at the SNS”. In: *Phys. Rev. D* 109.9 (2024), p. 092005. DOI: 10.1103/PhysRevD.109.092005. arXiv: 2311.13032 [hep-ex] (cit. on pp. 75–77, 126, 129, 181).

[188] M. Howell et al. “SNS proton power upgrade”. In: 2017. URL: https://iopscience.iop.org/article/10.1088/1757-899X/278/1/012185 (cit. on p. 75).

[189] D. Akimov et al. “Simulating the neutrino flux from the Spallation Neutron Source for the COHERENT experiment”. In: *Phys. Rev. D* 106.3 (2022), p. 032003. DOI: 10.1103/PhysRevD.106.032003. arXiv: 2109.11049 [hep-ex] (cit. on p. 75).

[190] C. M. Lewis and J. I. Collar. “Response of undoped cryogenic CsI to low-energy nuclear recoils”. In: *Phys. Rev. C* 104.1 (2021), p. 014612. DOI: 10.1103/PhysRevC.104.014612. arXiv: 2101.03264 [physics.ins-det] (cit. on pp. 76, 119).

[191] Glen Cowan et al. “Asymptotic formulae for likelihood-based tests of new physics”. In: *Eur. Phys. J. C* 71 (2011). [Erratum: Eur.Phys.J.C 73, 2501 (2013)], p. 1554. DOI: 10.1140/epjc/s10052-011-1554-0. arXiv: 1007.1727 [physics.data-an] (cit. on p. 77).

[192] Lorenzo Perissé et al. “Comprehensive revision of the summation method for the prediction of reactor $\bar{\nu}_e$ fluxes and spectra”. In: *Phys. Rev. C* 108.5 (2023), p. 055501. DOI: 10.1103/PhysRevC.108.055501. arXiv: 2304.14992 [nucl-ex] (cit. on pp. 80–82, 103).

[193] Lorenzo Périssé. “Modeling of reactor antineutrino spectra”. IRFU, CEA, Université Paris-Saclay, F-91191 Gif-sur-Yvette, France, 2021 (cit. on pp. 80, 81).

[194] Chao Zhang, Xin Qian, and Muriel Fallot. “Reactor antineutrino flux and anomaly”. In: *Prog. Part. Nucl. Phys.* 136 (2024), p. 104106. DOI: 10.1016/j.ppnp.2024.104106. arXiv: 2310.13070 [hep-ph] (cit. on p. 80).

[195] Patrick Huber. “On the determination of anti-neutrino spectra from nuclear reactors”. In: *Phys. Rev. C* 84 (2011). [Erratum: Phys.Rev.C 85, 029901 (2012)], p. 024617. DOI: 10.1103/PhysRevC.85.029901. arXiv: 1106.0687 [hep-ph] (cit. on pp. 81, 82).

[196] Th. A. Mueller et al. “Improved Predictions of Reactor Antineutrino Spectra”. In: *Phys. Rev. C* 83 (2011), p. 054615. DOI: 10.1103/PhysRevC.83.054615. arXiv: 1101.2663 [hep-ex] (cit. on pp. 81, 82).

[197] M. Estienne et al. “Updated Summation Model: An Improved Agreement with the Daya Bay Antineutrino Fluxes”. In: *Phys. Rev. Lett.* 123.2 (2019), p. 022502. DOI: 10.1103/PhysRevLett.123.022502. arXiv: 1904.09358 [nucl-ex] (cit. on pp. 81, 82).

[198] P. Vogel and J. Engel. "Neutrino Electromagnetic Form-Factors". In: *Phys. Rev. D* 39 (1989), p. 3378. DOI: 10.1103/PhysRevD.39.3378 (cit. on pp. 81, 82).

[199] V. I. Kopeikin, L. A. Mikaelyan, and V. V. Sinev. "Search for the neutrino magnetic moment in the nonequilibrium reactor anti-neutrino energy spectrum". In: *Phys. Atom. Nucl.* 63 (2000), pp. 1012–1015. DOI: 10.1134/1.855741. arXiv: hep-ph/9904384 (cit. on pp. 81, 82).

[200] V. I. Kopeikin. "Flux and spectrum of reactor antineutrinos". In: *Phys. Atom. Nucl.* 75 (2012), pp. 143–152. DOI: 10.1134/S1063778812020123 (cit. on pp. 81, 82).

[201] Alexis Aguilar-Arevalo et al. "Exploring low-energy neutrino physics with the Coherent Neutrino Nucleus Interaction Experiment". In: *Phys. Rev. D* 100.9 (2019), p. 092005. DOI: 10.1103/PhysRevD.100.092005. arXiv: 1906.02200 [physics.ins-det] (cit. on pp. 82, 84).

[202] A. Aguilar-Arevalo et al. "Results of the Engineering Run of the Coherent Neutrino Nucleus Interaction Experiment (CONNIE)". In: *JINST* 11.07 (2016), P07024. DOI: 10.1088/1748-0221/11/07/P07024. arXiv: 1604.01343 [physics.ins-det] (cit. on pp. 82, 100, 131).

[203] Alexis Aguilar-Arevalo et al. "Search for coherent elastic neutrino-nucleus scattering at a nuclear reactor with CONNIE 2019 data". In: *JHEP* 05 (2022), p. 017. DOI: 10.1007/JHEP05(2022)017. arXiv: 2110.13033 [hep-ex] (cit. on pp. 82, 100, 112).

[204] Alexis Aguilar-Arevalo et al. "Search for light mediators in the low-energy data of the CONNIE reactor neutrino experiment". In: *JHEP* 04 (2020), p. 054. DOI: 10.1007/JHEP04(2020)054. arXiv: 1910.04951 [hep-ex] (cit. on pp. 82, 177, 181).

[205] Alexis A. Aguilar-Arevalo et al. "Search for reactor-produced millicharged particles with Skipper-CCDs at the CONNIE and Atucha-II experiments". In: (May 2024). arXiv: 2405.16316 [hep-ex] (cit. on p. 82).

[206] H. Bonet et al. "Large-size sub-keV sensitive germanium detectors for the CONUS experiment". In: *Eur. Phys. J. C* 81.3 (2021), p. 267. DOI: 10.1140/epjc/s10052-021-09038-3. arXiv: 2010.11241 [physics.ins-det] (cit. on pp. 82, 84).

[207] H. Bonet et al. “Constraints on elastic neutrino nucleus scattering in the fully coherent regime from the CONUS experiment”. In: *Phys. Rev. Lett.* 126.4 (2021), p. 041804. DOI: 10.1103/PhysRevLett.126.041804. arXiv: 2011.00210 [hep-ex] (cit. on pp. 82, 88, 99, 100).

[208] H. Bonet et al. “Novel constraints on neutrino physics beyond the standard model from the CONUS experiment”. In: *JHEP* 05 (2022), p. 085. DOI: 10.1007/JHEP05(2022)085. arXiv: 2110.02174 [hep-ph] (cit. on pp. 82, 181).

[209] I. Alekseev et al. “First results of the νGeN experiment on coherent elastic neutrino-nucleus scattering”. In: *Phys. Rev. D* 106.5 (2022), p. L051101. DOI: 10.1103/PhysRevD.106.L051101. arXiv: 2205.04305 [nucl-ex] (cit. on pp. 82, 84, 99, 100).

[210] N. Ackermann et al. “Final CONUS results on coherent elastic neutrino nucleus scattering at the Brokdorf reactor”. In: (Jan. 2024). arXiv: 2401.07684 [hep-ex] (cit. on pp. 83, 100, 112).

[211] G. Angloher et al. “Exploring CEνNS with NUCLEUS at the Chooz nuclear power plant”. In: *Eur. Phys. J. C* 79.12 (2019), p. 1018. DOI: 10.1140/epjc/s10052-019-7454-4. arXiv: 1905.10258 [physics.ins-det] (cit. on pp. 83, 84, 101, 102, 105, 109).

[212] R. Strauss et al. “The ν-cleus experiment: A gram-scale fiducial-volume cryogenic detector for the first detection of coherent neutrino-nucleus scattering”. In: *Eur. Phys. J. C* 77 (2017), p. 506. DOI: 10.1140/epjc/s10052-017-5068-2. arXiv: 1704.04320 [physics.ins-det] (cit. on pp. 83, 84, 104–106).

[213] C. Augier et al. “Fast neutron background characterization of the future Ricochet experiment at the ILL research nuclear reactor”. In: *Eur. Phys. J. C* 83.1 (2023), p. 20. DOI: 10.1140/epjc/s10052-022-11150-x. arXiv: 2208.01760 [astro-ph.IM] (cit. on pp. 83, 84).

[214] J. Colas et al. “Development of Data Processing and Analysis Pipeline for the Ricochet Experiment”. In: *J. Low Temp. Phys.* 211.5-6 (2023), pp. 310–319. DOI: 10.1007/s10909-022-02907-5. arXiv: 2111.12856 [physics.ins-det] (cit. on p. 83).

[215] J. Billard et al. “Coherent Neutrino Scattering with Low Temperature Bolometers at Chooz Reactor Complex”. In: *J. Phys. G* 44.10 (2017), p. 105101. DOI: 10.1088/1361-6471/aa83d0. arXiv: 1612.09035 [physics.ins-det] (cit. on p. 83).

[216] C. Augier et al. “First demonstration of 30 eVee ionization energy resolution with Ricochet germanium cryogenic bolometers”. In: *Eur. Phys. J. C* 84.2 (2024), p. 186. DOI: 10.1140/epjc/s10052-024-12433-1. arXiv: 2306.00166 [astro-ph.IM] (cit. on p. 83).

[217] G. Agnolet et al. “Background Studies for the MINER Coherent Neutrino Scattering Reactor Experiment”. In: *Nucl. Instrum. Meth. A* 853 (2017), pp. 53–60. DOI: 10.1016/j.nima.2017.02.024. arXiv: 1609.02066 [physics.ins-det] (cit. on pp. 83, 84, 106, 131).

[218] D. Yu Akimov et al. “First ground-level laboratory test of the two-phase xenon emission detector RED-100”. In: *JINST* 15.02 (2020), P02020. DOI: 10.1088/1748-0221/15/02/P02020. arXiv: 1910.06190 [physics.ins-det] (cit. on p. 83).

[219] J. J. Choi et al. “Exploring coherent elastic neutrino-nucleus scattering using reactor electron antineutrinos in the NEON experiment”. In: *Eur. Phys. J. C* 83.3 (2023), p. 226. DOI: 10.1140/epjc/s10052-023-11352-x. arXiv: 2204.06318 [hep-ex] (cit. on pp. 83, 84).

[220] Henry Tsz-King Wong. “Taiwan EXperiment On NeutrinO — History and Prospects”. In: *The Universe* 3.4 (2015), pp. 22–37. DOI: 10.1142/S0217751X18300144. arXiv: 1608.00306 [hep-ex] (cit. on pp. 83, 84).

[221] D. Aristizabal Sierra et al. “Coherent elastic neutrino-nucleus scattering with the νBDX-DRIFT directional detector at next generation neutrino facilities”. In: *Phys. Rev. D* 104.3 (2021), p. 033004. DOI: 10.1103/PhysRevD.104.033004. arXiv: 2103.10857 [hep-ph] (cit. on pp. 83, 84).

[222] D. Aristizabal Sierra et al. “Rock neutron backgrounds from FNAL neutrino beamlines in the νBDX-DRIFT detector”. In: *Phys. Rev. D* 107.1 (2023), p. 013003. DOI: 10.1103/PhysRevD.107.013003. arXiv: 2210.08612 [hep-ex] (cit. on pp. 83, 84).

[223] C. Awe et al. “High Energy Physics Opportunities Using Reactor Antineutrinos”. In: (Mar. 2022). arXiv: 2203.07214 [hep-ex] (cit. on pp. 83, 84).

[224] A. Cruciani et al. “BULLKID: Monolithic array of particle absorbers sensed by kinetic inductance detectors”. In: *Appl. Phys. Lett.* 121.21 (2022), p. 213504. DOI: 10.1063/5.0128723. arXiv: 2209.14806 [physics.ins-det] (cit. on pp. 83, 84, 105).

[225] A. Simón. “GanESS: detecting coherent elastic neutrino-nucleus scattering with noble gases”. In: *JINST* 19.04 (2024), p. C04041. DOI: 10.1088/1748-0221/19/04/C04041 (cit. on pp. 83, 84).

[226] J. Colaresi et al. “Measurement of Coherent Elastic Neutrino-Nucleus Scattering from Reactor Antineutrinos”. In: *Phys. Rev. Lett.* 129.21 (2022), p. 211802. DOI: 10.1103/PhysRevLett.129.211802. arXiv: 2202.09672 [hep-ex] (cit. on pp. 83–86, 89, 98–100).

[227] Pilar Coloma et al. “Bounds on new physics with data of the Dresden-II reactor experiment and COHERENT”. In: *JHEP* 05 (2022), p. 037. DOI: 10.1007/JHEP05(2022)037. arXiv: 2202.10829 [hep-ph] (cit. on pp. 83, 86, 98, 100, 114, 137, 138, 178).

[228] Anirban Majumdar et al. “Physics implications of recent Dresden-II reactor data”. In: *Phys. Rev. D* 106.9 (2022), p. 093010. DOI: 10.1103/PhysRevD.106.093010. arXiv: 2208.13262 [hep-ph] (cit. on p. 83).

[229] Peter B. Denton and Julia Gehrlein. “New constraints on the dark side of non-standard interactions from reactor neutrino scattering data”. In: *Phys. Rev. D* 106.1 (2022), p. 015022. DOI: 10.1103/PhysRevD.106.015022. arXiv: 2204.09060 [hep-ph] (cit. on p. 83).

[230] Michael Berglund and Michael E. Wieser. “Isotopic compositions of the elements 2009 (IUPAC Technical Report)”. In: *Pure and Applied Chemistry* 83.2 (2011), pp. 397–410. DOI: doi:10.1351/PAC-REP-10-06-02. URL: https://doi.org/10.1351/PAC-REP-10-06-02 (cit. on p. 86).

[231] J Lindhard et al. “INTEGRAL EQUATIONS GOVERNING RADIATION EFFECTS. (NOTES ON ATOMIC COLLISIONS, III)”. In: *Kgl. Danske Videnskab., Selskab. Mat. Fys. Medd.* 33, 10 (Jan. 1963). URL: https://www.osti.gov/biblio/4701226 (cit. on p. 88).

[232] K. W. Jones and H. W. Kraner. “Energy lost to ionization by 254-eV ^{73}Ge atoms stopping in Ge”. In: *Phys. Rev. A* 11 (4 Apr. 1975), pp. 1347–1353. DOI: 10.1103/PhysRevA.11.1347. URL: https://link.aps.org/doi/10.1103/PhysRevA.11.1347 (cit. on pp. 88, 89).

[233] K. W. Jones and H. W. Kraner. "Stopping of 1- to 1.8-keV ^{73}Ge Atoms in Germanium". In: *Phys. Rev. C* 4 (1 July 1971), pp. 125–129. DOI: 10.1103/PhysRevC.4.125. URL: https://link.aps.org/doi/10.1103/PhysRevC.4.125 (cit. on pp. 88, 89).

[234] C. E. Aalseth et al. "CoGeNT: A search for low-mass dark matter using p-type point contact germanium detectors". In: *Phys. Rev. D* 88 (1 July 2013), p. 012002. DOI: 10.1103/PhysRevD.88.012002. URL: https://link.aps.org/doi/10.1103/PhysRevD.88.012002 (cit. on pp. 88, 89).

[235] M. F. Albakry et al. "Ionization yield measurement in a germanium CDMSlite detector using photo-neutron sources". In: *Phys. Rev. D* 105.12 (2022), p. 122002. DOI: 10.1103/PhysRevD.105.122002. arXiv: 2202.07043 [physics.ins-det] (cit. on pp. 88, 89).

[236] A. Bonhomme et al. "Direct measurement of the ionization quenching factor of nuclear recoils in germanium in the keV energy range". In: *Eur. Phys. J. C* 82.9 (2022), p. 815. DOI: 10.1140/epjc/s10052-022-10768-1. arXiv: 2202.03754 [physics.ins-det] (cit. on pp. 88, 89).

[237] Y. Messous. "Calibration of a Ge crystal with nuclear recoils for the development of a dark matter detector". In: *Astropart. Phys.* 3 (1995), pp. 361–366. DOI: 10.1016/0927-6505(95)00007-4 (cit. on pp. 88, 89).

[238] Ruan Xi-chao et al. "Nuclear recoil quenching factor, measurement for HPGe detector". In: *Nuclear recoil quenching factor measurement for HPGe detector, presented at Application of Germanium Detector in fundamental research, Tsinghua University* (Mar. 2011), pp. 24–26 (cit. on pp. 88, 89).

[239] B. J. Scholz et al. "Measurement of the low-energy quenching factor in germanium using an ^{88}Y/Be photoneutron source". In: *Phys. Rev. D* 94.12 (2016), p. 122003. DOI: 10.1103/PhysRevD.94.122003. arXiv: 1608.03588 [physics.ins-det] (cit. on p. 89).

[240] E. Armengaud et al. "Performance of the EDELWEISS-III experiment for direct dark matter searches". In: *JINST* 12.08 (2017), P08010. DOI: 10.1088/1748-0221/12/08/P08010. arXiv: 1706.01070 [physics.ins-det] (cit. on p. 89).

[241] A. R. L. Kavner and I. Jovanovic. "Measurement of Ionization Produced by 254 eVnr Nuclear Recoils in Germanium". In: (May 2024). arXiv: 2405.10405 [nucl-ex] (cit. on pp. 88, 89).

[242] J. Colaresi et al. “First results from a search for coherent elastic neutrino-nucleus scattering at a reactor site”. In: *Phys. Rev. D* 104.7 (2021), p. 072003. DOI: 10.1103/PhysRevD.104.072003. arXiv: 2108.02880 [hep-ex] (cit. on pp. 88, 89).

[243] J. I. Collar, A. R. L. Kavner, and C. M. Lewis. “Germanium response to sub-keV nuclear recoils: a multipronged experimental characterization”. In: *Phys. Rev. D* 103.12 (2021), p. 122003. DOI: 10.1103/PhysRevD.103.122003. arXiv: 2102.10089 [nucl-ex] (cit. on pp. 88, 97).

[244] Jiajun Liao, Hongkai Liu, and Danny Marfatia. “Coherent neutrino scattering and the Migdal effect on the quenching factor”. In: *Phys. Rev. D* 104.1 (2021), p. 015005. DOI: 10.1103/PhysRevD.104.015005. arXiv: 2104.01811 [hep-ph] (cit. on p. 89).

[245] Jiajun Liao, Hongkai Liu, and Danny Marfatia. “Implications of the first evidence for coherent elastic scattering of reactor neutrinos”. In: *Phys. Rev. D* 106.3 (2022), p. L031702. DOI: 10.1103/PhysRevD.106.L031702. arXiv: 2202.10622 [hep-ph] (cit. on pp. 89, 137, 138).

[246] Peter Sorensen. “Atomic limits in the search for galactic dark matter”. In: *Phys. Rev. D* 91.8 (2015), p. 083509. DOI: 10.1103/PhysRevD.91.083509. arXiv: 1412.3028 [astro-ph.IM] (cit. on p. 90).

[247] A. Migdal. “Ionizatsiya atomov pri yadernykh reaktsiyakh (Ionization of atoms in nuclear reactions)”. In: *ZhETF* 9 (1939), pp. 1163–1165 (cit. on p. 90).

[248] A. Migdal. “Ionization of atoms accompanying α- and β-decay”. In: *J. Phys. Acad. Sci. USSR* 4 (1941), pp. 449–453 (cit. on p. 90).

[249] E. L. Feinberg. “Ionization of the atom due to β-decay”. In: *J. Phys. Acad. Sci. USSR* 4 (1941), p. 423 (cit. on p. 90).

[250] J. S. Levinger. “Effects of Radioactive Disintegrations on Inner Electrons of the Atom”. In: *Phys. Rev.* 90 (1953), pp. 11–25. DOI: 10.1103/PhysRev.90.11 (cit. on p. 90).

[251] A. B. Migdal. *Qualitative Methods In Quantum Theory*. CRC Press, 1977. DOI: 10.1201/9780429497940 (cit. on p. 90).

[252] M. S. Rapaport. *Atomic electron shake-off accompanying alpha decay*. Tech. rep. (LBL–2978). Lawrence Berkeley National Laboratory, 1974. DOI: 10.2172/4262551 (cit. on p. 90).

[253] M. S. Rapaport et al. "K-shell electron shake-off accompanying alpha decay". In: *Phys. Rev. C.* 11 (1975), pp. 1740–1745. DOI: 10.1103/PhysRevC.11.1740 (cit. on p. 90).

[254] M. S. Rapaport et al. "L- and M-shell electron shake-off accompanying alpha decay". In: *Phys. Rev. C.* 11 (1975), pp. 1746–1754. DOI: 10.1103/PhysRevC.11.1746 (cit. on p. 90).

[255] F. Boehm and C. S. Wu. "Internal Bremsstrahlung and Ionization Accompanying Beta Decay". In: *Phys. Rev.* 93 (1954), pp. 518–523. DOI: 10.1103/PhysRev.93.518 (cit. on p. 90).

[256] C. Couratin et al. "First Measurement of Pure Electron Shakeoff in the β Decay of Trapped $^{6}\mathrm{He}^{+}$ Ions". In: *Phys. Rev. L.* 108 (2012), p. 243201. DOI: 10.1103/PhysRevLett.108.243201 (cit. on p. 90).

[257] X. Fabian et al. "Electron shakeoff following the β^{+} decay of $^{19}\mathrm{Ne}^{+}$ and $^{35}\mathrm{Ar}^{+}$ trapped ions". In: *Phys. Rev. A.* 97 (2018), p. 023402. DOI: 10.1103/PhysRevA.97.023402 (cit. on p. 90).

[258] Peter Cox et al. "Precise predictions and new insights for atomic ionization from the Migdal effect". In: *Phys. Rev. D* 107.3 (2023), p. 035032. DOI: 10.1103/PhysRevD.107.035032. arXiv: 2208.12222 [hep-ph] (cit. on pp. 91, 92).

[259] Jingke Xu et al. "Search for the Migdal effect in liquid xenon with keV-level nuclear recoils". In: *Phys. Rev. D* 109.5 (2024), p. L051101. DOI: 10.1103/PhysRevD.109.L051101. arXiv: 2307.12952 [hep-ex] (cit. on p. 91).

[260] Masahiro Ibe et al. "Migdal Effect in Dark Matter Direct Detection Experiments". In: *JHEP* 03 (2018), p. 194. DOI: 10.1007/JHEP03(2018)194. arXiv: 1707.07258 [hep-ph] (cit. on pp. 91–94).

[261] Rouven Essig et al. "Relation between the Migdal Effect and Dark Matter-Electron Scattering in Isolated Atoms and Semiconductors". In: *Phys. Rev. Lett.* 124.2 (2020), p. 021801. DOI: 10.1103/PhysRevLett.124.021801. arXiv: 1908.10881 [hep-ph] (cit. on pp. 91, 94).

[262] Giovanni Grilli di Cortona, Andrea Messina, and Stefano Piacentini. "Migdal effect and photon Bremsstrahlung: improving the sensitivity to light dark matter of liquid argon experiments". In: *JHEP* 11 (2020), p. 034. DOI: 10.1007/JHEP11(2020)034. arXiv: 2006.02453 [hep-ph] (cit. on p. 91).

[263] C. P. Liu et al. “Model-independent determination of the Migdal effect via photoabsorption”. In: *Phys. Rev. D* 102.12 (2020), p. 121303. DOI: 10.1103/PhysRevD.102.121303. arXiv: 2007.10965 [hep-ph] (cit. on pp. 91, 94, 95).

[264] E. Aprile et al. “Search for Light Dark Matter Interactions Enhanced by the Migdal Effect or Bremsstrahlung in XENON1T”. In: *Phys. Rev. Lett.* 123.24 (2019), p. 241803. DOI: 10.1103/PhysRevLett.123.241803. arXiv: 1907.12771 [hep-ex] (cit. on p. 91).

[265] M. F. Albakry et al. “Search for low-mass dark matter via bremsstrahlung radiation and the Migdal effect in SuperCDMS”. In: *Phys. Rev. D* 107.11 (2023), p. 112013. DOI: 10.1103/PhysRevD.107.112013. arXiv: 2302.09115 [hep-ex] (cit. on p. 91).

[266] Nicole F. Bell et al. “Low-mass inelastic dark matter direct detection via the Migdal effect”. In: *Phys. Rev. D* 104.7 (2021), p. 076013. DOI: 10.1103/PhysRevD.104.076013. arXiv: 2103.05890 [hep-ph] (cit. on p. 91).

[267] Nicole F. Bell et al. “Observing the Migdal effect from nuclear recoils of neutral particles with liquid xenon and argon detectors”. In: *Phys. Rev. D* 105.9 (2022), p. 096015. DOI: 10.1103/PhysRevD.105.096015. arXiv: 2112.08514 [hep-ph] (cit. on pp. 91, 94, 96).

[268] Nicole F. Bell et al. “Migdal effect and photon bremsstrahlung in effective field theories of dark matter direct detection and coherent elastic neutrino-nucleus scattering”. In: *Phys. Rev. D* 101.1 (2020), p. 015012. DOI: 10.1103/PhysRevD.101.015012. arXiv: 1905.00046 [hep-ph] (cit. on p. 93).

[269] B.L. Henke, E.M. Gullikson, and J.C. Davis. “X-Ray Interactions: Photoabsorption, Scattering, Transmission, and Reflection at E = 50-30,000 eV, Z = 1-92”. In: *Atomic Data and Nuclear Data Tables* 54.2 (1993), pp. 181–342. ISSN: 0092-640X. DOI: https://doi.org/10.1006/adnd.1993.1013. URL: https://www.sciencedirect.com/science/article/pii/S0092640X83710132 (cit. on pp. 95, 96, 161).

[270] Simon Knapen, Jonathan Kozaczuk, and Tongyan Lin. “Migdal Effect in Semiconductors”. In: *Phys. Rev. Lett.* 127.8 (2021), p. 081805. DOI: 10.1103/PhysRevLett.127.081805. arXiv: 2011.09496 [hep-ph] (cit. on p. 97).

[271] Simon Knapen, Jonathan Kozaczuk, and Tongyan Lin. "python package for dark matter scattering in dielectric targets". In: *Phys. Rev. D* 105.1 (2022), p. 015014. DOI: 10.1103/PhysRevD.105.015014. arXiv: 2104.12786 [hep-ph] (cit. on p. 97).

[272] Duncan Adams et al. "Measuring the Migdal effect in semiconductors for dark matter detection". In: *Phys. Rev. D* 107.4 (2023), p. L041303. DOI: 10.1103/PhysRevD.107.L041303. arXiv: 2210.04917 [hep-ph] (cit. on p. 97).

[273] Zheng-Liang Liang et al. "Phonon-mediated Migdal effect in semiconductor detectors". In: *Phys. Rev. D* 106.4 (2022). [Erratum: Phys.Rev.D 106, 109901 (2022)], p. 043004. DOI: 10.1103/PhysRevD.106.043004. arXiv: 2205.03395 [hep-ph] (cit. on p. 97).

[274] Yonatan Kahn, Gordan Krnjaic, and Bashi Mandava. "Dark Matter Detection with Bound Nuclear Targets: The Poisson Phonon Tail". In: *Phys. Rev. Lett.* 127.8 (2021), p. 081804. DOI: 10.1103/PhysRevLett.127.081804. arXiv: 2011.09477 [hep-ph] (cit. on p. 97).

[275] Noah Kurinsky et al. "Dark matter interpretation of excesses in multiple direct detection experiments". In: *Phys. Rev. D* 102.1 (2020), p. 015017. DOI: 10.1103/PhysRevD.102.015017. arXiv: 2002.06937 [hep-ph] (cit. on p. 97).

[276] Tanner Trickle et al. "Multi-Channel Direct Detection of Light Dark Matter: Theoretical Framework". In: *JHEP* 03 (2020), p. 036. DOI: 10.1007/JHEP03(2020)036. arXiv: 1910.08092 [hep-ph] (cit. on p. 97).

[277] F. Ardellier et al. "Double Chooz: A Search for the neutrino mixing angle theta(13)". In: (June 2006). arXiv: hep-ex/0606025 (cit. on p. 102).

[278] Y. Abe et al. "Indication of Reactor $\bar{\nu}_e$ Disappearance in the Double Chooz Experiment". In: *Phys. Rev. Lett.* 108 (2012), p. 131801. DOI: 10.1103/PhysRevLett.108.131801. arXiv: 1112.6353 [hep-ex] (cit. on p. 102).

[279] Y. Abe et al. "Reactor electron antineutrino disappearance in the Double Chooz experiment". In: *Phys. Rev. D* 86 (2012), p. 052008. DOI: 10.1103/PhysRevD.86.052008. arXiv: 1207.6632 [hep-ex] (cit. on p. 102).

[280] A. Erhart et al. “A plastic scintillation muon veto for sub-Kelvin temperatures”. In: *Eur. Phys. J. C* 84.1 (2024), p. 70. DOI: 10.1140/epjc/s10052-023-12375-0. arXiv: 2310.08457 [physics.ins-det] (cit. on pp. 102, 105).

[281] R. Strauss et al. “Gram-scale cryogenic calorimeters for rare-event searches”. In: *Phys. Rev. D* 96.2 (2017), p. 022009. DOI: 10.1103/PhysRevD.96.022009. arXiv: 1704.04317 [physics.ins-det] (cit. on p. 103).

[282] Johannes Felix Martin Rothe. “Low-Threshold Cryogenic Detectors for Low-Mass Dark Matter Search and Coherent Neutrino Scattering”. PhD thesis. Munich, Tech. U., Munich, Tech. U., 2021 (cit. on pp. 104, 105).

[283] G. Angloher et al. “Results on light dark matter particles with a low-threshold CRESST-II detector”. In: *Eur. Phys. J. C* 76.1 (2016), p. 25. DOI: 10.1140/epjc/s10052-016-3877-3. arXiv: 1509.01515 [astro-ph.CO] (cit. on pp. 104, 106).

[284] A. H. Abdelhameed et al. “First results from the CRESST-III low-mass dark matter program”. In: *Phys. Rev. D* 100.10 (2019), p. 102002. DOI: 10.1103/PhysRevD.100.102002. arXiv: 1904.00498 [astro-ph.CO] (cit. on pp. 104, 106, 107).

[285] G. Angloher et al. “Results from the first cryogenic NaI detector for the COSINUS project”. In: *JINST* 12.11 (2017), P11007. DOI: 10.1088/1748-0221/12/11/P11007. arXiv: 1705.11028 [physics.ins-det] (cit. on p. 104).

[286] G. Angloher et al. “First measurements of remoTES cryogenic calorimeters: Easy-to-fabricate particle detectors for a wide choice of target materials”. In: *Nucl. Instrum. Meth. A* 1045 (2023), p. 167532. DOI: 10.1016/j.nima.2022.167532. arXiv: 2111.00349 [physics.ins-det] (cit. on p. 104).

[287] N. Ferreiro Iachellini et al. “Operation of an Archaeological Lead $PbWO_4$ Crystal to Search for Neutrinos from Astrophysical Sources with a Transition Edge Sensor”. In: *J. Low Temp. Phys.* 209.5-6 (2022), pp. 872–878. DOI: 10.1007/s10909-022-02823-8. arXiv: 2111.07638 [physics.ins-det] (cit. on p. 104).

[288] L. Cardani et al. “Al/Ti/Al phonon-mediated KIDs for UV–vis light detection over large areas”. In: *Supercond. Sci. Technol.* 31.7 (2018), p. 075002. DOI: 10.1088/1361-6668/aac1d4. arXiv: 1801.08403 [physics.ins-det] (cit. on p. 105).

[289] Giorgio Del Castello. “Development of energy calibration and data analysis systems for the NUCLEUS experiment”. MA thesis. Rome U., 2021. arXiv: 2302.02843 [physics.ins-det] (cit. on p. 105).

[290] I. Colantoni et al. “BULLKID: BULky and Low-Threshold Kinetic Inductance Detectors”. In: *J. Low Temp. Phys.* 199.3-4 (2020), pp. 593–597. DOI: 10.1007/s10909-020-02408-3 (cit. on p. 105).

[291] D. Delicato et al. “Low-energy spectrum of the BULLKID detector array operated on surface”. In: *Eur. Phys. J. C* 84.4 (2024), p. 353. DOI: 10.1140/epjc/s10052-024-12714-9. arXiv: 2308.14399 [hep-ex] (cit. on pp. 105, 107).

[292] Prakruth Adari et al. “EXCESS workshop: Descriptions of rising low-energy spectra”. In: *SciPost Phys. Proc.* 9 (2022). Ed. by A. Fuss et al., p. 001. DOI: 10.21468/SciPostPhysProc.9.001. arXiv: 2202.05097 [astro-ph.IM] (cit. on pp. 106, 107).

[293] D. S. Akerib et al. “Investigation of background electron emission in the LUX detector”. In: *Phys. Rev. D* 102.9 (2020), p. 092004. DOI: 10.1103/PhysRevD.102.092004. arXiv: 2004.07791 [physics.ins-det] (cit. on p. 106).

[294] Kai Nordlund et al. “Defect recombination origin of low energy excess in semiconductor detectors”. In: (Aug. 2024). arXiv: 2408.07518 [cond-mat.mtrl-sci] (cit. on p. 106).

[295] Matteo Cappelli, Giorgio del Castello, and Marco Vignati. “Estimation of waveform deformation with the matched filter”. In: *JINST* 19.06 (2024), P06034. DOI: 10.1088/1748-0221/19/06/P06034. arXiv: 2405.02300 [physics.ins-det] (cit. on pp. 106, 108).

[296] A. Aguilar-Arevalo et al. “Results on low-mass weakly interacting massive particles from a 11 kg-day target exposure of DAMIC at SNOLAB”. In: *Phys. Rev. Lett.* 125 (2020), p. 241803. DOI: 10.1103/PhysRevLett.125.241803. arXiv: 2007.15622 [astro-ph.CO] (cit. on p. 106).

[297] E. Armengaud et al. “Searching for low-mass dark matter particles with a massive Ge bolometer operated above-ground”. In: *Phys. Rev. D* 99.8 (2019), p. 082003. DOI: 10.1103/PhysRevD.99.082003. arXiv: 1901.03588 [astro-ph.GA] (cit. on p. 106).

[298] Q. Arnaud et al. “First results from the NEWS-G direct dark matter search experiment at the LSM”. In: *Astropart. Phys.* 97 (2018), pp. 54–62. DOI: 10.1016/j.astropartphys.2017.10.009. arXiv: 1706.04934 [astro-ph.IM] (cit. on p. 106).

[299] A. H. Abdelhameed et al. “Description of CRESST-III Data”. In: (May 2019). arXiv: 1905.07335 [astro-ph.CO] (cit. on pp. 106, 107).

[300] Margarita Kaznacheeva. *New excess measurements from NUCLEUS*. Talk presented at EXCESS24 Workshop, 06 Jul 2024 (cit. on pp. 106, 107).

[301] G. Angloher et al. “DoubleTES detectors to investigate the CRESST low energy background: results from above-ground prototypes”. In: (Apr. 2024). arXiv: 2404.02607 [physics.ins-det] (cit. on p. 106).

[302] Giorgio Del Castello. “Calibration and commissioning results of the NUCLEUS experiment”. PhD thesis. La Sapienza, Rome, U., 2025 (cit. on p. 107).

[303] Adrienne L. Erickcek et al. “Constraints on the Interactions between Dark Matter and Baryons from the X-ray Quantum Calorimetry Experiment”. In: *Phys. Rev. D* 76 (2007), p. 042007. DOI: 10.1103/PhysRevD.76.042007. arXiv: 0704.0794 [astro-ph] (cit. on pp. 110, 111, 182).

[304] D. Abrams et al. “Exclusion Limits on the WIMP Nucleon Cross-Section from the Cryogenic Dark Matter Search”. In: *Phys. Rev. D* 66 (2002), p. 122003. DOI: 10.1103/PhysRevD.66.122003. arXiv: astro-ph/0203500 (cit. on p. 110).

[305] S. Yellin. “Finding an upper limit in the presence of an unknown background”. In: *Physical Review D* 66.3 (Aug. 2002). ISSN: 1089-4918. DOI: 10.1103/physrevd.66.032005. URL: http://dx.doi.org/10.1103/PhysRevD.66.032005 (cit. on p. 110).

[306] M. Shafi Mahdawi and Glennys R. Farrar. “Closing the window on $\sim$GeV Dark Matter with moderate ($\sim \mu$b) interaction with nucleons”. In: *JCAP* 12 (2017), p. 004. DOI: 10.1088/1475-7516/2017/12/004. arXiv: 1709.00430 [hep-ph] (cit. on p. 111).

[307] O. G. Miranda et al. “Implications of the first detection of coherent elastic neutrino-nucleus scattering (CEvNS) with Liquid Argon”. In: *JHEP* 05 (2020). [Erratum: JHEP 01, 067 (2021)], p. 130. DOI: 10.1007/JHEP05(2020)130. arXiv: 2003.12050 [hep-ph] (cit. on pp. 113, 174, 178).

[308] M. Cadeddu et al. “New insights into nuclear physics and weak mixing angle using electroweak probes”. In: *Phys. Rev. C* 104.6 (2021), p. 065502. DOI: 10.1103/PhysRevC.104.065502. arXiv: 2102.06153 [hep-ph] (cit. on pp. 113, 115, 117, 123, 129–131).

[309] D. K. Papoulias et al. “Constraining nuclear physics parameters with current and future COHERENT data”. In: *Phys. Lett. B* 800 (2020), p. 135133. DOI: 10.1016/j.physletb.2019.135133. arXiv: 1903.03722 [hep-ph] (cit. on p. 113).

[310] M. Cadeddu et al. “Neutrino, electroweak, and nuclear physics from COHERENT elastic neutrino-nucleus scattering with refined quenching factor”. In: *Phys. Rev. D* 101.3 (2020), p. 033004. DOI: 10.1103/PhysRevD.101.033004. arXiv: 1908.06045 [hep-ph] (cit. on pp. 113, 129, 130).

[311] Dimitrios K. Papoulias. “COHERENT constraints after the COHERENT-2020 quenching factor measurement”. In: *Phys. Rev. D* 102.11 (2020), p. 113004. DOI: 10.1103/PhysRevD.102.113004. arXiv: 1907.11644 [hep-ph] (cit. on pp. 113, 168, 176).

[312] D. Aristizabal Sierra, Valentina De Romeri, and N. Rojas. “COHERENT analysis of neutrino generalized interactions”. In: *Phys. Rev. D* 98 (2018), p. 075018. DOI: 10.1103/PhysRevD.98.075018. arXiv: 1806.07424 [hep-ph] (cit. on pp. 113, 172, 173).

[313] Matteo Cadeddu and Francesca Dordei. “Reinterpreting the weak mixing angle from atomic parity violation in view of the Cs neutron rms radius measurement from COHERENT”. In: *Phys. Rev. D* 99.3 (2019), p. 033010. DOI: 10.1103/PhysRevD.99.033010. arXiv: 1808.10202 [hep-ph] (cit. on pp. 113, 115, 123).

[314] V. De Romeri et al. “Physics implications of a combined analysis of COHERENT CsI and LAr data”. In: *JHEP* 04 (2023), p. 035. DOI: 10.1007/JHEP04(2023)035. arXiv: 2211.11905 [hep-ph] (cit. on pp. 113, 114, 118, 145, 147, 178).

[315] Xu-Run Huang and Lie-Wen Chen. "Neutron Skin in CsI and Low-Energy Effective Weak Mixing Angle from COHERENT Data". In: *Phys. Rev. D* 100.7 (2019), p. 071301. DOI: 10.1103/PhysRevD.100.071301. arXiv: 1902.07625 [hep-ph] (cit. on p. 113).

[316] M. B. Tsang et al. "Constraints on the symmetry energy and neutron skins from experiments and theory". In: *Phys. Rev. C* 86 (2012), p. 015803. DOI: 10.1103/PhysRevC.86.015803. arXiv: 1204.0466 [nucl-ex] (cit. on p. 113).

[317] G. F. Burgio and I. Vidana. "The Equation of State of Nuclear Matter : from Finite Nuclei to Neutron Stars". In: *Universe* 6.8 (2020), p. 119. DOI: 10.3390/universe6080119. arXiv: 2007.04427 [nucl-th] (cit. on p. 113).

[318] Hong Shen et al. "Effects of symmetry energy on equation of state for simulations of core-collapse supernovae and neutron-star mergers". In: *Astrophys. J.* 891 (2020), p. 148. DOI: 10.3847/1538-4357/ab72fd. arXiv: 2001.10143 [nucl-th] (cit. on p. 113).

[319] M. Centelles et al. "Nuclear symmetry energy probed by neutron skin thickness of nuclei". In: *Phys. Rev. Lett.* 102 (2009), p. 122502. DOI: 10.1103/PhysRevLett.102.122502. arXiv: 0806.2886 [nucl-th] (cit. on p. 113).

[320] C. J. Horowitz. "Neutron rich matter in the laboratory and in the heavens after GW170817". In: *Annals Phys.* 411 (2019), p. 167992. DOI: 10.1016/j.aop.2019.167992. arXiv: 1911.00411 [astro-ph.HE] (cit. on p. 113).

[321] Jin-Biao Wei et al. "Are nuclear matter properties correlated to neutron star observables?" In: *Eur. Phys. J. A* 56.2 (2020), p. 63. DOI: 10.1140/epja/s10050-020-00058-3. arXiv: 1907.08761 [nucl-th] (cit. on p. 113).

[322] M. Thiel et al. "Neutron skins of atomic nuclei: per aspera ad astra". In: *J. Phys. G* 46.9 (2019), p. 093003. DOI: 10.1088/1361-6471/ab2c6d. arXiv: 1904.12269 [nucl-ex] (cit. on pp. 113, 114).

[323] D. Adhikari et al. "Accurate Determination of the Neutron Skin Thickness of ^{208}Pb through Parity-Violation in Electron Scattering". In: *Phys. Rev. Lett.* 126.17 (2021), p. 172502. DOI: 10.1103/PhysRevLett.126.172502. arXiv: 2102.10767 [nucl-ex] (cit. on pp. 113, 114, 123, 130).

[324] S. Abrahamyan et al. “Measurement of the Neutron Radius of 208Pb Through Parity-Violation in Electron Scattering”. In: *Phys. Rev. Lett.* 108 (2012), p. 112502. DOI: 10.1103/PhysRevLett.108.112502. arXiv: 1201.2568 [nucl-ex] (cit. on pp. 114, 123, 130).

[325] D. Adhikari et al. “Precision Determination of the Neutral Weak Form Factor of Ca48”. In: *Phys. Rev. Lett.* 129.4 (2022), p. 042501. DOI: 10.1103/PhysRevLett.129.042501. arXiv: 2205.11593 [nucl-ex] (cit. on pp. 114, 124, 130).

[326] Y. Huang et al. “Neutron radius determination of 133Cs and its impact on the interpretation of CEνNS-CsI measurement”. In: *Phys. Lett. B* 856 (2024), p. 138902. DOI: 10.1016/j.physletb.2024.138902. arXiv: 2403.03566 [nucl-ex] (cit. on pp. 114, 125).

[327] M. S. Safronova et al. “Search for New Physics with Atoms and Molecules”. In: *Rev. Mod. Phys.* 90.2 (2018), p. 025008. DOI: 10.1103/RevModPhys.90.025008. arXiv: 1710.01833 [physics.atom-ph] (cit. on p. 114).

[328] M. Cadeddu et al. “Muon and electron g-2 and proton and cesium weak charges implications on dark Zd models”. In: *Phys. Rev. D* 104.1 (2021), p. 011701. DOI: 10.1103/PhysRevD.104.L011701. arXiv: 2104.03280 [hep-ph] (cit. on pp. 114, 124, 166).

[329] Ross Daniel Young et al. “Testing the standard model by precision measurement of the weak charges of quarks”. In: *Phys. Rev. Lett.* 99 (2007), p. 122003. DOI: 10.1103/PhysRevLett.99.122003. arXiv: 0704.2618 [hep-ph] (cit. on p. 114).

[330] J. Guena, M. Lintz, and M. A. Bouchiat. “Measurement of the parity violating 6S-7S transition amplitude in cesium achieved within 2 x 10(-13) atomic-unit accuracy by stimulated-emission detection”. In: *Phys. Rev. A* 71 (2005), p. 042108. DOI: 10.1103/PhysRevA.71.042108. arXiv: physics/0412017 (cit. on pp. 115, 122).

[331] Jason Newby. *The Neutrino Laboratory at the Spallation Neutron Source*. Talk presented at Magnificent CEνNS 2023, 22–29 Mar 2023. URL: https://indico.cern.ch/event/1215362/contributions/5300031/ (cit. on p. 116).

[332] D. Akimov et al. “Measurement of scintillation response of CsI[Na] to low-energy nuclear recoils by COHERENT”. In: *JINST* 17.10 (2022), P10034. DOI: 10.1088/1748-0221/17/10/P10034. arXiv: 2111.02477 [physics.ins-det] (cit. on p. 119).

[333] A. V. Viatkina et al. “Dependence of atomic parity-violation effects on neutron skins and new physics”. In: *Physical Review C* 100.3 (Sept. 2019). ISSN: 2469-9993. DOI: 10.1103/physrevc.100.034318. URL: http://dx.doi.org/10.1103/PhysRevC.100.034318 (cit. on p. 122).

[334] D. M. Meekhof et al. “High-precision measurement of parity nonconserving optical rotation in atomic lead”. In: *Phys. Rev. Lett.* 71 (21 Nov. 1993), pp. 3442–3445. DOI: 10.1103/PhysRevLett.71.3442. URL: https://link.aps.org/doi/10.1103/PhysRevLett.71.3442 (cit. on p. 122).

[335] A. Trzcinska et al. “Neutron density distributions deduced from anti-protonic atoms”. In: *Phys. Rev. Lett.* 87 (2001), p. 082501. DOI: 10.1103/PhysRevLett.87.082501 (cit. on p. 123).

[336] C. J. Horowitz et al. “Parity violating measurements of neutron densities”. In: *Phys. Rev. C* 63 (2 Jan. 2001), p. 025501. DOI: 10.1103/PhysRevC.63.025501. URL: https://link.aps.org/doi/10.1103/PhysRevC.63.025501 (cit. on p. 123).

[337] Matteo Cadeddu et al. “Simultaneous Extraction of the Weak Radius and the Weak Mixing Angle from Parity-Violating Electron Scattering on ^{12}C”. In: (July 2024). arXiv: 2407.09743 [hep-ph] (cit. on pp. 123, 130, 131).

[338] S. G. Porsev et al. “Development of the configuration-interaction + all-order method and application to the parity-nonconserving amplitude and other properties of Pb”. In: *Phys. Rev. A* 93 (1 Jan. 2016), p. 012501. DOI: 10.1103/PhysRevA.93.012501. URL: https://link.aps.org/doi/10.1103/PhysRevA.93.012501 (cit. on p. 123).

[339] B. K. Sahoo, B. P. Das, and H. Spiesberger. “New physics constraints from atomic parity violation in Cs133”. In: *Phys. Rev. D* 103.11 (2021), p. L111303. DOI: 10.1103/PhysRevD.103.L111303. arXiv: 2101.10095 [hep-ph] (cit. on p. 125).

[340] M. Abdullah et al. “Coherent elastic neutrino-nucleus scattering: Terrestrial and astrophysical applications”. In: (Mar. 2022). arXiv: 2203.07361 [hep-ph] (cit. on p. 127).

[341] R. R. Rossi, G. Sanchez Garcia, and M. Tórtola. "Probing nuclear properties and neutrino physics with current and future CEνNS experiments". In: *Phys. Rev. D* 109.9 (2024), p. 095044. DOI: 10.1103/PhysRevD.109.095044. arXiv: 2311.17168 [hep-ph] (cit. on p. 129).

[342] Dominik Becker et al. "The P2 experiment". In: *Eur. Phys. J. A* 54.11 (2018), p. 208. DOI: 10.1140/epja/i2018-12611-6. arXiv: 1802.04759 [nucl-ex] (cit. on pp. 130, 131).

[343] Manfred Lindner, Thomas Rink, and Manibrata Sen. "Light vector bosons and the weak mixing angle in the light of future germanium-based reactor CEνNS experiments". In: *JHEP* 08 (2024), p. 171. DOI: 10.1007/JHEP08(2024)171. arXiv: 2401.13025 [hep-ph] (cit. on pp. 131, 181).

[344] B. C. Cañas et al. "Future perspectives for a weak mixing angle measurement in coherent elastic neutrino nucleus scattering experiments". In: *Phys. Lett. B* 784 (2018), pp. 159–162. DOI: 10.1016/j.physletb.2018.07.049. arXiv: 1806.01310 [hep-ph] (cit. on p. 131).

[345] J. Benesch et al. "The MOLLER Experiment: An Ultra-Precise Measurement of the Weak Mixing Angle Using M\oller Scattering". In: (Nov. 2014). arXiv: 1411.4088 [nucl-ex] (cit. on p. 131).

[346] P. S. Bhupal Dev et al. "Searching for Z' bosons at the P2 experiment". In: *JHEP* 06 (2021), p. 039. DOI: 10.1007/JHEP06(2021)039. arXiv: 2103.09067 [hep-ph] (cit. on p. 131).

[347] J. Schechter and J. W. F. Valle. "Majorana Neutrinos and Magnetic Fields". In: *Phys. Rev. D* 24 (1981). [Erratum: Phys.Rev.D 25, 283 (1982)], pp. 1883–1889. DOI: 10.1103/PhysRevD.25.283 (cit. on pp. 133, 135).

[348] Robert E. Shrock. "Electromagnetic Properties and Decays of Dirac and Majorana Neutrinos in a General Class of Gauge Theories". In: *Nucl. Phys. B* 206 (1982), pp. 359–379. DOI: 10.1016/0550-3213(82)90273-5 (cit. on pp. 133, 135).

[349] Palash B. Pal and Lincoln Wolfenstein. "Radiative Decays of Massive Neutrinos". In: *Phys. Rev. D* 25 (1982), p. 766. DOI: 10.1103/PhysRevD.25.766 (cit. on pp. 133, 135).

[350] Jose F. Nieves. "Electromagnetic Properties of Majorana Neutrinos". In: *Phys. Rev. D* 26 (1982), p. 3152. DOI: 10.1103/PhysRevD.26.3152 (cit. on pp. 133–135).

[351] Boris Kayser. “Majorana Neutrinos and their Electromagnetic Properties”. In: *Phys. Rev. D* 26 (1982), p. 1662. DOI: 10.1103/PhysRevD.26.1662 (cit. on pp. 133–135).

[352] Boris Kayser. “CPT, CP, and c Phases and their Effects in Majorana Particle Processes”. In: *Phys. Rev. D* 30 (1984), p. 1023. DOI: 10.1103/PhysRevD.30.1023 (cit. on pp. 133, 134).

[353] Nicole F. Bell et al. “How magnetic is the Dirac neutrino?” In: *Phys. Rev. Lett.* 95 (2005), p. 151802. DOI: 10.1103/PhysRevLett.95.151802. arXiv: hep-ph/0504134 (cit. on p. 133).

[354] Nicole F. Bell et al. “Model independent bounds on magnetic moments of Majorana neutrinos”. In: *Phys. Lett. B* 642 (2006), pp. 377–383. DOI: 10.1016/j.physletb.2006.09.055. arXiv: hep-ph/0606248 (cit. on p. 133).

[355] H. Novales-Sanchez et al. “Effects of physics beyond the standard model on the neutrino charge radius: an effective Lagrangian approach”. In: *Phys. Rev. D* 78 (2008), p. 073014. DOI: 10.1103/PhysRevD.78.073014. arXiv: 0805.4177 [hep-ph] (cit. on p. 133).

[356] C. Broggini, C. Giunti, and A. Studenikin. “Electromagnetic Properties of Neutrinos”. In: *Adv. High Energy Phys.* 2012 (2012), p. 459526. DOI: 10.1155/2012/459526. arXiv: 1207.3980 [hep-ph] (cit. on p. 134).

[357] Carlo Giunti et al. “Electromagnetic neutrinos in laboratory experiments and astrophysics”. In: *Annalen Phys.* 528 (2016), pp. 198–215. DOI: 10.1002/andp.201500211. arXiv: 1506.05387 [hep-ph] (cit. on pp. 134, 135).

[358] Kazuo Fujikawa and Robert Shrock. “The Magnetic Moment of a Massive Neutrino and Neutrino Spin Rotation”. In: *Phys. Rev. Lett.* 45 (1980), p. 963. DOI: 10.1103/PhysRevLett.45.963 (cit. on p. 135).

[359] Z. Daraktchieva et al. “Final results on the neutrino magnetic moment from the MUNU experiment”. In: *Phys. Lett. B* 615 (2005), pp. 153–159. DOI: 10.1016/j.physletb.2005.04.030. arXiv: hep-ex/0502037 (cit. on pp. 136, 137, 163).

[360] L. A. Ahrens et al. “Determination of electroweak parameters from the elastic scattering of muon-neutrinos and anti-neutrinos on electrons”. In: *Phys. Rev. D* 41 (1990). Ed. by A. K. Mann et al., pp. 3297–3316. DOI: 10.1103/PhysRevD.41.3297 (cit. on pp. 136, 137, 149, 163).

[361] R. C. Allen et al. “Study of electron-neutrino electron elastic scattering at LAMPF”. In: *Phys. Rev. D* 47 (1993), pp. 11–28. DOI: 10.1103/PhysRevD.47.11 (cit. on pp. 136, 137, 149, 163).

[362] L. B. Auerbach et al. “Measurement of electron - neutrino - electron elastic scattering”. In: *Phys. Rev. D* 63 (2001), p. 112001. DOI: 10.1103/PhysRevD.63.112001. arXiv: hep-ex/0101039 (cit. on pp. 136, 137, 143, 149, 163).

[363] D. Aristizabal Sierra, V. De Romeri, and D. K. Papoulias. “Consequences of the Dresden-II reactor data for the weak mixing angle and new physics”. In: *JHEP* 09 (2022), p. 076. DOI: 10.1007/JHEP09(2022)076. arXiv: 2203.02414 [hep-ph] (cit. on p. 138).

[364] C. Caprini, S. Biller, and P. G. Ferreira. “Constraints on the electrical charge asymmetry of the universe”. In: *JCAP* 02 (2005), p. 006. DOI: 10.1088/1475-7516/2005/02/006. arXiv: hep-ph/0310066 (cit. on p. 138).

[365] Konstantin A. Kouzakov and Alexander I. Studenikin. “Electromagnetic properties of massive neutrinos in low-energy elastic neutrino-electron scattering”. In: *Phys. Rev. D* 95.5 (2017). [Erratum: Phys.Rev.D 96, 099904 (2017)], p. 055013. DOI: 10.1103/PhysRevD.95.055013. arXiv: 1703.00401 [hep-ph] (cit. on pp. 139, 160).

[366] S. N. Gninenko, N. V. Krasnikov, and A. Rubbia. “Search for millicharged particles in reactor neutrino experiments: A Probe of the PVLAS anomaly”. In: *Phys. Rev. D* 75 (2007), p. 075014. DOI: 10.1103/PhysRevD.75.075014. arXiv: hep-ph/0612203 (cit. on pp. 141, 142).

[367] H. B. Li et al. “Limit on the electron neutrino magnetic moment from the Kuo-Sheng reactor neutrino experiment”. In: *Phys. Rev. Lett.* 90 (2003), p. 131802. DOI: 10.1103/PhysRevLett.90.131802. arXiv: hep-ex/0212003 (cit. on pp. 141, 142).

[368] Alexander Studenikin. "New bounds on neutrino electric millicharge from limits on neutrino magnetic moment". In: *EPL* 107.2 (2014). [Erratum: EPL 107, 39901 (2014), Erratum: Europhys.Lett. 107, 39901 (2014)], p. 21001. DOI: 10.1209/0295-5075/107/21001. arXiv: 1302.1168 [hep-ph] (cit. on pp. 141, 142).

[369] Jiunn-Wei Chen et al. "Constraints on millicharged neutrinos via analysis of data from atomic ionizations with germanium detectors at sub-keV sensitivities". In: *Phys. Rev. D* 90.1 (2014), p. 011301. DOI: 10.1103/PhysRevD.90.011301. arXiv: 1405.7168 [hep-ph] (cit. on pp. 142, 162).

[370] K. -N. Huang and W. R. Johnson. "Multiconfiguration relativistic random-phase approximation. Theory". In: *Phys. Rev. A* 25 (2 Feb. 1982), pp. 634–649. DOI: 10.1103/PhysRevA.25.634. URL: https://link.aps.org/doi/10.1103/PhysRevA.25.634 (cit. on p. 142).

[371] Arindam Das et al. "Neutrino charge constraints from scattering to the weak gravity conjecture to neutron stars". In: *Phys. Rev. D* 102.11 (2020), p. 115009. DOI: 10.1103/PhysRevD.102.115009. arXiv: 2005.12304 [hep-ph] (cit. on p. 143).

[372] K. Abe et al. "Search for exotic neutrino-electron interactions using solar neutrinos in XMASS-I". In: *Phys. Lett. B* 809 (2020), p. 135741. DOI: 10.1016/j.physletb.2020.135741. arXiv: 2005.11891 [hep-ex] (cit. on pp. 143, 163).

[373] J. Bernabeu et al. "On the charge radius of the neutrino". In: *Phys. Rev. D* 62 (2000), p. 113012. DOI: 10.1103/PhysRevD.62.113012. arXiv: hep-ph/0008114 (cit. on p. 144).

[374] J. Bernabeu, J. Papavassiliou, and J. Vidal. "On the observability of the neutrino charge radius". In: *Phys. Rev. Lett.* 89 (2002). [Erratum: Phys.Rev.Lett. 89, 229902 (2002)], p. 101802. DOI: 10.1103/PhysRevLett.89.101802. arXiv: hep-ph/0206015 (cit. on p. 144).

[375] J. Bernabeu, J. Papavassiliou, and J. Vidal. "The Neutrino charge radius is a physical observable". In: *Nucl. Phys. B* 680 (2004), pp. 450–478. DOI: 10.1016/j.nuclphysb.2003.12.025. arXiv: hep-ph/0210055 (cit. on pp. 144, 145).

[376] L. A. Ahrens et al. “Determination of electroweak parameters from the elastic scattering of muon neutrinos and antineutrinos on electrons”. In: *Phys. Rev. D* 41 (11 June 1990), pp. 3297–3316. DOI: 10.1103/PhysRevD.41.3297. URL: https://link.aps.org/doi/10.1103/PhysRevD.41.3297 (cit. on pp. 145, 147–151).

[377] G. S. Vidyakin et al. “Limitations on the magnetic moment and charge radius of the electron-anti-neutrino”. In: *JETP Lett.* 55 (1992), pp. 206–210 (cit. on p. 149).

[378] P. Vilain et al. “Experimental study of electromagnetic properties of the muon-neutrino in neutrino - electron scattering”. In: *Phys. Lett. B* 345 (1995), pp. 115–118. DOI: 10.1016/0370-2693(94)01678-6 (cit. on p. 149).

[379] Matteo Cadeddu et al. “Neutrino Charge Radii From Coherent Elastic Neutrino-nucleus Scattering”. In: *Phys. Rev. D* 98.11 (2018). [Erratum: Phys.Rev.D 101, 059902 (2020)], p. 113010. DOI: 10.1142/9789811233913_0013. arXiv: 1810.05606 [hep-ph] (cit. on pp. 149, 150).

[380] Martin Hirsch, Enrico Nardi, and Diego Restrepo. “Bounds on the tau and muon neutrino vector and axial vector charge radius”. In: *Phys. Rev. D* 67 (2003), p. 033005. DOI: 10.1103/PhysRevD.67.033005. arXiv: hep-ph/0210137 (cit. on p. 150).

[381] E. Aprile et al. “Excess electronic recoil events in XENON1T”. In: *Phys. Rev. D* 102.7 (2020), p. 072004. DOI: 10.1103/PhysRevD.102.072004. arXiv: 2006.09721 [hep-ex] (cit. on p. 154).

[382] Luca Di Luzio et al. “Solar axions cannot explain the XENON1T excess”. In: *Phys. Rev. Lett.* 125.13 (2020), p. 131804. DOI: 10.1103/PhysRevLett.125.131804. arXiv: 2006.12487 [hep-ph] (cit. on p. 154).

[383] Amir N. Khan. “Can Nonstandard Neutrino Interactions explain the XENON1T spectral excess?” In: *Phys. Lett. B* 809 (2020), p. 135782. DOI: 10.1016/j.physletb.2020.135782. arXiv: 2006.12887 [hep-ph] (cit. on p. 154).

[384] Bartosz Fornal et al. “Boosted Dark Matter Interpretation of the XENON1T Excess”. In: *Phys. Rev. Lett.* 125.16 (2020), p. 161804. DOI: 10.1103/PhysRevLett.125.161804. arXiv: 2006.11264 [hep-ph] (cit. on p. 154).

[385] M Szydagis et al. “NEST: a comprehensive model for scintillation yield in liquid xenon”. In: *Journal of Instrumentation* 6.10 (Oct. 2011), P10002–P10002. ISSN: 1748-0221. DOI: 10.1088/1748-0221/6/10/p10002. URL: http://dx.doi.org/10.1088/1748-0221/6/10/P10002 (cit. on p. 155).

[386] J. Aalbers et al. “Cosmogenic production of Ar37 in the context of the LUX-ZEPLIN experiment”. In: *Phys. Rev. D* 105.8 (2022), p. 082004. DOI: 10.1103/PhysRevD.105.082004. arXiv: 2201.02858 [hep-ex] (cit. on p. 157).

[387] ShivaSankar K. A. et al. “Implications of first LZ and XENONnT results: A comparative study of neutrino properties and light mediators”. In: *Phys. Lett. B* 839 (2023), p. 137742. DOI: 10.1016/j.physletb.2023.137742. arXiv: 2208.06415 [hep-ph] (cit. on pp. 159, 162).

[388] Amir N. Khan. “Light new physics and neutrino electromagnetic interactions in XENONnT”. In: *Phys. Lett. B* 837 (2023), p. 137650. DOI: 10.1016/j.physletb.2022.137650. arXiv: 2208.02144 [hep-ph] (cit. on pp. 159, 162).

[389] Carlo Giunti and Christoph A. Ternes. “Testing neutrino electromagnetic properties at current and future dark matter experiments”. In: *Phys. Rev. D* 108.9 (2023), p. 095044. DOI: 10.1103/PhysRevD.108.095044. arXiv: 2309.17380 [hep-ph] (cit. on p. 159).

[390] D. W. Liu et al. “Limits on the neutrino magnetic moment using 1496 days of Super-Kamiokande-I solar neutrino data”. In: *Phys. Rev. Lett.* 93 (2004), p. 021802. DOI: 10.1103/PhysRevLett.93.021802. arXiv: hep-ex/0402015 (cit. on pp. 159, 163).

[391] S. Arceo-Díaz et al. “Constraint on the magnetic dipole moment of neutrinos by the tip-RGB luminosity in Centauri”. In: *Astroparticle Physics* 70 (2015), p. 1. ISSN: 0927-6505. DOI: https://doi.org/10.1016/j.astropartphys.2015.03.006. URL: https://www.sciencedirect.com/science/article/pii/S0927650515000468 (cit. on p. 160).

[392] S. Arceo-Díaz et al. “Constraint on the axion-electron coupling constant and the neutrino magnetic dipole moment by using the tip-RGB luminosity of fifty globular clusters”. In: (Oct. 2019). arXiv: 1910.10568 [astro-ph.SR] (cit. on p. 160).

[393] A. H. Córsico et al. “Constraining the neutrino magnetic dipole moment from white dwarf pulsations”. In: *JCAP* 08 (2014), p. 054. DOI: 10.1088/1475-7516/2014/08/054. arXiv: 1406.6034 [astro-ph.SR] (cit. on p. 160).

[394] Chung-Chun Hsieh et al. “Discovery potential of multiton xenon detectors in neutrino electromagnetic properties”. In: *Phys. Rev. D* 100.7 (2019), p. 073001. DOI: 10.1103/PhysRevD.100.073001. arXiv: 1903.06085 [hep-ph] (cit. on p. 161).

[395] L. Singh et al. “Constraints on millicharged particles with low threshold germanium detectors at Kuo-Sheng Reactor Neutrino Laboratory”. In: *Phys. Rev. D* 99.3 (2019), p. 032009. DOI: 10.1103/PhysRevD.99.032009. arXiv: 1808.02719 [hep-ph] (cit. on p. 161).

[396] H. Bonet et al. “First upper limits on neutrino electromagnetic properties from the CONUS experiment”. In: *Eur. Phys. J. C* 82.9 (2022), p. 813. DOI: 10.1140/epjc/s10052-022-10722-1. arXiv: 2201.12257 [hep-ex] (cit. on p. 163).

[397] Michael E. Peskin and Daniel V. Schroeder. *An Introduction to quantum field theory*. Reading, USA: Addison-Wesley, 1995. DOI: 10.1201/9780429503559 (cit. on p. 166).

[398] Peter Athron et al. “New physics explanations of a_μ in light of the FNAL muon $g-2$ measurement”. In: *JHEP* 09 (2021), p. 080. DOI: 10.1007/JHEP09(2021)080. arXiv: 2104.03691 [hep-ph] (cit. on p. 166).

[399] Manfred Lindner, Moritz Platscher, and Farinaldo S. Queiroz. “A Call for New Physics : The Muon Anomalous Magnetic Moment and Lepton Flavor Violation”. In: *Phys. Rept.* 731 (2018), pp. 1–82. DOI: 10.1016/j.physrep.2017.12.001. arXiv: 1610.06587 [hep-ph] (cit. on p. 166).

[400] D. P. Aguillard et al. “Measurement of the Positive Muon Anomalous Magnetic Moment to 0.20 ppm”. In: *Phys. Rev. Lett.* 131.16 (2023), p. 161802. DOI: 10.1103/PhysRevLett.131.161802. arXiv: 2308.06230 [hep-ex] (cit. on p. 166).

[401] B. Abi et al. “Measurement of the Positive Muon Anomalous Magnetic Moment to 0.46 ppm”. In: *Phys. Rev. Lett.* 126.14 (2021), p. 141801. DOI: 10.1103/PhysRevLett.126.141801. arXiv: 2104.03281 [hep-ex] (cit. on pp. 166, 177).

[402] G. W. Bennett et al. “Final Report of the Muon E821 Anomalous Magnetic Moment Measurement at BNL”. In: *Phys. Rev. D* 73 (2006), p. 072003. DOI: 10.1103/PhysRevD.73.072003. arXiv: hep-ex/0602035 (cit. on p. 166).

[403] Fred Jegerlehner and Andreas Nyffeler. “The Muon g-2”. In: *Phys. Rept.* 477 (2009), pp. 1–110. DOI: 10.1016/j.physrep.2009.04.003. arXiv: 0902.3360 [hep-ph] (cit. on pp. 166, 177).

[404] D. G. Cerdeno et al. “Muon anomalous magnetic moment in supersymmetric scenarios with an intermediate scale and nonuniversality”. In: *Phys. Rev. D* 64 (2001), p. 093012. DOI: 10.1103/PhysRevD.64.093012. arXiv: hep-ph/0104242 (cit. on p. 166).

[405] Alex Keshavarzi, Kim Siang Khaw, and Tamaki Yoshioka. “Muon g-2: A review”. In: *Nucl. Phys. B* 975 (2022), p. 115675. DOI: 10.1016/j.nuclphysb.2022.115675. arXiv: 2106.06723 [hep-ex] (cit. on p. 166).

[406] Song Li, Yang Xiao, and Jin Min Yang. “A pedagogical review on muon $g-2$”. In: *Mod. Phys.* 4 (2021), pp. 40–47. arXiv: 2110.04673 [hep-ph] (cit. on p. 166).

[407] T. Aoyama et al. “The anomalous magnetic moment of the muon in the Standard Model”. In: *Phys. Rept.* 887 (2020), pp. 1–166. DOI: 10.1016/j.physrep.2020.07.006. arXiv: 2006.04822 [hep-ph] (cit. on p. 166).

[408] Tatsumi Aoyama et al. “Complete Tenth-Order QED Contribution to the Muon g-2”. In: *Phys. Rev. Lett.* 109 (2012), p. 111808. DOI: 10.1103/PhysRevLett.109.111808. arXiv: 1205.5370 [hep-ph] (cit. on p. 166).

[409] Tatsumi Aoyama, Toichiro Kinoshita, and Makiko Nio. “Theory of the Anomalous Magnetic Moment of the Electron”. In: *Atoms* 7.1 (2019), p. 28. DOI: 10.3390/atoms7010028 (cit. on p. 166).

[410] Andrzej Czarnecki, William J. Marciano, and Arkady Vainshtein. “Refinements in electroweak contributions to the muon anomalous magnetic moment”. In: *Phys. Rev. D* 67 (2003). [Erratum: Phys.Rev.D 73, 119901 (2006)], p. 073006. DOI: 10.1103/PhysRevD.67.073006. arXiv: hep-ph/0212229 (cit. on p. 166).

[411] C. Gnendiger, D. Stöckinger, and H. Stöckinger-Kim. “The electroweak contributions to $(g-2)_\mu$ after the Higgs boson mass measurement”. In: *Phys. Rev. D* 88 (2013), p. 053005. DOI: 10.1103/PhysRevD.88.053005. arXiv: 1306.5546 [hep-ph] (cit. on p. 166).

[412] Michel Davier et al. “Reevaluation of the hadronic vacuum polarisation contributions to the Standard Model predictions of the muon $g-2$ and $\alpha(m_Z^2)$ using newest hadronic cross-section data”. In: *Eur. Phys. J. C* 77.12 (2017), p. 827. DOI: 10.1140/epjc/s10052-017-5161-6. arXiv: 1706.09436 [hep-ph] (cit. on p. 166).

[413] Alexander Keshavarzi, Daisuke Nomura, and Thomas Teubner. “Muon $g-2$ and $\alpha(M_Z^2)$: a new data-based analysis”. In: *Phys. Rev. D* 97.11 (2018), p. 114025. DOI: 10.1103/PhysRevD.97.114025. arXiv: 1802.02995 [hep-ph] (cit. on p. 166).

[414] Gilberto Colangelo, Martin Hoferichter, and Peter Stoffer. “Two-pion contribution to hadronic vacuum polarization”. In: *JHEP* 02 (2019), p. 006. DOI: 10.1007/JHEP02(2019)006. arXiv: 1810.00007 [hep-ph] (cit. on p. 166).

[415] Martin Hoferichter, Bai-Long Hoid, and Bastian Kubis. “Three-pion contribution to hadronic vacuum polarization”. In: *JHEP* 08 (2019), p. 137. DOI: 10.1007/JHEP08(2019)137. arXiv: 1907.01556 [hep-ph] (cit. on p. 166).

[416] M. Davier et al. “A new evaluation of the hadronic vacuum polarisation contributions to the muon anomalous magnetic moment and to $\boldsymbol{\alpha(m_Z^2)}$”. In: *Eur. Phys. J. C* 80.3 (2020). [Erratum: Eur.Phys.J.C 80, 410 (2020)], p. 241. DOI: 10.1140/epjc/s10052-020-7792-2. arXiv: 1908.00921 [hep-ph] (cit. on p. 166).

[417] Alexander Keshavarzi, Daisuke Nomura, and Thomas Teubner. “$g-2$ of charged leptons, $\alpha(M_Z^2)$, and the hyperfine splitting of muonium”. In: *Phys. Rev. D* 101.1 (2020), p. 014029. DOI: 10.1103/PhysRevD.101.014029. arXiv: 1911.00367 [hep-ph] (cit. on p. 166).

[418] Kirill Melnikov and Arkady Vainshtein. “Hadronic light-by-light scattering contribution to the muon anomalous magnetic moment revisited”. In: *Phys. Rev. D* 70 (2004), p. 113006. DOI: 10.1103/PhysRevD.70.113006. arXiv: hep-ph/0312226 (cit. on p. 166).

[419] Pere Masjuan and Pablo Sanchez-Puertas. “Pseudoscalar-pole contribution to the $(g_\mu-2)$: a rational approach”. In: *Phys. Rev. D* 95.5 (2017), p. 054026. DOI: 10.1103/PhysRevD.95.054026. arXiv: 1701.05829 [hep-ph] (cit. on p. 166).

[420] Gilberto Colangelo et al. “Dispersion relation for hadronic light-by-light scattering: two-pion contributions”. In: *JHEP* 04 (2017), p. 161. DOI: 10.1007/JHEP04(2017)161. arXiv: 1702.07347 [hep-ph] (cit. on p. 166).

[421] Martin Hoferichter et al. “Dispersion relation for hadronic light-by-light scattering: pion pole”. In: *JHEP* 10 (2018), p. 141. DOI: 10.1007/JHEP10(2018)141. arXiv: 1808.04823 [hep-ph] (cit. on p. 166).

[422] Antoine Gérardin, Harvey B. Meyer, and Andreas Nyffeler. “Lattice calculation of the pion transition form factor with $N_f = 2 + 1$ Wilson quarks”. In: *Phys. Rev. D* 100.3 (2019), p. 034520. DOI: 10.1103/PhysRevD.100.034520. arXiv: 1903.09471 [hep-lat] (cit. on p. 166).

[423] Johan Bijnens, Nils Hermansson-Truedsson, and Antonio Rodríguez-Sánchez. “Short-distance constraints for the HLbL contribution to the muon anomalous magnetic moment”. In: *Phys. Lett. B* 798 (2019), p. 134994. DOI: 10.1016/j.physletb.2019.134994. arXiv: 1908.03331 [hep-ph] (cit. on p. 166).

[424] Gilberto Colangelo et al. “Longitudinal short-distance constraints for the hadronic light-by-light contribution to $(g-2)_\mu$ with large-N_c Regge models”. In: *JHEP* 03 (2020), p. 101. DOI: 10.1007/JHEP03(2020)101. arXiv: 1910.13432 [hep-ph] (cit. on p. 166).

[425] Vladyslav Pauk and Marc Vanderhaeghen. “Single meson contributions to the muon‘s anomalous magnetic moment”. In: *Eur. Phys. J. C* 74.8 (2014), p. 3008. DOI: 10.1140/epjc/s10052-014-3008-y. arXiv: 1401.0832 [hep-ph] (cit. on p. 166).

[426] Igor Danilkin and Marc Vanderhaeghen. “Light-by-light scattering sum rules in light of new data”. In: *Phys. Rev. D* 95.1 (2017), p. 014019. DOI: 10.1103/PhysRevD.95.014019. arXiv: 1611.04646 [hep-ph] (cit. on p. 166).

[427] Friedrich Jegerlehner. *The Anomalous Magnetic Moment of the Muon*. Vol. 274. Cham: Springer, 2017. DOI: 10.1007/978-3-319-63577-4 (cit. on p. 166).

[428] M. Knecht et al. “Scalar meson contributions to a μ from hadronic light-by-light scattering”. In: *Phys. Lett. B* 787 (2018), pp. 111–123. DOI: 10.1016/j.physletb.2018.10.048. arXiv: 1808.03848 [hep-ph] (cit. on p. 166).

[429] Gernot Eichmann, Christian S. Fischer, and Richard Williams. "Kaon-box contribution to the anomalous magnetic moment of the muon". In: *Phys. Rev. D* 101.5 (2020), p. 054015. DOI: 10.1103/PhysRevD.101.054015. arXiv: 1910.06795 [hep-ph] (cit. on p. 166).

[430] Pablo Roig and Pablo Sanchez-Puertas. "Axial-vector exchange contribution to the hadronic light-by-light piece of the muon anomalous magnetic moment". In: *Phys. Rev. D* 101.7 (2020), p. 074019. DOI: 10.1103/PhysRevD.101.074019. arXiv: 1910.02881 [hep-ph] (cit. on p. 166).

[431] Thomas Blum et al. "Hadronic Light-by-Light Scattering Contribution to the Muon Anomalous Magnetic Moment from Lattice QCD". In: *Phys. Rev. Lett.* 124.13 (2020), p. 132002. DOI: 10.1103/PhysRevLett.124.132002. arXiv: 1911.08123 [hep-lat] (cit. on p. 166).

[432] Gilberto Colangelo et al. "Remarks on higher-order hadronic corrections to the muon g−2". In: *Phys. Lett. B* 735 (2014), pp. 90–91. DOI: 10.1016/j.physletb.2014.06.012. arXiv: 1403.7512 [hep-ph] (cit. on p. 166).

[433] Hartmut Wittig. "Progress on $(g-2)_\mu$ from Lattice QCD". In: *57th Rencontres de Moriond on Electroweak Interactions and Unified Theories*. June 2023. arXiv: 2306.04165 [hep-ph] (cit. on p. 166).

[434] M. Della Morte et al. "The hadronic vacuum polarization contribution to the muon $g-2$ from lattice QCD". In: *JHEP* 10 (2017), p. 020. DOI: 10.1007/JHEP10(2017)020. arXiv: 1705.01775 [hep-lat] (cit. on p. 166).

[435] Sz. Borsanyi et al. "Leading hadronic contribution to the muon magnetic moment from lattice QCD". In: *Nature* 593.7857 (2021), pp. 51–55. DOI: 10.1038/s41586-021-03418-1. arXiv: 2002.12347 [hep-lat] (cit. on p. 166).

[436] Seungwon Baek et al. "Muon anomalous g-2 and gauged L(muon) - L(tau) models". In: *Phys. Rev. D* 64 (2001), p. 055006. DOI: 10.1103/PhysRevD.64.055006. arXiv: hep-ph/0104141 (cit. on pp. 166, 179).

[437] Ernest Ma, D. P. Roy, and Sourov Roy. "Gauged L(mu) - L(tau) with large muon anomalous magnetic moment and the bimaximal mixing of neutrinos". In: *Phys. Lett. B* 525 (2002), pp. 101–106. DOI: 10.1016/S0370-2693(01)01428-9. arXiv: hep-ph/0110146 (cit. on p. 166).

[438] Wolfgang Altmannshofer, Marcela Carena, and Andreas Crivellin. "$L_\mu - L_\tau$ theory of Higgs flavor violation and $(g-2)_\mu$". In: *Phys. Rev. D* 94.9 (2016), p. 095026. DOI: 10.1103/PhysRevD.94.095026. arXiv: 1604.08221 [hep-ph] (cit. on p. 166).

[439] D. W. P. Amaral et al. "Confirming $U(1)_{L_\mu - L_\tau}$ as a solution for $(g-2)_\mu$ with neutrinos". In: *Eur. Phys. J. C* 81.10 (2021), p. 861. DOI: 10.1140/epjc/s10052-021-09670-z. arXiv: 2104.03297 [hep-ph] (cit. on p. 166).

[440] Shun Zhou. "Neutrino masses, leptonic flavor mixing, and muon (g−2) in the seesaw model with the gauge symmetry". In: *Chin. Phys. C* 46.1 (2022), p. 011001. DOI: 10.1088/1674-1137/ac2a25. arXiv: 2104.06858 [hep-ph] (cit. on p. 166).

[441] Timothy Hapitas, Douglas Tuckler, and Yue Zhang. "General kinetic mixing in gauged U(1)Lμ-Lτ model for muon g-2 and dark matter". In: *Phys. Rev. D* 105.1 (2022), p. 016014. DOI: 10.1103/PhysRevD.105.016014. arXiv: 2108.12440 [hep-ph] (cit. on p. 166).

[442] Yu Cheng, Xiao-Gang He, and Jin Sun. "Widening the U(1)Lμ−LτZ' mass range for resolving the muon g-2 anomaly". In: *Phys. Lett. B* 827 (2022), p. 136989. DOI: 10.1016/j.physletb.2022.136989. arXiv: 2112.09920 [hep-ph] (cit. on p. 166).

[443] Dorian Warren Praia do Amaral et al. "Solar neutrino probes of the muon anomalous magnetic moment in the gauged $\mathrm{U}(1)_{L_\mu - L_\tau}$". In: *JHEP* 12 (2020), p. 155. DOI: 10.1007/JHEP12(2020)155. arXiv: 2006.11225 [hep-ph] (cit. on pp. 166, 170, 171).

[444] O. G. Miranda et al. "Probing new neutral gauge bosons with $CE\nu NS$ and neutrino-electron scattering". In: *Phys. Rev. D* 101.7 (2020), p. 073005. DOI: 10.1103/PhysRevD.101.073005. arXiv: 2002.01482 [hep-ph] (cit. on p. 166).

[445] Stanley J. Brodsky and Eduardo De Rafael. "SUGGESTED BOSON - LEPTON PAIR COUPLINGS AND THE ANOMALOUS MAGNETIC MOMENT OF THE MUON". In: *Phys. Rev.* 168 (1968), pp. 1620–1622. DOI: 10.1103/PhysRev.168.1620 (cit. on p. 166).

[446] Miguel Escudero et al. "Cosmology with A Very Light $\mathrm{L}_\mu - \mathrm{L}_\tau$ Gauge Boson". In: *JHEP* 03 (2019), p. 071. DOI: 10.1007/JHEP03(2019)071. arXiv: 1901.02010 [hep-ph] (cit. on p. 167).

[447] David G. Cerdeño et al. “Medium effects in supernovae constraints on light mediators”. In: *Phys. Rev. D* 104.6 (2021), p. 063013. DOI: 10.1103/PhysRevD.104.063013. arXiv: 2106.11660 [hep-ph] (cit. on p. 167).

[448] David G. Cerdeño, Marina Cermeño, and Yasaman Farzan. “Constraints from the duration of supernova neutrino burst on on-shell light gauge boson production by neutrinos”. In: *Phys. Rev. D* 107.12 (2023), p. 123012. DOI: 10.1103/PhysRevD.107.123012. arXiv: 2301.00661 [hep-ph] (cit. on p. 167).

[449] Paul Langacker. “The Physics of Heavy Z' Gauge Bosons”. In: *Rev. Mod. Phys.* 81 (2009), pp. 1199–1228. DOI: 10.1103/RevModPhys.81.1199. arXiv: 0801.1345 [hep-ph] (cit. on pp. 168, 178).

[450] Jiajun Liao and Danny Marfatia. “COHERENT constraints on nonstandard neutrino interactions”. In: *Phys. Lett. B* 775 (2017), pp. 54–57. DOI: 10.1016/j.physletb.2017.10.046. arXiv: 1708.04255 [hep-ph] (cit. on pp. 168, 175, 176, 196).

[451] D. K. Papoulias and T. S. Kosmas. “COHERENT constraints to conventional and exotic neutrino physics”. In: *Phys. Rev. D* 97.3 (2018), p. 033003. DOI: 10.1103/PhysRevD.97.033003. arXiv: 1711.09773 [hep-ph] (cit. on pp. 168, 176, 196).

[452] Julien Billard, Joseph Johnston, and Bradley J. Kavanagh. “Prospects for exploring New Physics in Coherent Elastic Neutrino-Nucleus Scattering”. In: *JCAP* 11 (2018), p. 016. DOI: 10.1088/1475-7516/2018/11/016. arXiv: 1805.01798 [hep-ph] (cit. on pp. 168, 176).

[453] Amir N. Khan and Werner Rodejohann. “New physics from COHERENT data with an improved quenching factor”. In: *Phys. Rev. D* 100.11 (2019), p. 113003. DOI: 10.1103/PhysRevD.100.113003. arXiv: 1907.12444 [hep-ph] (cit. on pp. 168, 174, 176, 196).

[454] M. Cadeddu et al. “Constraints on light vector mediators through coherent elastic neutrino nucleus scattering data from COHERENT”. In: *JHEP* 01 (2021), p. 116. DOI: 10.1007/JHEP01(2021)116. arXiv: 2008.05022 [hep-ph] (cit. on pp. 168, 170, 171, 175, 176, 178, 179).

[455] Enrico Bertuzzo, Giovanni Grilli di Cortona, and Lucas Magno D. Ramos. "Probing light vector mediators with coherent scattering at future facilities". In: *JHEP* 06 (2022), p. 075. DOI: 10.1007/JHEP06(2022)075. arXiv: 2112.04020 [hep-ph] (cit. on pp. 168, 171, 176, 178, 179).

[456] B. C. Allanach, Joe Davighi, and Scott Melville. "An Anomaly-free Atlas: charting the space of flavour-dependent gauged $U(1)$ extensions of the Standard Model". In: *JHEP* 02 (2019). [Erratum: JHEP 08, 064 (2019)], p. 082. DOI: 10.1007/JHEP02(2019)082. arXiv: 1812.04602 [hep-ph] (cit. on p. 168).

[457] Hye-Sung Lee and Ernest Ma. "Gauged $B - x_i L$ origin of R Parity and its implications". In: *Phys. Lett. B* 688 (2010), pp. 319–322. DOI: 10.1016/j.physletb.2010.04.032. arXiv: 1001.0768 [hep-ph] (cit. on p. 169).

[458] Takeshi Araki, Julian Heeck, and Jisuke Kubo. "Vanishing Minors in the Neutrino Mass Matrix from Abelian Gauge Symmetries". In: *JHEP* 07 (2012), p. 083. DOI: 10.1007/JHEP07(2012)083. arXiv: 1203.4951 [hep-ph] (cit. on p. 169).

[459] Wolfgang Altmannshofer et al. "Neutrino Tridents at DUNE". In: *Phys. Rev. D* 100.11 (2019), p. 115029. DOI: 10.1103/PhysRevD.100.115029. arXiv: 1902.06765 [hep-ph] (cit. on pp. 170, 171, 179).

[460] Heerak Banerjee and Sourov Roy. "Signatures of supersymmetry and $L_\mu - L_\tau$ gauge bosons at Belle-II". In: *Phys. Rev. D* 99.3 (2019), p. 035035. DOI: 10.1103/PhysRevD.99.035035. arXiv: 1811.00407 [hep-ph] (cit. on pp. 170, 171, 179).

[461] Heerak Banerjee, Bhaskar Dutta, and Sourov Roy. "Probing Lμ-Lτ models with CEνNS: A new look at the combined COHERENT CsI and Ar data". In: *Phys. Rev. D* 104.1 (2021), p. 015015. DOI: 10.1103/PhysRevD.104.015015. arXiv: 2103.10196 [hep-ph] (cit. on pp. 170, 171, 175, 179).

[462] Manfred Lindner, Werner Rodejohann, and Xun-Jie Xu. "Coherent Neutrino-Nucleus Scattering and new Neutrino Interactions". In: *JHEP* 03 (2017), p. 097. DOI: 10.1007/JHEP03(2017)097. arXiv: 1612.04150 [hep-ph] (cit. on p. 172).

[463] Yasaman Farzan et al. "Probing neutrino coupling to a light scalar with coherent neutrino scattering". In: *JHEP* 05 (2018), p. 066. DOI: 10.1007/JHEP05(2018)066. arXiv: 1802.05171 [hep-ph] (cit. on pp. 172, 173).

[464] D. Aristizabal Sierra et al. “Coherent elastic neutrino-nucleus scattering in multi-ton scale dark matter experiments: Classification of vector and scalar interactions new physics signals”. In: *JHEP* 12 (2019), p. 124. DOI: 10.1007/JHEP12(2019)124. arXiv: 1910.12437 [hep-ph] (cit. on pp. 172, 173).

[465] Martin Hoferichter et al. “High-Precision Determination of the Pion-Nucleon σ Term from Roy-Steiner Equations”. In: *Phys. Rev. Lett.* 115 (2015), p. 092301. DOI: 10.1103/PhysRevLett.115.092301. arXiv: 1506.04142 [hep-ph] (cit. on pp. 173, 174).

[466] S. Durr et al. “Lattice computation of the nucleon scalar quark contents at the physical point”. In: *Phys. Rev. Lett.* 116.17 (2016), p. 172001. DOI: 10.1103/PhysRevLett.116.172001. arXiv: 1510.08013 [hep-lat] (cit. on pp. 173, 174).

[467] John Ellis, Natsumi Nagata, and Keith A. Olive. “Uncertainties in WIMP Dark Matter Scattering Revisited”. In: *Eur. Phys. J. C* 78.7 (2018), p. 569. DOI: 10.1140/epjc/s10052-018-6047-y. arXiv: 1805.09795 [hep-ph] (cit. on p. 173).

[468] C. Alexandrou et al. “Nucleon axial, tensor, and scalar charges and σ-terms in lattice QCD”. In: *Phys. Rev. D* 102.5 (2020), p. 054517. DOI: 10.1103/PhysRevD.102.054517. arXiv: 1909.00485 [hep-lat] (cit. on pp. 173, 174).

[469] J. M. Alarcón. “Brief history of the pion–nucleon sigma term”. In: *Eur. Phys. J. ST* 230.6 (2021), pp. 1609–1622. DOI: 10.1140/epjs/s11734-021-00145-6. arXiv: 2205.01108 [hep-ph] (cit. on p. 174).

[470] Jacobo Ruiz de Elvira et al. “Extracting the σ-term from low-energy pion-nucleon scattering”. In: *J. Phys. G* 45.2 (2018), p. 024001. DOI: 10.1088/1361-6471/aa9422. arXiv: 1706.01465 [hep-ph] (cit. on p. 174).

[471] E. Friedman and A. Gal. “The pion-nucleon σ term from pionic atoms”. In: *Phys. Lett. B* 792 (2019), pp. 340–344. DOI: 10.1016/j.physletb.2019.03.036. arXiv: 1901.03130 [nucl-th] (cit. on p. 174).

[472] Andreas Crivellin, Martin Hoferichter, and Massimiliano Procura. “Accurate evaluation of hadronic uncertainties in spin-independent WIMP-nucleon scattering: Disentangling two- and three-flavor effects”. In: *Phys. Rev. D* 89

(2014), p. 054021. DOI: 10.1103/PhysRevD.89.054021. arXiv: 1312.4951 [hep-ph] (cit. on p. 174).

[473] Anna M. Suliga and Irene Tamborra. "Astrophysical constraints on non-standard coherent neutrino-nucleus scattering". In: *Phys. Rev. D* 103.8 (2021), p. 083002. DOI: 10.1103/PhysRevD.103.083002. arXiv: 2010.14545 [hep-ph] (cit. on pp. 174, 180).

[474] Marco Cirelli, Eugenio Del Nobile, and Paolo Panci. "Tools for model-independent bounds in direct dark matter searches". In: *JCAP* 10 (2013), p. 019. DOI: 10.1088/1475-7516/2013/10/019. arXiv: 1307.5955 [hep-ph] (cit. on p. 174).

[475] Peter B. Denton, Yasaman Farzan, and Ian M. Shoemaker. "Testing large non-standard neutrino interactions with arbitrary mediator mass after COHERENT data". In: *JHEP* 07 (2018), p. 037. DOI: 10.1007/JHEP07(2018)037. arXiv: 1804.03660 [hep-ph] (cit. on p. 175).

[476] Bhaskar Dutta et al. "Searching for Beyond the Standard Model Physics with COHERENT Energy and Timing Data". In: *Phys. Rev. Lett.* 123.6 (2019), p. 061801. DOI: 10.1103/PhysRevLett.123.061801. arXiv: 1903.10666 [hep-ph] (cit. on pp. 175, 196).

[477] Mohammad Abdullah et al. "Coherent elastic neutrino nucleus scattering as a probe of a Z' through kinetic and mass mixing effects". In: *Phys. Rev. D* 98.1 (2018), p. 015005. DOI: 10.1103/PhysRevD.98.015005. arXiv: 1803.01224 [hep-ph] (cit. on p. 175).

[478] Philip Ilten et al. "Serendipity in dark photon searches". In: *JHEP* 06 (2018), p. 004. DOI: 10.1007/JHEP06(2018)004. arXiv: 1801.04847 [hep-ph] (cit. on p. 175).

[479] E. M. Riordan et al. "A Search for Short Lived Axions in an Electron Beam Dump Experiment". In: *Phys. Rev. Lett.* 59 (1987), p. 755. DOI: 10.1103/PhysRevLett.59.755 (cit. on p. 175).

[480] J. D. Bjorken et al. "Search for Neutral Metastable Penetrating Particles Produced in the SLAC Beam Dump". In: *Phys. Rev. D* 38 (1988), p. 3375. DOI: 10.1103/PhysRevD.38.3375 (cit. on p. 175).

[481] A. Bross et al. "A Search for Shortlived Particles Produced in an Electron Beam Dump". In: *Phys. Rev. Lett.* 67 (1991), pp. 2942–2945. DOI: 10.1103/PhysRevLett.67.2942 (cit. on p. 175).

[482] A. Konaka et al. “Search for Neutral Particles in Electron Beam Dump Experiment”. In: *Phys. Rev. Lett.* 57 (1986). Ed. by S. C. Loken, p. 659. DOI: 10.1103/PhysRevLett.57.659 (cit. on p. 175).

[483] M. Davier and H. Nguyen Ngoc. “An Unambiguous Search for a Light Higgs Boson”. In: *Phys. Lett. B* 229 (1989), pp. 150–155. DOI: 10.1016/0370-2693(89)90174-3 (cit. on p. 175).

[484] James D. Bjorken et al. “New Fixed-Target Experiments to Search for Dark Gauge Forces”. In: *Phys. Rev. D* 80 (2009), p. 075018. DOI: 10.1103/PhysRevD.80.075018. arXiv: 0906.0580 [hep-ph] (cit. on p. 175).

[485] Sarah Andreas, Carsten Niebuhr, and Andreas Ringwald. “New Limits on Hidden Photons from Past Electron Beam Dumps”. In: *Phys. Rev. D* 86 (2012), p. 095019. DOI: 10.1103/PhysRevD.86.095019. arXiv: 1209.6083 [hep-ph] (cit. on p. 175).

[486] J. Blumlein et al. “Limits on neutral light scalar and pseudoscalar particles in a proton beam dump experiment”. In: *Z. Phys. C* 51 (1991), pp. 341–350. DOI: 10.1007/BF01548556 (cit. on p. 175).

[487] J. Blumlein et al. “Limits on the mass of light (pseudo)scalar particles from Bethe-Heitler e+ e- and mu+ mu- pair production in a proton - iron beam dump experiment”. In: *Int. J. Mod. Phys. A* 7 (1992), pp. 3835–3850. DOI: 10.1142/S0217751X9200171X (cit. on p. 175).

[488] Johannes Blumlein and Jurgen Brunner. “New Exclusion Limits for Dark Gauge Forces from Beam-Dump Data”. In: *Phys. Lett. B* 701 (2011), pp. 155–159. DOI: 10.1016/j.physletb.2011.05.046. arXiv: 1104.2747 [hep-ex] (cit. on p. 175).

[489] Johannes Blümlein and Jürgen Brunner. “New Exclusion Limits on Dark Gauge Forces from Proton Bremsstrahlung in Beam-Dump Data”. In: *Phys. Lett. B* 731 (2014), pp. 320–326. DOI: 10.1016/j.physletb.2014.02.029. arXiv: 1311.3870 [hep-ph] (cit. on p. 175).

[490] F. Bergsma et al. “Search for Axion Like Particle Production in 400-GeV Proton - Copper Interactions”. In: *Phys. Lett. B* 157 (1985), pp. 458–462. DOI: 10.1016/0370-2693(85)90400-9 (cit. on p. 175).

[491] S. N. Gninenko. “Constraints on sub-GeV hidden sector gauge bosons from a search for heavy neutrino decays”. In: *Phys. Lett. B* 713 (2012), pp. 244–248. DOI: 10.1016/j.physletb.2012.06.002. arXiv: 1204.3583 [hep-ph] (cit. on p. 175).

[492] P. Astier et al. “Search for heavy neutrinos mixing with tau neutrinos”. In: *Phys. Lett. B* 506 (2001), pp. 27–38. DOI: 10.1016/S0370-2693(01)00362-8. arXiv: hep-ex/0101041 (cit. on p. 175).

[493] G. Bernardi et al. “Search for Neutrino Decay”. In: *Phys. Lett. B* 166 (1986), pp. 479–483. DOI: 10.1016/0370-2693(86)91602-3 (cit. on p. 175).

[494] S. N. Gninenko. “Stringent limits on the $\pi^0 \to \gamma X, X \to e + e-$ decay from neutrino experiments and constraints on new light gauge bosons”. In: *Phys. Rev. D* 85 (2012), p. 055027. DOI: 10.1103/PhysRevD.85.055027. arXiv: 1112.5438 [hep-ph] (cit. on p. 175).

[495] H. Merkel et al. “Search at the Mainz Microtron for Light Massive Gauge Bosons Relevant for the Muon g-2 Anomaly”. In: *Phys. Rev. Lett.* 112.22 (2014), p. 221802. DOI: 10.1103/PhysRevLett.112.221802. arXiv: 1404.5502 [hep-ex] (cit. on p. 175).

[496] S. Abrahamyan et al. “Search for a New Gauge Boson in Electron-Nucleus Fixed-Target Scattering by the APEX Experiment”. In: *Phys. Rev. Lett.* 107 (2011), p. 191804. DOI: 10.1103/PhysRevLett.107.191804. arXiv: 1108.2750 [hep-ex] (cit. on p. 175).

[497] J. P. Lees et al. “Search for a Dark Photon in e^+e^- Collisions at BaBar”. In: *Phys. Rev. Lett.* 113.20 (2014), p. 201801. DOI: 10.1103/PhysRevLett.113.201801. arXiv: 1406.2980 [hep-ex] (cit. on p. 175).

[498] F. Archilli et al. “Search for a vector gauge boson in ϕ meson decays with the KLOE detector”. In: *Phys. Lett. B* 706 (2012), pp. 251–255. DOI: 10.1016/j.physletb.2011.11.033. arXiv: 1110.0411 [hep-ex] (cit. on p. 175).

[499] A. Anastasi et al. “Limit on the production of a new vector boson in $\mathrm{e^+e^-} \to \mathrm{U}\gamma$, $\mathrm{U} \to \pi^+\pi^-$ with the KLOE experiment”. In: *Phys. Lett. B* 757 (2016), pp. 356–361. DOI: 10.1016/j.physletb.2016.04.019. arXiv: 1603.06086 [hep-ex] (cit. on p. 175).

[500] Roel Aaij et al. “Search for Dark Photons Produced in 13 TeV pp Collisions”. In: *Phys. Rev. Lett.* 120.6 (2018), p. 061801. DOI: 10.1103/PhysRevLett.120.061801. arXiv: 1710.02867 [hep-ex] (cit. on p. 175).

[501] J. R. Batley et al. “Search for the dark photon in π^0 decays”. In: *Phys. Lett. B* 746 (2015), pp. 178–185. DOI: 10.1016/j.physletb.2015.04.068. arXiv: 1504.00607 [hep-ex] (cit. on p. 175).

[502] D. Banerjee et al. “Improved limits on a hypothetical X(16.7) boson and a dark photon decaying into e^+e^- pairs”. In: *Phys. Rev. D* 101.7 (2020), p. 071101. DOI: 10.1103/PhysRevD.101.071101. arXiv: 1912.11389 [hep-ex] (cit. on p. 175).

[503] J. P. Lees et al. “Search for Invisible Decays of a Dark Photon Produced in e^+e^- Collisions at BaBar”. In: *Phys. Rev. Lett.* 119.13 (2017), p. 131804. DOI: 10.1103/PhysRevLett.119.131804. arXiv: 1702.03327 [hep-ex] (cit. on p. 175).

[504] Pilar Coloma, M. C. Gonzalez-Garcia, and Michele Maltoni. “Neutrino oscillation constraints on U(1)’ models: from non-standard interactions to long-range forces”. In: *JHEP* 01 (2021). [Erratum: JHEP 11, 115 (2022)], p. 114. DOI: 10.1007/JHEP01(2021)114. arXiv: 2009.14220 [hep-ph] (cit. on pp. 176, 178).

[505] Rabindra N. Mohapatra. “From Old Symmetries to New Symmetries: Quarks, Leptons and B-L”. In: *Int. J. Mod. Phys. A* 29.29 (2014), p. 1430066. DOI: 10.1142/S0217751X1430066X. arXiv: 1409.7557 [hep-ph] (cit. on p. 178).

[506] Satomi Okada. “Z' Portal Dark Matter in the Minimal $B-L$ Model”. In: *Adv. High Energy Phys.* 2018 (2018), p. 5340935. DOI: 10.1155/2018/5340935. arXiv: 1803.06793 [hep-ph] (cit. on p. 178).

[507] Leon M. G. de la Vega et al. “Complementarity between dark matter direct searches and CEνNS experiments in U(1)’ models”. In: *JHEP* 09 (2021), p. 146. DOI: 10.1007/JHEP09(2021)146. arXiv: 2107.04037 [hep-ph] (cit. on p. 178).

[508] X. G. He et al. “NEW Z-prime PHENOMENOLOGY”. In: *Phys. Rev. D* 43 (1991), pp. 22–24. DOI: 10.1103/PhysRevD.43.R22 (cit. on p. 179).

[509] Sergei Gninenko and Dmitry Gorbunov. “Refining constraints from Borexino measurements on a light Z’-boson coupled to Lμ-Lτ current”. In: *Phys. Lett. B* 823 (2021), p. 136739. DOI: 10.1016/j.physletb.2021.136739. arXiv: 2007.16098 [hep-ph] (cit. on p. 179).

[510] Albert M Sirunyan et al. “Search for an $L_\mu - L_\tau$ gauge boson using Z$\to 4\mu$ events in proton-proton collisions at $\sqrt{s} = 13$ TeV”. In: *Phys. Lett. B* 792 (2019), pp. 345–368. DOI: 10.1016/j.physletb.2019.01.072. arXiv: 1808.03684 [hep-ex] (cit. on p. 179).

[511] J. P. Lees et al. “Search for a muonic dark force at BABAR”. In: *Phys. Rev. D* 94.1 (2016), p. 011102. DOI: 10.1103/PhysRevD.94.011102. arXiv: 1606.03501 [hep-ex] (cit. on p. 179).

[512] S. R. Mishra et al. “Neutrino Tridents and W Z Interference”. In: *Phys. Rev. Lett.* 66 (1991), pp. 3117–3120. DOI: 10.1103/PhysRevLett.66.3117 (cit. on p. 179).

[513] Wolfgang Altmannshofer et al. “Neutrino Trident Production: A Powerful Probe of New Physics with Neutrino Beams”. In: *Phys. Rev. Lett.* 113 (2014), p. 091801. DOI: 10.1103/PhysRevLett.113.091801. arXiv: 1406.2332 [hep-ph] (cit. on p. 179).

[514] G. Bellini et al. “Precision measurement of the 7Be solar neutrino interaction rate in Borexino”. In: *Phys. Rev. Lett.* 107 (2011), p. 141302. DOI: 10.1103/PhysRevLett.107.141302. arXiv: 1104.1816 [hep-ex] (cit. on p. 179).

[515] Ayuki Kamada and Hai-Bo Yu. “Coherent Propagation of PeV Neutrinos and the Dip in the Neutrino Spectrum at IceCube”. In: *Phys. Rev. D* 92.11 (2015), p. 113004. DOI: 10.1103/PhysRevD.92.113004. arXiv: 1504.00711 [hep-ph] (cit. on p. 179).

[516] Riccardo Barbieri and Torleif Erik Oskar Ericson. “Evidence Against the Existence of a Low Mass Scalar Boson from Neutron-Nucleus Scattering”. In: *Phys. Lett. B* 57 (1975), pp. 270–272. DOI: 10.1016/0370-2693(75)90073-8 (cit. on p. 179).

[517] J. Schmiedmayer, H. Rauch, and P. Riehs. “Measurement of the Electric Polarizability of the Neutron”. In: *Phys. Rev. Lett.* 61 (1988), pp. 1065–1068. DOI: 10.1103/PhysRevLett.61.1065 (cit. on p. 179).

[518] H. Leeb and J. Schmiedmayer. "Constraint on hypothetical light interacting bosons from low-energy neutron experiments". In: *Phys. Rev. Lett.* 68 (1992), pp. 1472–1475. DOI: 10.1103/PhysRevLett.68.1472 (cit. on p. 179).

[519] Jeffrey M. Berryman et al. "Lepton-Number-Charged Scalars and Neutrino Beamstrahlung". In: *Phys. Rev. D* 97.7 (2018), p. 075030. DOI: 10.1103/PhysRevD.97.075030. arXiv: 1802.00009 [hep-ph] (cit. on p. 179).

[520] Mikhail S. Bilenky and Arcadi Santamaria. "'Secret' neutrino interactions". In: *Neutrino Mixing: Meeting in Honor of Samoil Bilenky's 70th Birthday*. Aug. 1999, pp. 50–61. arXiv: hep-ph/9908272 (cit. on p. 179).

[521] A. P. Lessa and O. L. G. Peres. "Revising limits on neutrino-Majoron couplings". In: *Phys. Rev. D* 75 (2007), p. 094001. DOI: 10.1103/PhysRevD.75.094001. arXiv: hep-ph/0701068 (cit. on p. 179).

[522] P. S. Pasquini and O. L. G. Peres. "Bounds on Neutrino-Scalar Yukawa Coupling". In: *Phys. Rev. D* 93.5 (2016). [Erratum: Phys.Rev.D 93, 079902 (2016)], p. 053007. DOI: 10.1103/PhysRevD.93.053007. arXiv: 1511.01811 [hep-ph] (cit. on p. 179).

[523] Gordan Krnjaic et al. "Probing Muonphilic Force Carriers and Dark Matter at Kaon Factories". In: *Phys. Rev. Lett.* 124.4 (2020), p. 041802. DOI: 10.1103/PhysRevLett.124.041802. arXiv: 1902.07715 [hep-ph] (cit. on p. 179).

[524] Vedran Brdar et al. "Revisiting neutrino self-interaction constraints from Z and τ decays". In: *Phys. Rev. D* 101.11 (2020), p. 115001. DOI: 10.1103/PhysRevD.101.115001. arXiv: 2003.05339 [hep-ph] (cit. on p. 179).

[525] M. Agostini et al. "Results on $\beta\beta$ decay with emission of two neutrinos or Majorons in^{76} Ge from GERDA Phase I". In: *Eur. Phys. J. C* 75.9 (2015), p. 416. DOI: 10.1140/epjc/s10052-015-3627-y. arXiv: 1501.02345 [nucl-ex] (cit. on p. 179).

[526] A. Gando et al. "Limits on Majoron-emitting double-beta decays of Xe-136 in the KamLAND-Zen experiment". In: *Phys. Rev. C* 86 (2012), p. 021601. DOI: 10.1103/PhysRevC.86.021601. arXiv: 1205.6372 [hep-ex] (cit. on p. 179).

[527] Kfir Blum, Yosef Nir, and Michal Shavit. “Neutrinoless double-beta decay with massive scalar emission”. In: *Phys. Lett. B* 785 (2018), pp. 354–361. DOI: 10.1016/j.physletb.2018.08.022. arXiv: 1802.08019 [hep-ph] (cit. on p. 179).

[528] N. Ackermann et al. “The CONUS+ experiment”. In: (July 2024). arXiv: 2407.11912 [hep-ex] (cit. on p. 181).

[529] D. K. Papoulias et al. “Novel neutrino-floor and dark matter searches with deformed shell model calculations”. In: *Adv. High Energy Phys.* 2018 (2018), p. 6031362. DOI: 10.1155/2018/6031362. arXiv: 1804.11319 [hep-ph] (cit. on p. 196).

[530] D. K. Papoulias, T. S. Kosmas, and Y. Kuno. “Recent probes of standard and non-standard neutrino physics with nuclei”. In: *Front. in Phys.* 7 (2019), p. 191. DOI: 10.3389/fphy.2019.00191. arXiv: 1911.00916 [hep-ph] (cit. on p. 196).